



**HAL**  
open science

## Wind erosion in presence of vegetation

Royston Fernandes

► **To cite this version:**

Royston Fernandes. Wind erosion in presence of vegetation. Ecology, environment. Université de Bordeaux, 2019. English. NNT : 2019BORD0194 . tel-02918326

**HAL Id: tel-02918326**

**<https://theses.hal.science/tel-02918326v1>**

Submitted on 20 Aug 2020

**HAL** is a multi-disciplinary open access archive for the deposit and dissemination of scientific research documents, whether they are published or not. The documents may come from teaching and research institutions in France or abroad, or from public or private research centers.

L'archive ouverte pluridisciplinaire **HAL**, est destinée au dépôt et à la diffusion de documents scientifiques de niveau recherche, publiés ou non, émanant des établissements d'enseignement et de recherche français ou étrangers, des laboratoires publics ou privés.

THÈSE PRÉSENTÉE  
POUR OBTENIR LE GRADE DE  
**DOCTEUR DE**  
**L'UNIVERSITÉ DE BORDEAUX**

ÉCOLE DOCTORALE SCIENCES ET ENVIRONNEMENTS  
SPÉCIALITÉ: PHYSIQUE DE L'ENVIRONNEMENT

Par Royston FERNANDES

**Wind erosion in presence of sparse vegetation**

Sous la direction de Sylvain DUPONT et co-encadrement de Eric LAMAUD

Soutenue le 29/10/2019

Membres du jury :

Mme. MARTICORENA, Beatrice	LISA	Président
Mme. CALMET, Isabelle,	ECN	Rapporteur
M. MARO, Denis,	IRSN	Rapporteur
M. CARISSIMO, Bertrand	CEREA	Examineur
M. LAMAUD, Eric	ISPA	Examineur (co-encadrant)
M. DUPONT, Sylvain	ISPA	Examineur (directeur de thèse)

UMR ISPA, INRA, Bordeaux Sciences Agro, Villenave d'Ornon, France





*“Big whirls have little whirls, that feed on their velocity;  
And little whirls have lesser whirls, and so on to viscosity”*

Lewis Fry Richardson

# Abstract

Atmospheric mineral dust resulting from aeolian soil erosion affects the Earth system. Their size-distribution (PSD) plays a key role on atmospheric radiation balance, cloud formation, atmospheric chemistry, and the productivity of terrestrial and marine ecosystems. However, climate models still fail to reproduce accurately the suspended dust PSD. This is explained by the poor representation of the dust emission mechanisms and the associated surface wind speed in these large-scale models. This is particularly true in the presence of surface roughnesses such as vegetation in semiarid regions. This thesis aims at improving the understanding of dust emission in semi-arid environments, characterized by heterogeneous surfaces with sparse seasonal vegetation. To this end, a combination of numerical and field experiments was employed, with investigations progressing from a bare erodible soil to surfaces with sparse vegetation.

A review of the existing dust emission schemes showed ambiguities in the parametrization of the processes influencing the emitted dust. A sensitivity analysis, using a 1D dust dispersal model, demonstrated (i) the importance of surface dust PSD and inter-particle cohesive bond parametrization on the emitted dust PSD, and (ii) the importance of the deposition process on the net dust flux PSD. Based on this analysis, a new emission scheme was incorporated into a 3D erosion model, coupled with a Large Eddy Simulation (LES) airflow model, and evaluated first on a bare surface against the WIND-O-V's 2017 field experiment in Tunisia. The model was able to reproduce the near-surface turbulent transport dissimilarity between dust and momentum observed during the experiment. This means that momentum and dust are not always transported by the same turbulent eddies. The model demonstrated that the main cause of this dissimilarity is the dust emission intermittency, which varies as a function of wind intensity and fetch.

The role of sparse vegetation on the net emitted dust flux was then explored using the WIND-O-V's 2018 experiment, conducted at the same site as the 2017 experiment. The resulting field measurements were used to evaluate the 3D erosion model, including vegetation characteristics. A comparison between the 2017 and 2018 experiments confirmed that sparse vegetation reduces dust emission by increasing the erosion threshold friction velocity, which depends on vegetation characteristics and wind direction relative to the vegetation arrangement. During the 2018 experiment, the net emitted dust flux PSD varied continuously, unlike the 2017

experiment, with a progressive impoverishment in coarse particles ( $1.50 \mu\text{m}$ ). This impoverishment was found independent of the vegetation, and resulted from the depletion of coarse particles at the surface due to longer emission periods in 2018 without surface tillage or precipitation. This non-influence of vegetation on the dust flux PSD was validated by the similarity of the dust flux PSD at the beginning of the 2018 experiment, when the vegetation was at its maximum height, with the one of the 2017 experiment without vegetation. It was further confirmed by the simulations that demonstrated (i) negligible re-deposition of coarse particles on to vegetation during emission events, and (ii) negligible effect of the turbulence induced by the vegetation on the PSD of the net emitted dust flux.

Our 3D erosion model appears as a promising tool for characterizing dust emissions over heterogeneous surfaces typical of semi-arid regions and for deriving dust emission schemes for climate models as a function of surface roughness properties.

# Résumé

La poussière minérale atmosphérique résultant de l'érosion éolienne des sols affecte le système terrestre. Leur distribution en taille (PSD) joue un rôle clé dans le bilan radiatif et la chimie atmosphérique, la formation des nuages et la productivité des écosystèmes terrestres et marins. Néanmoins les modèles climatiques peinent à reproduire précisément la PSD de la poussière émise. Ceci vient de la mauvaise représentation dans ces modèles à grandes échelles des mécanismes d'émission de poussière et des vitesses de vent de surface associées. C'est particulièrement vrai en présence d'éléments de rugosité de surface comme la végétation en région semi-aride. Cette thèse vise à améliorer la compréhension de l'émission de poussière en environnement semi-aride, caractérisé par des surfaces hétérogènes liées à la végétation saisonnière éparse. A cette fin, une combinaison d'expériences numériques et de terrain a été employée, en partant d'un sol nu érodable, puis de surfaces couvertes en végétation éparse.

Une revue des schémas existants a montré des ambiguïtés dans la paramétrisation des processus influençant l'émission de poussière. Une analyse de sensibilité utilisant un modèle 1D de dispersion de poussière a démontré (i) l'importance de la PSD de la poussière à la surface et de la paramétrisation de la cohésion entre les particules sur la PSD de la poussière émise, et (ii) l'importance du processus de dépôt sur la PSD du flux net de poussière. A partir de cette analyse, un nouveau schéma d'émission a été incorporé à un modèle 3D d'érosion, couplé à un modèle turbulent Large Eddy Simulation (LES), et évalué sur une surface nue sur la base de l'expérimentation WIND-O-V 2017 en Tunisie. Le modèle a été capable de reproduire la dissimilarité entre les transports turbulents de la poussière et de la quantité de mouvement dans la couche de surface, telle que observée durant l'expérience. Cela signifie que la poussière et la quantité de mouvement ne sont pas toujours transportées par les mêmes tourbillons. Le modèle a démontré que la cause principale de cette dissimilarité est l'intermittence de l'émission des poussières, qui varie avec l'intensité du vent et le *fetch*.

L'impact de la végétation éparse sur le flux net de poussière émis a ensuite été étudié sur la base de l'expérimentation WIND-O-V 2018, conduite sur le même site que celle de 2017. Les mesures ont été utilisées pour évaluer le modèle 3D d'érosion incluant les caractéristiques de la végétation. La comparaison entre les expérimentations 2017 et 2018 a confirmé que la végétation éparse réduit l'émission de poussière en augmentant la vitesse de frottement seuil de l'érosion, qui dépend des caractéristiques de la végétation et de la direction du vent par rapport à l'arrangement de la végétation. Nous avons observé que la PSD du flux net de poussière

émis a varié au cours de l'expérimentation 2018, contrairement à 2017, avec un appauvrissement progressif en grosses particules ( $1.50 \mu\text{m}$ ). Il s'est avéré que cet appauvrissement n'était pas lié à la présence de végétation, mais à l'épuisement du sol en grosses particules en raison de périodes d'émission plus longues en 2018 sans travail de la surface ou précipitations. Cette absence d'influence de la végétation sur la PSD du flux de poussière a été validée par la similarité entre la PSD du flux de poussière au début de l'expérimentation 2018, quand la végétation était à sa hauteur maximum, et celle de 2017 sans végétation. Elle a été aussi confirmée par les simulations qui ont montré (i) une re-déposition négligeable des grosses particules sur la végétation durant les émissions, et (ii) un effet négligeable de la turbulence induite par la végétation sur la PSD du flux net de poussière émis.

Notre modèle 3D d'érosion apparaît comme un outil prometteur pour caractériser les émissions de poussière sur des surfaces hétérogènes représentatives des régions semi-arides et pour établir des schémas d'émission de poussière pour les modèles climatiques en fonction des propriétés de rugosité de la surface.



# Acknowledgements

This thesis is not a solitary accomplishment. It is the combined effort of numerous people, who knowingly and unknowingly contributed towards its advancement and success.

There are no proper words to convey my deep gratitude and respect for my thesis director Dr. Sylvain Dupont. He has inspired me to become an independent researcher and helped me realize the power of critical reasoning. He also demonstrated what a brilliant and hard-working scientist can accomplish. If I become only half the thinker, half the teacher, half the person that Sylvain is, it will surely be one of my greatest accomplishments.

I am grateful to my thesis co-director Dr. Eric Lamaud. His witty remarks, difficult questions, insightful anecdotes, and long discussions formed some of the most memorable moments of my doctoral journey. His lasting impression on my attitude is summed up through his famous words “don’t believe until you have seen, like Saint Thomas!”

My gratitude to Dr. Isabelle Calmet, without whose encouragement I wouldn’t have commenced this journey. My sincere thanks must also go to the members of my thesis advisory committee and jury for their generous time and valuable comments. I thank the collaborators of the WIND-O-V project for their support and advice, particularly Dr Jean-Louis Rajot for looking after me in Tunisia. A very special gratitude to everyone at ISPA (INRA) for making my three year stay comfortable, especially Dr Mark Irvine, Tovo Rabenmanantsoa, Caroline Bidot, Christelle Aluome, Christophe Moisy, Didier Garrigou, Françoise Prudhomme, Jean-Marc Bonnefond and Patricia Braconnier for their continuous support. I also thank the French Research Agency (ANR) and INRA (department of EA) for funding my doctoral work.

I cannot forget my parents, my family and my friends; Jean-Rene and Maryline Faure who first hosted me in Bordeaux, the Bertin family of Nantes, Gabrielle Chevalier of Saint-Nazaire, and Sophie of Pessac, whose selflessness made this journey quite comfortable. And finally, I thank my dear partner Ezma D’cruz and my best friend Rima Ayoubi, the two formidable pillars of my life, whose unconditional and unflinching love encourages me to aim higher! Without them, my life is irrelevant and bears no meaning.

Thank you all for your encouragement!





# Contents

<b>Abstract</b>	<b>iii</b>
<b>Résumé</b>	<b>v</b>
<b>Acknowledgements</b>	<b>vii</b>
<b>Contents</b>	<b>ix</b>
<b>List of abbreviations</b>	<b>xxvii</b>
<b>List of Symbols</b>	<b>xxix</b>
<b>1 Introduction</b>	<b>1</b>
1.1 Motivation . . . . .	1
1.2 Objectives . . . . .	6
1.3 Structure of this thesis . . . . .	6
<b>2 An introduction to wind erosion</b>	<b>9</b>
2.1 Atmospheric flow . . . . .	9
2.1.1 Turbulence . . . . .	11
2.1.2 Turbulent fluxes . . . . .	11
2.1.3 Flux Gradient (FG) similarity . . . . .	13
2.1.4 Mean wind at neutral stratification . . . . .	14
2.1.5 Monin-Obukhov similarity . . . . .	15
2.1.6 Turbulence spectrum . . . . .	15
2.1.7 Internal boundary layer (IBL) . . . . .	17
2.1.8 Flow with sparse vegetation . . . . .	18
2.2 Wind erosion . . . . .	19
2.2.1 Soil characteristics . . . . .	19
2.2.2 Erosion threshold . . . . .	20
2.2.3 Modes of eroded particle motion . . . . .	22
2.2.4 Saltation . . . . .	22
Near-surface flow with saltation . . . . .	24
Saltation equilibrium . . . . .	25
Saltation intermittency . . . . .	26
2.2.5 Sandblasting (Dust emission) . . . . .	26

2.2.6	Dust dispersion . . . . .	27
2.2.7	Dust deposition . . . . .	28
<b>3</b>	<b>Field and numerical experiments</b>	<b>31</b>
3.1	The WIND-O-V project . . . . .	31
3.1.1	Objectives . . . . .	31
3.1.2	Workflow . . . . .	32
3.2	The WIND-O-V's field campaigns . . . . .	33
3.2.1	Study site . . . . .	35
3.2.2	Measurements . . . . .	36
3.2.3	EC data processing . . . . .	39
3.2.4	Results . . . . .	40
3.3	3D erosion model . . . . .	40
3.3.1	ARPS LES airflow model . . . . .	41
3.3.2	Erosion modelling . . . . .	43
	Saltation . . . . .	43
	Dust Dispersion . . . . .	45
	Deposition over vegetation . . . . .	46
<b>4</b>	<b>The role of deposition on the size-distribution of near-surface dust flux during erosion events.</b>	<b>47</b>
4.1	Introduction . . . . .	49
4.2	One-dimensional dust-dispersal model . . . . .	51
4.2.1	Wind . . . . .	51
4.2.2	Dust transport . . . . .	52
4.2.3	Saltation . . . . .	53
4.2.4	Dust emission . . . . .	54
4.2.5	Dust Deposition . . . . .	55
4.2.6	Simulation configurations . . . . .	56
4.3	Model evaluation . . . . .	57
4.3.1	Dust flux versus wind intensity compared to existing dust emission schemes	57
4.3.2	Dust concentration vertical profile compared to analytical solution . . . . .	58
4.3.3	Dust flux enrichment in small particles compared to Dupont <i>et al.</i> [2015] large-eddy simulation . . . . .	59
4.3.4	Dust flux PSD compared to Alfaro <i>et al.</i> [1997] wind-tunnel experiment . . . . .	60
4.3.5	Dust flux PSD compared to Kok [2011b] parametrization . . . . .	61
4.4	Sensitivity of the dust flux PSD . . . . .	62
4.5	Discussion and conclusion . . . . .	65
<b>5</b>	<b>Origins of turbulent transport dissimilarity between dust and momentum in semi-arid regions</b>	<b>69</b>

5.1	Introduction . . . . .	71
5.2	Material and method . . . . .	72
5.2.1	Simulation details . . . . .	72
5.2.2	Data analysis . . . . .	74
5.3	Model evaluation . . . . .	75
5.3.1	Wind dynamics . . . . .	75
5.3.2	Saltation dynamics . . . . .	78
5.3.3	Dust dynamics . . . . .	79
5.3.4	Instantaneous behavior . . . . .	81
5.4	Sensitivity of the dust - momentum turbulent transport dissimilarity . . . . .	82
5.4.1	Influence of the wind intensity . . . . .	83
5.4.2	Influence of the fetch length . . . . .	84
5.4.3	Influence of the dust emission intermittency . . . . .	85
5.5	Discussion . . . . .	86
5.6	Conclusions . . . . .	88
<b>6</b>	<b>A field investigation of sparse vegetation impact on dust suspension in a semi-arid environment</b>	<b>89</b>
6.1	Introduction . . . . .	91
6.2	Dust emission events of the 2018 campaign . . . . .	92
6.3	Results . . . . .	95
6.3.1	Wind dynamics during dust emission . . . . .	95
6.3.2	Dust emission threshold . . . . .	97
6.3.3	Aerodynamic roughness length ( $z_0$ ) . . . . .	99
6.3.4	Near-surface turbulent dust transport . . . . .	100
6.3.5	Particle Size Distribution (PSD) of the 3 m high EC dust flux . . . . .	101
6.4	Discussion on the dust flux PSD variability . . . . .	103
6.4.1	Comparison of EC and FG dust fluxes . . . . .	103
6.4.2	Variability in soil characteristics . . . . .	104
6.4.3	Enhanced re-deposition with vegetation . . . . .	104
6.4.4	Thermal buoyancy effect on particle transport . . . . .	105
6.4.5	Fetch (foot-print) limitation . . . . .	106
6.4.6	Source depletion . . . . .	108
6.5	Conclusions . . . . .	110
<b>7</b>	<b>Investigating sparse vegetation impact on the suspended dust during emission events</b>	<b>113</b>
7.1	Introduction . . . . .	115
7.2	Material and method . . . . .	117
7.2.1	Simulation details . . . . .	117
7.2.2	Data analysis . . . . .	120
7.3	Model evaluation . . . . .	122

7.3.1	Flow dynamics . . . . .	122
7.3.2	Erosion dynamics . . . . .	126
7.3.3	Near-surface dust turbulent transport . . . . .	128
7.4	Instantaneous behaviour . . . . .	132
7.5	Evaluating deposition over vegetation . . . . .	135
7.5.1	Sensitivity of $F_{wd}$ PSD to brownian deposition due to vegetation . . . . .	136
7.5.2	Sensitivity of $F_{wd}$ PSD to interception and impaction due to vegetation . . . . .	138
7.6	Conclusion . . . . .	139
<b>8</b>	<b>Conclusions and perspectives</b>	<b>141</b>
8.1	Conclusions . . . . .	141
8.2	Direction for future work . . . . .	144
<b>A</b>	<b>Appendix A: Aerodynamic Parameters Over an Eroding Bare Surface: Reconciliation of the Law of the Wall and Eddy Covariance Determinations</b>	<b>147</b>
<b>B</b>	<b>Appendix B: Dissimilarity Between Dust, Heat, and Momentum Turbulent Transports During Aeolian Soil Erosion</b>	<b>167</b>
	<b>References</b>	<b>195</b>

# List of Figures

1.1	(a) Satellite observations of continental dust transport between the Sahara desert and the Amazon rainforest. Source: <a href="#">NASA</a> . (b) The 7 day progression of the 2000 km long dust cloud that originated on April 14, 1998 in the Takla Makan desert of western China and reached the pacific US on April 25. Source: Husar <i>et al.</i> 2001. (c) Image of a dust storm in Phoenix, Arizona. Source: Washington Post. (d) Dune displacement due to wind force in the Sahara. Source: Google. (e) Wind erosion resultant sandstone formations in New Mexico. Source: Google. (f) Wind erosion over a cultivated field. Source: <a href="#">Ecomerge</a> (g) Sandblast damage to heritage structures. Source: Google. . . . .	2
1.2	Schematic representation of the three wind erosion processes - creep (500-2000 $\mu\text{m}$ ), saltation (70-500 $\mu\text{m}$ ) and dust suspension ( $< 20 \mu\text{m}$ ). . . . .	4
2.1	(a) Schematic representation of the diurnal variation of the Atmospheric Boundary Layer (ABL). Source: Stull [1988]. (b) The depth of the ABL over typical terrain at midday presented as a dot-line. Source: Wikipedia. . . . .	9
2.2	Schematic representation of the atmospheric temperature profiles for stable, unstable and neutral (adiabatic) stratification. . . . .	10
2.3	Schematic representation of turbulent dust transport leading to a positive dust flux. The red line is the typical vertical dust concentration profile. . . . .	12
2.4	Schematic representation of the turbulence spectrum with length scale on the x-axis and the Turbulent Kinetic Energy (TKE) on the y-axis. . . . .	16
2.5	Development of internal boundary layers over an heterogeneous surface with different roughnesses. . . . .	17
2.6	Schematic representation of the wind flow around an isolated vegetation element. Adapted from Judd <i>et al.</i> [1996] . . . . .	18
2.7	Schematics of the near-surface flow regimes associated with different vegetation arrangements. Adapted from Mayaud <i>et al.</i> [2016b] . . . . .	18
2.8	Particle size-distribution of dust in number $dN/d\log d_p$ (unfilled symbols) and mass $dM/d\log d_p$ (filled symbols) for the same erosive soil sample. . . . .	20
2.9	Schematic representation of anti-erosion forces on a soil particle at the surface . .	21
2.10	Schematic representation of the wind erosion processes - creep, saltation and dust suspension. Adapted from Tatarko <i>et al.</i> [2009]. . . . .	22

2.11	Variation with height of the momentum flux retained by the fluid motion ( $\tau_a$ ) and that absorbed by the saltating particles ( $\tau_p$ ) in the saltation layer. Here $\tau_{*f}$ is the threshold momentum flux and $z_m$ is the height of the saltation layer. Adapted from Owen [1964]. . . . .	24
2.12	(a) Vertical profiles of the mean horizontal wind velocity $u(z)$ normalized by its reference value $u_{ref}$ at $z_{ref} = 2\text{m}$ , and (b) vertical profiles of the mean momentum flux $\langle u'w' \rangle$ , with and without saltation. The shaded area represents the saltation layer. Source: Dupont <i>et al.</i> [2013] . . . . .	25
2.13	Aeolian streamers on a beach. Source: Personal communication with Dr. Andreas Baas [Baas <i>et al.</i> 2005] . . . . .	26
2.14	Ambiguities between predicted dust fluxes and experimental observations as a function of $u_*$ . Source: Shao [2008]. . . . .	27
2.15	Schematic representation of the dust life cycle including emission (sandblasting), dispersion and deposition. $R_a$ and $R_b$ refer to the aerodynamic and quasi-laminar resistance to dust deposition explained in section 2.2.7. . . . .	28
2.16	Partition between different dry deposition processes for suspended dust as a function of particle size at a very high wind speed. Source: Petroff <i>et al.</i> [2010]. . . . .	28
3.1	The WIND-O-V work-flow with the different work-packages assigning responsibilities to the project partners. The project is managed by Dr. Sylvain Dupont (ISPA, INRA) through WP0. Adapted from the WIND-O-V project proposal. . . . .	32
3.2	Geolocalisation of the WIND-O-V's experimental site in south Tunisia. Source: Google Maps. . . . .	33
3.3	Plan-view of the semi-circular 150 m radius WIND-O-V's site in South Tunisia during (a) the bare soil experiment of 2017, and (b) the 2018 experiment with sparse vegetation. (c) The time variation of the mean vegetation and sand-tail heights during the 2018 experiment, with the error bars indicating their standard deviations. (d) Top-view of the sand-tails in the lee of the barley tufts. (e) The representation of mean vegetation height as proportional to the intensity of the green markings. (f) The main instrumentation mast, the flux-gradient scaffolding and the saltation sensors. (g) The positions of the 3 sonic-2D anemometers relative to the main mast and the barley tufts. Source: Internal communication with Dr. Jean-Louis Rajot. . . . .	34
3.4	Evolution of two barley tufts (A and B) over three different dates - March 29, April 15, and May 02 - during the 2018 experiment. Source: Internal communication with Dr. Jean-Louis Rajot. . . . .	35
3.5	Barley tufts on the study site during the 2018 experiment. Source: Internal communication with Dr. Jean-Louis Rajot. . . . .	36

3.6	The schematic representation of the WIND-O-V's 2018 experiment with two measurement hubs - the Eddy-Covariance (EC) mast and the Flux-Gradient (FG) scaffolding. Adapted from Dupont <i>et al.</i> [2019a]. . . . .	36
3.7	The main measurement (lattice) mast with the meteorological and Eddy-Covariance (EC) dust flux measurement systems. Source: Internal communication with Dr. Jean-Louis Rajot. . . . .	37
3.8	(a) The Eddy Covariance (EC) dust flux system with the particle spectrometer coupled to the sonic 3D anemometer at 3.0 m on the lattice mast. (b) The Flux Gradient (FG) particle spectrometers at 2.0 m and 4.3 m on the scaffolding to the left and the two TEOM spectrometers at 2.0 m and 4.3 m to the right. (c) The eight PM20 filters, four each at 2.0 m and 4.3 m from the surface. Source: Internal communication with Dr. Jean-Louis Rajot. . . . .	38
3.9	Correction coefficients applied on the EC dust concentration deduced from the inter-comparison experiment involving all 3 spectrometers. Adapted from Dupont <i>et al.</i> [2019a]. . . . .	38
3.10	Example of the high-frequency correction (shaded area) identified from the cospectrum of the 2.5 $\mu\text{m}$ dust fluxes ( $S_{wd}$ ) for the March 09 2017 erosion event. Presented also is the cospectrum of the momentum flux ( $S_{uw}$ ). Adapted from Dupont <i>et al.</i> [2019a]. . . . .	39
4.1	Schematic representation of the 1D computational domain used in this chapter. .	52
4.2	Variation of the deposition velocity ( $v_{dep}$ ) with dust particle diameter ( $d_p$ ) for five wind intensities ( $u_* = 0.30, 0.40, 0.50, 0.60$ and $0.80 \text{ ms}^{-1}$ ). . . . .	55
4.3	Size distributions in number (a) and in mass (b) of dust particles available at the surface considered in our simulations (D1, D2, D3 and D4) as well as reported in the wind-tunnel experiment of Alfaro <i>et al.</i> [1997] and used in Shao [2001] and Kok [2011a] numerical experiments. . . . .	56
4.4	Vertical dust flux ( $F_{wd,tot}$ ), including all particle sizes, as a function of the friction velocity ( $u_*$ ) obtained from our 1D model and compared with the empirical parametrizations of (1) Marticorena <i>et al.</i> [1995]: $F_{wd,tot} = \gamma Q_{tot}$ , with $\gamma = 10^{-2}$ , and (2) Shao <i>et al.</i> [1993]: $F_{wd,tot} = C\rho_d(u_*^2 - u_{*t}^2)$ , with $C = 4$ and $u_{*t} = 0.2 \text{ ms}^{-1}$ . Note that the dust emission coefficient ( $\alpha_{em}$ ) of our model (Eq. 4.13) was chosen so as $F_{wd,tot}$ fits the value obtained from Shao <i>et al.</i> [1993] scheme at $u_* = 0.40 \text{ ms}^{-1}$ . . . . .	57
4.5	Variation with the fetch length of the simulated vertical dust concentration profiles (dot-lines) and comparison at steady state against the analytical profile (solid line) for 16 $\mu\text{m}$ dust particle in a 35 m high domain, and with $u_* = 0.40 \text{ ms}^{-1}$ . The analytical profile responds to $c_b(z) = c_b(z_r) (z/z_r)^{v_{s,b}/(\kappa u_*)}$ , where $z_r$ is a reference height corresponding here to 1 m. . . . .	58



- 4.6 Time variation of the fraction in number of the turbulent-diffusive fluxes ( $F_{wd,b}$ ) at 2 m height of  $1.5 \mu\text{m}$  (blue,  $b=1$ ),  $6.7 \mu\text{m}$  (green,  $b=2$ ) and  $14.2 \mu\text{m}$  (red,  $b=3$ ) particle diameters, on the total turbulent-diffusive dust flux  $F_{wd,tot}$ , for three wind conditions ( $u_*$ ) simulated by our model (solid lines) in comparison with those from Dupont *et al.* [2015] (dotted lines). . . . . 59
- 4.7 The mass size distribution of the vertical dust fluxes ( $F_{wd}$ ) as simulated by our model (line-dots) for three wind conditions ( $u_*$ ), and compared with the wind-tunnel observations from Alfaro *et al.* [1997] (filled squares). In one simulation, the PSD of available dust at the surface ( $p_d$ ) is independent of  $u_*$  ( $\zeta_d = 1$ ) while in the other simulation  $p_d$  depends on  $u_*$  as suggested by Alfaro *et al.* [1997] ( $\zeta_d \neq 1$ ) . . . . . 60
- 4.8 Variation with the fetch length of the size distribution in number (top row) and in mass (bottom row) of the 3-m high vertical dust fluxes ( $F_{wd}$ ) as simulated by our model (line-dots) for three wind conditions ( $u_*$ ) (line-dots), and compared with the prediction of Kok [2011b] (solid line-filled squares). The fetch ranges from 5 m to 10 km. . . . . 61
- 4.9 Size distributions in number of emitted dust at the surface ( $F_{emi}$ ) obtained from our model for various PSD of available dust at the surface (D1, D2, D3 and D4, see Fig. 4.3) and according to the inter-particle cohesive bond exponent  $\beta$  (from -1 to +3) . . . . . 63
- 4.10 Variation with the fetch length of the size-distribution in number of the 3-m high  $F_{wd}$  according to (a) the wind intensity ( $u_* = 0.30, 0.40$  and  $0.50 \text{ ms}^{-1}$ ), (b) the surface dust-size distributions (D2, D3 and D4, see Fig. 4.3), and (c) the inter-particle cohesive bond exponents ( $\beta = -1, 0, 1$  and 3). The fetch ranges from 5 m to 10 km. The dust particle range is divided into 4 bins: Z1 ( $d_p \leq 0.3 \mu\text{m}$ ) - particles with dominant brownian deposition, Z2 ( $0.3 \mu\text{m} < d_p \leq 2 \mu\text{m}$ ) - particles the least likely to deposit, Z3 ( $2 \mu\text{m} < d_p \leq 8 \mu\text{m}$ ) - particles with the deposition velocity the most sensitive to wind intensity, and Z4 ( $d_p > 8 \mu\text{m}$ ) - particles the most likely to deposit. . . . . 64
- 4.11 Variation with the fetch length of the fraction in number (left figures) and in mass (right figures) of the 3-m high  $F_{wd}$  on the total turbulent-diffusive dust flux  $F_{wd,tot}$  according to (a) the wind intensity ( $u_* = 0.30, 0.40$  and  $0.50 \text{ ms}^{-1}$ ), (b) the surface dust-size distributions (D2, D3 and D4, see Fig. 4.3), and (c) the inter-particle cohesive bond exponents ( $\beta = -1, 0, 1$  and 3).  $F_{wd}$  is divided into 4 bins: Z1 ( $d_p \leq 0.3 \mu\text{m}$ ) - particles with dominant brownian deposition, Z2 ( $0.3 \mu\text{m} < d_p \leq 2 \mu\text{m}$ ) - particles the least likely to deposit, Z3 ( $2 \mu\text{m} < d_p \leq 8 \mu\text{m}$ ) - particles with the deposition velocity the most sensitive to wind intensity, and Z4 ( $d_p > 8 \mu\text{m}$ ) - particles the most likely to deposit. The fractions at the smallest fetch lengths are equivalent to those of the surface emitted dust flux ( $F_{emi}$ ). . . . . 66

- 5.1 Particle size distributions of the saltating particles ( $p_s(D)$ ) and dust available at the surface ( $p_d(d_b)$ ) considered in the simulations. The size distribution of the 3-m high dust turbulent diffusive flux ( $F_{wd}$ ) obtained from simulation C1 (symbols) is compared to  $p_d(d_b)$ . The distribution  $p_s(D)$  was deduced from the soil granulometry of the WIND-O-V's site. . . . . 73
- 5.2 Comparison between the C1 simulation (lines) and the field measurements (symbols) on the mean vertical profiles of (a) the longitudinal wind velocity ( $u$ ), (b) the local friction velocity ( $u_*$ ), and (c) the standard deviations of the three velocity components ( $\sigma_u, \sigma_v, \sigma_w$ ). The error bars refer to the standard deviations of the experimental values for periods with similar wind intensity. . . . . 76
- 5.3 Time variation of the quadrant partitioning of the momentum flux  $F_{uw}$  (a) and dust flux  $F_{wd}$ , in magnitude ( $F_{Qi}$ ) and in event number ( $N_{Qi}$ ), as defined in equations 5.1 and 5.2, obtained from the 10-min simulated erosion event C1 at four heights (0.4, 1.5, 2.0 and 4.0 m) and compared with the mean fractions obtained at 3 m height from the WIND-O-V field experiment. The dust flux includes all particle sizes. Note that measurement data are averaged values with no time variation. . . . . 77
- 5.4 (a) Time variation of the total number of numerically resolved saltators within the computational domain during the 10-min simulated erosion event C1. (b-d) Time variation of the dust number concentration (including all particle sizes) at 1.0 m height and  $x_{fetch} = 50$  m during the 10-min simulated erosion events C1 and C5, respectively. . . . . 78
- 5.5 Comparison between simulated (dots), WIND-O-V field measurements (solid line) and semi-empirical parametrizations (broken lines) of (a) the saltation flux ( $F_{salt,tot}$ ), (b) the saltation roughness length ( $z_{0s}$ ), and (c) the turbulent diffusive dust flux including all particle sizes ( $F_{wd,tot}$ ) at  $z/x_{fetch} \sim 0.02$ , against the saltation friction velocity  $u_{*0}$  normalized by its threshold value  $u_{*t}$ . In (a) the simulated  $F_{salt,tot}$  is compared with the parametrizations of Bagnold [1937]:  $F_{salt,tot} = 1.5 (D/D_{ref})^{1/2} \rho_a/gu_{*0}^3$  with  $D_{ref} = 250 \mu\text{m}$ ; Kamawura [1951]:  $F_{salt,tot} = 2.61 \rho_a/g (1 - u_{*t}/u_{*0}) (1 + u_{*t}/u_{*0})^2$ ; and Owen [1964]:  $F_{salt,tot} = (0.25 + 0.33v_{sed}/u_{*0}) \rho_a/gu_{*0}^3 (1 - u_{*t}^2/u_{*0}^2)$ , with  $D$  the saltating particle diameter,  $\rho_a$  the air density,  $g$  the gravitational acceleration and  $v_{sed}$  the settling velocity. In (b) the simulated  $z_{0s}$  is compared with the parametrizations of Rasmussen *et al.* [1985] and Owen [1964]:  $z_{0s} = C_c u_{*0}^2/g$  with  $C_c = 0.08$  and  $0.02$ , respectively. In (c),  $F_{wd,tot}$  is compared with Shao *et al.* [1993]:  $F_{wd,tot} = C\rho_a(u_{*0}^2 - u_{*t}^2)$ , with  $C = 4$ . The dust fluxes have been normalized by their values at  $u_{*0}/u_{*t} = 2.5$ . . . . . 79

5.6 (a) Time-averaged dust number concentration field  $c_{tot}$  (including all particle sizes) as obtained from simulation C1. The depth of the dust boundary layer developing from the upwind edge of the erodible plot ( $x = 0$  m) is also shown for simulations C1 to C5. This depth ( $z_d$ ) was defined as the distance above the surface from which the dust concentration reduces by 99.9% of the surface dust concentration. (b) Variation with height of the turbulent diffusive dust flux ( $F_{wd}$ ), including all particle sizes, normalized by the dust flux at the surface ( $F_{wd,surf}$ ) for simulations C1, C5 and C6, respectively. . . . . 80

5.7 Snapshots of horizontal cross section ( $x - y$ ) of the (a) vertically integrated sand concentration ( $C_p$ ) normalized by its maximum value ( $C_{pmax}$ ), (b) 1-m high sweep motions ( $-u^+w^-$ ), (c) 1-m high ejection motions ( $-u^-w^+$ ), and (d) dust ejections ( $w^+d^+$ ) at the surface, for simulations C1 (top figures) and C5 (bottom figures), at the 7th minute of the erosion event. White areas represent regions with low intensity of the corresponding quantity. . . . . 81

5.8 Ensemble-average dust concentration fluctuations  $\tilde{c}$  (background color), vertically integrated sand concentration  $C_p$  (white line), and wind vectors, associated with (a) sweep ( $u^+w^-$ ) and (b) ejection ( $u^-w^+$ ) motions at  $x = 30$  m and  $z = 0.4$  m, as obtained from simulations C1 (top) and C5 (bottom). Dust and sand concentrations have been normalized by their maximum values,  $\tilde{c}_{max}$  and  $C_{pmax}$ , respectively. . . . . 83

5.9 Variation with the normalized friction velocity  $u_{*0}$  of the quadrant partitioning in magnitude ( $F_{Qi}$ ) and in event number ( $N_{Qi}$ ) of the momentum flux  $F_{uw}$  (a) and dust flux  $F_{wd}$  including all particle size (b), at 3 heights (0.4, 1.5 and 4.0 m), obtained from simulations C1 to C5. . . . . 84

5.10 Time variation of the quadrant partitioning in magnitude ( $F_{Qi}^{wd}$ ) and in event number ( $N_{Qi}^{wd}$ ) of the dust flux  $F_{wd}$  compared to the quadrant partitioning of the momentum flux  $F_{uw}$ , at 4 heights (0.4, 1.5, 2.0 and 4.0 m) as obtained from simulation C6. The dust flux includes all particle sizes. . . . . 85

5.11 Same as Fig 5.10 but for simulation C7. . . . . 85

- 6.1 Plan-view images of the semi-circular 150 m radius WIND-O-V's site in South Tunisia during (a) the bare soil experiment of 2017, and (b) the 2018 experiment with sparse vegetation. (c) The time variation of the mean vegetation and sand-tail heights during the 2018 experiment, with the error bars indicating their standard deviations. (d) Top-view of the sand-tails in the lee of the barley tufts. (e) The representation of mean vegetation height as proportional to the intensity of the green markings. Superposed on it is the variation of the wind direction for the 9 erosion events of the 2018 experiment. (f) The main instrumentation mast, the flux-gradient scaffolding and the saltation sensors. (g) The positions of the 3 sonic-2D anemometers relative to the main mast. Source: Internal communication with Dr. Jean-Louis Rajot. . . . . 93
- 6.2 Main characteristics of the 9 erosion events: time variations of the (a) mean wind direction and the mean wind speed, (b) surface friction velocity ( $u_{*0}$ ) deduced from the sonic anemometers according to Dupont *et al.* [2018], (c) stability ( $z/L$ ), (d) sensible heat flux ( $H$ ), (e) dust number flux ( $F_{wd}$ ), and (f) mean size-resolved dust number concentration. All values, except  $u_{*0}$ , were measured at 3 m from the surface. The shaded areas highlight the selected erosion periods. . . . . 94
- 6.3 Vertical profiles of the (a) wind velocity deduced from the cup (square) and sonic (circle) anemometers, (b) standard deviations of the longitudinal (circle), lateral (square) and vertical (triangle) velocity components, and (c) friction velocity for the selected erosion events of the 2018 campaign. The error bars indicate the standard deviation of each variable.  $\langle \rangle$  denotes the ensemble average over all selected 15-minute time periods for each erosion event. . . . . 96
- 6.4 Variation of the dust number flux (including all particle sizes) with surface friction velocity ( $u_{*0}$ ) and wind direction for the 2017 and 2018 events of the WIND-O-V's campaign, along with the best fit in the form  $F_d = A(u_{*0} - u_{*t})^3$ . Each point corresponds to a 15 minute time average. . . . . 98
- 6.5 Variation of the aerodynamic roughness length ( $z_0$ ) as a function of (a) surface friction velocity ( $u_{*0}$ ) for 2017 and 2018 erosion events, and wind direction for the (b) selected 2018 erosion events, and (c) entire 2018 experimental duration. Each data point represents a 15 minute time period. . . . . 100
- 6.6 Particle size distribution (PSD) of the 3 m high EC dust number flux normalized by that of (a) the smallest bin and (b) all bins, for 2017 (unfilled symbols) and 2018 (filled symbols) erosion events, as a function of the wind direction. The PSD is the average of all 15 minute time periods for an event. . . . . 101
- 6.7 The variation with surface friction velocity ( $u_{*0}$ ) of the dust number flux for four particle sizes - 0.60, 1.50, 2.50 and 4.40  $\mu\text{m}$  for the 2017 (unfilled symbols) and 2018 (filled symbols) erosion events. Each data point represents a selected 15-minute time period. . . . . 102

6.8	Variation of the ratio of the dust fluxes of the 2 principal modes ( $m_1 = 0.60 \mu\text{m}$ and $m_2 = 1.50 \mu\text{m}$ ) as a function of wind direction for the 2017 (unfilled circles) and 2018 (filled triangles) erosion events. Each data point represents a selected 15-minute time period. . . . .	103
6.9	Comparison between the size-distributions of the dust fluxes estimated using the Eddy-Covariance (EC) and the Flux-Gradient (FG) methods for the first 7 erosion events of the 2018 campaign. During the May 28 and June 04 events, the 2 gradient spectrometers were placed at the same height for inter-comparison validations. The PSDs correspond to the average of all 15 minute periods for an event. . . . .	104
6.10	Variation of the ratio of the dust fluxes of the 2 principal modes ( $m_1 = 0.60 \mu\text{m}$ and $m_2 = 1.50 \mu\text{m}$ ), estimated using the FG and EC methods, with the sensible heat flux. The FG dust flux for the last two events cannot be estimated as the two spectrometers were under inter-comparison at the same height. Each data point represents a 15 minute averaging period. . . . .	105
6.11	Schematic representation of the EC dust flux system (a) well within and (b) outside the internal dust boundary layer. . . . .	106
6.12	Variation with wind speed of the Q1 quadrant partition of the 15-minute averaged dust flux in event number ( $N_{wd}^{Q_1}$ ) for the 2 principal modes, $0.60 \mu\text{m}$ (filled squares) and $1.50 \mu\text{m}$ (unfilled squares), for the 2017 experiment. Each data point represents a 15 minute averaging period. . . . .	106
6.13	Same as figure 6.12 for the 9 selected emission events of the 2018 experiment. . . . .	107
6.14	Time variation of (a) the ratio of the dust fluxes of the $1.5 \mu\text{m}$ and $0.6 \mu\text{m}$ modes, (b) the ratio of the transfer velocities of the $1.5 \mu\text{m}$ and $0.6 \mu\text{m}$ modes, and (c) the cumulative wind speed (solid line) and surface friction velocity (dotted line) during the WIND-O-V's 2018 field experiment. The fluxes and transfer velocities correspond to emission events with the wind blowing along $100^\circ < \theta < 270^\circ$ . The cumulative values in (c) cover the entire duration of the experiment, regardless of the wind direction, for winds stronger than the bare soil threshold ( $u_{*t} > 0.22 \text{ ms}^{-1}$ ). The blue circles correspond to rain events and the brown circles to tilling operation (surface preparation). Z1, Z2, and Z3 are the three emission periods. . . . .	109
6.15	Same as Fig 6.14 for the WIND-O-V's 2017 field experiment. . . . .	109
7.1	Particle size distribution (PSD) of the surface dust as the percentage contribution of the individual bins in number ( $dN/d\log D_p$ - solid line) and mass ( $dM/d\log D_p$ - dotted line). . . . .	117
7.2	The plan-view of the vegetation on the WIND-O-V's experimental site in 2018 and the schematic of the simulated vegetation. Here $l_v$ represents the inter-plant distance along the mean wind direction. . . . .	118

7.3	Schematic representation of the plan-view of the simulated vegetation layouts L1, L2, and L3 (top figures) and the diagonal cross section of L1 (bottom figure). . . . .	120
7.4	Schematic representation of the calculation of the equivalent saltation friction velocity $u_{*sb}$ over bare sand from the wind profiles simulated over vegetated surfaces composed of shrubs. Source: Dupont <i>et al.</i> [2014] . . . . .	121
7.5	Comparison between simulations (lines with unfilled symbols) C1 (squares) and C2 (triangles) and the field measurements (filled symbols) on the mean vertical profiles of (a) the longitudinal wind velocity ( $u$ ), (b) the local friction velocity ( $u_*$ ), and (c) the standard deviations of the three velocity components ( $\sigma_u$ , $\sigma_v$ , $\sigma_w$ ) for C1. The error bars refer to the standard deviations of the experimental values for periods with similar wind intensity. . . . .	122
7.6	Variation with wind direction of the simulated aerodynamic roughness length $z_{0sv}$ (filled circles) in comparison with the observations from the 2018 field experiment. Similar to Fig. 6.5. . . . .	123
7.7	Time variation of the quadrant partitioning of the momentum flux $F_{uw}$ in magnitude ( $F_{Qi}$ ) and in event number ( $N_{Qi}$ ), as defined in equations 5.1 and 5.2, obtained from the 10-min simulated erosion event C1 at four heights (0.2, 1.5, 2.0 and 4.0 m) and compared with the mean fractions obtained at 3 m height from the WIND-O-V's 2018 field experiment. . . . .	124
7.8	Same as Fig. 7.7 for the bare surface with $u_{*0} = 0.34 \text{ ms}^{-1}$ . . . . .	124
7.9	Variation of the ratio between the velocity in the lee of the vegetation element and the averaged velocity of inter-row region for cases C1 and C2 with inter-plant distances $l_v = 2.5$ and $3.5$ m respectively. . . . .	125
7.10	Simulated saltation fluxes as a function of the equivalent bare friction velocity ( $u_{*sb}$ ) normalized by the saltation threshold ( $u_{*t}$ ) for erosion over the bare surface (solid line) and with vegetation (filled symbols). . . . .	126
7.11	Simulated 3 m high dust fluxes as a function of the equivalent bare friction velocity for erosion over the bare surface (solid line) and with vegetation (filled symbols). The unfilled circles represent the selected events of the WIND-O-V 2018 experiment. . . . .	127
7.12	Particle size distribution (PSD) of the 3 m high dust flux after 10 minutes of simulated erosion for cases C1, C2, C3, C4, and C5 in comparison with that emitted dust at the surface. . . . .	127
7.13	Time-averaged horizontal cross section ( $x - y$ ) of the dust emissions for case C4 at $z = 0.1$ m. . . . .	128

7.14	Time variation of the quadrant partitioning of the dust flux $F_{wd}$ in magnitude ( $F_{Qi}$ ) and in event number ( $N_{Qi}$ ), as defined in equations 5.1 and 5.2, obtained from the 10-min simulated erosion event C1 at four heights (0.2, 1.5, 2.0 and 4.0 m) and compared with the mean fractions of the momentum flux $F_{uw}$ obtained at 3 m height from the WIND-O-V's 2018 field experiment. The quadrants correspond to the $1.5 \mu\text{m}$ dust size. . . . .	129
7.15	Same as Fig. 7.14 but for periodic dust dispersion over the bare surface (C6 in Chapter 5). . . . .	129
7.16	Time variation of the fractions in magnitude ( $F_{Qi}$ ) and in event number ( $N_{Qi}$ ) of the momentum flux in each quadrant, at $z = 0.2 \text{ m}$ , associated with positive or negative dust concentration ( $d^+, d^-$ ) fluctuations for the bare soil simulations and the sparsely vegetated case C1, both with comparable wind intensities $u_{*sb} \approx 0.33 \text{ ms}^{-1}$ . The solid lines correspond to positive dust fluctuations $d^+$ and the dotted lines to $d^-$ . . . . .	130
7.17	Time variation of the quadrant partitioning of the dust flux $F_{wd}$ in magnitude ( $F_{Qi}$ ) and in event number ( $N_{Qi}$ ), as defined in equations 5.1 and 5.2, obtained from the 10-min simulated erosion event C1 at 0.2 m height for 4 dust particle sizes ( $d_{p,b} = 0.45, 2.50, 7.50, \text{ and } 10.00 \mu\text{m}$ ) and compared with the mean fractions of the momentum flux $F_{uw}$ obtained at 3 m height from the WIND-O-V's 2018 field experiment. . . . .	131
7.18	Same as Fig. 7.14 for simulation C5 with 20 minutes of erosion. . . . .	131
7.19	Instantaneous snapshots of horizontal cross section ( $x - y$ ) of the vertically integrated sand concentration ( $C_p$ ) normalized by its maximum value ( $C_{p,max}$ ) for cases (a) C1 ( $u_{*sb} = 0.33 \text{ ms}^{-1}$ ), (b) C3 ( $u_{*sb} = 0.32 \text{ ms}^{-1}$ ), (c) C4 ( $u_{*sb} = 0.54 \text{ ms}^{-1}$ ), and (d) C5 ( $u_{*sb} = 0.54 \text{ ms}^{-1}$ ). The circles represent the vegetation elements. White areas represent regions with low intensity of the corresponding quantity. . . . .	133
7.20	Instantaneous snapshots of horizontal cross section ( $x - y$ ) of the vertically integrated sand concentration ( $C_p$ ) normalized by its maximum value ( $C_{p,max}$ ) and the surface dust ejections ( $w^+ d^+$ at $z \approx 0.1 \text{ m}$ ) normalized its maximum value for cases (a) C1 with $u_{*sb} = 0.33 \text{ ms}^{-1}$ , (b) C2 with $u_{*sb} = 0.60 \text{ ms}^{-1}$ and (c) C5 with $u_{*sb} = 0.54 \text{ ms}^{-1}$ . The circles represent the vegetation elements. White areas represent regions with low intensity of the corresponding quantity. . . . .	134
7.21	Variation with particle size of the simulated deposition velocity ( $V_{dep}$ ) in the presence of vegetation in comparison with published literature (over grass and forest canopies). . . . .	135
7.22	Variation with particle size of (a) the deposition velocity ( $V_{dep}$ ), (b-c) the percentage contribution to the 3 m high dust flux in number and mass, respectively, and (d) the ratios of the emission and deposition fluxes for cases C1 and C1-M1. . . . .	136
7.23	Similar to Fig. 7.22 for cases C1-M1 and C4-M1. . . . .	137
7.24	Similar to Fig. 7.22 for cases C4-M1 and C4-M2. . . . .	138

7.25	Similar to Fig. 7.22 for cases C4-M1 and C1-M3. . . . .	139
8.1	Schematic representation of the different dust size-distributions including that of the emitted dust flux ( $F_{emi}$ ) and the net-emitted ( $F_{wd}$ ) dust flux. . . . .	142
8.2	Schematic representation of the positioning of dust flux measurement sensors relative to the internal boundary layer as a function of the fetch length. . . . .	143





# List of Tables

2.1	Different saltation flux parametrizations. Here $v_{sed}$ is the gravitational settling velocity of the particle. . . . .	23
4.1	Dust flux notation. . . . .	51
4.2	Main input parameters of our 1D dust dispersal model. . . . .	57
4.3	Range of values of the parameters considered in our sensitivity analysis of the dust flux PSD. . . . .	62
5.1	Main characteristics of the seven simulations: ratios between the surface friction velocity ( $u_{*0}$ ) and the threshold friction velocity ( $u_{*t} = 0.22\text{ms}^{-1}$ ), dust lateral boundary condition, fetch length of the erodible plot at the end of the computational domain, and parametrization of the dust emission. Simulations C1 to C5 are comparable to the WIND-O-V field experiment with various wind conditions. . . . .	74
6.1	The main characteristics of the selected 2018 and 2017 erosion events: surface friction velocity ( $u_{*0}$ ), wind direction, stability ( $z/L$ ), 3 m high mean wind speed ( $u$ ), dust concentration from the EC OPC including all particle sizes, dust number flux from the 3 m high EC system for particle modes $0.60\ \mu\text{m}$ and $1.50\ \mu\text{m}$ , and the number of 15-minute averaging periods. The values presented are averages of all selected 15-minute time periods with the standard deviations within parentheses. The criteria to select the 15-minute time periods is described in Dupont <i>et al.</i> [2018]. . . . .	95
6.2	Mean wind speed and the standard deviation (within parentheses) measured at 0.45 m from the surface at 3 different locations for four wind directions - north ( $11^\circ$ ), north-east ( $55^\circ$ ), east ( $102^\circ$ ) and west ( $-78^\circ$ ). The mean values are the average of all 15 minute time periods. . . . .	97
6.3	Mean fraction values in flux magnitude and in number of events of the 3 m high dust flux in each quadrant as defined in section 5.2.2 for the 9 selected dust emission events of the 2018 experiment for the $2.5\ \mu\text{m}$ dust particle. Also presented is the averaged values across all 2017 events. . . . .	100

- 7.1 Main characteristics of the twelve simulations: the vegetation surface cover ( $c_v$ ), inter-plant distance along the mean wind direction ( $l_v$ ), vegetation layout, wind direction, and the equivalent bare surface friction velocity ( $u_{*sb}$ ). Simulations C1 and C2 are comparable with the WIND-O-V's 2018 field experiment detailed in Chapter 6. The first set of simulations (C1 - C5) have deposition parametrized as detailed in Chapter 3, and the second set (C1-M1, C4-M1, C4-M2, and C1-M3) feature modified deposition parameterized - detailed later in this chapter. The estimation of  $u_{*sb}$  is detailed in section 7.2.2 . . . . . 119
- 7.2 Saltation flux reduction due to vegetation as against that over a bare surface. . . 126

# List of Abbreviations

ABL	Atmospheric Boundary Layer
ANR	Agence Nationale de la Recherche, France
ARPS	Advanced Regional Prediction System
ASL	Atmospheric Surface Layer
BSNE	Big Spring Number Eight
CNRS	Centre National de la Recherche Scientifique
EC	Eddy-Covariance
EEA	European Environment Agency
FG	Flux-Gradient
IBL	Internal Boundary Layer
iEES	Institut d'écologie et des sciences de l'environnement, Paris
INRA	Institut National de la Recherche Agronomique
IPBES	Intergovernmental Science-Policy Platform on Biodiversity and Ecosystem Services
IRA	Institut des Régions Arides, Tunisia
ISPA	Interactions Sol Plante Atmosphère, Bordeaux
LAI	Lead Area Index
LES	Large Eddy Simulation
LISA	Laboratoire Interuniversitaire des Systèmes Atmosphériques, Paris
LMFA	Laboratoire de Mécanique des Fluides et d'Acoustique, Lyon
MWAC	Modified Wilson and Cook
OPC	Optical Particle Counter
PSD	Particle Size Distribution
SGS	Sub-Grid Scale
WIND-O-V	WIND erOsion in presence of sparse Vegetation
1D	One dimensional
3D	Three dimensional



# List of Symbols

Symbol	Description	Value
$A_f$	frontal area density of vegetation	
$A_h$	horizontal area density of vegetation	
$c$	dust particle concentration	
$C_d$	drag coefficient	
$c_p$	specific heat at constant pressure	
$c_v$	specific heat at constant volume	
$c_s$	percentage of saltator impact energy lost to the surface	
$C_c$	Cunningham slip correction factor	
$d_p$	soil particle diameter	
$d_n$	needle diameter of vegetation	
$D_g$	Brownian diffusivity of a particle in the $bth$ size bin	
$E$	inter-particle cohesive bonding energy	
$E_d$	efficiency of saltator impaction onto vegetation	
$E_{imp}$	saltator impact energy	
$E_{reb}$	saltator rebound energy	
$E_{ej}$	saltator splash energy	
$E_{fr}$	friction energy lost during sandblasting	
$f$	eddy frequency	
$F$	flux	
$g$	gravitational acceleration	9.81 ms <sup>-1</sup>
$H$	sensible heat flux	
$H_s$	characteristic height of the saltation layer	
$h_v$	mean vegetation height	
$K$	eddy diffusivity	
$K_m$	momentum eddy diffusivity	
$K_h$	heat eddy diffusivity	$\approx 0.8K_m$
$K_d$	dust eddy diffusivity	
$l$	turbulent mixing length	
$l_{tv}$	vertical turbulent mixing length	
$l_{th}$	horizontal turbulent mixing length	
$l_v$	inter-plant distance along the mean wind direction	
$L$	Monin-Obukhov length	

$m_p$	particle mass
$N_{emi}$	number of dust particles emitted
$P_r$	Prandtl number
$p_s$	PSD of the saltating particles at the surface
$p_d$	PSD of dust particles at the surface
$R_a$	aerodynamic resistance to dust deposition
$R_b$	quasi-laminar resistance to dust deposition
$S_c$	Schmidt number
$S_t$	Stokes number
$u_*$	friction velocity
$u, v, w$	stream-wise, lateral and vertical wind speed
$v_{br}$	brownian dust deposition velocity
$v_{dep}$	particle deposition velocity
$v_{imp}$	saltator impact velocity
$v_{im}$	dust deposition velocity by impaction on to vegetation
$v_{int}$	dust deposition velocity by interception by vegetation
$v_{reb}$	saltator rebound velocity
$v_{sed}$	particle settling velocity
$x, y, z$	coordinate along the stream-wise, lateral and vertical direction
$z_0$	aerodynamic roughness length
$z_{0s}$	saltation roughness length
$z_{0sb}$	bare surface equivalent roughness length
$z_{0sv}$	roughness length of vegetated surface

---

### Greek letters

$\alpha$	ratio of $v_{reb}$ to $v_{imp}$	0.5 - 0.6
$\alpha_{em}$	dust emission coefficient	
$\alpha_{ej}$	saltator ejection angle	
$\alpha_{vej}$	saltator vertical ejection angle	
$\alpha_{hej}$	saltator horizontal ejection angle	
$\alpha_{reb}$	saltator rebound angle	
$\alpha_{vreb}$	saltator vertical rebound angle	
$\alpha_{hreb}$	saltator horizontal rebound angle	
$\alpha_{sb}$	sandblasting efficiency ( $F_{wd}/F_{salt}$ )	$10^{-4}$ to $10^{-6}$ $\text{cm}^{-1}$
$\beta$	Inter-particle cohesive bond exponent	
$\delta_{i,j}$	Kronecker delta	
$\Delta x, \Delta y, \Delta z$	grid dimensions along $x, y, z$ directions	
$\Delta t$	simulation time step	
$\epsilon$	eddy energy dissipation rate	
$\epsilon_d$	fraction of $E_{fr}$ available for dust emissions	

$\epsilon_{ijk}$	Levi-Civita symbol	
$\eta$	eddy dissipation length	
$\gamma$	Eulers constant	0.577216
$\gamma_{reb}$	empirical constant in splash scheme	$2 \text{ sm}^{-1}$
$\Gamma$	empirical constant in Shao <i>et al.</i> 2000 erosion threshold scheme	
$\kappa$	von Karman constant	
$\Omega$	angular velocity of earth	
$\Phi$	universal stability function	
$\Lambda$	mean free path of gas molecules	$6.6 \times 10^{-6} \text{ cm}$
$\nu_a$	kinematic viscosity of air	$1.81 \times 10^{-5} \text{ Pa.s}$
$\nu_t$	eddy viscosity	
$\rho_a$	density of air	$1.2 \text{ kgm}^{-3}$
$\rho_p$	density of soil particles (saltators and dust)	$2500 \text{ kgm}^{-3}$
$\tau$	shear stress	
$\tau_{ij}$	shear stress tensor	
$\theta$	air potential temperature	

---

### Indices

0	at the surface
$b$	dust particles from the $b$ th bin
$emi$	dust emission
$dep$	dust deposition
$i$	= 1,2,3 for stream-wise, lateral and vertical directions
$j$	lateral direction
$k$	vertical direction
$salt$	saltation
$sed$	sedimentation (gravitational settling)
$t$	threshold value
$tot$	including all particle sizes
$uw$	momentum flux
$wd$	dust flux

---

### Notations

$\bar{X}$	time average of $X$
$X'$	deviation from $\bar{X}$
$\langle \rangle$	ensemble average
$\sigma$	standard deviation





# 1 Introduction

## 1.1 Motivation

Soil erosion has always intrigued mankind. For millennia, the erosion of civilizations has been synonymous with the erosion of soil. The demise of some of the greatest civilizations - the Greek, Roman, Meso-American, Mesopotamian, Sumerian, and Mayan - are all attributed to some extent to wind erosion [Lowdermilk 1975; Katsuyuki 2009]. The interest in understanding erosion dates back to Plato (400 BC), who commented on its dangers [Montgomery 2007]. Thousands of miles away, the ancient Koreans attributed religious significance to dust storms, believing them to be God's warning [Chun *et al.* 2008]. But, it was only after Charles Darwin, who provided one of the first modern scientific accounts of large-scale dust transport [Darwin 1909], that scientific intrigue on wind erosion started to develop. This initial interest gained momentum following the catastrophic dust storm of the 1930's in west USA. This storm aroused a great deal of scientific and political interest in understanding wind erosion as it destroyed 100 million acres of farmland in a region thereafter called the dust-bowl, forcing the US Congress to pass the first soil conservation legislation [McLeman *et al.* 2014]. The subsequent pioneering work of Ralph Bagnold [Bagnold 1941], an US Army Engineer, laid the foundation towards understanding wind erosion and gave rise to a wide range of associated research disciplines. Over the years, the study of wind erosion has evolved into a complex inter-disciplinary science including soil physics, atmospheric boundary layers, fluid dynamics, turbulence, climatology, cloud physics, surface hydrology, agricultural sciences and land management. Today, there exists a plethora of scientific literature on wind erosion. Nevertheless, its comprehension remains limited.

Wind erosion, referred to also as the aeolian process, is the displacement of soil particles by aerodynamic forces, resulting in the local transfer of sand [Pye *et al.* 1990] and the long range intercontinental transport of mineral dust [Husar 2004] (Figs. 1.1a,b). It is responsible for dust storms (Fig. 1.1b,c), the evolution of geological formations like sand seas, dunes etc. (Fig. 1.1d,e), the loss of arable land (Fig. 1.1f), and the degradation of cultural heritage (Fig. 1.1g). Airborne mineral dust influences climate [Claquin *et al.* 2003; Otto *et al.* 2007] by affecting atmospheric radiation balance [Ackerman *et al.* 1992], cloud formation [Harikishan *et al.* 2015], atmospheric chemistry [Maria *et al.* 2018], and precipitation [Sequeira 1993]. Recent estimates peg the annual natural mineral dust emissions at 1000–4000 million metric tons, accounting for 32% of the natural atmospheric aerosol concentrations [IPCC 2014]. A large portion of this dust

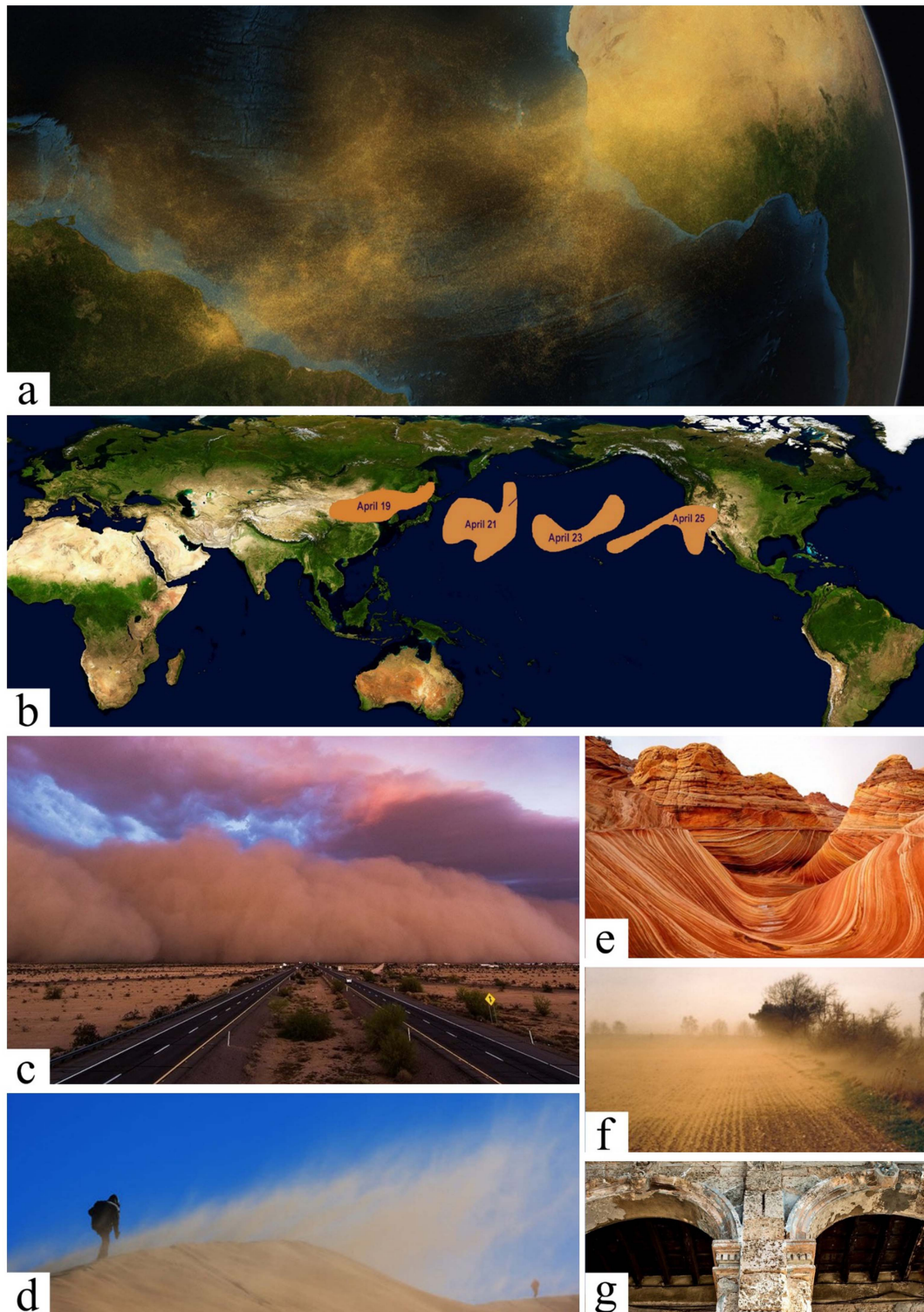


FIGURE 1.1: (a) Satellite observations of continental dust transport between the Sahara desert and the Amazon rainforest. Source: [NASA](#). (b) The 7 day progression of the 2000 km long dust cloud that originated on April 14, 1998 in the Takla Makan desert of western China and reached the pacific US on April 25. Source: Husar *et al.* 2001. (c) Image of a dust storm in Phoenix, Arizona. Source: Washington Post. (d) Dune displacement due to wind force in the Sahara. Source: Google. (e) Wind erosion resultant sandstone formations in New Mexico. Source: Google. (f) Wind erosion over a cultivated field. Source: [Ecomerge](#) (g) Sandblast damage to heritage structures. Source: Google.

is sourced from deserts and deposited into the oceans [Tegen *et al.* 1995], the principal source of nutrients to marine ecosystems and an important control on ocean productivity [Martin *et al.* 1991]. Similarly, the productivity of many terrestrial ecosystems, most notably the Amazon rainforest, is heavily influenced by the deposition of airborne dust [Swap *et al.* 1992] (Fig. 1.1a). Moreover, severe dust emission events can also promote dust storms (Fig. 1.1c) forming dust plumes several thousand kilometres in size, resulting in acute air pollution and associated health hazards [Hagen *et al.* 1973], and can also spread pathogens [Knippertz *et al.* 2014].

Wind erosion most commonly occurs in parched environments, where scanty rainfall and high temperatures result in an easily erodible soil [Ravi *et al.* 2010]. It is of particular concern in semi-arid regions, home to nearly half of the global population [Middleton *et al.* 1997]. Here, the seasonal sparse vegetation and cultivated land patches significantly affect erosion dynamics. Furthermore, the excessive clearance of native vegetation, over grazing, and unsustainable agricultural practices fuel wind erosion [Pimentel *et al.* 1995] (Fig. 1.1f) and promote desertification [Arnalds *et al.* 2013]. Sustained erosion of agricultural lands, 25% of which are semi-arid [Mekonnen *et al.* 2011], can reduce arability and cause crop damage [Sterk 2003] resulting in annual productivity losses exceeding \$100 billion [Telles *et al.* 2011], with its severity increasing with decreasing national development indices [IPBES 2018]. Today, a third of the human population stands directly affected by erosion, with 38% of the Earth's surface area desertified [Nuñez *et al.* 2013]. Current rates of soil erosion are greater than the rates of soil formation, threatening basic food production capabilities in populous parts of the world [Scherr 1999]. Furthermore, erosion induced land degradation increases vulnerability to social instability, particularly in dry-land areas, where prolonged periods of extremely low rainfall have been associated with an increase in violent conflict [IPBES 2018].

In the next couple of decades, anthropogenic climate change is projected to accelerate wind erosion, particularly in semi-arid environments through changes in precipitation and vegetation cover [Munson *et al.* 2011]. Indirect effects of increasing atmospheric CO<sub>2</sub>, associated with global warming, on vegetation growth may further aggravate erosion in such environments [Simonneaux *et al.* 2015]. Climate change is expected to increase the aridity of wetter environments bordering semi-arid regions, like that between central Europe and the Mediterranean [Sharratt *et al.* 2015], increasing the land area susceptible to wind erosion. Furthermore, climate change can intensify the frequency of land abandonment, a common practice in semi-arid regions, potentially increasing wind erosion [Cerdà 1997].

The direct relationship between soil erosion and environmental sustainability, including human health, climate, food security, motivates the understanding of wind erosion. This is important because of the (i) significant impact of airborne dust on the accuracy of climate simulations and weather predictions, and (ii) rising need for efficient land management and erosion control solutions with implications on food and social security. This thesis focusses on the former.

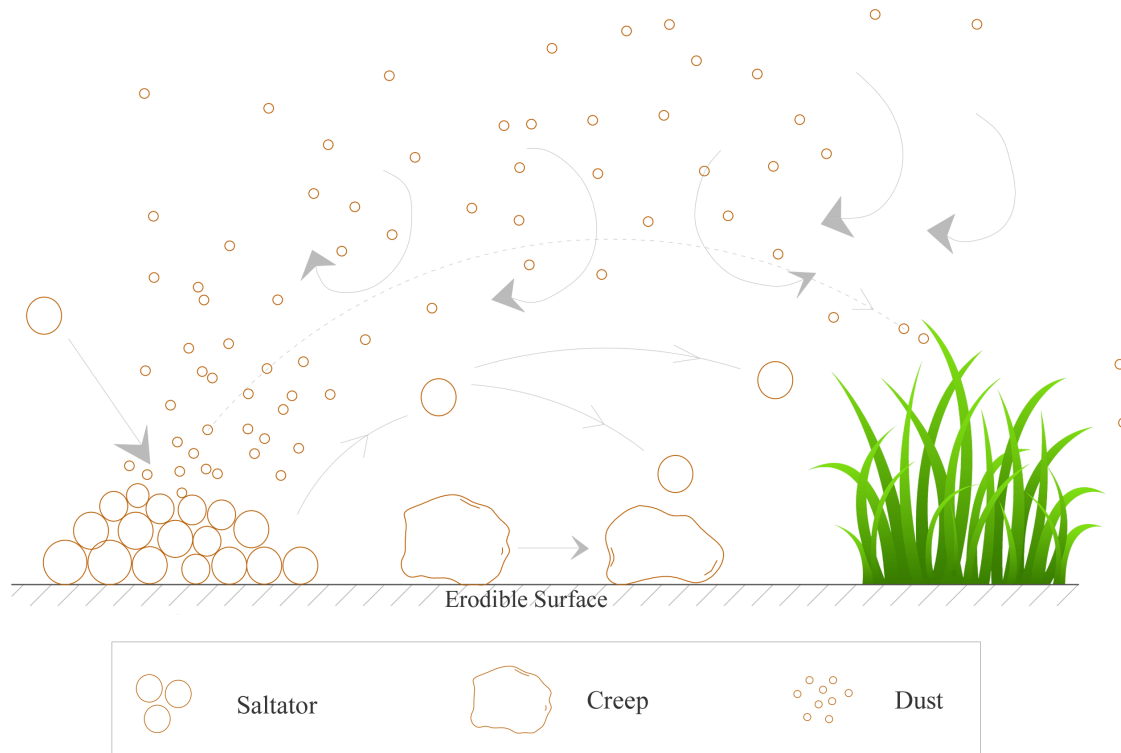


FIGURE 1.2: Schematic representation of the three wind erosion processes - creep (500-2000  $\mu\text{m}$ ), saltation (70-500  $\mu\text{m}$ ) and dust suspension ( $< 20 \mu\text{m}$ ).

Wind erosion is initiated when the near-surface wind speeds exceed a certain threshold, energizing surface sand grains and soil aggregates into motion. This threshold, representing the susceptibility of the surface particles to be excited into motion, is a function of particle size, surface moisture, vegetation, surface texture, topography etc. [Shao 2008]. Once energized, the largest of the erodible soil particles / aggregates measuring 500-2000  $\mu\text{m}$  roll along the surface, too heavy to be airborne by the wind force. This rolling motion is called creep (Fig. 1.2), and may result in aggregates losing some of their mass due to abrasion. Relatively smaller soil grains / aggregates in the range 70-500  $\mu\text{m}$  also roll along the surface, gaining momentum from the flow to be eventually lifted away from the surface. However, their weight prevents them from being transported far away by the wind, and they fall back to the surface within a few centimetres. Upon impacting the surface, they may rebound and splash more particles into motion [Shao 2008; Knippertz *et al.* 2014], and so on. Their motion, thus, resembles hopping along the surface in ballistic trajectories, and this process is called saltation [Bagnold 1941]. The saltation process is an interesting physical problem involving both flow-surface and flow-particle interactions, and can transport large quantities of soil during an erosion event, leading to the development of sand dunes and evolution of sand seas in deserts. This makes it of particular interest in wind erosion studies.

The saltating particles, known as saltators, upon impacting the surface can also release dust, by breaking the surface inter-particle cohesive bonds holding dust particles ( $< 20 \mu\text{m}$ ) at the surface. This process, called sandblasting, is the primary driver of dust emissions [Shao *et al.*

1993; Marticorena *et al.* 1995; Alfaro *et al.* 1997; Shao *et al.* 2000; Shao 2001]. Once released, airborne dust depending on their size can remain suspended over long periods, and be dispersed by turbulence in the atmosphere over large distances [Knippertz *et al.* 2014]. This process, in addition to causing a net loss of fertile soil, affects the Earth system [EEA 2014; Weuve *et al.* 2012; Derbyshire 2007; Griffin *et al.* 2001; Swap *et al.* 1992]. Its understanding, however, remains limited.

As in all scientific fields, the current understanding of wind erosion is based largely on natural process observations. They include field measurements [e.g. Gillette *et al.* 1972; Washington *et al.* 2006a; Baas *et al.* 2007; Ash *et al.* 1983; Ishizuka *et al.* 2008; Sow *et al.* 2011; Dupont *et al.* 2019b, etc.], wind-tunnel experiments [e.g. Shao *et al.* 1993; Alfaro *et al.* 1997; Sutton *et al.* 2008; Burri *et al.* 2011; Zhang *et al.* 2014, etc.], and remote sensing studies [e.g. Sabbah *et al.* 2012; She *et al.* 2018; Sowden *et al.* 2018; Feuerstein *et al.* 2019, etc.]. Such observations are most often restricted in their spatio-temporal scales due to instrumentation limitation. For example, remotely sensed satellite observations provide reliable information on inter-continental dust transport (Fig. 1.1a) but are unable to observe processes closer to the surface (source / sink), while near-surface field observations or wind-tunnel experiments provide no information on large-scale dust dispersion. Another problem of observing wind erosion is the multiplicity of scales over which its processes occur, varying from the near-surface wind-particle interactions at millimetre spatial scale and temporal scale  $< 1$  s [Bechet *et al.* 2015], sand transport (saltation) at meter spatial scale and minute temporal scale [Ellis *et al.* 2012], and dust dispersion over inter-continental spatial scales and day-annual temporal scales [Husar 2004]. Adding to this are the limitations of existing instrumentation in observing erosion processes at the finest of scales. Consequently, our understanding of wind erosion, especially of dust dispersion, remains limited and often contradictory. Nevertheless, from these observations have evolved empirical / semi-empirical models attempting to explain wind erosion, including saltation, sandblasting, and dust suspension.

An important application of wind erosion modelling is in the size-relative quantification of suspended dust in climate models. As mentioned before, airborne dust has significant impact on climate and weather. However, the quantification of suspended dust in climate models remains insufficient, especially over heterogeneous surfaces in semi-arid environments. This is due to the poor representation of the surface wind and the dust emission mechanisms in the presence of different surface roughnesses. Furthermore, semi-arid regions are characterized by a wide variety of seasonal vegetation, changing land-use patterns, and soil types, leading to continuously evolving differences in the emitted dust. A global mapping of dust emissions through field experiments is both tedious and expensive. An alternative to this lies in numerical experiments.

Over the last couple of decades, a new generation of erosion models, combining traditional erosion schemes with high resolution airflow models like Large Eddy Simulations (LES) [Dupont *et al.* 2013; Klose *et al.* 2013; Dupont *et al.* 2015] and Direct Numerical Simulation (DNS) [Durán

*et al.* 2014; Ouchene *et al.* 2018] have been developed. Their advantage is in their ability to explicitly simulate and quantify the influence of different processes on soil-particle entrainment and transport, unlike natural process observations. They however demand large computational resources. Nonetheless, they are increasingly being relied upon to understand the fine-scale erosion processes, especially those closer to the surface (source / sink), in the quest to improve large-scale parametrizations incorporated into climate models. This thesis, and its parent ANR project WIND-O-V (2016-2020), were developed around this problematic. To this end, recent advancements in high frequency near-surface erosion observations and Large Eddy Simulation (LES) modelling techniques have been explored.

## 1.2 Objectives

The goal of this thesis is to investigate the role of sparse vegetation on the suspended dust in semi-arid regions. These regions are characterized by landscape-scale heterogeneities, with seasonal vegetation and cultivation. Therefore, a two step approach is followed, by first examining dust emissions over bare erodible surfaces and then over sparsely vegetated surfaces. These investigations were driven by the following questions:

1. What is the impact of surface properties, the surface wind and the re-deposition process on the size-distribution of the suspended dust during emission events?
2. Is the emitted dust transported similarly to momentum near the surface, i.e. by the same turbulent eddies?
3. How does the dust emission process differ in the presence of sparse vegetation as against that over the bare surface?

Finally, we intend to present a reliable 3D erosion model, coupled to a Large Eddy Simulation (LES) airflow model, capable of quantifying dust emission patterns in different semi-arid environments. This model would potentially help in improving regional scale dust emission models and thereby improve the representation of airborne dust in climate models - the larger goal of the WIND-O-V project of which this thesis is a part.

## 1.3 Structure of this thesis

The investigative work of this thesis follows a step by step approach, starting from the study of bare surface dust emissions and then emissions over sparsely vegetated surfaces, relying on both numerical and field experiments.

This dissertation begins with an introduction to wind erosion, in Chapter 2, describing atmospheric boundary layer flows, flow-surface interactions driving saltation, flow-particle interactions during saltation, sandblasting, and dust suspension. Thereafter, Chapter 3 presents the

WIND-O-V's project and its field experiments, and the 3D erosion model evaluated and used in this thesis.

The theme of Chapters 4 and 5 is dust emission and its near surface turbulent transport over bare erodible surfaces, attempting to answer the first two questions that define this thesis. In Chapter 4, a sensitivity analysis of the parameters and processes influencing the suspended dust flux and its size-distribution during erosion events is presented. It compares the existing dust emission schemes and identifies ambiguities in their quantification of the influence of surface properties (soil granulometry and inter-particle cohesive bond strength), wind intensity, and the deposition processes on the quantity and size of the suspended dust. A new dust emission scheme resulting from this analysis is incorporated into a 3D erosion model in Chapter 5, coupled to a Large Eddy Simulation (LES) airflow model, and evaluated over a bare surface against the WIND-O-V's 2017 field experiment in Tunisia. Thereafter, this 3D erosion model is used to investigate the origins of the dissimilarity between dust and momentum turbulent transport observed during the WIND-O-V's 2017 field experiment. Here, the dissimilar transport indicates that dust and momentum were not always transported by the same eddies during the field experiment.

Chapters 6 and 7 focus on the impact of sparse vegetation, a seasonal feature of semi-arid environments, on the suspended dust during erosion events. In Chapter 6 is presented the results of the WIND-O-V's 2018 experiment, conducted at the same site as the 2017 experiment but with sparse uniform vegetation. Here, the role of sparse vegetation on dust emissions is explored through a comparative analysis between the WIND-O-V's 2017 and 2018 experiments, i.e. over bare and vegetated surfaces. The experimental data is subsequently used to evaluate the 3D erosion model, extended in Chapter 7 to include vegetation characteristics. Finally, this model is used to investigate the role of near-surface turbulence and deposition on the size-distribution of the suspended dust during erosion events over sparsely vegetated surfaces.

This dissertation terminates with a summary of conclusions, in Chapter 8, answering the 3 key questions that guided our investigations, and thereafter presents some prospective research ideas aimed at furthering the implications of this study.





## 2 An introduction to wind erosion

Wind erosion results from the wind induced abrasion of Earth's surface through a series of flow-surface, flow-particle and particle-particle interactions. A review of the current understanding of these interactions is the first step towards investigating wind erosion. This review is presented here in two parts - (i) an understanding of the atmospheric flow, and (ii) an introduction to different erosion mechanisms.

### 2.1 Atmospheric flow

The Earth's atmosphere is the layer of air extending up to 500 km above its surface, comprised predominantly of Nitrogen (78%) and Oxygen (21%). It is divided into four layers - troposphere, stratosphere, mesosphere and thermosphere - each with distinct physical, chemical, and thermal properties. Most processes affecting the surface (precipitation, wind erosion, aerosol transport etc. ) occur in the troposphere, the lowest layer of the atmosphere, extending up to about 10 km above Earth's surface. The lowest part of the troposphere, in contact with the surface, is the Atmospheric Boundary Layer (ABL). The region above this layer is the free atmosphere (Fig. 2.1).

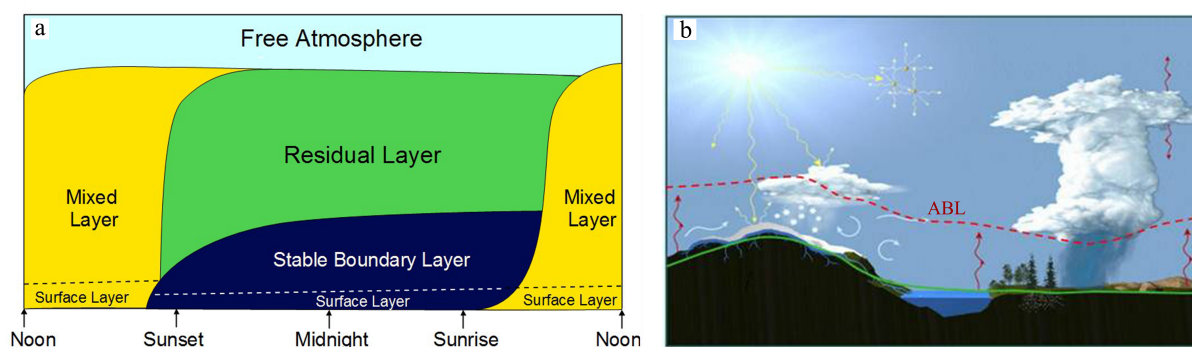


FIGURE 2.1: (a) Schematic representation of the diurnal variation of the Atmospheric Boundary Layer (ABL). Source: Stull [1988]. (b) The depth of the ABL over typical terrain at midday presented as a dot-line. Source: Wikipedia.

A characteristic feature of the ABL is its diurnal evolution (Fig. 2.1a), with its depth varying from about 1 km during the day to around 100 m at night, from the heating-cooling of the Earth's surface. At midday, the solar heating of the surface results in the convection of warm moist air upwards, vertically mixing with the surrounding air parcels and resulting in a mixed layer. Such vertical mixing continues until the free atmosphere, where an entrainment zone is

formed hosting clouds (Fig. 2.1b). The surface heating disappears after sunset and with it the convective mixing. Air from the surface no longer mixes with air throughout the boundary layer, and the air that was mixed during the day stays above the much lower night-time stable boundary layer (Fig. 2.1), in the residual layer. The surface heating resumes after sunrise restarting the convective mixing. This mixing entrains air from the residual layer, reducing its depth as the day progresses, and increasing the depth of the ABL. Eventually, the air driven by convection reaches its maximum turbulent energy level which influences the depth of the boundary layer.

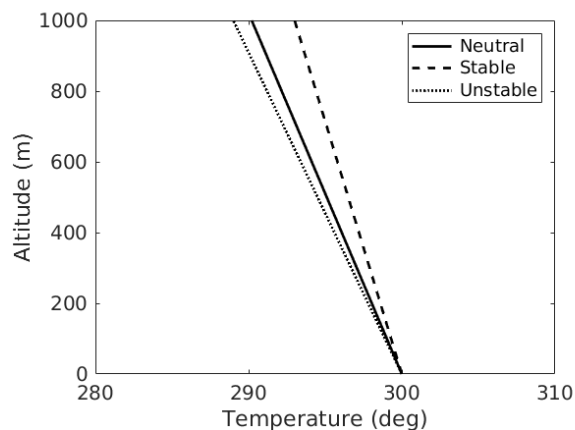


FIGURE 2.2: Schematic representation of the atmospheric temperature profiles for stable, unstable and neutral (adiabatic) stratification.

The diurnal heating-cooling of the Earth's surface results in three stratifications influencing the tropospheric flow and turbulence, namely -unstable, stable and neutral. As a rule, the air temperature in the troposphere decreases with altitude, ideally at the rate of  $-9.8^{\circ}\text{K}/\text{km}$ , called the adiabatic lapse rate (Fig. 2.2). At this rate, a displaced air parcel does not exchange heat with its neighbours. At night, the cooling of the Earth's surface decreases the vertical air temperature gradient and the atmosphere is said to be stable. Under such conditions, an air parcel if disturbed will return back to its original position,

reducing turbulent mixing. During hot days, the heating of the Earth's surface increases the vertical air temperature gradient leading to instability, and the warmer less dense air parcels move upwards, continuing to rise until they have lost enough heat to lose their buoyancy. This results in strong convective mixing (Fig. 2.1a). In between these two conditions, at dusk and dawn, the atmospheric temperature gradient is close to the adiabatic lapse rate, an air parcel displaced up or down would have the same density as the surrounding air and have zero buoyancy, leading to neutral stability.

Key processes of wind erosion occur predominantly in the lowest portion of the ABL, within the first 10% of its depth, referred to as the Atmospheric Surface Layer (ASL) (Fig. 2.1a). In this layer, constant (momentum, heat, dust etc.) fluxes are assumed throughout its depth [Kaimal *et al.* 1994]. The importance of the constant flux layer is in estimation of near-surface fluxes through single level flux measurements, reducing complexity and cost. In reality, most Earth surfaces are heterogeneous, particularly in semi-arid environments characterized of sparse seasonal vegetation which are of particular interest in this thesis. In such cases, ASL divides into one or more internal boundary layers, discussed later in this chapter.

The wind in the atmospheric surface layer drives erosion. It comprises of (i) a mean wind responsible for the horizontal advection of quantities like momentum, heat, and mass, and (ii)

turbulence - the perturbation around the mean - responsible for the vertical mixing of these quantities.

### 2.1.1 Turbulence

The Oxford dictionary defines turbulence as *the violent or unsteady movement of air or water, or of some other fluid*. G.I. Taylor, a pioneer of turbulence study, defined it as *an irregular motion which in general makes its appearance in fluids, gaseous or liquid, when they flow past solid surfaces or even when neighbouring streams of the same fluid flow past or over one another* [Kaimal et al. 1994]. The study of turbulence dates back to Leonardo Da Vinci who used the term *turbolenza*, writing in the context of water, *the smallest eddies are almost numberless, and large things are rotated only by large eddies and not by small ones, and small things are turned by small eddies and large*, giving a visual representation of turbulence structures and transport.

Turbulence in atmospheric flows is characterized by the irregular and random motion of air parcels around a mean state. It is generated by (i) wind shear due to friction at the flow-surface interface and (ii) buoyancy (thermal convection) due to the heating of the Earth's surface. Wind shear turbulence is caused by the absorption of fluid momentum (flow energy) by the surface roughness elements (topography, vegetation, buildings etc.) resulting in mixing of air parcels carrying positive/negative momentum. Thermal turbulence is due to the vertical mixing of air parcels transporting hotter air upwards and cooler air towards the surface.

A simple view of turbulence can be obtained from the Reynolds decomposition [Reynolds 1895] of the wind velocity:

$$u_i(t) = \bar{u}_i + u'_i(t), \quad (2.1)$$

where  $u_i(t)$  is the  $i^{\text{th}}$  component of the wind velocity ( $i = 1, 2, 3$  respectively for stream-wise, lateral and vertical components) at any instant  $t$  defined as the sum of the mean wind  $\bar{u}_i$  and the turbulent part  $u'_i(t)$ . From this decomposition is defined the turbulence variance  $\sigma_{ui}^2 = (\sum_1^N \overline{u_i'^2})/N$ , where  $N$  is the number of discrete equispaced (time) measurements. Based on  $\sigma_{ui}^2$  two characteristics of turbulence are defined, namely, (i) *stationary*: if  $\sigma_{ui}^2$  is relatively steady, i.e. if the mean turbulence is invariant under a translation in time, and (ii) *homogeneity*: if  $\sigma_{ui}^2$  is relatively uniform in space.

### 2.1.2 Turbulent fluxes

Turbulence acts to transport momentum, heat and mass vertically within the atmosphere. This transport is expressed as fluxes - the transfer of a quantity across unit area in unit time, with its divergence indicating a local temporal change. The flux of a quantity  $q$  in the ASL can be expressed as  $f_i = u_i q + k_p \partial q / \partial x_i$ , where  $u_i q$  is the flux contribution due to air movement and

$k_p \partial q / \partial x_i$  is that due to molecular diffusion, with  $k_p$  the coefficient of diffusivity. In atmospheric flows, the flux contribution due to molecular diffusion is negligible.

Statistically, using Reynolds decomposition, any flux, for example the turbulent dust flux can be decomposed as

$$\overline{u_i c} = \overline{u_i} \overline{c} + \overline{u'_i c'}, \quad (2.2)$$

where  $c$  is the dust concentration. Here  $\overline{u_i} \overline{c}$  represents the dust transported by the mean flow and  $\overline{u'_i c'}$  is the dust flux due to turbulent motion. Similarly, the momentum flux can be decomposed as

$$\overline{u_i u_j} = \overline{u_i} \overline{u_j} + \overline{u'_i u'_j}, \quad (2.3)$$

with the mean term  $\overline{u'_i u'_j}$  is referred to as the Reynolds shear stress. Its component  $\overline{u w}$  at the surface quantifies the shear exerted by the flow on it and is an important scaling quantity in erosion studies. In general, the vertical fluxes for atmospheric flows  $\overline{u w}$  and  $\overline{w c}$  are equal to  $\overline{u' w'}$  and  $\overline{w' c'}$ , respectively, since  $\overline{w} = 0$ .

The turbulent transport of quantities in the atmospheric surface layer can be better understood by examining the definition of fluxes, for example the dust flux. Typical airborne dust concentration profiles exhibit an exponential decrease with height as shown in Fig. 2.3. Near the surface, turbulence can be imagined to be eddy motions mixing air parcels downwards from position 1 to position 2 (negative  $w'$ ) and vice versa (positive  $w'$ ). Therefore, the mean mass transfer ( $\rho_a \overline{w' c'}$ ) associated with this process is zero. However, the downward moving air parcels are associated with lower dust concentrations ( $c' < 0$ ) resulting in a positive dust flux  $w' c'$ . Similarly, the upward moving air parcels are associated with larger dust concentrations ( $c' > 0$ ) also resulting in positive  $w' c'$ . Therefore, the average turbulent dust flux is positive (net upward dust transfer) for such an eddy motion, while a negative turbulent dust flux (net downward dust transfer) would result if the dust concentration gradient is positive. Thereby, the instantaneous flux of any quantity can be positive or negative, but the average turbulent fluxes are pointed in the direction opposite to the vertical gradient of that quantity. This allows for similitude to be drawn between turbulent and molecular diffusions, both of which are driven by concentration gradients.

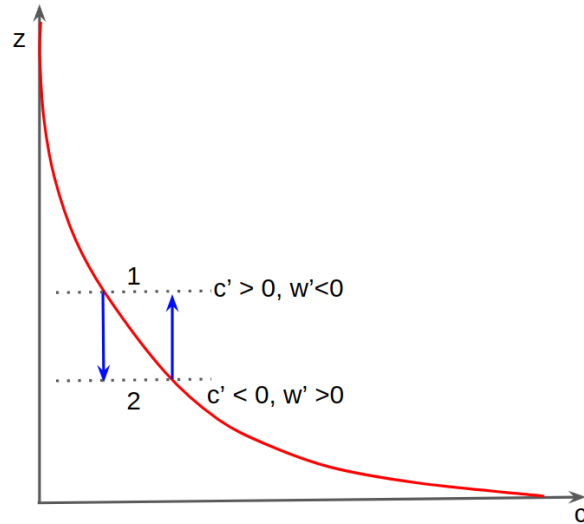


FIGURE 2.3: Schematic representation of turbulent dust transport leading to a positive dust flux. The red line is the typical vertical dust concentration profile.

### 2.1.3 Flux Gradient (FG) similarity

The analogy with molecular diffusion is often assumed to derive turbulent fluxes in atmospheric flows through the application of Fick's law of diffusion. Accordingly, the vertical flux of any quantity  $q$  across a vertical plane in the atmosphere is a function of an eddy diffusivity,  $K$  ( $\text{m}^2\text{s}^{-1}$ ), times the vertical concentration gradient  $\partial\bar{q}/\partial z$ , defined as:

$$F = -K \frac{\partial\bar{q}}{\partial z}. \quad (2.4)$$

This extension of molecular diffusion to turbulent fluxes is called the K-theory [Shao 2008]. The negative sign is imposed so that the fluxes away from the surface are positive, adding material to the atmosphere, and those towards it are negative, removing material from the atmosphere. Here, molecular diffusivity is neglected as turbulence motions are many orders of magnitude greater than molecular motions.

Following the FG similarity, the mean momentum ( $F_{uw}$ ), heat ( $H$ ) and dust ( $F_{wd}$ ) fluxes can be expressed in terms of the vertical gradients of wind velocity, temperature, and dust concentration, respectively as,

$$F_{uw} = -K_m \frac{\partial\bar{u}}{\partial z}, \quad (2.5)$$

$$H = -K_h \frac{\partial\bar{\theta}}{\partial z}, \quad (2.6)$$

$$F_{wd} = -K_d \frac{\partial\bar{c}}{\partial z}, \quad (2.7)$$

where  $K_m$ ,  $K_h$  and  $K_d$  are the coefficients of turbulent exchange for momentum, heat and dust, respectively,  $c_p$  is the specific heat of air at constant pressure,  $\theta$  is the mean potential air temperature, and  $c$  is the dust concentration. In practice, it is widely assumed that momentum and dust are transported similarly by the turbulence, leading to simplification  $K_m = K_d$ , referred to as the Reynolds similarity [Gillette *et al.* 1972]. For heat,  $K_h \approx 0.8K_m$ .

The advantage of the FG similarity is in estimating near-surface fluxes, through the measurement of the vertical gradient at two heights. In doing this, it supposes a constant flux along the vertical, i.e. between the two measurement heights. The constant vertical flux has been relatively well observed for momentum and heat near the surface (in the ASL) during field experiments over homogeneous flat surfaces [Kaimal *et al.* 1994]. The same is often assumed for dust particles ( $d_p < 10 \mu\text{m}$ ) [Gillette *et al.* 1974; Gomes *et al.* 2003; Sow *et al.* 2011], thereby relating near-surface and surface fluxes, but has never been verified during field experiments.

### 2.1.4 Mean wind at neutral stratification

The Earth's surface roughness elements absorb momentum from the wind flow through viscous effects and pressure drag. This is quantified as the surface friction velocity ( $u_{*0}$ ):

$$u_{*0} = \sqrt{\frac{\tau_0}{\rho_a}} = \sqrt[4]{\overline{u'w'^2}_{z \rightarrow 0} + \overline{v'w'^2}_{z \rightarrow 0}} \quad (2.8)$$

an important scaling parameter for erosion fluxes. In the above equation,  $\tau_0$  refers to the shear stress acting on the surface. Following K-theory and assuming a steady wind direction ( $\overline{u'w'} \gg \overline{v'w'}$ ) the momentum flux can be rewritten as:

$$-\rho_a u_{*0}^2 = -\rho_a K_m \frac{\partial \bar{u}}{\partial z}. \quad (2.9)$$

This allows for expressing the momentum eddy coefficient as a function of the surface friction velocity and wind velocity gradient as:

$$K_m = \frac{u_{*0}^2}{\partial \bar{u} / \partial z}. \quad (2.10)$$

Under neutral stratification,  $K_m$  is approximated as a function of the distance from the surface  $z$ , leading to:

$$\frac{\partial \bar{u}}{\partial z} = \frac{u_{*0}}{\kappa z}, \quad (2.11)$$

where  $\kappa$  is the von Karman constant with values ranging between 0.35 and 0.43. In this thesis it is taken as 0.40, the most commonly used value in erosion studies [Shao 2008]. Integrating the above equation between  $z_0$  near the surface and  $z$  farther above yields:

$$u(z) = \frac{u_{*0}}{\kappa} \ln\left(\frac{z}{z_0}\right). \quad (2.12)$$

Here,  $z_0$  is the distance above the surface where  $u(z) = 0$ , and is referred to as aerodynamic roughness length. Eq. 2.12 implies that for a given wind speed, larger  $z_0$  implies a larger  $u_{*0}$ , indicating a greater momentum absorption by the surface. Therefore,  $z_0$  quantifies the capacity of the surface to absorb momentum and is an important quantity for wind erosion studies used to express the erodibility of a surface. In practice,  $z_0$  is often estimated by extrapolating the wind profile to the point where  $u(z) = 0$  near the surface [Dupont *et al.* 2018]. In the constant flux layer (ASL),  $u_{*0} \approx u_*(z)$  can be estimated by fitting the logarithmic wind velocity profile (Eq. 2.12) from velocity at different heights, or directly from single point high frequency measurements of the 3D wind velocity (Eq. 2.8).

### 2.1.5 Monin-Obukhov similarity

Under non-neutral stratification, arising from the diurnal variations in surface temperatures, the surface layer turbulent mixing changes and the vertical wind profile deviates from the logarithmic form of Eq. 2.12. To compensate for this, Monin *et al.* [1954] recalibrated the FG similarity using Buckingham's Pi Theorem. They defined a dimensionless parameter  $z/L$  to characterize the processes in the surface layer, where  $L$  is the Obukhov length expressed as:

$$L = \frac{-u_*^3 \bar{\theta}}{\kappa g w' \theta'}. \quad (2.13)$$

Physically,  $L$  is the height above the surface at which turbulence produced by buoyancy equals that produced by shear. Subsequently,  $z/L$  has become a commonly used indicator of atmospheric stability with  $z/L > 0$  for stable,  $z/L < 0$  for unstable, and  $z/L = 0$  for neutral stratification.

Monin-Obukhov Similarity modifies the profile equations (Eqs. 2.5 - 2.7) through the introduction of an universal stability function  $\Phi(z/L)$  as:

$$F_{uw} = -\frac{u_* k z}{\Phi_m(z/L)} \frac{\partial \bar{u}}{\partial z'} \quad (2.14)$$

$$H = -\frac{u_* k z}{\Phi_h(z/L)} \frac{\partial \bar{\theta}}{\partial z'} \quad (2.15)$$

$$F_{wd} = -\frac{u_* k z}{\Phi_d(z/L)} \frac{\partial \bar{c}}{\partial z'} \quad (2.16)$$

$\Phi(z/L)$  accounts for the effects of stronger mixing under unstable stratification, leading to a decrease in the vertical gradient and an increase in the flux, and vice versa for stable stratification. Numerous empirical expressions for  $\Phi(z/L)$  have been proposed, with  $\Phi_h(z/L)$  taken approximately equal to  $\Phi_m(z/L)$  for stable stratification, and equal to  $\Phi_m^2(z/L)$  for unstable conditions. The expressions for  $\Phi_m(z/L)$  as recalculated by Högström [1988] are:

$$\Phi_m(z/L) = (1 - 19.3z/L)^{-0.25}, z/L < 0, \quad (2.17)$$

$$\Phi_m(z/L) = (1 + 6z/L), z/L > 0. \quad (2.18)$$

In erosion studies,  $\Phi_d(z/L)$  is often taken equal to  $\Phi_m(z/L)$  assuming transport similarity between momentum and dust [Gillette 1977].

### 2.1.6 Turbulence spectrum

Surface layer turbulence comprises of eddies of many scales coexisting at any given height, with a wide range of length and time scales from millimetres and milliseconds to kilometers and hours. In the atmosphere, the larger eddies are energized by the mean fluid motion and



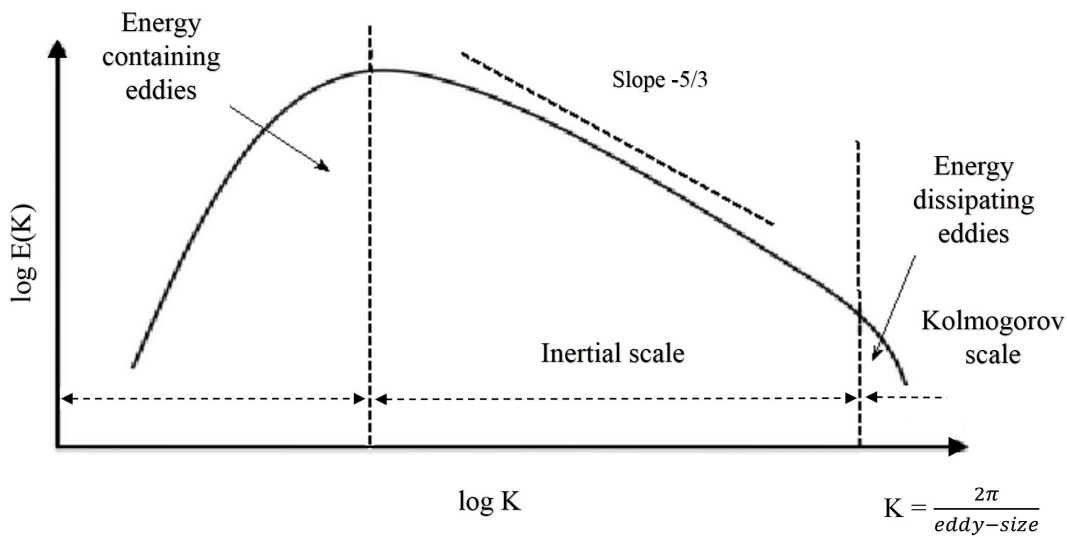


FIGURE 2.4: Schematic representation of the turbulence spectrum with length scale on the x-axis and the Turbulent Kinetic Energy (TKE) on the y-axis.

they transmit energy to the smaller eddies by a cascade process. At the smallest scales, this energy is dissipated as viscosity. This cascade process was first described in Fry Richardson's poem - *big whorls have little whorls which feed on their velocity, and little whorls have lesser whorls and so on to viscosity*. This cascade can be represented graphically through the energy spectrum, following Kolmogorov [1941] (Fig. 2.4) by plotting eddy energy ( $E(K)$ ) as a function of eddy frequency ( $K$ ).

The turbulence spectrum is divided into three distinct regions (scales). The region with the lowest frequencies ( $f \approx 10^{-4}$  Hz) containing the largest eddies (10 - 500 m) is called the energy containing region wherein the eddies gain energy from the mean fluid motion [Kaimal *et al.* 1994]. Following this range is the inertial sub-range where the cascading process of energy transfer to the smaller eddies takes place. This process follows the well-defined Kolmogorov's  $-5/3$  law that predicts a decrease in energy density by five decades when the frequency increases by three decades for state variables. For fluxes of quantities such as momentum, heat and dust, it suggests a  $f^{-4/3}$  decrease in the fluxes multiplied by the frequency  $f$ . Finally, at the smallest scales (Kolmogorov's micro-scale with  $f \approx 10 - 30$  Hz), the inertial sub-range merges into the dissipation range, where energy is lost as heat. The typical dissipation length scale of the Kolmogorov's micro-scale is  $\eta = \nu^{3/4} \epsilon^{-1/4}$ , typically about  $10^{-3}$  m, where  $\epsilon$  is the dissipation rate and  $\nu$  the kinematic viscosity.

An important property of atmospheric turbulence is the increase in turbulent length scales with distance from the surface, indicating the increasing significance of the smaller eddies closer to the surface. Therefore, most often, the turbulence spectrum is plotted against a dimensionless frequency  $n$ , equal to  $f$  normalized by the wind speed  $u(z)$  and the height  $z$ ,

i.e.  $n = fz/u(z)$ . An important implication of the height dependency of eddy-size is the increasing sensing frequency towards the surface, limiting field measurements. The knowledge of the turbulence spectrum is important during field experiments for choosing sensors and measurement strategies. It is a key validator of atmospheric measurements by assessing if the measurement frequency includes the main turbulent structures and deciding the optimal averaging time period [See for momentum, heat and dust fluxes in Dupont *et al.* 2019b]. Finally, it remains at the foundation of the current knowledge of turbulence, including numerical Large Eddy Simulations (LES) models which are extensively used in this study.

### 2.1.7 Internal boundary layer (IBL)

The above description of atmospheric flows is based on an idealized scenario of surface homogeneity, resulting in a single well-developed boundary layer (ABL). In semi-arid environments, heterogeneities such as seasonal sparse vegetation, dispersed cultivated land parcels, and humidity patches lead to surface roughness variations generating different wind profiles (Eq. 2.12) that are shifted downstream by the horizontal wind field forming layers of discontinuities inside the ABL called Internal Boundary Layers (IBL). Thereby the upwind profiles of wind, temperature and other scalars (like dust) will require a certain distance (fetch) to attain equilibrium with the new surface leading to changes in the turbulent exchanges. Therefore, over heterogeneous surfaces, the turbulent exchanges are not just influenced by local surface characteristics, but also those farther upwind.

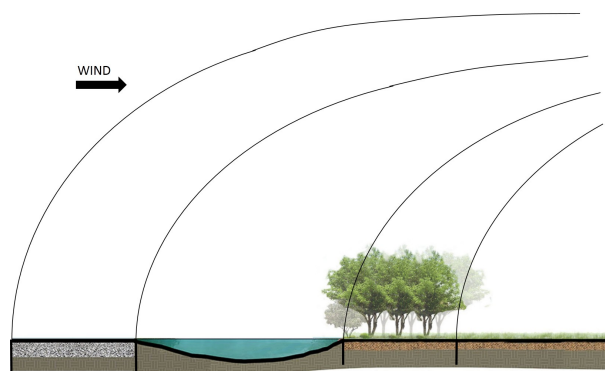


FIGURE 2.5: Development of internal boundary layers over an heterogeneous surface with different roughnesses.

The depth of the momentum IBL is often defined as the distance from the surface where  $\tau(z)$  is 99% of the upwind value at the same height [Kaimal *et al.* 1994]. Inside the IBL, the flow is influenced predominantly by the local surface characteristics. Above it, the flow is characteristic of the upwind surfaces. A constant flux layer is expected within the first 10% of the IBL depth. Furthermore, IBL formation is not limited to momentum fluxes alone, as non-homogeneous and/or discontinuous sources/sinks of scalars may lead to the development of IBLs as well, with the quantities not mixed within the entire depth of the ABL.

### 2.1.8 Flow with sparse vegetation

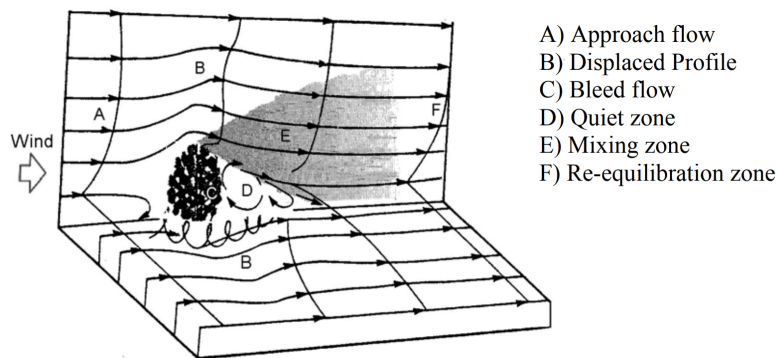


FIGURE 2.6: Schematic representation of the wind flow around an isolated vegetation element. Adapted from Judd *et al.* [1996]

Semi-arid environments are characterized by sparse seasonal vegetation that act as individual roughness elements affecting the flow. Judd *et al.* [1996] identified five distinct regions wherein the airmass is either accelerated or decelerated by an isolated vegetation element (Fig. 2.6). Such flow disturbance affects not just the mean wind and turbulent exchanges, but may also affect soil erosion.

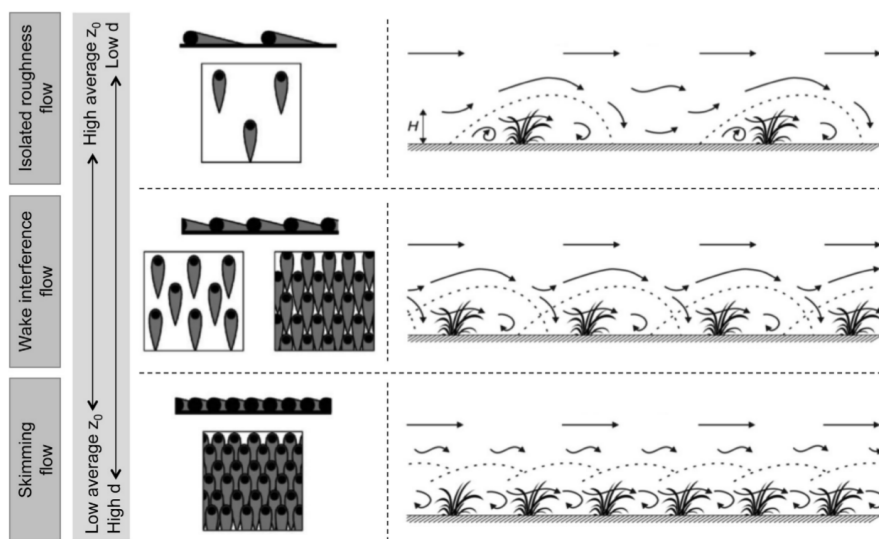


FIGURE 2.7: Schematics of the near-surface flow regimes associated with different vegetation arrangements. Adapted from Mayaud *et al.* [2016b]

As air approaches an isolated vegetation (A in Fig. 2.6), the majority of its mass is diverted above and around it with an increased velocity (B). A small portion of the approaching air mass flows through the porous vegetation reducing in speed, creating a region of bleed flow in its lee (C). A triangular shaped sheltered zone of reduced wind speed is formed in the lee of the vegetation element (D). The turbulent characteristics in this zone are smaller and less energetic than those upwind, influenced by the morphology of the element and the approaching wind. With dense elements (high LAI), the flow in the sheltered zone can reverse in direction to

form a recirculating eddies [Cleugh 1998]. Above the sheltered zone (D) is the mixing layer (E) which develops from the edge of the vegetation element towards the surface sufficiently downwind of the obstacle where the wind speed appears comparable to that downwind of the element. Such a flow separation can lead to localized increase / decrease in erosion as demonstrated in the experiments of Logie [1982], Wolfe *et al.* [1993], Ash *et al.* [1983], Hagen [1994], Lancaster *et al.* [1998], Gibbens *et al.* [1983], Brazel *et al.* [1987], Sutton *et al.* [2008], and Burri *et al.* [2011]. Their effect over larger spatial scales (several hundred meters / kilometers) on erosion is, however, still being debated.

Another factor influencing near-surface flows is the vegetation density (arrangement) on the surface (Fig. 2.7). For sparse vegetation elements covering < 16 % of the surface area [Wolfe *et al.* 1993] with inter-plant distances greater than 3.3 times the vegetation width, individual plants act as roughness elements shedding turbulent eddies by diverting wind-flow above and around them as discussed before. Here, the disturbed wind has sufficient upwind distance to readjust before encountering the next vegetation element. When the vegetation surface density increases to 16–40 % and decreasing inter-plant distances, as in some cultivated fields, the disturbed wind has insufficient distance to re-adjust before encountering the downwind element. Therefore, the wakes formed in the lee of the vegetation element are not sufficiently developed before they encounter the next upwind element. For high vegetation density (Fig. 2.7), a skimming flow regime exists wherein the bulk of the flow skims over the canopy, leading to a flow separation with that within the canopy with one or more eddies trapped inside the canopy. These flow regimes are most often associated with cultivated vegetation, common to semi-arid regions, each affecting erosion differently. This too is yet to be fully explored.

## 2.2 Wind erosion

### 2.2.1 Soil characteristics

The Earth's surface soil is extremely diverse, with differences in granulometry, morphology and chemical properties. The influence of the soil characteristics on the erosion process, including particle entrainment, transport and deposition, is still being explored [Shao 2008]. Many of these properties, especially morphological, are difficult to be measured. Nevertheless, their adequate description is essential in understanding wind erosion and for its modelling.

An important physical property of soil grains is their shape, describing aspects of external morphology such as form, roundness, and surface roughness. Nearly all existing erosion models and parametrizations assume soil particles to be spherical. However, observations of different soils have revealed highly irregular shapes from spheres to plates, from very angular to well-rounded, and from rough to smooth [Pye *et al.* 1990]. Nevertheless, the assumption of sphericity simplifies erosion modelling and is based on the estimation of an equivalent particle size

(diameter)  $d_p$  to which certain aerodynamic or optical properties are identical. Accordingly, for a particle of mass  $m_p$ ,  $d_p = \sqrt[3]{6m_p/\pi\rho_p}$ . The importance of the accuracy of  $d_p$  is in the size-dependency of the erosion processes, particularly dust suspension.

Traditionally in wind erosion studies, soil particles are divided into three categories [Shao 2008] - sand ( $63 \mu\text{m} < d_p < 2000 \mu\text{m}$ ), silt ( $4 \mu\text{m} < d_p < 63 \mu\text{m}$ ), and clay ( $d_p < 4 \mu\text{m}$ ). Silt and clay are most commonly referred to as dust. Most soils are composed of all three types of particles with variations in their mass (number) contributions. This is expressed using a particle size-distribution (PSD) by defining the size-relative probability of a particle of a size  $d_p$  being present in the erodible soil sample. It is most commonly expressed as a log-normal distribution in terms of the mass (M) or number (N) fractions of the particles. For a particle of size  $d_p$ , the log-normal number size-distribution is given by,

$$\frac{dN}{d \log d_p} = \frac{1}{\sqrt{2\pi} \ln(\sigma_g)} \exp \left[ -\frac{1}{2} \left( \frac{\ln(d_p) - \ln(d_{pm})}{\ln(\sigma_g)} \right)^2 \right], \quad (2.19)$$

where  $d_{pm}$  and  $\sigma_g$  are the geometric mean and standard deviations. It must be noted here that soils generally are made up of multiple PSDs, each with its dominant mode. The mass distribution  $dM/d \log d_p$  can also be similarly expressed. Fig. 2.8 shows the relative importance of the mass and number size-distributions for the same soil, with the former emphasizing on the coarser particles and vice versa. Most often, like in Fig. 2.8 the PSDs are expressed as the percentage contribution of each particle size, but they can also be expressed as percentages relative to a fixed size or as the absolute value of the concentration. Such graphical presentation is also used while representing airborne particulate matter, especially mineral dust.

### 2.2.2 Erosion threshold

Wind erosion is initiated when the wind shear force acting on the surface exceeds the inter-particle bonding forces holding back the particles. These forces opposing erosion include a complex ensemble of particle weight and inter-particle cohesive bonds [Shao *et al.* 2000], including electrostatic, Van der Waals and cementation forces (Fig. 2.9). They are, however, difficult to measure explicitly even under controlled experimental conditions [Shao *et al.* 1993;

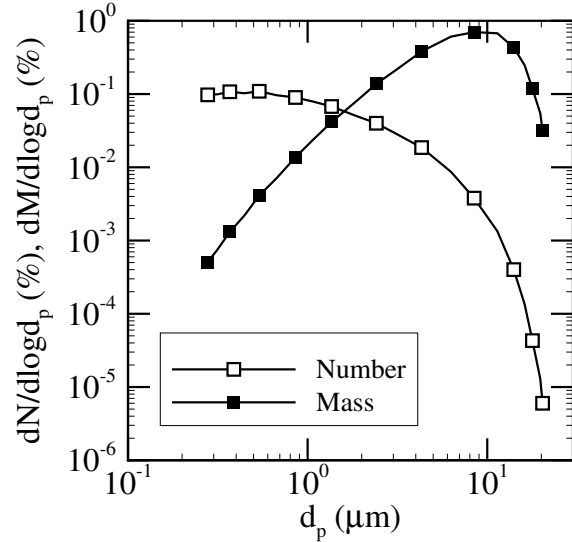


FIGURE 2.8: Particle size-distribution of dust in number  $dN/d \log d_p$  (unfilled symbols) and mass  $dM/d \log d_p$  (filled symbols) for the same erosive soil sample.

Shao 2001]. To overcome this limitation, these counteracting forces are quantified as a function of the threshold friction velocity ( $u_{*t}$ ), which for any given surface (with roughness  $z_0$ ) indicates the wind velocity ( $u(z)$ ) above which erosion is initiated (Eq. 2.12).

The simplest expression for  $u_{*t}$  was provided by Bagnold [1941] as the balance between the gravity force ( $\propto d_p$ ) and surface wind shear force ( $\propto u_{*0}$ ), suggesting an increasing erosion threshold with particle size. Subsequent wind tunnel experiments by Chepil [1951] revealed increasing threshold with decreasing particle size below  $100 \mu\text{m}$ , which was theorized to be due to enhanced inter-particle cohesion. Later, Iversion *et al.* [1982] extrapolated from large wind tunnel data sets an expression for  $u_{*t}$  assuming a power law relation between inter-particle cohesive bond strength and particle size, accounting for both an increase in threshold with increasing particle size for sand grains larger than  $100 \mu\text{m}$  and with decreasing particle size for sand grains smaller than  $100 \mu\text{m}$ .

More recently, Shao *et al.* [2000] improved the formulation of  $u_{*t}$  and presented a physically based parametrization accounting for van der Waals and electrostatic forces as

$$u_{*t}(d_p) = \sqrt{0.0123 \left[ \frac{\rho_p g d_p}{\rho_a} + \frac{\Gamma}{\rho_a d_p} \right]}, \quad (2.20)$$

Here, the term  $\rho_p g d_p / \rho_a$  accounts for the particle weight (gravity force) and  $\Gamma / (\rho_a d_p)$  for the inter-particle cohesive forces, with  $\Gamma$  an empirical constant approximated from wind tunnel measurements. Interesting inferences can be derived from equation 2.20. First, it suggests that for dust particles ( $d_p < 20 \mu\text{m}$ ),  $u_{*t}$  is generally  $> 1 \text{ ms}^{-1}$  implying a 10 m high velocity of the order of  $35 \text{ ms}^{-1}$  (for  $z_0 \approx 10^{-5} \text{ m}$  from Eq. 2.12). Such high wind speeds are rarely attained even during dust storms, suggesting that direct aerodynamic dust emissions are a rare occurrence. Second, it indicates a minimum threshold friction velocity at  $60 \mu\text{m}$  implying that soils with strong concentration of grains around this size are more easily erodible. Finally, it demonstrates that the inverse size dependency of  $u_{*t}$  on cohesive forces and particle weight leads to erosion being a size-segregating process during which the mobilized particle size-distribution may differ from that of the parent soil.

Equation 2.20 is, however, limited to flat, bare, and dry surfaces, where the absorption of

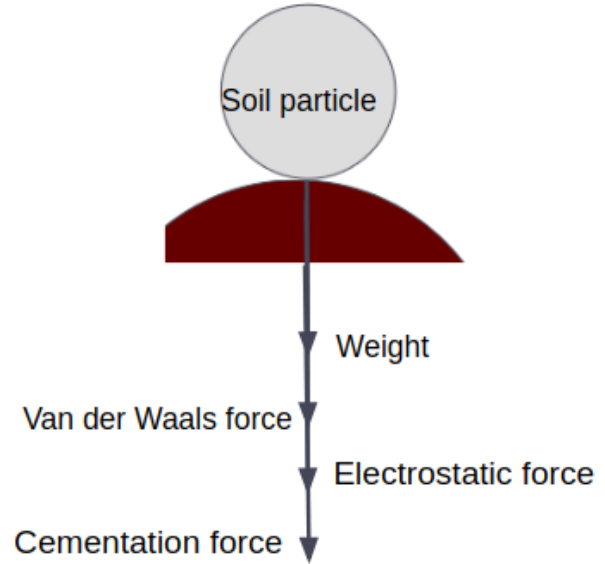


FIGURE 2.9: Schematic representation of anti-erosion forces on a soil particle at the surface

momentum by the surface can be directly linked to the entrainment of soil grains. This is true for most existing threshold parametrizations, as they are based on idealized wind tunnel or field experimental data sets. However, in semi-arid environments, the heterogeneity of the surfaces with humidity and vegetation patches complicates the estimation of an universal  $u_{*t}$ . In such regions, the presence of surface moisture is known to increase the inter-particle cohesion and therefore increase the energy required to mobilize particles, represented by an increase in  $u_{*t}$  [Neuman 2004]. Similarly, the presence of vegetation leads to a partitioning of the flow momentum between that absorbed by the vegetation and that transferred to the surface (available for erosion), resulting in an increase in the energy required to initiate erosion represented by an increase in  $u_{*t}$  [Raupach 1991]. Despite these difficulties,  $u_{*t}$  is still widely used to define the erodability of surfaces. Nevertheless, it must be noted that  $u_{*t}$  is not a universal function, and is highly sensitive to soil type, surface characteristics, and erosion conditions [Marticorena *et al.* 1995] and hence cannot not be generalized.

### 2.2.3 Modes of eroded particle motion

When the surface wind friction velocity ( $u_{*0}$ ) exceeds the erosion threshold ( $u_{*t}$ ), soil grains are energized into motion. At wind speeds above the threshold, the fluid drag preferentially sets into motion sand particles larger than  $60 \mu\text{m}$ . These particles begin to roll on the surface, and those in the range  $60\text{--}500 \mu\text{m}$  gain enough momentum to be lifted away from it. Once lifted, these particles hop along the surface, in ballistic trajectories [Bagnold 1941], in the direction of the prevailing wind in a process called saltation (Fig. 2.10). These hopping particles called saltators, when airborne absorb momentum from the flow and strike the surface with an increased velocity. Upon impact, they can rebound, splash more sand grains into saltation and release dust [Shao *et al.* 1993; Alfaro *et al.* 1997]. Erodible particles larger than  $500 \mu\text{m}$  can be mobilized both by the wind shear and the impacting saltators but do not enter into saltation due to their large inertia, and instead roll or slide along the surface in a motion called creep [Bagnold 1941]. Larger soil aggregates creeping along the surface may loose some material due to friction, and eventually enter into saltation.

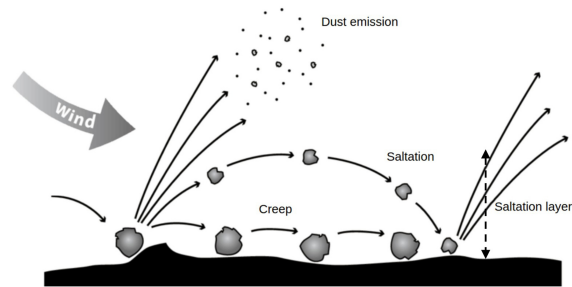


FIGURE 2.10: Schematic representation of the wind erosion processes - creep, saltation and dust suspension. Adapted from Tatarko *et al.* [2009].

(Fig. 2.10). These hopping particles called saltators, when airborne absorb momentum from the flow and strike the surface with an increased velocity. Upon impact, they can rebound, splash more sand grains into saltation and release dust [Shao *et al.* 1993; Alfaro *et al.* 1997]. Erodible particles larger than  $500 \mu\text{m}$  can be mobilized both by the wind shear and the impacting saltators but do not enter into saltation due to their large inertia, and instead roll or slide along the surface in a motion called creep [Bagnold 1941]. Larger soil aggregates creeping along the surface may loose some material due to friction, and eventually enter into saltation.

### 2.2.4 Saltation

Saltation is an important wind erosion process, driving other processes like dust emissions [e.g., Shao *et al.* 1993; Marticorena *et al.* 1995; Alfaro *et al.* 1997; Shao *et al.* 2000; Kok 2011b].

Once initiated, the number of sand grains in saltation increases exponentially as airborne grains absorb momentum from the flow and splash more sand particles into saltation. This leads to a decrease in the near-surface wind speed leading to a decrease in fluid energy driving saltation. Consequently, an equilibrium is reached wherein every impacting saltator energizes a new grain into saltation. Thereafter, the process remains in a state of equilibrium as long as the mean wind remains well above the erosion threshold.

Expression	Constant value	Source
$F_{salt} = c \frac{\rho_a}{g} \sqrt{\frac{d_p}{D}} u_{*0}^3$	$c = 1.5 - 2.8; D = 250 \mu\text{m}$	Bagnold [1941]
$F_{salt} = c \frac{\rho_a}{g} u_{*0}^3 \left(1 - \frac{u_{*t}^2}{u_{*0}^2}\right)$	$c = 0.25 + v_{sed} / (3u_{*0})$	Owen [1964]
$F_{salt} = c \frac{\rho_a}{g} \sqrt{\frac{d_p}{D}} u_{*0}^3 \left(1 - \frac{u_{*t}}{u_{*0}}\right)$	$c = 4.2$	Lettau <i>et al.</i> [1978]
$F_{salt} = c \frac{\rho_a}{g} u_{*0}^3 \left(1 - \frac{u_{*t}}{u_{*0}}\right) \left(1 + \frac{u_{*t}}{u_{*0}}\right)^2$	$c = 2.61$	White [1979]

TABLE 2.1: Different saltation flux parametrizations. Here  $v_{sed}$  is the gravitational settling velocity of the particle.

Saltation results in the predominant horizontal transport of sand grains, and its flux is, therefore, most commonly referred to as the horizontal flux. It is defined as the mass of the saltators crossing a vertical surface of unit width and infinite height, perpendicular to both the erodible surface and the wind direction, in unit time. Bagnold [1941] who first studied sand transport as a function of wind intensity, proposed the saltation flux ( $F_{salt}$ ) to be proportional to the cube of the friction velocity ( $u_*^3$ ). The concept of the erosion threshold ( $u_{*t}$ ) was only introduced later by Kawamura [1964] who proposed the saltation flux as

$$F_{salt} = c \frac{\rho_a}{g} u_{*0}^3 \left(1 - \frac{u_{*t}}{u_{*0}}\right) \left(1 + \frac{u_{*t}}{u_{*0}}\right)^2, \quad (2.21)$$

with the constant  $c$  varying between 1.8 and 3.1. Thereafter, different expressions for  $F_{salt}$  were proposed, based on experimental data sets, similar to equation 2.21 (see Table 2.1). These parametrizations, though widely accepted, often differ by a factor 3 for typical erosive wind speeds [Shao 2008], mainly due to the generalization between different erosive environments, assuming universality in surface characteristics and erosion dynamics.



### Near-surface flow with saltation

Saltating particles, due to their larger sizes (compared to dust), are limited to within the first meter of the surface in a zone called the saltation layer [Owen 1964] (Fig. 2.10). In this layer, a saltator extracts momentum from the flow and loses momentum on impacting the surface. Hence, the total momentum flux ( $\tau$ ) transferred to the saltation layer at height  $z$  by the prevailing wind is partitioned between that absorbed by the particle and that retained by the fluid motion, given by

$$\tau(z) = \tau_a(z) + \tau_p(z), \quad (2.22)$$

where  $\tau_a$  is the momentum flux retained by the fluid motion and  $\tau_p$  is that absorbed by the particles. For equilibrium saltation, Owen [1964] hypothesized that  $\tau_a$  in the saltation layer decreases exponentially as  $z \rightarrow 0$  (Fig. 2.11). Raupach [1991] expressed this variation as

$$\tau_a(z) = \rho_a u_*^2 \left[ 1 - (1 - \sqrt{r}) e^{-z/H_s} \right]^2, \quad (2.23)$$

with  $r = \tau_a(0)/\tau$ , describing the partitioning between airborne and particle-borne stresses at the surface. At the surface,  $\tau_a(0) = \rho_a u_{*t}$ , the Owen's self-limiting hypothesis. This leads to  $r = u_{*t}^2/u_*^2$  for  $u_* > u_{*t}$ , and  $r = 1$  otherwise. Therefore, at the surface,  $\tau_p = \rho_a (u_*^2 - u_{*t}^2)$ , while  $\tau_p$  disappears at the edge of the saltation layer when  $z \sim z_m$ . The characteristic height  $H_s$  of the saltation layer, in the above equation, is a function of the maximum hopping distance of the saltators ( $z_m$ ) given by

$$H_s = \frac{b_r a^2 u_*^2}{2g}, \quad (2.24)$$

where  $b_r$  the first order coefficient relating  $H_s$  and  $z_m$ , and  $a = 0.63$  is an empirical constant. By substituting equations 2.22 and 2.23 in equation 2.11, we get,

$$\frac{du}{dz} = \frac{u_*}{k} \left[ \frac{1}{z} - (1 - r) \frac{e^{-z/H_s}}{z} \right]. \quad (2.25)$$

Integrating the above equation from  $z_0$  to  $z$  leads to

$$u(z) = \frac{u_*}{\kappa} \left[ \ln \left( \frac{z}{z_0} \right) + (1 - \sqrt{r}) \left[ \gamma + \ln \left( \frac{z_0}{H_s} \right) + E \left( \frac{z}{H_s} \right) \right] \right], \quad (2.26)$$

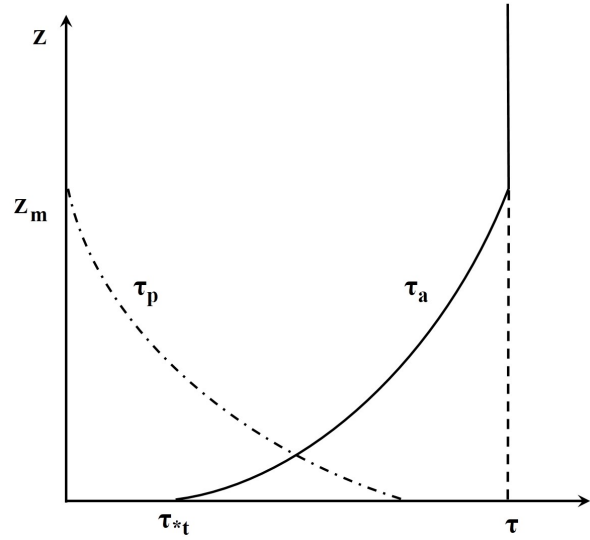


FIGURE 2.11: Variation with height of the momentum flux retained by the fluid motion ( $\tau_a$ ) and that absorbed by the saltating particles ( $\tau_p$ ) in the saltation layer. Here  $\tau_{*t}$  is the threshold momentum flux and  $z_m$  is the height of the saltation layer. Adapted from Owen [1964].

where  $\gamma = 0.577216$  is the Euler's constant and  $E(x) = \int_x^\infty \exp(-t)/t dt$  [Raupach 1991]. Above the saltation layer, this modification of the wind profile due to saltation is equivalent to replacing  $z_0$  in Equation 2.12 by a saltation roughness length  $z_{0s} = [H_s \exp(-\gamma)]^{(1-\sqrt{r})} z_0^{\sqrt{r}}$ .

The modification of the wind profile due to saltation is shown in Fig. 2.12a, adapted from the Large Eddy Simulations of Dupont *et al.* [2013]. It demonstrates a decrease in the mean wind speed in the saltation layer (shaded area) on account of an increased momentum absorption by the saltators. This change in momentum absorption is seen in the sharp increase in the momentum flux (Fig. 2.12b) during saltation and an increase in the aerodynamic roughness length ( $z_{0s}$ ) [Shao 2008]

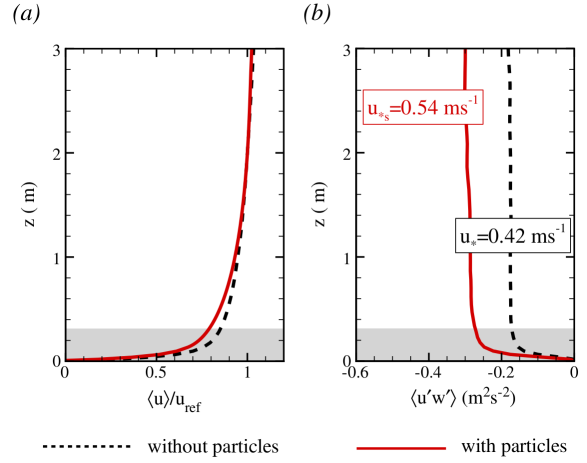


FIGURE 2.12: (a) Vertical profiles of the mean horizontal wind velocity  $u(z)$  normalized by its reference value  $u_{ref}$  at  $z_{ref} = 2m$ , and (b) vertical profiles of the mean momentum flux  $\langle u'w' \rangle$ , with and without saltation. The shaded area represents the saltation layer. Source: Dupont *et al.* [2013]

### Saltation equilibrium

Existing parametrizations and numerical models all assume equilibrium saltation, wherein the splash process drives the lift of new grains into saltation with negligible direct aerodynamic entrainment. This is represented as a probabilistic scheme called the splash scheme, based on partitioning the energy of the impacting saltator ( $E_{imp}$ ) into that used to rebound ( $E_{reb}$ ), splash new particles into saltation ( $E_{ej}$ ), and that lost to the surface ( $E_{fr}$ ). Following Anderson *et al.* [1991], this energy partition is expressed as a simple linear summation:  $E_{imp} = E_{reb} + E_{ej} + E_{fr}$  with

$$E_{imp} = \frac{mv_{imp}^2}{2} \quad (2.27)$$

$$E_{reb} = 0.95m(\alpha v_{imp})^2(1 - e^{-\gamma_{reb}v_{imp}}) \quad (2.28)$$

$$E_{ej} = \frac{c_s m v_{imp}^2}{2} - E_{reb} \quad (2.29)$$

Here,  $m$  is the particle mass,  $v_{imp}$  is the impact velocity of the saltator,  $\gamma_{reb}$  is an empirical coefficient with value  $2 \text{ sm}^{-1}$ ,  $\alpha$  is the ratio the rebound velocity  $v_{reb}$  to  $v_{imp}$  with values between 0.5 to 0.6, and  $(1 - c_s)$  is the fraction of the energy lost to the surface ( $E_{fr} = (1 - c_s)E_{imp}$ ).

### Saltation intermittency



FIGURE 2.13: Aeolian streamers on a beach.  
Source: Personal communication with Dr.  
Andreas Baas [Baas *et al.* 2005]

Field observations of saltation over beaches and in deserts suggests a high degree of spatio-temporal variability of sand transport (Fig. 2.13), with the process being highly intermittent [Gares *et al.* 1996; Jackson *et al.* 2006; Stout *et al.* 1997; Dupont *et al.* 2013]. This intermittency is due to the turbulence of the flow and surface heterogeneities such as moisture, topography, soil texture, roughness elements etc. Understanding and modelling saltation intermittency is important because it is a source of dust emission intermittency [Dupont *et al.* 2019b].

Aeolian streamers (Fig. 2.13) - elongated regions of intense sand transport in the stream-wise direction [Baas *et al.* 2005] - provide a visual demonstration of saltation intermittency. They are visual footprints of eddies which propagate towards the surface, i.e. sweeps of gusts that penetrate towards the surface driving saltation [Shao 2008]. These streamers meander laterally, and may bifurcate as they move downstream. Under moderate wind speeds, most commonly associated with erosion in semi-arid environments, saltation is characterized by individual streamers surrounded by regions of little or no sand transport. With increasing wind speeds, these streamers get embedded into larger saltation structures, and the sand transport becomes more homogeneous in time and space, reducing intermittency. The formation and development of streamers depends on surface characteristics, in particular the degree of surface homogeneity influenced by humidity patches, vegetation elements etc [Baas *et al.* 2005].

#### 2.2.5 Sandblasting (Dust emission)

The impacting saltators release dust particles ( $d_p < 20 \mu\text{m}$ ) through a process called sandblasting [Gillette 1977; Gillette *et al.* 1988; Marticorena *et al.* 1995; Alfaro *et al.* 1997; Shao 2001], often involving the disintegration of surface aggregates. Synchronous measurements of saltation and dust fluxes reveal a strong correlation between saltation and dust emission [Gillette 1977]. This correlation is referred to as sandblasting efficiency ( $\alpha_{sb}$ ), defined as ratio of the saltation and dust fluxes, given by  $\alpha_{sb} = F_{wd}/F_{salt}$ . It generally varies between  $10^{-4}$  and  $10^{-6} \text{ cm}^{-1}$ , indicating that dust emissions contribute to only a tiny fraction of the soil particles entrained. This direct correlation enabled Gillette *et al.* [1988] to propose from field experimental data sets a simple expression for dust emission fluxes, given by  $F_{wd} \propto u_*^n$ , with  $n$  varying between 3 and 5. Later, Marticorena *et al.* [1995] considered the dust emission flux to be a

constant fraction of the saltation flux based on the percentage of clay (dust) present in the soil. These first expressions of  $F_{wd}$  are empirical schemes with large variations in their predictions (Fig. 2.14).

Alternatively, physically based dust emission models, based on the energy balance between saltator impact and the binding energy of dust particles, started developing, starting with the Shao *et al.* [1993] model and the Alfaro *et al.* [2001] scheme, assuming (i) proportionality between saltator impact energy and  $u_{*0}$ , and (ii) inverse proportionality between the dust particle binding energy and size ( $d_p$ ). However, they are limited by their use of proportionality coefficients derived from small data sets not fully representative of the entire soil spectrum. Subsequently, Shao [2001] improved upon the physical description of dust emissions by considering it to be a resultant of three processes: aerodynamic entrainment, sandblasting and aggregate disintegration. He suggested that in addition to the proportionality between dust emissions and saltation, the dust emission process depends on soil resistance expressed by soil plastic pressure, characterized by the ability of the soil to flow (like a liquid) when subjected to particle impact. This model has been demonstrated to predict dust emission rates from a variety of soils, provided the soil characteristics are well defined. Recently, Kok [2011a] adopted a different approach to dust emissions by proposing an analogy between the dust emission process and the fragmentation of brittle materials. His theory differs from existing schemes by suggesting that the size of the emitted dust was independent of the wind intensity, and purely a function of the surface dust availability. Despite these advances, large ambiguities exist in the quantity and size of the emitted dust predicted by these models. These ambiguities are discussed in Chapter 4 through a sensitivity analysis.

### 2.2.6 Dust dispersion

Emitted dust particles are transported by the wind over large distances [Knippertz *et al.* 2014] from their source regions, significantly affecting the Earth system processes in their path and after deposition (Fig. 2.15). This transport is represented by the conservation equation for the suspended dust concentration  $c$  at any height  $z$  from the surface and instant  $t$  given by:

$$\frac{\partial c}{\partial t} = -\frac{\partial F_{wd}}{\partial z} + v_{sed} \frac{\partial c}{\partial z}, \quad (2.30)$$

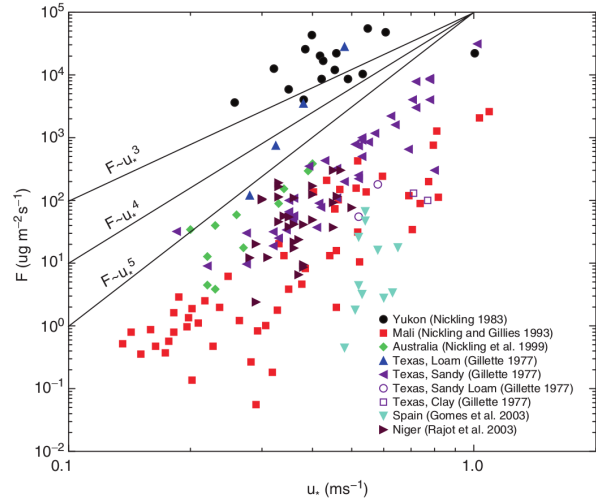


FIGURE 2.14: Ambiguities between predicted dust fluxes and experimental observations as a function of  $u_*$ . Source: Shao [2008].

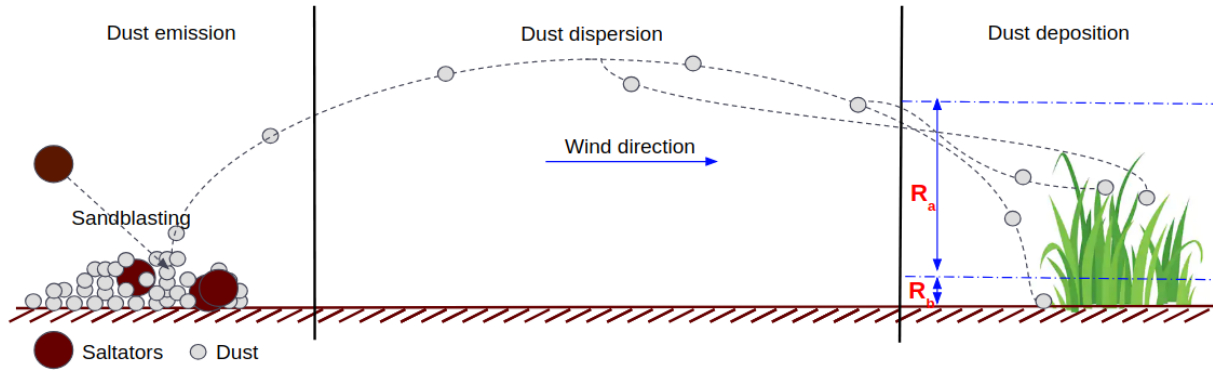


FIGURE 2.15: Schematic representation of the dust life cycle including emission (sandblasting), dispersion and deposition.  $R_a$  and  $R_b$  refer to the aerodynamic and quasi-laminar resistance to dust deposition explained in section 2.2.7.

where  $v_{sed}$  is the gravitational settling velocity of the emitted dust particles and  $F_{wd}$  is the turbulent-diffusive dust flux. The above equation implies that the vertical mixing of the emitted dust increases with time (downwind distance from the source) and wind intensity (influencing  $K_d$  and thus  $F_{wd}$ ), and decreases with particle size ( $v_{sed}$ ). This results in the formation of a boundary layer similar to the internal boundary layer for momentum flux due to changing surface roughnesses (Sec. 2.1.7), within which the dust concentration decreases exponentially away the surface, leading to  $\partial c / \partial z = 0$  at the top. At the surface, the dust flux  $F_{wd}$  is equal to the balance between the emission and deposition fluxes expressed as  $F_{wd,surf} = F_{emi} + F_{dep}$ .

## 2.2.7 Dust deposition

Suspended dust particles, through a combination of atmospheric conditions and particle-size, are eventually deposited back onto the surface. This occurs through two competing processes [Shao 2008] - (i) wet deposition during rain events wherein the air is washed clean of dust particles, and (ii) dry deposition otherwise. In this section, and in this thesis, we focus solely on dry deposition, the dominant dust deposition mechanism in semi-arid regions. It is also the sole deposition process during dust emission events.

Dry deposition is characterized by four size-dependent processes (Fig. 2.16) namely, (i) *Brownian diffusion* for particles less than  $1 \mu\text{m}$  with deposition rate inversely proportional to particle size ( $d_p$ ), (ii) *turbulent processes* (interception,

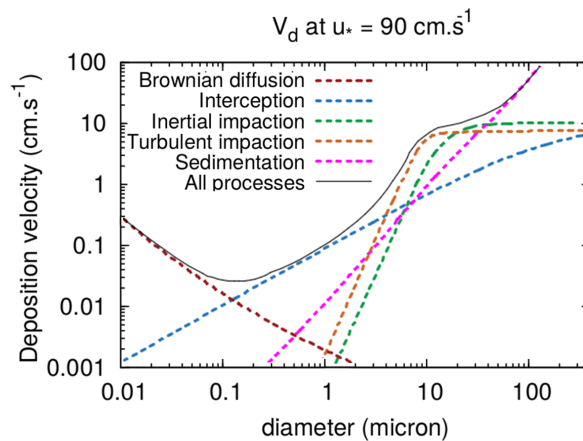


FIGURE 2.16: Partition between different dry deposition processes for suspended dust as a function of particle size at a very high wind speed. Source: Petroff *et al.* [2010].

inertial and turbulent impaction and turbophoresis) for particles in the range 1 to 10  $\mu\text{m}$ , (iii) *gravitational settling* for all particles, with deposition rate proportional to  $d_p$ , and (iv) *sedimentation* over obstacles other than the soil surface (like vegetation) due to gravitational settling. This size-dependency implies that the deposition process could influence the PSD of the dust flux. The effectiveness of these removal mechanisms depends on surface characteristics and the presence of vegetation elements [Petroff *et al.* 2010], with deposition enhanced in the presence of vegetation through the increase in surface area for interception, impaction and sedimentation. Furthermore these processes, except for gravitational settling and sedimentation, are functions of wind intensity with the removal efficiency increasing with wind speed.

Particle removal through brownian diffusion affects the smallest particles wherein their random (brownian) motion increases the tendency to impact a surface and get deposited onto it, following Fick's law of diffusion. Interception occurs when dust particles of small inertia (size), which perfectly follow the streamlines of the mean flow field, pass in the vicinity of an obstacle and are held back because the distance between the particle centre and the surface is smaller than half the diameter [Fuchs 1964]. Larger dust particles transported by the flow towards an obstacle, due to their larger inertia, cannot follow the streamlines and impact the obstructing surface [Petroff *et al.* 2008]. Turbophoresis refers to the tendency of particles to migrate in the direction of decreasing turbulent energy [Katul *et al.* 2010], i.e. in the presence of large vertical velocity gradients near the surface. However, its effect was found to be negligible over vegetated surfaces reviewed by Petroff *et al.* [2008] and Pryor *et al.* [2008]. Furthermore, Katul *et al.* [2010] demonstrated that turbophoresis in the presence of vegetation is most relevant for particles smaller than 0.1  $\mu\text{m}$ , in the range not explored in this thesis.

Current dry deposition parametrizations assume a homogeneous surface and a constant vertical dust flux layer. They are based on the analogy of electrical resistances [Wesely 1989] assuming that the different deposition mechanisms act in parallel. They divide the atmosphere into (i) a turbulent zone away from the surface where turbulent diffusion is dominant, and (ii) an inertial zone within the first centimeter from any surface where brownian diffusion, inertial impaction, interception and turbophoresis are dominant, with the two layers operating as resistances in series. Accordingly, the dry deposition velocity  $v_{dep,b}$  of a particle of the  $b^{th}$  bin over a bare homogeneous surface can be expressed as a set of electrical resistances with an aerodynamic resistance  $R_a$  in the turbulent layer and a quasi-laminar resistance  $R_{b,b}$  in the inertial layer close to the surface, given by:

$$v_{dep,b} = v_{sed,b} + \frac{1}{R_a + R_{b,b} + R_a R_{b,b} v_{sed,b}} \quad (2.31)$$

Here,  $R_a$  accounts for turbulent diffusion of dust particles as a function of surface roughness and atmospheric stability, expressed as  $R_a = \left(1/(ku_{*0})\right) \left(\ln(z/z_0) - \Phi_m\right)$ .  $R_{b,b}$  accounts for particle transfer (of the  $b^{th}$  bin) through brownian diffusion ( $d_p < 1\mu\text{m}$ ) and inertial impaction

( $d_p > 1\mu\text{m}$ ) given by  $R_{b,b} = 1 / \left( u_{*0} \left[ Sc_b^{-2/3} + 10^{-3/St_b} \right] \right)$ , where the Schmidt number ( $Sc_b = \nu_a D_{g,b}^{-1}$ ) is the surface collection efficiency of particles deposited through brownian diffusion with  $\nu_a$  the kinematic viscosity of air and  $D_{g,b}$  the brownian diffusivity [Davies 1960]. The Stokes number ( $St_b$ ) quantifies the susceptibility of a particle of the  $b^{\text{th}}$  bin to inertial impaction, given by  $St_b = u_{*0}^2 v_{sed,b} / g \nu_a$ . This susceptibility to impaction increases with particle size due to higher inertia reducing the ability of the particles to follow the flow streamlines and avoid obstacles.

The presence of vegetation enhances the efficiency of dust particle removal by enhancing interception, and introducing impaction and sedimentation, as functions of vegetation density. These removal mechanisms are accounted for by modifying the quasi-laminar resistance  $R_{b,b}$  in Eq. 2.31 as:

$$R'_{b,b} = \frac{1}{u_{*0} \left( Sc_b^{-2/3} + 10^{-3/St_b} \right) + v_{br,b} + v_{int,b} + v_{im,b}}, \quad (2.32)$$

where  $v_{br,b}$ ,  $v_{int,b}$  and  $v_{im,b}$  are the deposition velocities due to brownian diffusion, interception and inertial impaction of the  $b^{\text{th}}$  particle bin onto vegetation. Davidson *et al.* [1982] estimated the deposition velocity due to brownian diffusion over vegetation canopies as  $v_{br,b} = (0.683 Sc_b^{1/3} Re^{0.466} D_{g,b}) / d_n$ , where  $Re$  is the Reynolds number and  $d_n$  is needle diameter of the vegetation elements. They also proposed the deposition velocity due to interception by the vegetation elements as  $v_{int,b} = (2 A_f u(z) d_p) / (\pi d_n)$ , where  $A_f$  is the frontal area density of the vegetation. The expression for inertial impaction due to vegetation was proposed by Legg *et al.* [1979] as  $v_{im,b} = (0.86 A_f u(z) St_b^2) / (St_b^2 + 0.442)$ . Sedimentation over vegetation elements is taken into account by modifying the gravitational velocity in Eq. 2.31 as  $v'_{sed,b} = (1 + A_h) v_{sed,b}$ , where  $A_h$  is the plan area density of the vegetation.

The above description of dry deposition, among many others [Slinn *et al.* 1980; Wiman *et al.* 1985; Peters *et al.* 1992; Zhang *et al.* 2014], is empirical based primarily on field and wind tunnel experiments indirectly measuring the deposition velocity as the ratio between the dust flux and the concentration during pure deposition events, assuming no surface emissions, given by  $v_{dep,b}(z) = -F_{dep,b}(z) / c_{dep,b}(z)$  [Pryor *et al.* 2008]. Unlike during emission events, the dust concentration during pure deposition decreases exponentially towards the surface with  $c_{dep,b}(0) \rightarrow 0$ . Assuming constant vertical dust flux, the above definition implies increasing  $v_{dep,b}$  tending to infinity as the dust particle approaches the surface. This definition of dust deposition has encouraged the assumption of negligible deposition during emission events, and is investigated in this thesis.



## 3 Field and numerical experiments

This chapter presents (i) the WIND-O-V project and its main objectives, (ii) WIND-O-V's field experiments detailing measurements and data processing, and (iii) 3D erosion model evaluated and used in this thesis.

### 3.1 The WIND-O-V project

**WIND-O-V** (WIND erOsion in presence of sparse Vegetation) is a collaborative research initiative by - (i) Interactions Sol Plante Atmosphère ([ISPA](#), [INRA](#), Bordeaux), (ii) Laboratoire Interuniversitaire des Systèmes Atmosphériques ([LISA](#), [CNRS](#), Paris), (iii) Laboratoire de Mécanique des Fluides et d'Acoustique ([LMFA](#), [ECL](#), Lyon), (iv) Institut d'écologie et des sciences de l'environnement ([iEES Paris](#), Paris) and (v) Institut des Régions Arides ([IRA](#), Tunisia). These institutes are well recognized experts in geophysics, sedimentology, and theoretical and environmental fluid mechanics, covering all spatial scales between local to regional associated with wind erosion. The project is financed by the French National Research Agency ([ANR](#)) under the grant [ANR-15-CE02-0013 \(2016-2020\)](#), which along with the department of Environment and Agronomy of INRA (Bordeaux) funded this doctoral work.

#### 3.1.1 Objectives

The objectives of the WIND-O-V project are:

- (i) To develop and evaluate a wind erosion model at landscape scale accounting for both saltation and dust suspension processes at fine resolution using a Lagrangian-Eulerian approach, with or without natural or cultivated vegetation, and coupled with a LES (Large-Eddy Simulation) airflow model that explicitly simulates wind gusts. This first objective defines this thesis.
- (ii) To improve the flow modelling in the saltation layer over bare soil by performing DNS (Direct Numerical Simulation) and wind-tunnel measurements to better characterize wind-saltation interaction and to improve the near-surface resolution of the LES model.



(iii) To quantify the chemical fractionation of particles along the soil-saltation-suspension continuum from field measurements to deduce a simple parametrization. Knowledge of the composition of erosion fluxes is necessary to evaluate precisely the soil nutrient losses and the dust impact on the radiative budget.

(iv) To develop a dust emission scheme for regional-scale models, accounting for vegetation, by applying the erosion model developed at the landscape scale for different vegetation arrangements. This scheme will be implemented in the regional model *Chimere-Dust* and validated over southern Tunisia.

### 3.1.2 Workflow

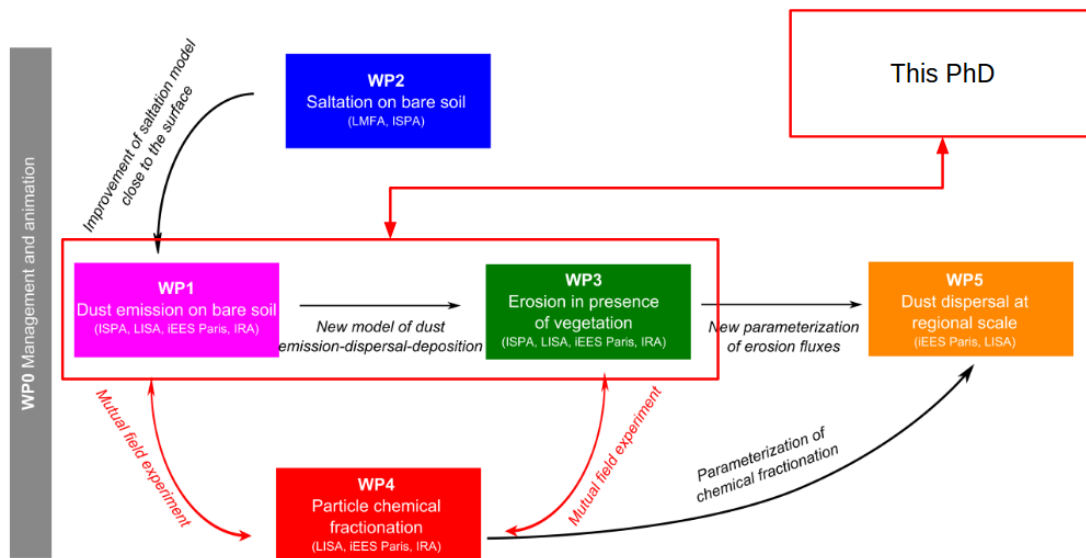


FIGURE 3.1: The WIND-O-V work-flow with the different work-packages assigning responsibilities to the project partners. The project is managed by Dr. Sylvain Dupont (ISPA, INRA) through WP0. Adapted from the WIND-O-V project proposal.

The pluridisciplinary objectives of WIND-O-V are fulfilled by dividing tasks and responsibilities (Fig. 3.1) between the project partners as follows:

(i) **WP0**: project design, costing and budgeting, planning and division of tasks between partners, liaising between partners, and progress monitoring.

(ii) **WP1**: generalization to multi-modal dust distribution of the preliminary version of the wind erosion model of Dupont *et al.* [2015], including saltation and dust suspension, and coupled with a Large-Eddy Simulation (LES) airflow model. Evaluation of the model on bare soils against a dedicated field experiment in Tunisia where wind dynamics, saltation and dust fluxes per size class were measured. Chapter 5 of this dissertation concerns this work-package.

(iii) **WP2**: improving the near-surface resolution of the LES model developed in WP1 by performing Direct Numerical Simulation (DNS) and wind-tunnel experiments of the wind-particle interaction near the surface.

(iv) **WP3**: quantification of the protective effect of the vegetation against erosion by performing simulations and field experiments over vegetation arrangements. Chapters 6 and 7 correspond to this work-package. WP3 also includes the development of a specific parametrization accounting for the impact of the vegetation on erosion fluxes for regional dust models.

(v) **WP4**: development of a parametrization for the chemical composition of particles according to the fractionation they are subjected to along the soil-saltation-suspension continuum, based on the size resolved chemical/mineralogical characterization of the saltation and dust fluxes measured during the field experiments.

(vi) **WP5**: implimentation of the new parametrizations developed in WP3 and WP4 in the 3D regional dust-transport model CHIMERE-Dust. Dust emission-transport-deposition will be simulated over south Tunisia for two years and validated against available in-situ measurements of the saltation flux and surface wind speed. The results from the new parametrization will be compared with the standard schemes to quantify its benefit as a function of land use and wind conditions.

At the time of writing, the WIND-O-V project commenced its terminal year, having produced 4 research publications - Dupont *et al.* [2018], Ouchene *et al.* [2018], Fernandes *et al.* [2019], and Dupont *et al.* [2019b], with 5 more in progress.

## 3.2 The WIND-O-V's field campaigns



FIGURE 3.2: Geolocalisation of the WIND-O-V's experimental site in south Tunisia.  
Source: Google Maps.



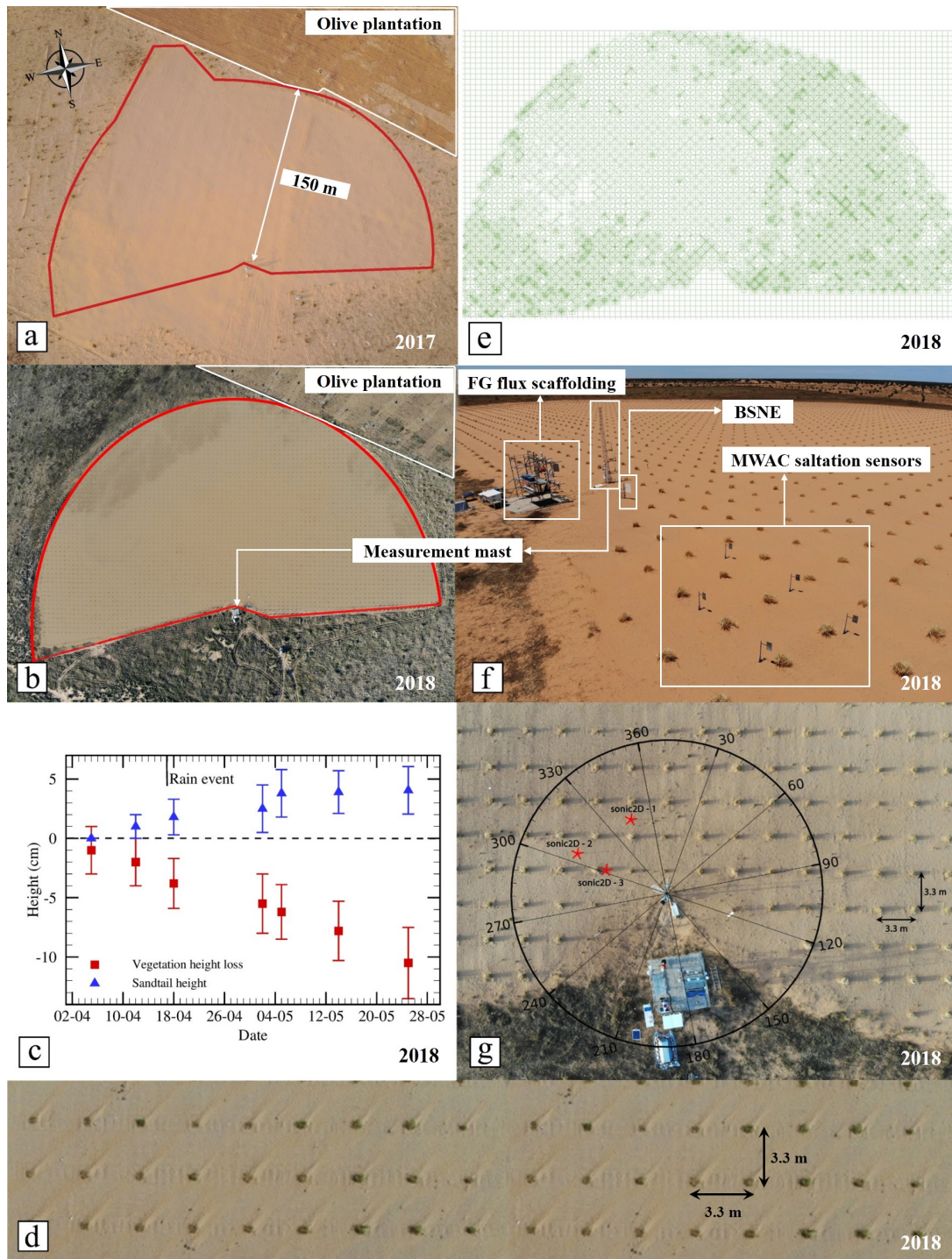


FIGURE 3.3: Plan-view of the semi-circular 150 m radius WIND-O-V's site in South Tunisia during (a) the bare soil experiment of 2017, and (b) the 2018 experiment with sparse vegetation. (c) The time variation of the mean vegetation and sand-tail heights during the 2018 experiment, with the error bars indicating their standard deviations. (d) Top-view of the sand-tails in the lee of the barley tufts. (e) The representation of mean vegetation height as proportional to the intensity of the green markings. (f) The main instrumentation mast, the flux-gradient scaffolding and the saltation sensors. (g) The positions of the 3 sonic-2D anemometers relative to the main mast and the barley tufts.

Source: Internal communication with Dr. Jean-Louis Rajot.

The WIND-O-V project comprised of two field experiments, conducted at the same site in south Tunisia (Fig. 3.2) from (i) March 01 to May 15, 2017 (Fig. 3.3a), and (ii) March 27 to June 04, 2018 (Fig. 3.3b). The experiments were assisted by four project partners - IRA, iEES Paris, LISA, and ISPA (INRA), with Dr. Jean-Louis Rajot (iEES Paris) as PI of the experiment. My main contribution to the WIND-O-V campaign was the analysis of the 2018 experimental data, following Dr. Sylvain Dupont's analysis of the 2017 experiment. All images concerning the experiment presented in this thesis were obtained via internal communications with Dr. Jean-Louis Rajot.

### 3.2.1 Study site

The field experiments were carried out at the Dar Dhaoui experimental range (33.3° N, 10.78° E) of the Institut des Regions Arides (IRA) of Medenine in South Tunisia (Fig. 3.2). This region is semi-arid with high temperatures and low rainfall from March to September. The semi-circular experimental plot had radius 150 m (Fig. 3.3a,b) surrounded by less erodible surfaces with olive plantations to the north-east and bushy-vegetation to the north-west (Fig. 3.3a,b). The higher rainfall before the 2018 experiment, in comparison with 2017, resulted in a denser off-plot vegetation. Prior to both experiments, the erodible (non-vegetated for 2018) surfaces of the site were tilled with a disk plough to flatten the surface and remove soil crusts and ridges.



FIGURE 3.4: Evolution of two barley tufts (A and B) over three different dates - March 29, April 15, and May 02 - during the 2018 experiment. Source: Internal communication with Dr. Jean-Louis Rajot.



The sparse vegetation in 2018 comprised of Barley (*Hordeum vulgare*), a low water-demand indigenous plant, cultivated to form vegetation tufts (Figs. 3.4 and 3.5) of mean height 0.4 m and 3.3 m apart covering less than 2% of the plot (Fig. 3.3c,d,e). This configuration was representative of the patchy seasonal vegetation characteristic of semi-arid climates [e.g., Meron *et al.* 2004; Bailey 2011; Stewart *et al.* 2014]. The mean vegetation height reduced by about 0.1 m during the course of the experiment (Figs. 3.3c and 3.4), and at any given instant the local vegetation presented some non-uniformity, especially between the eastern and western quarters (Fig. 3.3e).



FIGURE 3.5: Barley tufts on the study site during the 2018 experiment. Source: Internal communication with Dr. Jean-Louis Rajot.

### 3.2.2 Measurements

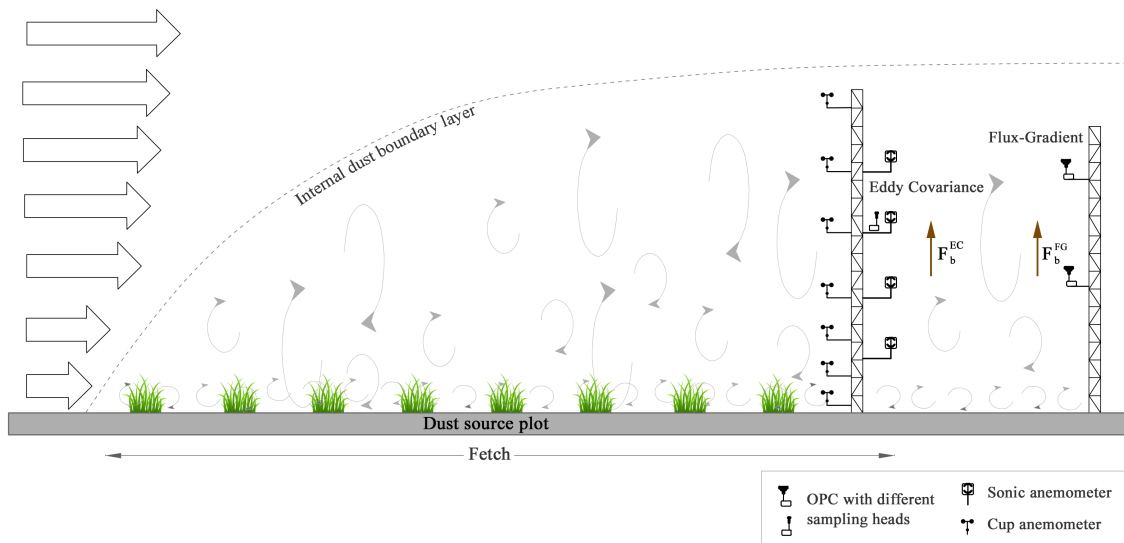


FIGURE 3.6: The schematic representation of the WIND-O-V's 2018 experiment with two measurement hubs - the Eddy-Covariance (EC) mast and the Flux-Gradient (FG) scaffolding. Adapted from Dupont *et al.* [2019a].

The WIND-O-V's field experiments featured two measurement hubs (Fig. 3.6):

(i) A 9 m high lattice mast (Fig. 3.7) erected at the center of the semi-circle (Fig. 3.3f) served as the center for meteorological and Eddy-Covariance (EC) dust flux measurements. On this mast were mounted - (i) four 3D sonic anemometers at heights 1.0, 1.9, 3.0, and 4.1 m measuring the turbulent velocity components at 60, 50, 50, and 20 Hz, respectively; (ii) seven cup anemometers at 0.2, 0.6, 1.3, 1.8, 3.0, 4.0, 5.2 m measuring the mean wind speed at 0.1 Hz; (iii)

four thermocouples at 0.4, 1.6, 3.7, 5.0 m measuring air temperature at 0.1 Hz; (iv) one weather vane in 2018 at 4.0 m sensing the mean wind direction; (v) one PALAS WELAS-2100 Optical Particle Counter (OPC) at 3.0 m measuring the number concentrations of airborne particles at 1.0 Hz (Fig. 3.8a); and (vi) one camera at 0.8 m facing north, capturing images of the experimental plot every minute.



FIGURE 3.7: The main measurement (lattice) mast with the meteorological and Eddy-Covariance (EC) dust flux measurement systems. Source: Internal communication with Dr. Jean-Louis Rajot.

(ii) A scaffolding erected south of the meteorological mast (Figs. 3.3f and 3.8b,c) served as the main aerosol concentration measurement station. It housed (i) two PALAS WELAS-2100 OPCs at 2.0 m and 4.3 m from the surface (Fig. 3.8b), measuring airborne dust number concentrations similarly to the OPC on the mast, (ii) two TEOM spectrometers at 2.0 m and 4.3 m measuring dust PM<sub>10</sub> concentrations at 0.0083 Hz (Fig. 3.8b), and (iii) 8 PM<sub>20</sub> filters, four each at 2.0 m and 4.3 m capturing airborne dust particles for granulometric and chemical analysis (Fig. 3.8c). All instruments on the scaffolding had standard TSP sampling heads (Fig.3.8b), and different from the in-house designed sampling head of the OPC on the main mast (Fig. 3.8a).

Saltation fluxes were measured using (i) one Big Spring Number Eight (BSNE) [Fryrear 1986] sensor comprising of a vertical array of five sediment traps at 0.1, 0.2, 0.4, 0.6 and 0.9 m from the surface (Fig. 3.3f), and (ii) five

MWAC saltation sensors in 2018 with sand traps at 0.06, 0.12, 0.20, 0.40 and 0.80 m. The saltation equipment had a sampling time ranging between 0.5 to 3 hours. Sand transport was also sensed at 0.1 Hz using two saltiphones at 0.07 m from the surface and close to the mast.

Additionally, during the 2018 experiment, the near-surface wind speeds around the Barley tufts were recorded using three Campbell Windsonic4-L sonic 2D anemometers at 0.45 m from the surface measuring the horizontal wind at 0.1 Hz (Fig. 3.3g).

During both experiments, ISPA (INRA) was responsible for the sonic anemometers and the EC dust flux measurements, while the other measurements were handled by LISA and iEES-Paris. IRA (Tunisia) provided the infrastructural and logistical support. The ISPA data acquisition

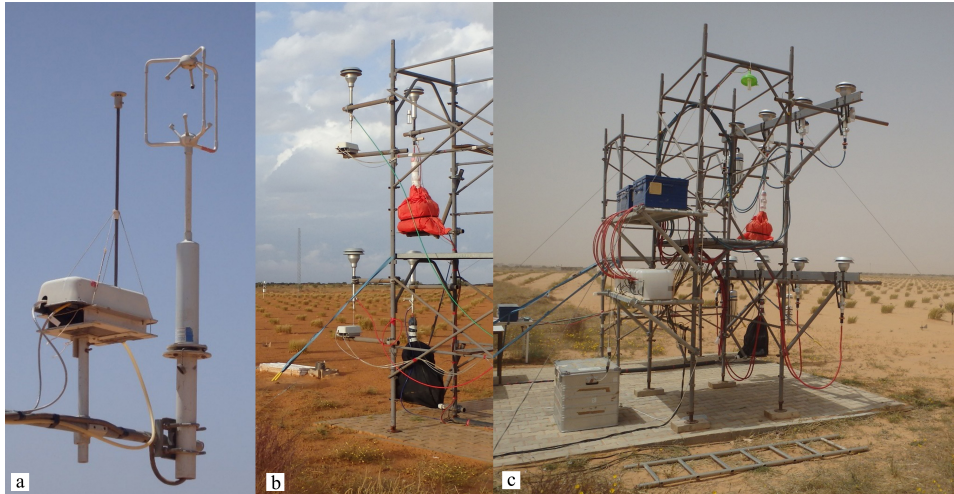


FIGURE 3.8: (a) The Eddy Covariance (EC) dust flux system with the particle spectrometer coupled to the sonic 3D anemometer at 3.0 m on the lattice mast. (b) The Flux Gradient (FG) particle spectrometers at 2.0 m and 4.3 m on the scaffolding to the left and the two TEOM spectrometers at 2.0 m and 4.3 m to the right. (c) The eight PM20 filters, four each at 2.0 m and 4.3 m from the surface. Source: Internal communication with Dr. Jean-Louis Rajot.

was enabled by a series of Raspberry PI mini computers connected through an internal network ensuring the same clock between the different Raspberry PIs. Prior to the experiment, the cup anemometers were inter-compared at a fixed height to test the consistency of their responses in natural conditions. A similar inter-comparison of the OPCs was conducted at the end of the experiment.

The PALAS WELAS-2100 OPC, used for both EC and FG dust flux estimation, measured airborne dust number concentrations in the range 0.3 - 17.0  $\mu\text{m}$ , with 16 intervals per decade at 1 Hz. Prior to the experiment, the three OPCs were calibrated using mono-disperse 1.28  $\mu\text{m}$   $\text{SiO}_2$  particles assuming the equivalence between the refractive indices of  $\text{SiO}_2$  and mineral dust. The two OPCs on the scaffolding were used for dust flux estimation through the Flux-Gradient (FG) approach with a standard TSP sampling head (Fig. 3.8b). The OPC on the main mast was coupled with the sonic 3D anemometer at the same level (Fig. 3.8a) to deduce size-resolved dust fluxes using the EC technique. For this, a small sampling head placed 0.2 m south from the head of the sonic anemometer was used so as to not disturb the anemometer measurements. This head constituted of a 0.25 m long and 0.01 m diameter tube with a drilled cover letting particles in while providing rain protection. Its impact on the measured size-wise dust concentration was evaluated from the inter-comparison

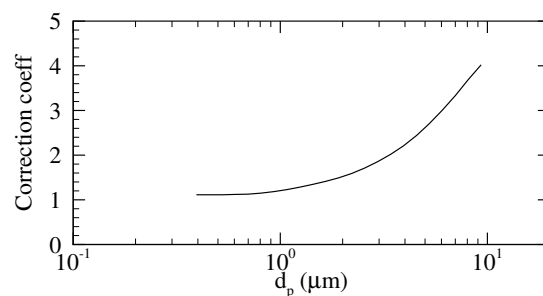


FIGURE 3.9: Correction coefficients applied on the EC dust concentration deduced from the inter-comparison experiment involving all 3 spectrometers. Adapted from Dupont *et al.* [2019a].

between the 3 OPCs placed at the same height. It revealed an underestimation of the dust concentration by the EC OPC with increasing particle size. This was corrected using a correction coefficient estimated by Dupont *et al.* [2019a] with high accuracy up to  $4 \mu\text{m}$  (Fig. 3.9).

### 3.2.3 EC data processing

Of the different measurements taken during the experiment, this thesis focuses mainly on EC measurements of momentum and dust fluxes estimated at the main measurement mast. Presented here is their preliminary (data) processing.

The velocity components recorded by the 3D sonic anemometers were rotated horizontally such that  $u$  represents the component along the mean wind direction  $x$ , and  $v$  the transverse velocity component. In order to account for possible errors in the vertical orientation of the sonic anemometers, a second rotation was performed at every height around the  $y$ -axis. Following the recommendations of Dupont *et al.* [2019b] for the 2017 experiment, a sampling time of 15 minutes was chosen for computing the statistics depicting the wind, temperature, and dust dynamics. The large-scale trend on the measured variables was removed from a sixth-order polynomial fit. Reynolds decomposition [Reynolds 1895] was applied to all variables of interest such as wind velocity components, air temperature, and dust concentration for every 15 minute period. Prior to calculating the EC dust flux, a time-lag correction varying between  $-1$  to  $+2\text{s}$  was applied (Fig. 3.8a).

The dust flux ( $wd$ ) cospectrum for the March 09 2017 event (Fig. 3.10), like other events presented in Dupont *et al.* [2019b], exhibits a parabolic shape, peaking around  $0.09 \text{ Hz}$ , similar to the momentum flux ( $uw$ ) cospectrum. Thereafter, it decreases with frequency up to the cut-off frequency of the OPC, while deviating from that of the  $uw$ -cospectrum. Ideally, by assuming similarity between dust and momentum transports, the  $wd$ -cospectrum needs to be corrected based on the  $uw$ -cospectrum. However, as demonstrated in Dupont *et al.* [2019b], dust transport was dissimilar to that of the momentum. Therefore, following Dupont *et al.* [2019a], the  $wd$ -cospectrum was fitted with the standard cospectrum shape formula to account for the high frequency attenuation [Horst 1997] due to the slow-response of the OPC, and the losses were estimated from the difference between

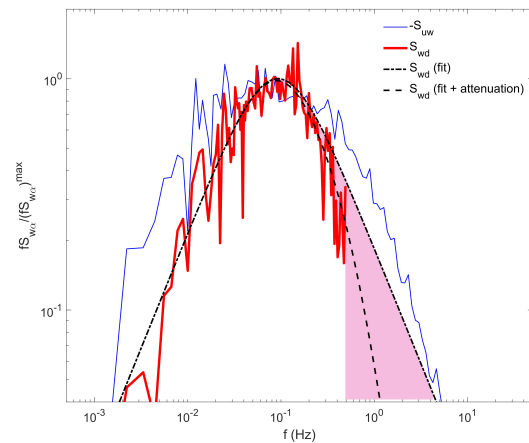


FIGURE 3.10: Example of the high-frequency correction (shaded area) identified from the cospectrum of the  $2.5 \mu\text{m}$  dust fluxes ( $S_{wd}$ ) for the March 09 2017 erosion event. Presented also is the cospectrum of the momentum flux ( $S_{uw}$ ). Adapted from Dupont *et al.* [2019a].



the averaged  $w d$ -cospectrum and the fitted attenuated parabolic shape. This correction was estimated for all the erosion events and applied independent of the particle size. It represented about +15% of the EC dust flux, with little variability between events.

### 3.2.4 Results

The wind speed measurements of the 2017 experiment were used to evaluate the relative accuracies of estimating aerodynamic parameters, such as surface friction velocity ( $u_{*0}$ ) and surface roughness length ( $z_0$ ), via the traditional Law of the Wall (LoW) and the direct Eddy-Covariance (EC) methods. This evaluation was motivated by the importance of these parameters in scaling the erosion (saltation and dust) fluxes in wind erosion models. Our resulting study published in Dupont *et al.* [2018] (Appendix A) recommends the estimation of  $u_{*0}$  and  $z_0$  independently of von karman constant  $k$  by deducing  $z_0$  from the regression of the logarithmic wind speed profile and  $u_{*0}$  from the EC approach.

The EC dust flux measurements of the 2017 experiment are presented in Dupont *et al.* [2019b] (Appendix B). Our analysis revealed a dissimilarity in the turbulent transport between momentum and dust, implying that the same eddies did not always transport momentum and dust simultaneously during emission (erosion) events. This dissimilarity was suggested to be most likely due to intermittent dust emissions as against a continuous momentum absorption at the surface, and its origins are further investigated in Chapter 5 through numerical experiments.

Measurements from the 2018 experiment are presented in Chapter 6, along with a comparative analysis with the 2017 experiment, i.e. between dust emissions over bare and vegetated surfaces. The analysis of the Flux-Gradient (FG) dust fluxes and saltation fluxes are being undertaken at the LISA laboratory. A comparison between the EC and FG dust flux methods is also currently being prepared in Dupont *et al.* [2019a].

## 3.3 3D erosion model

This section presents the 3D erosion model evaluated and used in this doctoral work. It couples erosion (saltation and dust emission) schemes with the ARPS Large Eddy Simulation (LES) airflow model. The ARPS (version 5.1.5) platform, developed as a complete weather forecast system, has been validated over the last decades for a variety of mesoscale flows. A detailed description of the standard version of ARPS and its validation cases are available in the ARPS User's Manual [Xue *et al.* 1995]. Here, we present briefly this model, focussing on the modifications required to incorporate saltation and dust suspension over sparsely vegetated surfaces. This 3D erosion model is evaluated over bare surfaces against the WIND-O-V's

2017 experiment in Chapter 5, and in Chapter 7 against the WIND-O-V's 2018 experiment over sparsely vegetated surfaces.

### 3.3.1 ARPS LES airflow model

The ARPS Large Eddy Simulation (LES) airflow model is a 3D, non-hydrostatic, compressible model that resolves Navier-Stokes equations in a terrain-following coordinate system. It comprises of an orthogonal grid, with equisized grid elements along the horizontal direction and a stretched grid with increasing grid size along the vertical. This vertical grid stretching allows for reducing computational costs while efficiently simulating the smaller turbulent structures closer to the surface.

ARPS solves the conservation equations for the three wind velocity components, pressure, potential temperature and humidity. The wind velocity components and the atmospheric base state variables (air density, atmospheric pressure and potential temperature) are split into (i) a base-state component (over-barred variable) that remains horizontally homogeneous, time invariant and hydrostatically balanced, and (ii) a deviation from the base-state (double-primed variables). For high spatial resolution, all conservation equations are filtered to separate the small scales from the large scales. The model therefore explicitly resolves all turbulent structures larger than the filter scale, and incorporates the effects of the smaller sub-grid-scale (SGS) turbulent structures on the larger ones using a 1.5-order turbulence closure scheme.

For a Boussinesq fluid, like air, the momentum equation in Einstein summation convention is written as,

$$\bar{\rho}_a \left( \frac{\partial \tilde{u}_i}{\partial t} + \tilde{u}_j \frac{\partial \tilde{u}_i}{\partial x_j} \right) = - \frac{\partial}{\partial x_i} \left( \tilde{p}'' - \alpha_d \frac{\partial \bar{\rho}_a \tilde{u}_j}{\partial x_j} \right) - 2 \bar{\rho}_a \epsilon_{ijk} \Omega_j (\tilde{u}_k - \bar{u}_k) - \bar{\rho}_a g \left( \frac{\tilde{\theta}''}{\theta} - \frac{c_p}{c_v} \frac{\tilde{p}''}{\bar{p}} \right) \delta_{i3} - \bar{\rho}_a \frac{\partial \tau_{ij}}{\partial x_j} - C_d A_f \sqrt{\tilde{u}_j \tilde{u}_j} \tilde{u}_i. \quad (3.1)$$

In this equation, the right-hand side terms refer respectively to the pressure-gradient term, Coriolis term, buoyancy term, turbulent transport term, and the pressure and viscous drag force terms induced by vegetation. Here, the overtilde refers to the filtered variables,  $t$  to the time,  $x$  to the coordinates and  $u$  the velocity component, with  $i, j, k$  referring respectively to the streamwise, lateral and vertical directions;  $\delta_{ij}$  is the the Kronecker symbol;  $\epsilon_{ijk}$  the Levi-Civita symbol;  $\Omega$  the angular velocity of earth;  $\alpha_d$  quantifies the artificial divergence damping to attenuate acoustic waves;  $g$  the gravitational acceleration;  $\rho_a$  the air density;  $\theta$  the potential temperature;  $c_p$  and  $c_v$  are the specific heat air at constant pressure and volume, respectively. The last right-hand side term in the above equation accounts for the influence of vegetation on the flow field through the mean canopy drag coefficient  $C_d$  and frontal area density of the vegetation  $A_f$ . This last term disappears over bare surfaces.

All simulations in this thesis were performed over a flat, dry terrain under neutral atmospheric stability conditions. The presence of the potential temperature terms in equation 3.1, despite neutral stratification, is because the potential temperature equation is solved to provide the

initial turbulent perturbations leading to the development of turbulent motions. The Coriolis force was neglected in our simulations.

The sub-grid scale (Reynolds) stress tensor  $\tau_{ij}$  is modelled through a SGS eddy viscosity model in its anisotropic form where two mixing lengths are computed for horizontal and vertical turbulent diffusion [Dupont *et al.* 2010], expressed as:

$$\tau_{ij} = - \left( (1 - \delta_{i3})v_{th} + \delta_{i3}v_{tv} \right) \left( \frac{\partial \tilde{u}_i}{\partial x_j} + \frac{\partial \tilde{u}_j}{\partial x_i} \right). \quad (3.2)$$

Here  $v_{th}$  and  $v_{tv}$  are the horizontal and vertical eddy viscosities modelled as a product of the horizontal and vertical length scales  $l_{th}$  and  $l_{tv}$ , respectively, and a velocity scale  $\sqrt{e}$  with  $e$  the SGS TKE. This is expressed as:

$$v_{th} = 0.1\sqrt{e}l_{th}, \quad (3.3)$$

$$v_{tv} = 0.1\sqrt{e}l_{tv}. \quad (3.4)$$

For a neutral atmosphere, the mixing lengths are a function of the grid spacing given by  $l_{th} = \sqrt{\Delta x \Delta y}$  and  $l_{tv} = \Delta z$ .

The sub-grid scale velocity scale is computed by resolving the conservation equation for the sub-grid scale turbulent kinetic energy  $e$ :

$$\frac{\partial e}{\partial t} + \tilde{u}_j \frac{\partial e}{\partial x_j} = -\tau_{ij} \frac{\partial \tilde{u}_i}{\partial x_j} - \frac{g}{\theta} \tau_{3\theta} + \frac{\partial}{\partial x_j} \left( 2 \left( (1 - \delta_{i3})v_{th} + \delta_{i3}v_{tv} \right) \frac{\partial e}{\partial x_j} \right) - C_\epsilon \frac{e^{3/2}}{l_{tv}} - 2C_d A_f \sqrt{\tilde{u}_j \tilde{u}_j} e. \quad (3.5)$$

Here the constant  $C_\epsilon$  is equal to 3.9 at the lowest model level and 0.93 above [Dupont *et al.* 2010]. The right-hand side terms in the above equation refer respectively to the dynamic shear production term, buoyancy production term, turbulent transport term, energy dissipation term and the sub-grid scale TKE cascade term. The last right-hand term represents the dissipation of turbulence energy to the vegetation canopy, as eddies of all scales larger than the vegetation elements loose energy through their interaction with vegetation. The sub-grid scale TKE production by wake motions behind vegetation elements is ignored, as their scales are much smaller than those making the bulk of the sub-grid scale TKE [Dupont *et al.* 2010]. The sub-grid heat flux in equation Eq. 3.5 is given by,

$$\tau_{3\theta} = - \frac{v_{tv}}{P_r} \frac{\partial \tilde{\theta}}{\partial x_3}, \quad (3.6)$$

where the Prandtl number  $P_r$  is taken equal to 1 in this study.

This version of the LES airflow model (with vegetation) has been extensively validated against both field measurements and wind tunnel experiments over different vegetation configurations by Dupont *et al.* [2010], Dupont *et al.* [2008a], Dupont *et al.* [2008b], and Dupont *et al.* [2014]. The model has also been evaluated over bare surfaces in Dupont *et al.* [2013].

### 3.3.2 Erosion modelling

As previously explained in Chapter 2, wind erosion involves the near-surface transport of sand particles through saltation, the emission of dust through sandblasting, and the dispersion of emitted dust in the atmosphere. Following Dupont *et al.* [2013], saltation is coupled to the ARPS airflow model using a Lagrangian approach, and dust dispersion through an Eulerian approach following Dupont *et al.* [2015]. This section presents the coupling between erosion schemes and the ARPS airflow model.

#### Saltation

The saltation process is reproduced by modelling (i) the two-way interaction between particle motions and the turbulent flow, (ii) the individual particle trajectories using a Lagrangian particle motion equation, and (iii) the surface splashing of the saltating grains, including rebound, ejection of new sand grains, and deposition. The saltation scheme resolves explicitly only a statistically representative number of particle trajectories represented by a ratio  $Q$  between the real number of particles and the number of numerically resolved particles. This last one reduces computational costs.

The effect of the saltating particles on the flow field is incorporated by adding a drag force term ( $F_p$ ) to the right hand side of Eq. 3.1, expressed as:

$$F_p = -\frac{Q}{V_{cell}} \sum_{p=1}^{n_{pcell}} \frac{1}{2} C_{dp} A_p |\vec{u}(x_p) - \vec{u}_p| (\tilde{u}_i(x_p) - u_{pi}), \quad (3.7)$$

where  $V_{cell} = \Delta x \Delta y \Delta z$  is the volume of the grid element,  $n_{pcell}$  the number of resolved particles in the grid cell,  $\tilde{u}_i(x_p)$  the resolved fluid velocity component along  $x_i$  at particle position  $x_p$ ,  $u_{pi}$  the instantaneous particle velocity component along  $x_i$ ,  $A_p = \pi d_p^2 / 4$  the particle section area, and  $C_{dp}$  the particle drag coefficient. Since the resolved fluid velocity components are only available at a discrete grid, their values at the particle position are deduced from a first order trilinear interpolation scheme. In the lower grid cell, the horizontal wind velocity components at the particle position are extrapolated from the resolved fluid components of the second grid cell using a logarithmic profile. The particle drag coefficient is evaluated as  $C_{dp} = f(Re_p) 24\nu / (|\vec{u}(x_p) - \vec{u}_p| d_p)$  [Clift *et al.* 1978], with  $f(Re_p)$  an empirical relation depending on the particle Reynolds number (Eq. 3.9).

The saltating particle motion equation is expressed following Vinkovic *et al.* [2005] and Dupont *et al.* [2013] as:

$$m_p \frac{du_{pi}}{dt} = \frac{1}{2} \rho_a C_{dp} A_p |\vec{u}(x_p) - \vec{u}_p| \left( \tilde{u}_i(x_p) - u_{pi} \right) + m_p g \delta_{i3}, \quad (3.8)$$

where  $m_p$  is the particle mass. Here the right hand side terms represent drag and gravity forces, respectively, acting on the particle. In the above consideration, the mid-air inter-particle collisions are neglected similarly to other saltation models, as it is significant only at very high wind speeds. In this thesis, we focus mainly on moderate winds most common of wind erosion. Furthermore, following Dupont *et al.* [2013], the SGS particle velocity has been neglected as the lifetime of the smallest resolved eddies is smaller than the particle response time. The effect of non-linear drag is included using an empirical relation following Clift *et al.* [1978] as:

$$C_{dp} = \frac{24v_a}{|\tilde{u}(x_p) - u_p|d_p} f(Re_p), \quad (3.9)$$

where  $f(Re_p)$  is an empirical relation depending on the particle Reynolds number [Clift *et al.* 1978].

The saltation model neglects direct aerodynamic entrainment of the sand grains. It assumes equilibrium (well-developed) saltation driven by the splash process (Sec. 2.2.4). Thereby, a splash scheme derived from the models of Anderson *et al.* [1991], Shao *et al.* [1999], Vinkovic *et al.* [2005], and Kok *et al.* [2009] is introduced into ARPS. To this end, the surface is parametrized to be composed of a particle bed with log-normally varying diameters (Sec. 2.2.1). A particle reaching 0.5 mm above the surface is considered to rebound, eject other particles or deposit on the surface, as a function of its velocity and size. The choice of 0.5 mm is due to the difficulty of defining the surface in a well-developed saltation event due to the high concentration of saltating particles at the surface, the neglecting of particle rolling and inter-particle collision.

Rebound and ejection of new particles are modelled following the probabilistic approach of Anderson *et al.* [1991]. Therefore, the probability that a particle rebounds is  $P_r = 0.95(1 - \exp(-\gamma_{reb}v_{imp}))$ , where  $v_{imp}$  is the impact velocity of the particle and  $\gamma_{reb}$  is an empirical parameter of the order of  $2 \text{ sm}^{-1}$  (See Eq. 2.29). Both rebound velocity ( $v_{reb}$ ) and rebound angle ( $\alpha_{reb}$ ) are modelled to follow normal distributions, with mean velocity  $\langle v_{reb} \rangle = 0.6\alpha v_{imp}$  and a standard deviation  $\sigma_{reb} = 0.25v_{imp}$ ; the mean vertical rebound angle  $\langle \alpha_{vreb} \rangle = 30^\circ$  and mean horizontal rebound angle  $\langle \alpha_{hreb} \rangle = 0^\circ$ . The rebound angles have standard deviations  $\sigma_{\alpha_{vreb}} = 15^\circ$  and  $\sigma_{\alpha_{hreb}} = 10^\circ$ , respectively. The number of particles ejected by an impacting saltator is  $N_{ej} = v_{imp}a/(g\langle d_p \rangle)$ , where  $a$  is a constant between 0.01 and 0.05 [Kok *et al.* 2009] and chosen to be 0.03 in this study. Following Anderson *et al.* [1991], an exponential distribution of particle ejection velocity is considered with mean velocity  $\langle v_{ej} \rangle = 0.08v_{imp}$  [Rice *et al.* 1995]. The particle ejection angles are modelled similarly to rebound following a normal distribution with mean vertical angle  $\langle \alpha_{vej} \rangle = 60^\circ$ , mean horizontal angle  $\langle \alpha_{hej} \rangle = 0^\circ$ , and standard deviations of  $\sigma_{\alpha_{vej}} = 15^\circ$  and  $\sigma_{\alpha_{hej}} = 10^\circ$ , respectively. The sizes of the newly ejected particles are taken randomly from the particle size distribution considered during modelling. It must be noted here that the surface deformation during saltation is neglected.

### Dust Dispersion

Dust dispersion is modelled using an Eulerian approach as described in Dupont *et al.* [2015]. The Eulerian approach is preferred to the Lagrangian one used for the saltation process because dust particles are much more numerous than saltating particles, thus explicitly resolving a statistically significant number of dust particles would be computationally expensive. Furthermore, the effect of airborne dust on the flow field can be neglected due to their small volume fraction. Thereby, dust dispersion is simulated by solving a conservation equation for dust concentration ( $\tilde{c}_b$ ), expressed as:

$$\frac{\partial \tilde{c}_b}{\partial t} + \frac{\partial \tau_{b,i}}{\partial x_i} + (u_i - v_{sed,b} \delta_{i3}) \frac{\partial \tilde{c}_b}{\partial x_i} = 0, \quad (3.10)$$

where the index  $b$  refers to the  $b$ th dust size bin;  $v_{sed,b}$  is the dust particle settling velocity estimated as  $v_{sed,b} = \rho_p g d_p^2 C_c / (18 \rho_a \nu_a)$  with  $d_p$  the dust particle size,  $\rho_p$  and  $\rho_a$  the densities of the dust and air, respectively,  $\nu_a$  the kinematic viscosity of air and  $C_c$  the Cunningham slip correction factor [Seinfeld *et al.* 1998]. The sub-grid dust flux  $\tau_{b,i}$  is given by

$$\tau_{b,i} = -K_d \frac{\partial \tilde{c}_b}{\partial x_i}, \quad (3.11)$$

where  $K_d$  is the dust eddy diffusivity. At the surface, this flux corresponds to the balance between the emission ( $F_{emi,b}$ ) and deposition ( $F_{dep,b}$ ) fluxes expressed as

$$\tau_{b,3} = F_{emi,b} - F_{dep,b}. \quad (3.12)$$

Here, the deposition flux is modelled after the classical dry deposition scheme [e.g., Seinfeld *et al.* 1998], given by

$$F_{dep,b} = v_{dep,b} c_b, \quad (3.13)$$

where  $v_{dep,b}$  is the dry deposition velocity of a particle of the  $b$ th bin. This is modelled as detailed in section 2.2.7.

Dust emission is purely driven by sandblasting. Following Fernandes *et al.* [2019], and explained later in Chapter 4, the energy for releasing dust particles is taken as a fraction  $\epsilon_d$  of the energy of the impacting saltator ( $E_{imp}$ ) lost to the surface ( $\epsilon_{fr} E_{imp}$ ), where  $\epsilon_{fr}$  is based on the splash scheme of Anderson *et al.* [1991]. Therefore, the number of dust particles of the  $b$ th bin released by an impacting saltator of size  $D$  are

$$N_{emi,b}(D) = \frac{\epsilon_d \epsilon_{fr} E_{imp,D}}{A d_b^\beta}, \quad (3.14)$$

where  $A$  is a constant, and the exponent  $\beta$  quantifies the surface bonding of the dust particles, with typical values between -0.02 and +3, and taken to +2 in this study. It follows that the emitted dust flux of the  $b$ th dust size bin due to sandblasting by sand particles in the range

$D_{S1}$  to  $D_{S2}$  is

$$F_{emi,b} = \frac{p_d(d_b)}{\Delta_x \Delta_y \Delta_t} \int_{D_{S1}}^{D_{S2}} N_{emi,b}(D) Q(D) p_s(D) \partial D, \quad (3.15)$$

where  $p_d(d_b)$  is the proportion of dust particles of the  $b$ th bin available at the surface, and  $p_s(D)$  is the size distribution of saltating particles.

### Deposition over vegetation

Vegetation elements, apart from influencing the turbulent flow, affect both the saltation process and the airborne dust concentration by acting as islands for deposition, capturing particles through a combination of sedimentation over the horizontal surfaces, interception and inertial impaction on to vertical surfaces, and increased brownian deposition of the finest (dust) particles. In our model, dust deposition velocity ( $v_{dep}$ ) is modelled as documented in section 2.2.7.

Over bare surfaces, saltating particles deposit through gravitational settling. In the presence of vegetation, they deposit over horizontal vegetation surfaces through sedimentation (gravitational settling) and are captured through interception and impaction by the vertical vegetation surfaces. The probability of a saltator encountering a horizontal vegetation surface during gravitational settling over a time interval  $dt$  is  $P_{horz} = A_h v_{sed} dt$ , with  $A_h$  the vegetation horizontal area density (assumed equal to  $A_f$  in this study), and  $v_{sed} = \rho_p g D^2 / (18 \rho_a \nu)$  is the particle settling velocity of a saltator of size  $D$ . Similarly, the probability that a saltator encounters a vertical surface, due to its inability to follow the flow streamlines around the vegetation elements, over a time interval  $dt$  is  $P_{vert} = A_f v_p E_d dt$ , where  $v_p$  is the horizontal particle velocity and  $E_d$  the efficiency of impaction (or interception), computed following Aylor [1982] as  $E_d = 0.86 / (1 + 0.442 St^{-1.967})$ . Here, the particle response time is computed from the settling velocity:  $v_{sed} / g$ . The eddies that influence the particle impaction and interception processes are of sizes equivalent to the length scale of the vegetation elements.

## 4 The role of deposition on the size-distribution of near-surface dust flux during erosion events.

This chapter focuses on the first question defining this doctoral work, i.e. the impact of surface characteristics, surface wind and the deposition process on the suspended dust. To this end, we present in this chapter a review of published dust emission schemes through a sensitivity analysis of the processes influencing the near-surface dust flux and its size-distribution during emission events. Based on this analysis a new 1D dust dispersion model is proposed and evaluated.

The published version of this chapter is: Fernandes R., Dupont S., and Lamaud E., Investigating the role of deposition on the size distribution of near-surface dust flux during erosion events, *Aeolian Research*, 37, 32-43, 2019. doi: [10.1016/j.aeolia.2019.02.002](https://doi.org/10.1016/j.aeolia.2019.02.002)

**Keywords:** Dust flux, Size distribution, Dust emission, Dust deposition, Deposition velocity, Fetch, Dust transport, Near-surface dust flux, Emitted dust flux



**Abstract:** Predicting the particle size distribution (PSD) of near-surface turbulent dust flux ( $F_{wd}$ ) is a key issue for estimating the size of atmospheric mineral dust. Existing dust emission schemes differ in their parametrization of the emitted dust ( $F_{emi}$ ) PSD, defining differently the surface inter-particle cohesive force and the influence of wind intensity. Moreover, these schemes have often been validated-fitted against field measurements, assuming PSD similarity between  $F_{wd}$  and  $F_{emi}$ . Here, we investigate numerically the main factors influencing  $F_{wd}$ -PSD during erosion events. To this effect, we developed a 1D dust-dispersal model. After evaluating the model against published results, it is shown that  $F_{wd}$ -PSD is influenced by both deposition and  $F_{emi}$ -PSD. This latter one is shaped by the inter-particle cohesive bond exponent and the surface dust PSD. A time-to-space conversion of the dust flux variations reveals an increasing enrichment of  $F_{wd}$  in small particles compared to  $F_{emi}$ . This enrichment remains lower than a few percent of the total dust flux (in number) for fetch lower than 100 m, but it can rise to more than 10% for fetch longer than 1 km. This fetch dependence of  $F_{wd}$ -PSD is explained by the slow deposition of particles having the lowest deposition velocities. Importantly, this difference between  $F_{wd}$  and  $F_{emi}$  PSDs is accentuated with wind intensity, with  $F_{emi}$ -PSD dominated by particles with large deposition velocities, and in presence of a large-scale background dust concentration. The role played by the deposition process in shaping the  $F_{wd}$ -PSD should be considered when evaluating dust emission schemes against near-surface field measurements.

## 4.1 Introduction

The entrainment of dust particles from the surface is driven by sandblasting [e.g., Shao *et al.* 1993; Marticorena *et al.* 1995; Alfaro *et al.* 1997; Shao *et al.* 2000; Alfaro *et al.* 2001; Shao 2001; Kok 2011b], and, to a lesser extent, by aerodynamic forces [e.g., Greeley *et al.* 1987]. Under saltation, dust particles are released when sufficient energy from an impacting saltator is available to break surface inter-particle cohesive bonds ( $E$ ). In dust emission schemes, saltation is considered as the necessary process for releasing dust. The dust flux is, therefore, often a function of the saltation flux [e.g., Shao *et al.* 1993; Marticorena *et al.* 1995; Alfaro *et al.* 2001; Shao 2001; Kok 2011b; Kok *et al.* 2014]. While the link between saltation and dust fluxes is well established, the processes shaping the PSD of the dust flux remain unclear.

In dust emission schemes, the emitted dust PSD is usually influenced by (1) the surface inter-particle cohesive bond, (2) the soil PSD, and/or (3) the wind intensity, as reviewed below.

*The surface inter-particle cohesive bond ( $E$ ).* The parametrization of  $E$  differs from one scheme to the other. In Shao *et al.* [1996],  $E$  was assumed proportional to the drag force acting on the particle multiplied by some length scale, leading to  $E \propto d_p^3$ , where  $d_p$  is the diameter of the released dust. Later, Shao [2001] related  $E$  to the van der Waals bond at the surface, leading to  $E \propto d_p^2$ . The same was considered by Kok *et al.* [2014]. Differently, Alfaro *et al.* [2001] proposed an inverse relationship between  $E$  and the particle size,  $E \propto d_p^{-0.018}$  (deduced from their Table 1). This allowed them to reproduce Alfaro *et al.* [1997] wind-tunnel experiment where finer particles were released under higher wind conditions, i.e., higher energy of the impacting saltators.

*The soil particle size distribution.* The influence of the soil PSD on the dust flux changes according to the dust emission schemes. Marticorena *et al.* [1995] related the dust flux PSD to the percentage of clay present in the soil, i.e., percentage of particles lower than  $3.9 \mu\text{m}$ . In Alfaro *et al.* [2001], the emission of dust is derived from a distribution with three log-normal modes, where the contribution of each mode depends on the strength of the inter-particle cohesive bond and on the wind intensity. In Shao [2001], the emission of dust is derived from two PSDs, minimally and fully disaggregated distributions, with an adjustable weight parameter to determine their relative contribution. Kok [2011b] suggested that aggregates behave like brittle materials where the emitted dust PSD is determined by patterns in which cracks nucleate and propagate. A compilation of published flux measurements in Kok *et al.* [2012] indicated a limited effect of soil texture on the observed dust flux PSD. This insensitivity of the dust flux PSD to the soil granulometry was also suggested in Reid *et al.* [2008].

*The wind intensity.* The influence of the wind intensity on the emitted dust PSD remains unclear. On one hand, Shao [2001] and Alfaro *et al.* [2001] considered an enrichment of the dust flux in smaller particles with increasing wind intensity, due to the stronger disintegration of aggregates by adjusting their weight parameters as a function of atmospheric forcing. On the

other hand, Kok [2011b] proposed the independence of the emitted dust PSD to the wind intensity, deduced from a compilation of field measurements showing negligible differences of the dust flux PSD under various wind conditions [Kok 2011a].

The definition of the dust flux simulated by dust emission schemes remained also vague in regard to the measured fluxes used to evaluate-fit them [e.g., Shao *et al.* 1993; Marticorena *et al.* 1995; Shao 2001; Alfaro *et al.* 2001; Kok *et al.* 2014]. The dust fluxes simulated by these schemes are the surface emitted dust fluxes since these schemes do not explicitly simulate turbulence nor consider the effect of deposition during emission. However, these simulated fluxes have most often been evaluated-fitted against field measurements performed well above the surface (several meters) and at various distances from the upwind border of the dust source area, i.e. fetch sizes ranging from 100 m to more than 10 km [e.g., Gillette 1977; Gomes *et al.* 2003; Gillies *et al.* 2004; Zobeck *et al.* 2006; Fratini *et al.* 2007; Sow *et al.* 2009]. This implies an hypothesis of PSD similarity between near-surface and surface fluxes, and thus a negligible impact of both the gravitational settling of the largest particles and the particle surface deposition across all sizes. Only Shao *et al.* [2011] applied a correction to the measured dust flux to account for the gravitational settling but without considering the full deposition process. Dupont *et al.* [2015] obtained from large-eddy simulations (LES) of aeolian erosion events an increasing difference in PSD with time between near-surface dust flux and emission flux as a result of a first particle sorting through turbulence diffusion, gravitational settling, and more importantly surface deposition. Their results were, however, limited to three particle sizes (1.40, 6.70 and 14.20  $\mu\text{m}$ ) and to one soil PSD with an equiprobable emission of the three dust particle sizes, limiting a more general view of the impact of dust deposition on the near-surface dust flux PSD according to the soil PSD. Interestingly, by converting the erosion duration of their simulations into a fetch size, their results mean that the difference in PSD between near-surface dust flux and emission flux should increase with the fetch. A quantification of this difference according to the fetch size and the soil PSD would benefit to the erosion community.

The goal of the present study is twofold: (1) investigate the role of deposition in shaping the PSD of near-surface dust flux during erosion events, and, more generally, (2) investigate the sensitivity of the PSD of near-surface dust flux to the surface inter-particle cohesive bond, the PSD of available dust at the surface, the wind intensity, and the fetch length. To that purpose we extend the initial study of Dupont *et al.* [2015] by considering (1) dust particles ranging from 0.1 to 16  $\mu\text{m}$ , (2) various soil PSDs, and (3) the influence of the inter-particle cohesive bond exponent ( $\beta$ ) on the emitted dust flux PSD. Because the LES approach used in Dupont *et al.* [2015] was too time consuming for performing such a detailed sensitivity analysis, we developed for this analysis a simple one-dimensional (1D) physically-based dust dispersal model, accounting for dust emission, transport, and deposition in the atmospheric surface boundary layer. After evaluating the model against published dust flux behaviours, the model is used to study the sensitivity of the PSD of the near-surface dust flux.

In this chapter, the near-surface dust flux will refer to the vertical turbulent-diffusive flux ( $F_{wd}$ )

<b>Flux Nomenclature</b>	
<b>Symbol</b>	<b>Description</b>
$F_{emi}$	Dust emission flux at the surface
$F_{dep}$	Dust deposition flux at the surface
$F_{wd}$	Near-surface dust turbulent-diffusive flux
$F_{sed}$	Dust gravitational settling flux
<b>Indices</b>	
$b$	Dust particles from the $b$ th bin
$tot$	All dust particle sizes

TABLE 4.1: Dust flux notation.

at several meters above the surface. It corresponds to the amount of particles transported away from the surface by the flow turbulence. This flux results from a balance between the emission ( $F_{emi}$ ) and deposition ( $F_{dep}$ ) fluxes, the storing rate of particles in the air, and the gravitational settling flux ( $F_{sed}$ ) due to particle weight. Importantly,  $F_{wd}$  does not include  $F_{sed}$  and it is not equivalent to the dust emission flux at the surface ( $F_{emi}$ ). See Table 7.1 for a summary of the flux notations used in this chapter.

## 4.2 One-dimensional dust-dispersal model

A simple 1D dust-dispersal model was developed to simulate the whole dust life-cycle in a column of air representative of the atmospheric surface boundary layer above an infinite bare erodible surface under neutral thermal stratification (Fig. 4.1). The model accounts for (1) dust emission through sandblasting, based on an energy budget linking the surface cohesive forces to the dust particle size, (2) dust turbulent transport within the surface boundary layer, and (3) dust deposition at the surface.

### 4.2.1 Wind

The wind intensity is quantified through the friction velocity ( $u_*$ ), which is related to the turbulent flow shear stress ( $\tau$ ) induced by the surface:

$$u_* = \sqrt{\tau/\rho_a}, \quad (4.1)$$

where  $\rho_a$  is the air density. The shear stress quantifies the momentum flux absorbed by the surface. Above an homogeneous surface,  $\tau$  is constant with height within the surface boundary layer. The similarity theory leads to the well-known logarithmic velocity profile expressed as:

$$u(z) = \frac{u_*}{\kappa} \ln\left(\frac{z}{z_0}\right), \quad (4.2)$$

where  $z$  is the vertical coordinate,  $z_0$  the surface roughness length, and  $\kappa$  the von Karman constant ( $= 0.40$ ).

In the presence of saltation, the total shear stress ( $\tau$ ) is partitioned within the saltation layer between the momentum flux absorbed by the surface and that absorbed by the saltators. The absorption of momentum by the saltators modifies the wind profile. This was accounted for in Raupach [1991] as:

$$u(z) = \frac{u_*}{\kappa} \left[ \ln \left( \frac{z}{z_0} \right) + (1 - \sqrt{r}) \left[ \gamma + \ln \left( \frac{z_0}{H_s} \right) + E \left( \frac{z}{H_s} \right) \right] \right], \quad (4.3)$$

where  $H_s = 0.3969u_*^2/2g$  is the average height of the saltation layer with  $g$  the gravitational acceleration,  $r = u_{*t}^2/u_*^2$  with  $u_{*t}$  the threshold friction velocity above which saltation starts,  $\gamma = 0.577216$  is the Euler's constant, and  $E(x) = \int_x^\infty \exp(-t)/tdt$ . Above the saltation layer, this modification of the wind profile due to saltation is equivalent to replacing  $z_0$  in Equation 4.2 by a saltation roughness length  $z_{0s} = [H_s \exp(-\gamma)]^{(1-\sqrt{r})} z_0^{\sqrt{r}}$  [Raupach 1991].

Unlike saltating particles, the relatively small volume fraction of dust particles has negligible effect on the flow field.

## 4.2.2 Dust transport

An Eulerian approach was used to describe the turbulent transport of dust particles in the atmospheric surface layer. Here, dust particles were assumed spherical, non magnetic, and electrically neutral. The size range of dust particles is divided into  $n_b$  bins, each bin being characterized by a mean particle diameter  $d_b$ . Hence, the conservation equation of the dust concentration  $c_b$  of the  $b$ th bin is given by:

$$\frac{\partial c_b(z,t)}{\partial t} = -\frac{\partial F_{wd,b}(z,t)}{\partial z} + v_{sed,b} \frac{\partial c_b(z,t)}{\partial z}, \quad (4.4)$$

where  $t$  is time,  $F_{wd,b}$  is the dust turbulent-diffusive flux of the  $b$ th size bin,  $v_{sed,b}$  is the settling velocity of the particles of the  $b$ th size bin given as  $v_{sed,b} = \rho_p g d_b^2 C_c / (18\rho_a \nu)$ , where  $\rho_p$  is the dust particle density,  $C_c$  is the Cunningham slip correction factor, and  $\nu$  is the kinematic viscosity of air [Seinfeld *et al.* 1998]. Equation 4.4 means that the dust concentration variation in a grid cell results from a balance between incoming and outgoing turbulent-diffusive ( $F_{wd,b}$ )

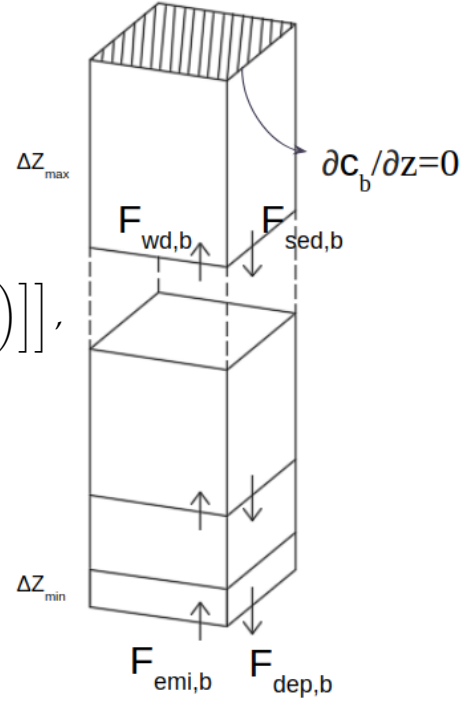


FIGURE 4.1: Schematic representation of the 1D computational domain used in this chapter.

and gravitational settling ( $F_{sed,b} = v_{sed,b}c_b$ ) fluxes due to turbulent motions and particle weight, respectively.

The turbulent-diffusive dust flux is simply estimated from a flux-gradient relationship:

$$F_{wd,b}(z,t) = -K_d \frac{\partial c_b(z,t)}{\partial z}, \quad (4.5)$$

where  $K_d = \kappa z u_* [1 - (1 - \sqrt{r}) \exp(-z/H_s)]$  is the dust eddy diffusivity assuming similarity in turbulent transport between momentum and dust particles [Gillette *et al.* 1972]. This expression of  $K_d$  converges to its surface layer value  $\kappa z u_*$  above the saltation layer [Raupach 1991].

At the surface, the total dust flux ( $F_{tot}$ ) accounting for both turbulent-diffusive and gravitational settling fluxes, is expressed as:

$$F_{tot,b}^{surf}(t) = F_{emi,b}(t) - F_{dep,b}(t), \quad (4.6)$$

where  $F_{emi,b}$  and  $F_{dep,b}$  are the emission and deposition fluxes at the surface of dust particles of the  $b$ th bin, respectively (Fig. 4.1).

### 4.2.3 Saltation

Saltating particles are characterized by a size distribution  $p_s$  whose diameters range from  $D_{S1}$  to  $D_{S2}$ . The total saltation flux is the integration of the saltation flux of all particle sizes according to  $p_s$ :

$$F_{salt,tot} = \int_{D_{S1}}^{D_{S2}} F_{salt}(D) p_s(D) \partial D, \quad (4.7)$$

where the saltation flux  $F_{salt}(D)$  of particles of diameter  $D$  is estimated from White [1979] as follows:

$$F_{salt}(D) = 2.61 \frac{\rho_a}{g} \left(1 - \frac{u_{*,t}(D)}{u_*}\right) \left(1 + \frac{u_{*,t}(D)}{u_*}\right)^2 u_*^3, \quad (4.8)$$

where  $u_{*,t}(D)$  is the threshold friction velocity deduced from Marticorena *et al.* [1995].

On average, the kinetic energy of the saltating particles of diameter  $D$  impacting the surface is:

$$E_{imp,D} = \frac{1}{2} m_{imp} v_{imp}^2, \quad (4.9)$$

where  $m_{imp} = \rho_p \pi D^3 / 6$  is the particle mass, and  $v_{imp}$  is the velocity of the impacting saltator. In a first order approximation,  $v_{imp}$  is estimated as  $v_{imp} = 5u_{*,t}(D)$  [Kok *et al.* 2014].

Using a probabilistic approach as often used in splash schemes, the kinetic energy of impacting saltators ( $E_{imp}$ ) is distributed between the energy used for saltator rebound (fraction  $\epsilon_{reb}$ ), the energy used for ejecting new saltators (fraction  $\epsilon_{ej}$ ), and the energy lost to the surface (fraction

$\epsilon_{fr}$ ), such as:

$$\epsilon_{reb} + \epsilon_{ej} + \epsilon_{fr} = 1. \quad (4.10)$$

Here,  $\epsilon_{reb} = 2\gamma^2 P_{reb}$ , where  $P_{reb}$  is the rebound probability [Anderson *et al.* 1986] and  $\gamma = 0.55$  [Rice *et al.* 1995]; and  $\epsilon_{fr} = 0.96(1 - \epsilon_{reb})$  [Ammi *et al.* 2009].

This energy distribution at the surface during the saltator impact does not account for the energy fraction used for releasing dust particles from sandblasting. We hypothesized that the energy for dust emission is a fraction  $\epsilon_d$  of the energy lost to the surface ( $\epsilon_{fr}E_{imp,D}$ ).

#### 4.2.4 Dust emission

At the surface, dust particles lie on larger sand grains, surrounded by other dust grains, forming aggregates. A particle in this system experiences short-range dielectric attractive forces known as van der Waals forces due to inter-particle interactions (dust-dust particles or dust-sand particles). Estimating the van der Waals forces between two spherical particles in contact is simple but it becomes much more complex when it comes to estimate the cohesive forces of particles in an aggregate [Shao 2001]. This explains the various parametrizations proposed in the literature for the inter-particle cohesive forces as mentioned in the introduction. Overall, these parametrizations express the inter-particle cohesive bond as a function of the dust particle diameter:

$$E_{coh,b} = Ad_b^\beta, \quad (4.11)$$

where  $\beta$  can be referred to as the inter-particle cohesive bond exponent defining the relationship between the dust particle diameter and the cohesive bond, and  $A$  is a constant. In existing dust emission schemes,  $\beta$  varies from  $-0.018$  to  $+3$  as reviewed in the introduction section.

The number of dust particles of bin  $b$  released by an impacting saltator of size  $D$  is defined as the ratio between the available energy for releasing dust and the energy required to eject one dust particle:

$$N_{emi,b} = \frac{\epsilon_d \epsilon_{fr} E_{imp,D}}{Ad_b^\beta}, \quad (4.12)$$

where  $\epsilon_d$  is the fraction of the energy lost to the surface by the impacting saltator ( $\epsilon_{fr}E_{imp,D}$ ) that is used to release dust. Equation 4.12 can be rewritten as:

$$N_{emi,b} = \alpha_{em} \frac{\epsilon_{fr} E_{imp,D}}{d_b^\beta}, \quad (4.13)$$

where  $\alpha_{em}$  is the dust emission coefficient resuming the two unknown constants  $\epsilon_d$  and  $A$ .

Hence, the emission dust flux at the surface of the  $b$ th bin is:

$$F_{emi,b} = \zeta_d(d_b, u_*) p_d(d_b) \int_{D_{S1}}^{D_{S2}} N_{emi,b}(D) \frac{F_{salt}(D)}{l(D)} p_s(D) \partial D, \quad (4.14)$$

where  $p_d(d_b)$  is the proportion of dust particles from the  $b$ th bin available at the surface,  $F_{salt}/l$  represents the vertical flux of saltating particles or in other words the flux of impacting saltators at the surface, with  $l$  the average hop length of the saltating particles. Here,  $l$  was simply deduced as the maximum horizontal distance travelled by a projectile launched with a lift-off velocity  $v_{ej}$  and a lift-off angle  $\alpha_{ej}$ :  $l = v_{ej}^2 \sin(2\alpha_{ej}) / g$ . We chose  $v_{ej} = 0.63u_*$  and  $\alpha_{ej} = 50^\circ$  [Shao 2008]. The coefficient  $\zeta_d(d_b, u_*)$  accounts for the modification of the size distribution of emitted dust due to the enhancement of aggregate disintegration with wind speed as proposed by Alfaro *et al.* [1997]. Unless otherwise specified,  $\zeta_d(d_b, u_*) = 1$  in our simulations, implying the size distribution of the emission dust flux is independent of the wind intensity.

#### 4.2.5 Dust Deposition

Dust deposition on soil occurs only through dry deposition accounting for gravitational settling, turbulent mixing, and brownian diffusion [e.g., Seinfeld *et al.* 1998]. Hence, the deposition flux of dust particles from the  $b$ th bin is:

$$F_{dep,b} = v_{dep,b} c_b^{surf}, \quad (4.15)$$

where  $c_b^{surf}$  is the dust concentration close to the surface (middle of the first grid cell, see Fig. 4.1), and  $v_{dep,b}$  is the particle dry deposition velocity that is classically parameterized as a set of resistances:

$$v_{dep,b} = \frac{1}{R_a + R_b + R_a R_b v_{sed,b}} + v_{sed,b}, \quad (4.16)$$

where  $R_a = \log(z_s/z_{0s}) / (\kappa u_*)$  is the aerodynamic resistance accounting for turbulent transfer near the surface ( $z_s$  is the middle of the first grid cell) with  $z_{0s}$  the saltation-layer roughness length estimated as per Raupach [1991];  $R_b = [u_* (S_c^{-2/3} + 10^{-3/S_t})]^{-1}$  is the quasi-laminar resistance accounting for brownian diffusion and inertial impaction on particles. Here,  $S_c = v/D_g$  is the Schmidt number,  $D_g = k_b T C_c / (3\pi\rho_p v d_b)$  is the brownian diffusivity, with  $k_b$  the Boltzman constant, and  $T$  the air temperature, set to  $27^\circ\text{C}$  in this study.  $S_t = u_*^2 v_{sed,b} / (g v)$  is the Stokes number.

Fig. 4.2 presents the variation of the deposition velocity with the dust particle size for different wind intensities. The deposition velocity exhibits a minimum for particles around  $0.5$  to  $1 \mu\text{m}$  in diameter. With increasing wind intensity, the deposition velocity increases, especially for the largest particles, due to the larger decrease of  $R_b$  with increasing particle size.

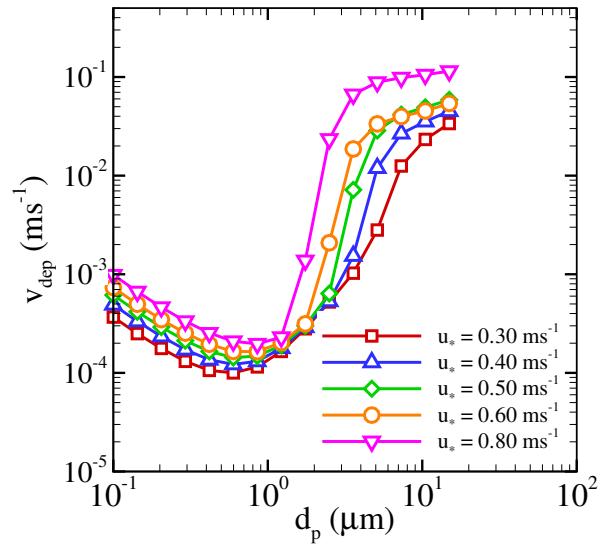


FIGURE 4.2: Variation of the deposition velocity ( $v_{dep}$ ) with dust particle diameter ( $d_p$ ) for five wind intensities ( $u_* = 0.30, 0.40, 0.50, 0.60$  and  $0.80 \text{ ms}^{-1}$ ).



### 4.2.6 Simulation configurations

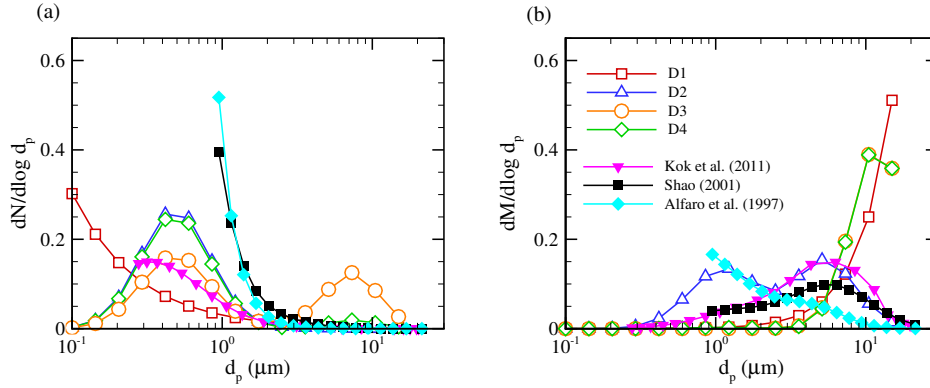


FIGURE 4.3: Size distributions in number (a) and in mass (b) of dust particles available at the surface considered in our simulations (D1, D2, D3 and D4) as well as reported in the wind-tunnel experiment of Alfaro *et al.* [1997] and used in Shao [2001] and Kok [2011a] numerical experiments.

The computational domain was meshed along the vertical using a stretched grid from the surface to the top of the domain. The grid size was varying from  $\Delta z_{min} = 0.01$  m at the surface to  $\Delta z_{max} = 0.24$  m at the top (Fig. 4.1). This mesh ensures a grid resolution fine enough to simulate exchanges close to the surface (where particle concentration is high), while reducing the computational time by considering larger grid cells for exchanges farther away. Unless otherwise specified, the total domain height was 200 m corresponding to the approximate depth of the atmospheric surface layer under neutral thermal stratification.

The dust conservation equation (Eq. 4.4) was solved using the Crank-Nicolson method [Crank *et al.* 1996]:

$$\frac{c_b^{t+\Delta t} - c_b^t}{\Delta t} = \frac{1}{2} \left[ F_i^{t+\Delta t} \left( c_b, z, t + \Delta t, \frac{\partial c_b}{\partial z}, \frac{\partial^2 c_b}{\partial z^2} \right) + F_i^t \left( c_b, z, t, \frac{\partial c_b}{\partial z}, \frac{\partial^2 c_b}{\partial z^2} \right) \right], \quad (4.17)$$

where  $\Delta t = 0.01$  s is the time step and  $F_i^t$  is the right-hand side term of Eq. 4.4 at time  $t$ . A Neuman boundary condition was applied at the top of the domain ( $\partial c_b / \partial z = 0$ ). This resolution method has the advantage of being implicit and of ensuring second order convergence in time. The spatial derivatives were discretized following a finite volume approach, ensuring the conservation of the amount of dust particles within the computational domain.

Table 7.2 summarizes the main input parameters required by our model to simulate dust dispersal during an erosion event. Simulations started with an air clean of dust. Saltating particles had a geometric mean diameter of  $210 \mu\text{m}$  and a geometric standard deviation of 1.8. Dust particle diameters ranged from 0.1 to  $16 \mu\text{m}$ , divided into 15 log-normal bins.

In our simulation analysis, the time variations of dust concentration and dust flux profiles were converted into spatial variations from an upwind virtual border of an erodible surface, corresponding to  $t = 0$  s, to distances  $x = U_{int}t$ , referring to the fetch length, where  $U_{int}$  is the

Parameter	Symbol
PSD of available dust at the surface	$p_d$
PSD of saltating particles	$p_s$
Dust emission coefficient modulating the number of emitted dust per saltator	$\alpha_{em}$
Inter-particle cohesive bond exponent	$\beta$
Function modifying $p_d$ according to the wind intensity	$\zeta_d$
Particle density	$\rho_p$
Surface roughness length	$z_0$
Wind friction velocity	$u_*$
Ambient air properties (temperature, density, kinematic viscosity)	$T, \rho_a, \nu$

TABLE 4.2: Main input parameters of our 1D dust dispersal model.

integral wind speed ( $U_{int} = \int_0^{z_{ref}} u(z) dz / z_{ref}$ , where  $z_{ref}$  was chosen equal to the height of the investigated dust flux, 3 m here, unless otherwise specified). This time-space conversion allows us to evaluate the sensitivity of the dust flux PSD to the deposition process according to the fetch length.

### 4.3 Model evaluation

Before using our model to investigate the sensitivity of the near-surface dust flux PSD, we find it important to evaluate its ability to reproduce published dust flux behaviours.

#### 4.3.1 Dust flux versus wind intensity compared to existing dust emission schemes

Existing dust emission schemes show a clear increase of the dust flux with increasing wind intensity. Here, our model was used to simulate 15-minute erosion events (fetch up to 20 km) with different stationary wind intensities ( $u_*$ ), starting with an air clean of dust. The surface dust size distribution ( $p_d$ ) was considered enriched in small particles (D1 distribution in Fig. 4.3). The cohesive bond exponent  $\beta$  was set to 2. This combination of  $\beta = 2$  and distribution D1 leads to an equiprobable PSD of emitted

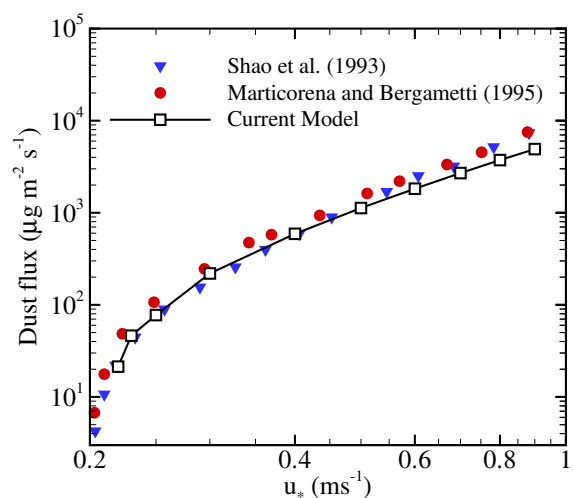


FIGURE 4.4: Vertical dust flux ( $F_{wd,tot}$ ), including all particle sizes, as a function of the friction velocity ( $u_*$ ) obtained from our 1D model and compared with the empirical parametrizations of (1) Marticorena *et al.* [1995]:  $F_{wd,tot} = \gamma Q_{tot}$ , with  $\gamma = 10^{-2}$ , and (2) Shao *et al.* [1993]:  $F_{wd,tot} = C \rho_d (u_*^2 - u_{*t}^2)$ , with  $C = 4$  and  $u_{*t} = 0.2 \text{ ms}^{-1}$ . Note that the dust emission coefficient ( $\alpha_{em}$ ) of our model (Eq. 4.13) was chosen so as  $F_{wd,tot}$  fits the value obtained from Shao *et al.* [1993] scheme at  $u_* = 0.40 \text{ ms}^{-1}$ .

dust. The dust emission coefficient ( $\alpha_{em}$ ) that modulates the amplitude of the dust flux in our model (Eq. 4.13), was chosen so as the simulated dust flux at  $u_* = 0.40 \text{ ms}^{-1}$  fits the one from Shao *et al.*'s (1993) scheme.

The 3-m high  $F_{wd,tot,r}$  including all particle sizes, as simulated by our model after 15-minute erosion, exhibits a similar trend with  $u_*$  as the fluxes obtained from the emission schemes of Shao *et al.* [1993] and Marticorena *et al.* [1995] (Fig. 4.4). This agreement confirms the accurate sensitivity to the wind intensity of the magnitude of the dust flux simulated by our model. The same was verified for different combinations of  $\beta$  and  $p_d$  by fitting different values of  $\alpha_{em}$ .

### 4.3.2 Dust concentration vertical profile compared to analytical solution

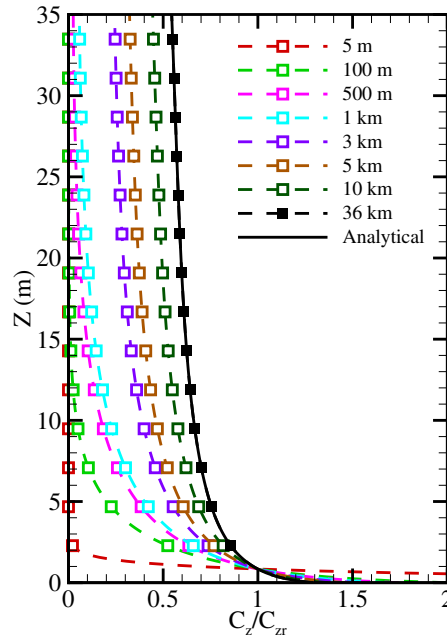


FIGURE 4.5: Variation with the fetch length of the simulated vertical dust concentration profiles (dot-lines) and comparison at steady state against the analytical profile (solid line) for  $16 \mu\text{m}$  dust particle in a 35 m high domain, and with  $u_* = 0.40 \text{ ms}^{-1}$ . The analytical profile responds to  $c_b(z) = c_b(z_r) (z/z_r)^{v_{s,b}/(\kappa u_*)}$ , where  $z_r$  is a reference height corresponding here to 1 m.

At steady state over an extended homogeneous surface ( $F_{emi,b} = F_{dep,b}$ ), the conservation equation of dust concentration (Eq. 4.4) leads to the following analytical solution [Shao 2008]:

$$c_b(z) = c_b(z_r) (z/z_r)^{v_{sed,b}/(\kappa u_*)}, \quad (4.18)$$

where  $z_r$  is a reference height.

The concentration profile simulated by our model at equilibrium between  $F_{emi,b}$  and  $F_{dep,b}$  is consistent with this analytical solution (Fig. 4.5). This was verified for an erosion event with

$u_* = 0.40 \text{ ms}^{-1}$  and  $16.0 \mu\text{m}$  dust particles, in a 35 m high domain. This equilibrium was reached for a fetch  $x_{eq} = 36 \text{ km}$ . With a larger domain,  $x_{eq}$  increases as the emitted dust particles have a larger volume to disperse, reducing the near-surface dust concentration, and thus the deposition. For typical surface atmospheric boundary layer of 200 m high,  $x_{eq} \approx 200 \text{ km}$ . The equilibrium fetch also increases with decreasing particle size. For 5 and  $10 \mu\text{m}$  dust particles and a 200 m high domain,  $x_{eq} \approx 320$  and  $640 \text{ km}$ , respectively. Simulations with particles smaller than  $5 \mu\text{m}$  led to an equilibrium fetch larger than a few thousand kilometers.

### 4.3.3 Dust flux enrichment in small particles compared to Dupont *et al.* [2015] large-eddy simulation

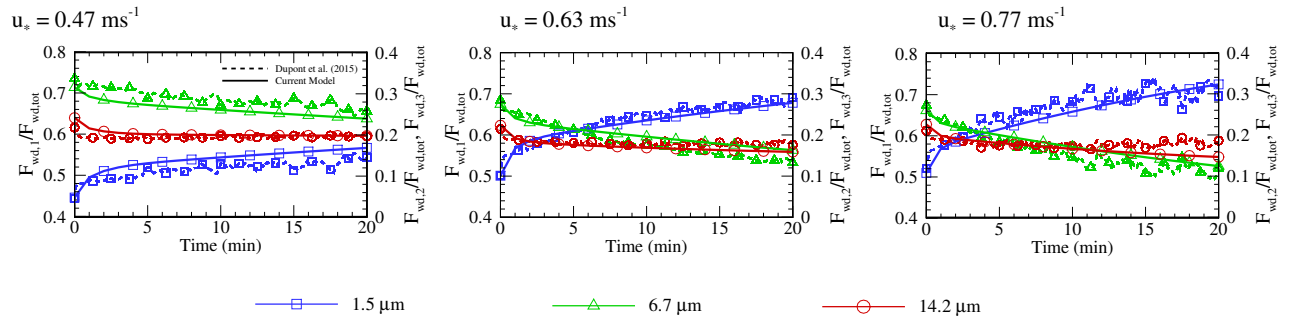


FIGURE 4.6: Time variation of the fraction in number of the turbulent-diffusive fluxes ( $F_{wd,b}$ ) at 2 m height of  $1.5 \mu\text{m}$  (blue,  $b=1$ ),  $6.7 \mu\text{m}$  (green,  $b=2$ ) and  $14.2 \mu\text{m}$  (red,  $b=3$ ) particle diameters, on the total turbulent-diffusive dust flux  $F_{wd,tot}$ , for three wind conditions ( $u_*$ ) simulated by our model (solid lines) in comparison with those from Dupont *et al.* [2015] (dotted lines).

Dupont *et al.* [2015] performed detailed three-dimensional simulations of soil erosion of a bare surface by representing the main erosion processes (saltation, sandblasting, dust suspension) within a large-eddy simulation (LES) airflow model that simulated instantaneous wind. They simulated 20-minute long erosion events, with three dust particle bins  $1.5$ ,  $6.7$ ,  $14.2 \mu\text{m}$ , under three wind conditions ( $u_* = 0.47, 0.63, 0.77 \text{ ms}^{-1}$ ). By assuming an equiprobable emission of the three size bins, they observed an enrichment of the 2-m high  $F_{wd}$  in small particles with time. This enrichment was explained by the nonstationarity of the erosion process, due to the lower deposition velocity of the smaller dust particles. Here, we reproduced these simulations with our simple 1D model using similar erosion configurations as in Dupont *et al.* [2015].

Fig. 4.6 presents the time variation of the fractions in number of  $F_{wd,b}$  on  $F_{wd,tot}$ , for the three size bins and three wind intensities, as estimated from our model and compared to Dupont *et al.* [2015]. Our 1D model reproduces quite efficiently the flux enrichment in the smallest bin ( $1.5 \mu\text{m}$ ) and the impoverishment in  $6.7 \mu\text{m}$  particles with time and with increasing wind intensities. The small differences between both models may be explained by the difference in modelling the turbulence in the saltation layer between both approaches.

#### 4.3.4 Dust flux PSD compared to Alfaro *et al.* [1997] wind-tunnel experiment

Alfaro *et al.* [1997] observed from a wind-tunnel experiment an enhancement of the emission of small dust particles with increasing wind intensity. This was observed from the mass size distribution of dust accumulated in a horizontal trap above the surface during a certain period (not specified by the authors). This led them to suggest the enrichment of the emitted dust in small particles with increasing wind intensity and to propose a time-independent dust emission scheme, equivalent to  $\beta = -0.018$ . Later, Shao [2001] validated his dust emission scheme by reproducing similar time-independent PSD of the dust flux as a function of the wind intensity. To obtain his result, he chose  $\beta = 2$  with a different surface dust size distribution than Alfaro *et al.* [1997].

Here, our 1D model is used to reproduce the Alfaro *et al.* [1997] experiment by simulating erosion events in a domain with the same vertical size (70 cm) as their wind tunnel. The inter-particle cohesive bond exponent  $\beta$  was set to -0.018 and the surface dust size distribution (Fig. 4.3) was chosen so as the  $F_{emi}$  PSD for  $u_* = 0.40 \text{ ms}^{-1}$  equates that observed by Alfaro *et al.* [1997]. Two simulations were conducted: one where  $F_{emi}$  PSD exhibited no dependence to the wind intensity ( $\zeta(d_b, u_*) = 1$  in Equation 4.14), and the other one where  $F_{emi}$  PSD followed the dependence to the wind intensity proposed by Alfaro *et al.* [1997] ( $\zeta(d_b, u_*) \neq 1$ ).

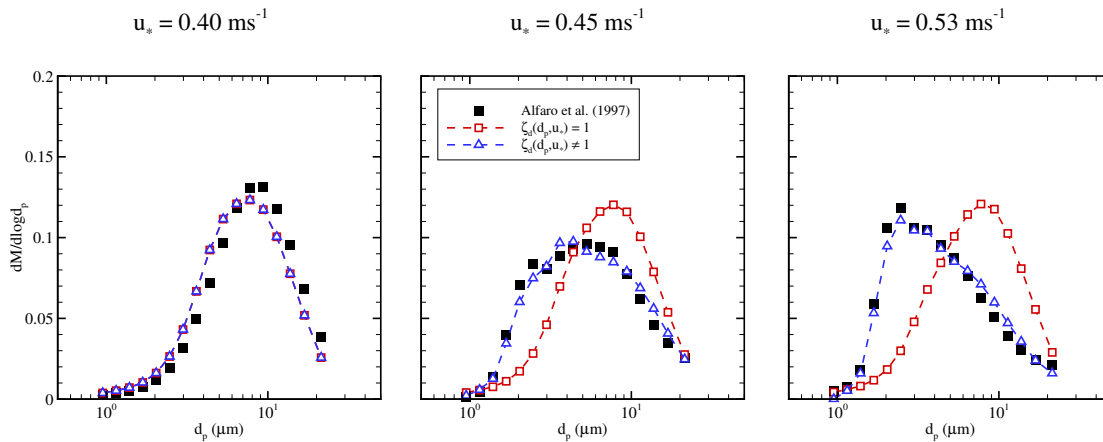


FIGURE 4.7: The mass size distribution of the vertical dust fluxes ( $F_{wd}$ ) as simulated by our model (line-dots) for three wind conditions ( $u_*$ ), and compared with the wind-tunnel observations from Alfaro *et al.* [1997] (filled squares). In one simulation, the PSD of available dust at the surface ( $p_d$ ) is independent of  $u_*$  ( $\zeta_d = 1$ ) while in the other simulation  $p_d$  depends on  $u_*$  as suggested by Alfaro *et al.* [1997] ( $\zeta_d \neq 1$ )

Fig. 4.7 compares the mass size distributions of  $F_{wd}$  simulated by the current model and observed by Alfaro *et al.* [1997], for a 5-m long fetch and three friction velocities. For  $u_* = 0.40 \text{ ms}^{-1}$ , our model agrees with the observations of Alfaro *et al.* [1997] regardless of  $\zeta(d_b)$ . At higher wind speeds, our results only agree with Alfaro *et al.*'s ones when  $F_{emi}$  PSD is a function of the wind speed ( $\zeta(d_b, u_*) \neq 1$ ). This result implies a negligible effect of deposition, sedimentation and turbulence, in shaping the PSD of the near-surface dust flux and, thus, in

differentiating the PSDs of  $F_{wd}$  and  $F_{emi}$ , for the conditions of the wind tunnel experiment. This result leaves open the possibility of the dust flux enrichment in small dust particles with wind intensity due to an enhancement of aggregate disintegration [Alfaro *et al.* 1997].

### 4.3.5 Dust flux PSD compared to Kok [2011b] parametrization

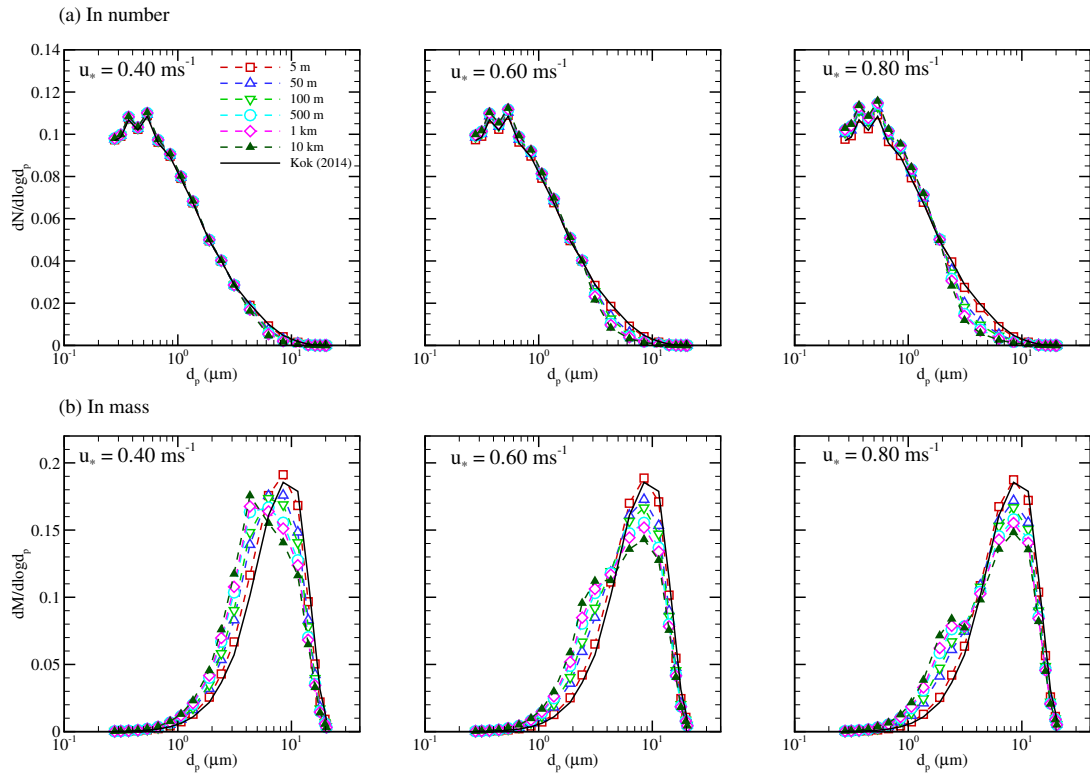


FIGURE 4.8: Variation with the fetch length of the size distribution in number (top row) and in mass (bottom row) of the 3-m high vertical dust fluxes ( $F_{wd}$ ) as simulated by our model (line-dots) for three wind conditions ( $u_*$ ) (line-dots), and compared with the prediction of Kok [2011b] (solid line-filled squares). The fetch ranges from 5 m to 10 km.

Kok [2011b] proposed a PSD of emitted dust independent of the soil granulometry and wind intensity. They based their proposition on several field data measured at a few meters above the surface and under various fetch magnitudes, ranging from 200 m to 10 km. Here, our model is used to simulate erosion events corresponding to a maximum fetch of 10-km with three wind conditions ( $u_*$ ),  $\beta = 2$ , and the surface dust size distribution proposed by Kok [2011b] (Fig. 4.3). The 3-m high  $F_{wd}$  PSD in number simulated by our model (Fig. 4.8a) is close to that of Kok [2011b] for small fetch lengths ( $< 5$  m). As the fetch increases, the fraction of the largest particles in the dust flux decreases due to their surface deposition, and thus the flux enriches in small particles. This enrichment in small particles (impoverishment in large particles) is accentuated with  $u_*$  as the deposition velocity increases (Fig. 4.2). The differences between the simulated near-surface dust flux PSD and the emitted flux PSD proposed by Kok

[2011b] are amplified when the PSDs are expressed in mass as it emphasizes the role of the largest particles (Fig. 4.8b).

#### 4.4 Sensitivity of the dust flux PSD

Parameter	Range of values
Friction velocity ( $u_*$ )	0.30, 0.40, 0.50 $\text{ms}^{-1}$
PSD of available dust at the surface ( $p_d$ )	D1, D2, D3, D4 (see, Fig. 4.3)
Inter-particle cohesive bond exponent ( $\beta$ )	-1, 0, 1, 2, 3

TABLE 4.3: Range of values of the parameters considered in our sensitivity analysis of the dust flux PSD.

To investigate the sensitivity of  $F_{wd}$  PSD, 10 simulations were conducted varying either (1) the inter-particle cohesive bond exponent ( $\beta$ ), (2) the surface dust-size distribution ( $p_d$ ), or (3) the wind intensity ( $u_*$ ). Each simulation started from an air clean of dust. This sensitivity of  $F_{wd}$  PSD is presented according to the fetch size, with values ranging from 5 m to 10 km. To focus solely on the possible impact of the deposition process on  $F_{wd}$  PSD, the  $F_{emi}$  PSDs were considered independent of the wind intensity, i.e.  $\zeta(d_b, u_*) = 1$  in Equation 4.14.

Table 4.3 summarizes the range of each parameter-forcing considered in this analysis. For  $p_d$ , four surface dust-size distributions (D1, D2, D3 and D4) were considered (Fig. 4.3). They were chosen so as to obtain for  $\beta = 2$  the following  $F_{emi}$  PSDs (Fig. 4.9d): equinumber emissions across bins (D1), strong emission around  $0.7 \mu\text{m}$  corresponding to particles with the lowest deposition velocity (D2), two emission peaks at  $0.7$  and  $8 \mu\text{m}$  (D3), and strong emission around  $8 \mu\text{m}$  corresponding to particles with large deposition velocity (D4). Fig. 4.9 presents the  $F_{emi}$  PSDs obtained for the different combinations of  $\beta$  and  $p_d$  considered in our analysis. These PSDs cover the usual distributions encountered in existing emission schemes [Alfaro *et al.* 2001; Shao 2001; Kok *et al.* 2014].

The variation of the 3-m high  $F_{wd}$  PSDs is presented in number in Fig. 4.10 according to the fetch size. Fig. 4.10 includes results for (a) three wind conditions ( $u_* = 0.30, 0.40$  and  $0.50 \text{ms}^{-1}$ ) with  $\beta = 2$  and the surface dust-size distribution D1, (b) three surface dust-size distributions (D2, D3 and D4) with  $\beta = 2$  and  $u_* = 0.40 \text{ms}^{-1}$ , and (c) four surface cohesive bond exponents ( $\beta = -1, 0, 1$  and  $3$ ) with the surface dust-size distribution D1 and  $u_* = 0.40 \text{ms}^{-1}$ . Additionally, Fig. 4.11 presents the fraction in number and in mass of  $F_{wd}$  partitioned in four bins (Z1 to Z4) on the total dust flux  $F_{wd,tot}$ , according to the fetch size. Here, these four bins cover the whole dust size range. They were defined based on the variations of the particle deposition velocity with the particle size (Fig. 4.2) such as Z1 bin ( $< 0.3 \mu\text{m}$ ) covers the region of predominant brownian deposition, Z2 bin ( $0.3 - 1.0 \mu\text{m}$ ) covers the region of minimum deposition velocity, Z3 bin ( $1.0 - 8.0 \mu\text{m}$ ) covers the region of sharp rise in deposition velocity, and Z4 bin ( $> 8.0 \mu\text{m}$ ) covers the region of predominant gravitational settling.

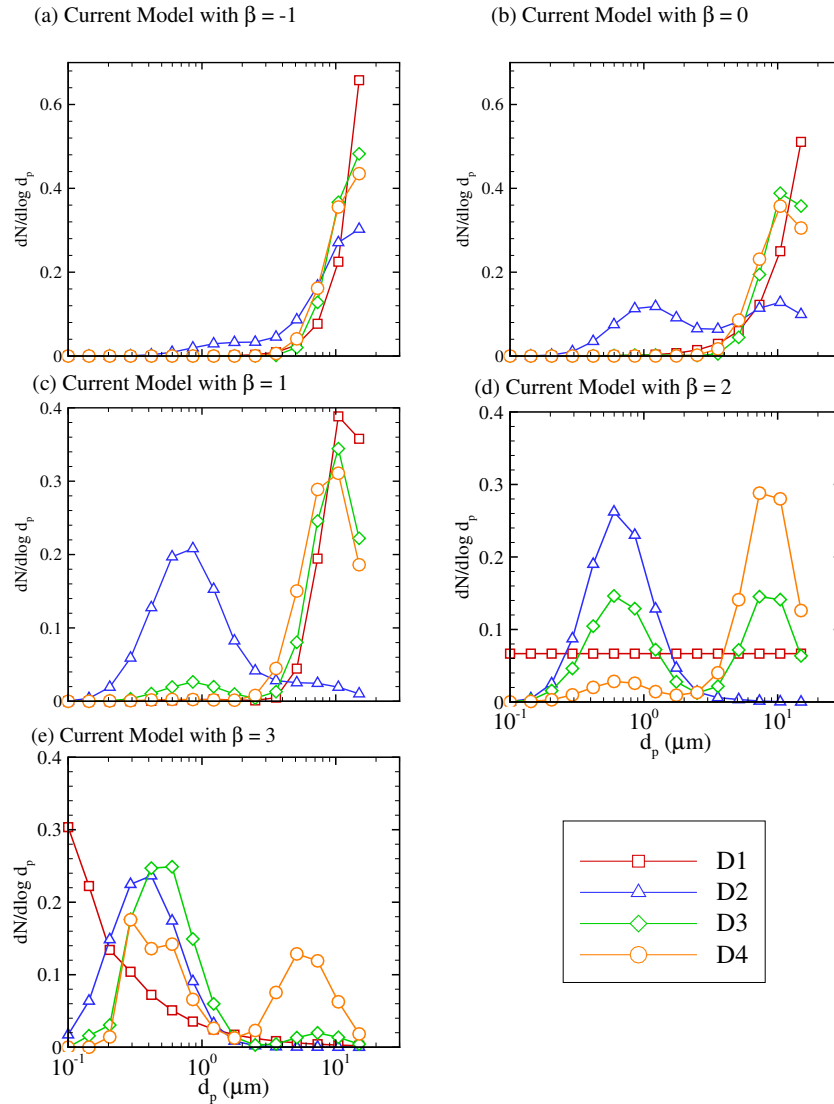


FIGURE 4.9: Size distributions in number of emitted dust at the surface ( $F_{emi}$ ) obtained from our model for various PSD of available dust at the surface (D1, D2, D3 and D4, see Fig. 4.3) and according to the inter-particle cohesive bond exponent  $\beta$  (from -1 to +3)

An enrichment of  $F_{wd}$  in particles with the lowest deposition velocity (Z2 bin) is observed with the fetch  $d$  when the emitted dust at the surface ( $F_{emi}$ ) is deprived in dust from the Z2 bin (Fig.4.10a; D3, D4 in Fig. 4.10b;  $\beta = 0, 1$  in Fig. 4.10c). This enrichment slightly extends to particles of the Z1 bin (Fig.4.11a; D3, D4 in Fig. 4.11b;  $\beta = 0, 1$  in Fig. 4.11c), and implies an impoverishment in particles from Z3 and Z4 bins. When  $F_{emi}$  is dominated by particles of the Z2 bin, no enrichment (impoverishment) is observed as  $F_{emi}$  is already dominated by particles the least likely to deposit (D2 in Figs. 4.10b, 4.11b and  $\beta = 3$  in Figs. 4.10c, 4.11c).

The resulting difference from this enrichment between  $F_{wd}$  and  $F_{emi}$  PSDs represents a few percent of the flux for fetch lengths around 100 m, but can rise to about 10% for fetch longer than 1 km (Fig. 4.11). These percentages are observed for fluxes expressed either in number or in mass. This modification of  $F_{wd}$  PSD with the fetch occurs mainly within the first few hundred meters from the upwind border of the source area, then it evolves slowly with the



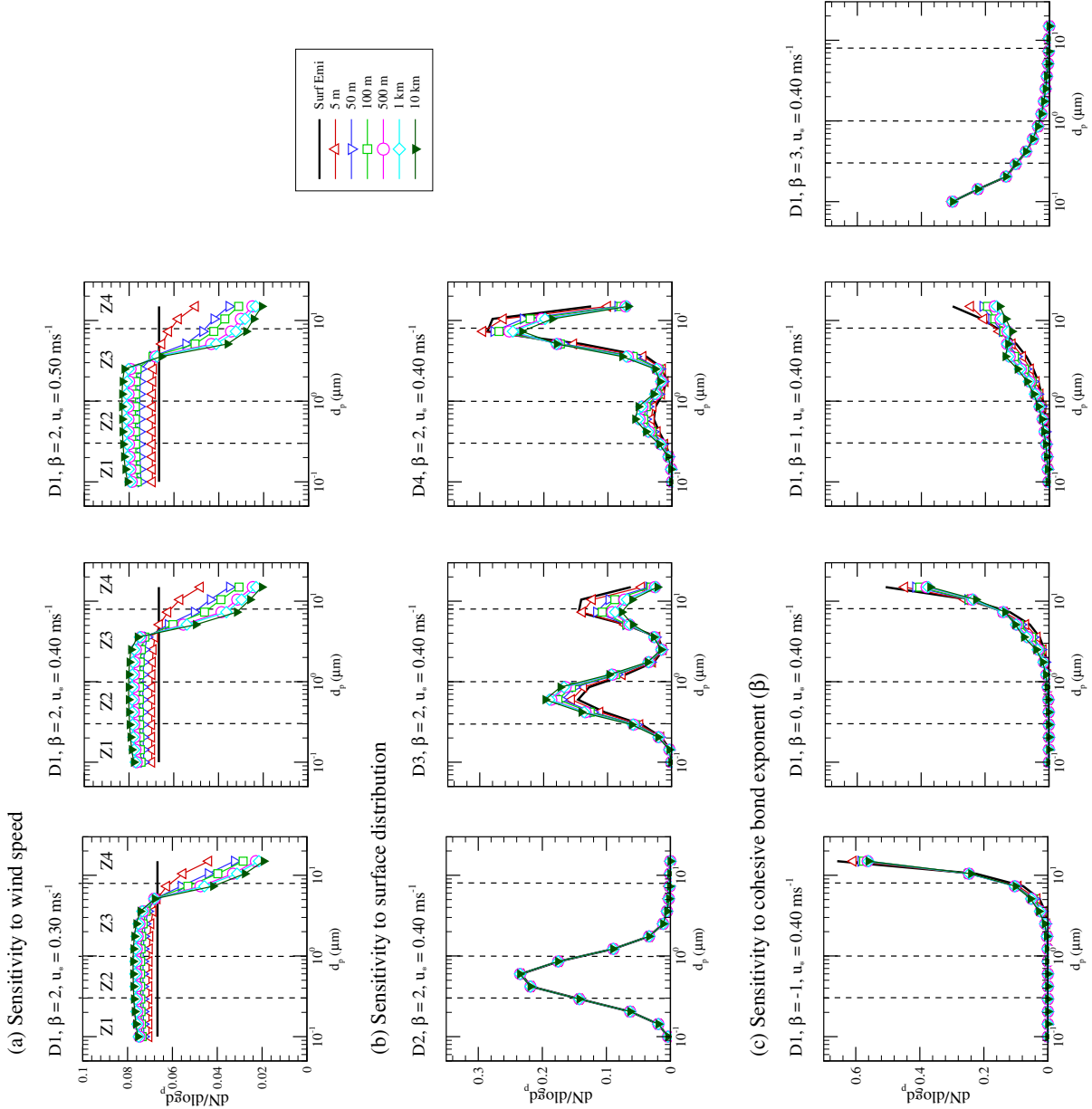


FIGURE 4.10: Variation with the fetch length of the size-distribution in number of the 3-m high  $F_{wd}$  according to (a) the wind intensity ( $u_* = 0.30, 0.40$  and  $0.50 \text{ ms}^{-1}$ ), (b) the surface dust-size distributions (D2, D3 and D4, see Fig. 4.3), and (c) the inter-particle cohesive bond exponents ( $\beta = -1, 0, 1$  and  $3$ ). The fetch ranges from 5 m to 10 km. The dust particle range is divided into 4 bins: Z1 ( $d_p \leq 0.3 \mu\text{m}$ ) - particles with dominant brownian deposition, Z2 ( $0.3 \mu\text{m} < d_p \leq 2 \mu\text{m}$ ) - particles the least likely to deposit, Z3 ( $2 \mu\text{m} < d_p \leq 8 \mu\text{m}$ ) - particles with the deposition velocity the most sensitive to wind intensity, and Z4 ( $d_p > 8 \mu\text{m}$ ) - particles the most likely to deposit.

fetch (Fig. 4.10a). This is visible, for example, in the simulation with the D1 surface PSD and  $u_* = 0.50 \text{ ms}^{-1}$  (Fig. 4.11a) where the fraction of  $F_{wd}$  from bins Z3 and Z4 decreases by nearly 5% within the first 200 m, followed by only a 2% decrease up to 10 km.

The enrichment of  $F_{wd}$  in particles of the Z2 bin is accentuated with the wind speed (Figs. 4.10a and 4.11a). For a D1 surface PSD and  $\beta = 2$ , the fraction of  $F_{wd}$  from bin Z2 increases by about 2% at a fetch around 100 m between  $u_* = 0.30$  and  $0.50 \text{ ms}^{-1}$ , and by about 5% at fetch longer

than 1 km (Fig. 4.11a). In a different way, for  $u_* = 0.50 \text{ ms}^{-1}$ ,  $F_{wd}$  from bin Z2 already reaches in number 39% of the total  $F_{wd}$  for a fetch of 100 m while a fetch of 10 km is needed to reach the same fraction for  $u_* = 0.30 \text{ ms}^{-1}$  (Fig. 4.11a). Furthermore, the particle size below which such enrichment occurs decreases from  $5 \mu\text{m}$  to  $3 \mu\text{m}$  (Fig. 4.10a) when  $u_*$  increases from 0.30 to  $0.50 \text{ ms}^{-1}$ , emphasizing the role of the wind speed in shaping  $F_{wd}$  PSD through its impact on the deposition velocity.

The strength of  $F_{wd}$  enrichment in small particles depends on the  $F_{emi}$  PSD. This latter one is shaped by the combination of the surface PSD and the inter-particle cohesive bond exponent ( $\beta$ ) (Fig. 4.9),  $\beta$  controlling the difference in PSD between the dust available at the surface and the dust emitted from the surface. Regardless of the surface PSD, a high positive value of  $\beta$  ( $\approx 3$ ) results in a strong emission of the smallest particles, and conversely a strong emission of the largest particles occurs for a small value of  $\beta$  ( $\approx -1$ ) (Figs. 4.10c and 4.11c). The enrichment of  $F_{wd}$  in dust of the Z2 bin is minimal for these extreme cases due to either the insignificant concentration of small particles ( $\beta \approx -1$ ) or the predominant concentration of particles of the Z1-Z2 bins ( $\beta \approx 3$ ) (Fig. 4.10c).

## 4.5 Discussion and conclusion

The particle size distribution (PSD) of the near-surface dust flux ( $F_{wd}$ ) was found to be mainly influenced by both the deposition process and the size distribution of the emitted dust ( $F_{emi}$ ).

The  $F_{emi}$  PSD appeared shaped from the mutual choice of the size distribution of available dust at the surface ( $p_d$ ) and the inter-particle cohesive bond exponent ( $\beta$ ) (Fig. 4.9). Different combinations of both quantities can lead to the same  $F_{emi}$  PSD. This explains why Shao [2001] and Alfaro *et al.* [2001] were able to reproduce from their schemes the  $F_{wd}$  PSD observed by Alfaro *et al.* [1997] while using different values of  $\beta$ , 2 and -0.018, respectively, and different surface dust size distributions (Fig. 4.3). Hence, the uncertainty of both quantities in existing dust emission schemes can be simply resolved by defining directly the  $F_{emi}$  PSD. Defining  $F_{emi}$  PSD becomes, however, all the more complex if  $p_d$  is wind speed dependent as suggested by Alfaro *et al.* [1997].

For constant wind and dust emission conditions, our simulations suggested a distinction between the PSDs of  $F_{emi}$  and  $F_{wd}$ . This PSD difference increases with the length of the fetch, i.e. the distance from the upwind border of the source area. A difference of a few percent in the flux fraction in number of small dust particles (0.3 to  $1 \mu\text{m}$ ) between  $F_{emi}$  and  $F_{wd}$  PSDs is observed for 100-m long fetch (Fig. 4.11). This difference can rise to 10% for fetch longer than 1 km. In mass, this difference affects rather larger particles ( $> 1 \mu\text{m}$ ). This modification of  $F_{emi}$  and  $F_{wd}$  PSDs is explained by the deposition process, as previously found by Dupont *et al.* [2015] from LES. The deposition of dust particles slowly increases with the fetch as the

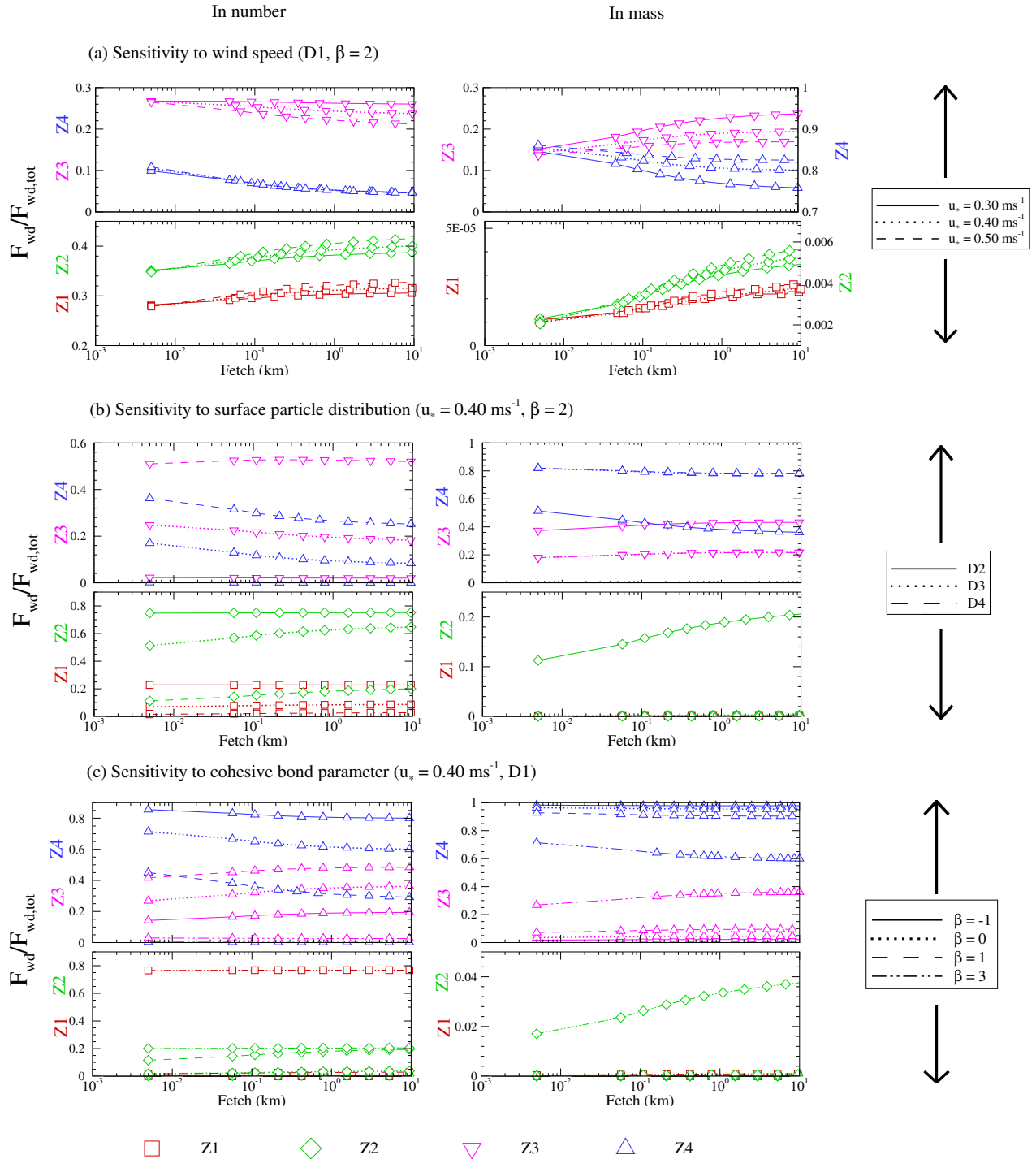


FIGURE 4.11: Variation with the fetch length of the fraction in number (left figures) and in mass (right figures) of the 3-m high  $F_{wd}$  on the total turbulent-diffusive dust flux  $F_{wd,tot}$  according to (a) the wind intensity ( $u_* = 0.30, 0.40$  and  $0.50 \text{ ms}^{-1}$ ), (b) the surface dust-size distributions (D2, D3 and D4, see Fig. 4.3), and (c) the inter-particle cohesive bond exponents ( $\beta = -1, 0, 1$  and  $3$ ).  $F_{wd}$  is divided into 4 bins: Z1 ( $d_p \leq 0.3 \mu\text{m}$ ) - particles with dominant brownian deposition, Z2 ( $0.3 \mu\text{m} < d_p \leq 2 \mu\text{m}$ ) - particles the least likely to deposit, Z3 ( $2 \mu\text{m} < d_p \leq 8 \mu\text{m}$ ) - particles with the deposition velocity the most sensitive to wind intensity, and Z4 ( $d_p > 8 \mu\text{m}$ ) - particles the most likely to deposit. The fractions at the smallest fetch lengths are equivalent to those of the surface emitted dust flux ( $F_{emi}$ ).

concentration of dust in the air is enhanced. This process is particle size dependent due to the dependence of the deposition velocity on the particle size (Fig. 4.2).

Theoretically, the dust deposition should increase with the fetch until an equilibrium is reached between deposition and emission (stationary state). Our simulations showed that this steady state occurs for fetch lengths larger than a few thousand kilometers for particles lower than  $5\ \mu\text{m}$  (section 4.3.2). This suggests a low probability of reaching a dust steady state during an erosion event. However, this result was obtained for an air clean of dust at the beginning of the simulation, i.e. a clean air upwind from the source area. For a background air already charged in dust particles passing through a source area, the deposition is expected to be larger and the equilibrium between deposition and emission should be reached for smaller fetch lengths. In that configuration of a background dust concentration, the magnitude of the difference in PSD between  $F_{emi}$  and  $F_{wd}$  should be larger than that observed from our simulations.

Emission and deposition appeared in our simulations as parallel inseparable processes, the impact of the deposition on the  $F_{wd}$  PSD being already visible (a few percent) for short fetch around 100 m (Fig. 4.11). These parallel emission and deposition processes may question the evaluation of existing dust emission schemes. As mentioned in the introduction, these schemes simulate the PSD of emitted dust at the surface ( $F_{emi}$ ) but have been usually evaluated against measurements performed well above the surface ( $F_{wd}$ ) where deposition should probably have started to sort particles. Since dust emission schemes do not account for deposition, it was assumed that the PSD of  $F_{emi}$  is identical to that of  $F_{wd}$ , and time-space independent for stationary wind conditions. Our results suggest that this evaluation procedure is not appropriate when comparing with field experiments, for which fetch lengths usually range from 100 m to several kilometers. However, the small fetch length of wind-tunnel experiments may ensure a PSD similarity between near-surface and surface emitted dust fluxes, as shown in our simulation of the wind-tunnel experiment of Alfaro *et al.* [1997] (section 4.3.4).

The wind intensity modifies the  $F_{wd}$  PSD by increasing the surface deposition, especially for large particles (Fig. 4.2), and thereby accelerating the attainment of equilibrium between emission and deposition. A rise of the friction velocity ( $u_*$ ) from  $0.30$  to  $0.50\ \text{ms}^{-1}$  leads to a 10% increase (decrease) of the dust flux fraction of small (large) particles for 1-km long fetch (Fig. 4.11a). Hence, an observed enrichment of  $F_{wd}$  in small particles with wind intensity could be explained by the enhancement of the deposition of larger particles for fetch lengths larger than 100 m, adding to the higher release of small dust through a stronger disintegration of aggregates as proposed by Alfaro *et al.* [1997].

The magnitude of the difference between  $F_{emi}$  and  $F_{wd}$  PSDs depends also on the difference in diameter between the particles the most emitted at the surface and the particles with the lowest deposition velocity (around  $0.7\text{-}2.0\ \mu\text{m}$  following Fig. 4.2). The farther the peak of  $F_{emi}$  PSD is from the minima of the deposition velocity, the greater is the difference in PSDs between  $F_{wd}$  and  $F_{emi}$  (Fig. 4.10b,c). Again, this is explained by the dependence of the deposition

velocity to the particle size. The near-surface dust flux enriches in particles with the lowest deposition velocity. For  $F_{emi}$  dominated by particles with the lowest deposition velocity, the PSDs between  $F_{emi}$  and  $F_{wd}$  remain similar regardless of the fetch (D2 in Fig. 4.10b,  $\beta=3$  in Fig. 4.10c). This similarity in PSD does not mean an equilibrium between the emission and deposition processes (steady state).

In conclusion, the role of the deposition process when evaluating existing dust emission schemes against field experiments should be considered, especially for large fetch lengths and/or with a large-scale background dust concentration. Improving our prediction of the PSD of  $F_{wd}$  requires not only a better understanding of the size distribution of  $F_{emi}$  but also a better understanding of the deposition velocity according to the particle size. This is all the more complex as both, emission and deposition processes, are difficult to disentangle in experiments.

## 5 Origins of turbulent transport dissimilarity between dust and momentum in semiarid regions

The new dust emission scheme developed in the previous chapter is incorporated here into the 3D erosion model, presented in Chapter 3, and evaluated over bare surfaces against the WIND-O-V's 2017 field experiment. Thereafter, this model is used to explore the second question defining this doctoral work - are dust and momentum transported similarly by turbulence near the surface?

This chapter has been submitted for publication as: Fernandes R., S. Dupont, and E. Lamaud, Origins of turbulent transport dissimilarity between dust and momentum in semiarid regions, *J. Geophys. Res. Atmos.*, 2019.

**Keywords:** Dust transport dissimilarity, Dust emission intermittency, Fetch, Large Eddy Simulations, Dust suspension model, Semiarid erosion

**Abstract:** *Turbulent transport of mineral dust away from erodible plots is usually assumed similar to the momentum transport. However, observations from the WIND-O-V (WIND erOsion in presence of sparse Vegetation's) 2017 field experiment over an isolated flat surface in Tunisia showed a dissimilar turbulent transport between dust and momentum. Here, the origin of this dissimilarity is explored from a numerical experiment using a detailed physically-based erosion model based on a Large-Eddy Simulation airflow model. Simulations support the findings of the WIND-O-V campaign, confirming the key role played by the dust emission intermittency to the transport dissimilarity with the momentum, this later one being more continuously absorbed at the surface. This dissimilarity diminishes with height as the intermittency of dust emission is progressively lost during the turbulent transport-mixing process. With wind intensity, the dissimilarity diminishes as well, dust emission becoming more spatially homogeneous, and thus less intermittent. Our simulations further highlight the additional role played by the fetch length limitation of the erodible plot to the turbulent transport dissimilarity. In presence of a short fetch, the dissimilarity between dust and momentum turbulent transports increases with height as the dust flux footprint integrates dust emission conditions from different surrounding surfaces. This latter process depends on the characteristics of the surrounded surfaces and is expected to be significant in semiarid regions.*

## 5.1 Introduction

Field campaigns have helped understand the dust cycle, focusing on both local scale – near-dust source – and global scale – the long-rang dust deposition [e.g., Washington *et al.* 2006b; Marsham *et al.* 2013; Shao *et al.* 2011; Lebel *et al.* 2010]. Still, large uncertainties remain on the quantification of the dust particles present in the atmosphere [IPCC 2014]. The mechanism of dust emission, including the dust turbulent transport and size-sorting within the first few meters above the surface, is still poorly understood, although dust is known to be primarily driven by sandblasting [e.g., Grini *et al.* 2002; Marticorena *et al.* 1995; Shao *et al.* 1993; Gomes *et al.* 1990].

Dust emission in semiarid regions is even more complex [Pierre *et al.* 2012] due to the presence of sparse short-lived vegetation cover [Ravi *et al.* 2010; Baas *et al.* 2007] and cultivated surfaces. Yet, a significant portion of atmospheric dust is sourced from semiarid regions, regions covering nearly 40% of the Earth's surface area [Edward 1997]. Estimating dust emission in such complex environment, characterized by a juxtaposition of surfaces with different levels of erodability, and thus short fetch lengths or isolated erodible surfaces, is challenging as existing near-surface dust flux measurement techniques have been developed for arid regions with an hypothesis of wild homogeneous erodible surfaces.

Recent findings from the WIND-O-V's 2017 field experiment [Dupont *et al.* 2019b] over an isolated erodible plot in Tunisia, with a 150 m long fetch, typical of semiarid regions, revealed a dissimilarity in the near-surface turbulent transport between momentum and dust, as opposed to traditional hypotheses [e.g., Gillette *et al.* 1972; Gillette *et al.* 1974; Nickling *et al.* 1993; Gomes *et al.* 2003; Sow *et al.* 2011; Shao *et al.* 2011]. This meant that momentum and dust were not always carried by the same eddies. It was suggested that this dissimilarity was driven by the intermittent nature of dust emission as opposed to the more continuous momentum absorption at the surface. The intermittency of dust emission is explained by the wind intensity threshold for initiating sandblasting. This dissimilarity seemed also to diminished with increasing wind speed but the moderate wind conditions of the experiment could not totally confirm this finding. Overall, these initial results question the role played by the dust emission intermittency, the wind intensity and the plot size (limited fetch), on the dissimilarity of the turbulent transport between momentum and dust.

This study aims at investigating the turbulent transport dissimilarity between momentum and dust in conditions similar to the WIND-O-V's field experiment using a numerical approach. To that purpose, the detailed physically-based soil erosion model developed by Dupont *et al.* [2015] will be used. The strength of this model is to represent explicitly the main erosion processes (saltation, sandblasting, dust suspension) within a Large-Eddy Simulation (LES) airflow model that simulates instantaneous wind and thus near-surface turbulent flow eddies and erosion intermittency. Compared to field experiments, this numerical approach will allow us to



investigate several erosive conditions in different constraining environments in order to disentangle the factors in play in the near-surface turbulent transport of momentum and dust. Prior to investigating the turbulent transport dissimilarity between dust and momentum, our LES erosion model is evaluated against the WIND-O-V's 2017 field experiment on its capacity to reproduce the wind dynamics and erosion main characteristics. Once evaluated, different erosion scenarios are simulated to gauge the sensitivity of the turbulent transport similarity between momentum and dust, to the plot size (fetch), wind intensity and dust emission intermittency.

## 5.2 Material and method

The 3D erosion model used here is described in Section 3.3.

### 5.2.1 Simulation details

Three-dimensional simulations of wind erosion were performed under neutral stratification over a flat bare surface, in conditions similar to the 7 and 9 March erosion events recorded during the WIND-O-V experiment. The computational domain extended over  $60 \times 45 \times 12$  m, corresponding to  $200 \times 150 \times 100$  grid points in the  $x$ ,  $y$  and  $z$  directions, respectively, where  $x$  represents the main wind direction. The domain was discretized with a 0.30 m grid spacing in the horizontal and a 0.01 m grid spacing at the surface in the vertical and stretched above. This fine resolution at the surface was chosen to simulate the main turbulent exchanges close to the surface where the concentration of dust particles is maximum.

To account for a fetch effect on the dust dispersal, representative of the isolated erodible plot of the WIND-O-V experiment, an air clean of dust was applied at the inlet of the domain and dust could simply exit at the outlet boundary, while periodic conditions were applied on the longitudinal boundaries. For the wind velocity and saltating particles, periodic conditions were applied on all horizontal boundaries in order to simulate a well-developed flow and steady-state saltation regimes.

The size-distribution of the saltating particles  $p_s(D)$  corresponded to a unimodal log-normal distribution with a mean diameter  $D = 100 \mu\text{m}$  and a geometric standard deviation of 1.2, in agreement with the granulometry of the soil of the WIND-O-V's experimental site (Fig. 5.1). The dust size distribution was divided in seven bins between  $0.45 \mu\text{m}$  and  $7.50 \mu\text{m}$ . The distribution of the dust particles available at the surface  $p_d(d_b)$  was derived from the size-distribution of the measured 3-m high dust flux during the 7 and 9 March events (Fig. 5.1). The dust size sorting between the surface and 3-m high dust fluxes was assumed negligible, the dust deposition being negligible for the 150 m long fetch of the experiment [Fernandes *et al.* 2019].

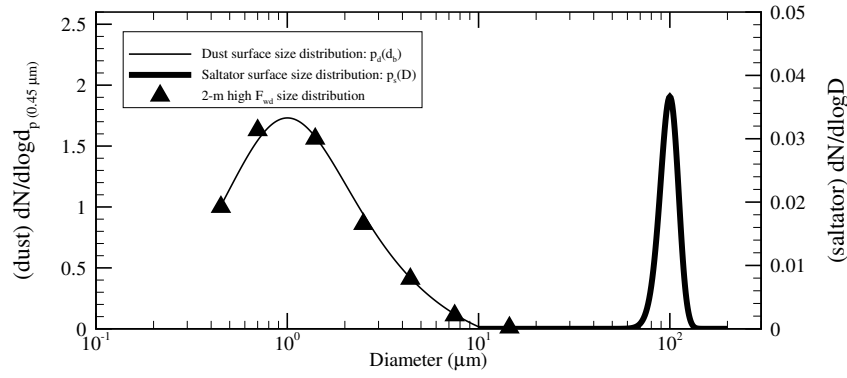


FIGURE 5.1: Particle size distributions of the saltating particles ( $p_s(D)$ ) and dust available at the surface ( $p_d(d_b)$ ) considered in the simulations. The size distribution of the 3-m high dust turbulent diffusive flux ( $F_{wd}$ ) obtained from simulation C1 (symbols) is compared to  $p_d(d_b)$ . The distribution  $p_s(D)$  was deduced from the soil granulometry of the WIND-O-V's site.

Following Dupont *et al.* [2013], a two-step procedure was employed to simulate wind erosion. First, the flow dynamics was simulated without erosion with an air free of dust until the flow equilibrates with the surface. Then, 10,000 initially resolved saltating particles were released randomly within 0.3 m from the surface, and the erosion modules were activated. Erosion events were then simulated for 10 minutes with a time step of  $\Delta t = 400 \mu s$ .

Our simulations differ in several points from the WIND-O-V experiment. First, our fetch is limited to  $x_{fetch} = 60$  m instead of 150 m and concerns only dust dispersal and not the wind dynamics and the saltation. These simplifications were chosen for computational reasons. The absence of fetch for the wind dynamics and saltation is a reasonable assumption compared to the WIND-O-V experiment as (1) a constant momentum flux layer was well verified up to 4 m high during the March events, and (2) saltation adjusts rapidly to a new surface, saltating particles remaining close to the surface. The shorter fetch in our simulations for the dust dispersal allowed us to reduce the domain size while keeping fine resolution. To keep the similitude with the field experiment, the simulated dust flux will be analysed closer to the surface in order to respect the equivalent height to fetch ratio  $z/x_{fetch} = 0.02$  of the experiment. Second, the air clean of dust reaching the erodible surface in the simulation is certainly too extreme compared to the field experiment. Indeed, the surrounded surfaces were much less erodible but were still a source of dust. Additionally, the background air was also loaded with dust emitted far away. This long-range transported dust should not contribute to the emitted dust flux. Third, the main wind characteristics such as the friction velocity remained constant along the simulations as opposed to the experiment where the wind intensity varies more or less with time depending on the mesoscale weather fronts. As a consequence, one simulation represents only a small period of an erosion event where the mean wind intensity remains stable.

Seven simulations of 10 min wind erosion were performed. The first five simulations, noted C1 to C5, were characterized by different wind intensities, the saltation friction velocity  $u_{*0}$  at

the surface normalized by the threshold friction velocity  $u_{*t}$  ( $= 0.22 \text{ ms}^{-1}$ ) ranging from 1.6 to 2.5 (see Table 7.1). These wind intensities correspond to different periods encountered during the 7 and 9 March erosion events. In C6, periodic conditions were applied on the dust field as for the wind and saltation fields in order to simulate an erosion event over a long erodible surface without fetch effect. Other characteristics of C6 were similar to C1. Finally, C7 was similar to C1 but the dust emission was imposed continuous at the surface, independently of the saltation, in order to verify the impact of the dust emission intermittency on the dust transport dissimilarity with momentum.

Simulation	$u_{*0}/u_{*t}$	Dust lateral boundary condition	Fetch (m)	Dust emission
C1	1.6	Non-periodic	60	Sandblasting (Eq 3.15)
C2	1.7	Non-periodic	60	Sandblasting (Eq 3.15)
C3	1.9	Non-periodic	60	Sandblasting (Eq 3.15)
C4	2.1	Non-periodic	60	Sandblasting (Eq 3.15)
C5	2.5	Non-periodic	60	Sandblasting (Eq 3.15)
C6	1.6	Periodic	$\rightarrow \infty$	Sandblasting (Eq 3.15)
C7	1.6	Non-periodic	60	Continuous

TABLE 5.1: Main characteristics of the seven simulations: ratios between the surface friction velocity ( $u_{*0}$ ) and the threshold friction velocity ( $u_{*t} = 0.22 \text{ ms}^{-1}$ ), dust lateral boundary condition, fetch length of the erodible plot at the end of the computational domain, and parametrization of the dust emission. Simulations C1 to C5 are comparable to the WIND-O-V field experiment with various wind conditions.

## 5.2.2 Data analysis

Wind dynamic and saltation quantities have been horizontally averaged over the entire domain since periodic conditions were considered for wind and saltation. For dust, horizontal averages were also performed over the entire domain for the C6 simulation where periodic conditions were considered for dust, while in C1-C5 and C7 simulations, the horizontal averages were limited to the last 20 m of the computational domain (between 40 and 60 m), corresponding to a mean 50 m long fetch ( $x_{fetch}$ ).

The dissimilarity in turbulent transport between momentum and dust was estimated from the partitioning of the near-surface momentum and dust fluxes according to the type of turbulent eddies responsible for these fluxes. This partitioning corresponded to a quadrant decomposition of the fluxes [Wallace 2016] as performed in Dupont *et al.* [2019b]. It consisted at dividing the turbulent flux  $\langle \alpha' \beta' \rangle$  into four quadrants based on the sign of the fluctuations of  $\alpha'$  and  $\beta'$  at any given instant around the mean quantities  $\langle \alpha \rangle$  and  $\langle \beta \rangle$ , respectively. The flux  $\langle \alpha' \beta' \rangle$  was decomposed as  $\langle \alpha' \beta' \rangle = \sum_{Qi} \langle \alpha' \beta' \rangle_{Qi}$ , where  $\langle \alpha' \beta' \rangle_{Qi}$  is the flux magnitude in quadrant  $Qi$ . Similarly, the number of events responsible for this flux was estimated as  $n^{\alpha\beta} = \sum_{Qi} n_{Qi}^{\alpha\beta}$ , where  $n_{Qi}^{\alpha\beta}$  is the number of events contributing the the flux in quadrant  $Qi$ . From this, the percentage

contribution of quadrant  $Q_i$  to the magnitude of flux was calculated as:

$$F_{Q_i}^{\alpha\beta} = \frac{\langle \alpha' \beta' \rangle_{Q_i}}{\sum_{Q_i} \langle \alpha' \beta' \rangle_{Q_i}} \times 100, \quad (5.1)$$

and that to the number of events as:

$$N_{Q_i}^{\alpha\beta} = \frac{n_{Q_i}^{\alpha\beta}}{\sum_{Q_i} n_{Q_i}^{\alpha\beta}} \times 100. \quad (5.2)$$

Here, the quadrants were defined: (1) for the momentum flux as Q1 ( $u' - w' +$ ), Q2 ( $u' + w' +$ ), Q3 ( $u' + w' -$ ) and Q4 ( $u' - w' -$ ), with Q1 and Q3 referring to the upward transfer of slow momentum fluid and the downward transfer of fast momentum fluid respectively; and (2) for the dust flux as Q1 ( $w' + d' +$ ), Q2 ( $w' + d' -$ ), Q3 ( $w' - d' -$ ) and Q4 ( $w' - d' +$ ), with Q1 and Q3 referring to the upward transfer of dust-rich air and the downward transfer of dust-impooverished clean air respectively.

### 5.3 Model evaluation

The model is first evaluated on its ability to simulate both the wind dynamics during erosive events and the average and instantaneous characteristics of saltation and dust dispersal, using data from the WIND-O-V experiment and the literature.

#### 5.3.1 Wind dynamics

The mean vertical profiles of the wind velocity ( $u$ ), local friction velocity ( $u_* = \sqrt[4]{\langle u'w' \rangle^2 + \langle v'w' \rangle^2}$ ), and standard deviations of the three velocity components ( $\sigma_u, \sigma_v, \sigma_w$ ), obtained from simulation C1 are compared with the corresponding profiles from the WIND-O-V's experiment, for a similar surface friction velocity  $u_{*0}$  (Fig. 5.2). Overall, the model reproduces well the expected logarithmic velocity profile (Fig. 5.2a) and the constant momentum flux layer (Fig. 5.2b). The slight overestimation of  $u$  could be explained by the strict neutral stratification in our simulation as opposed to the slightly unstable stratification during the experiment [see Dupont *et al.* 2018]. As expected, within the saltation layer,  $u_*$  exhibits an exponential decrease with depth as saltating particles absorbed momentum from the flow. Both  $\sigma_u$  and  $\sigma_w$  fit also well the experimental values, only  $\sigma_v$  appears underestimated (Fig. 5.2c). This last discrepancy could be related to (1) the perfectly constant mean wind direction in our simulation as opposed to small mesoscale variations during the field experiment, and/or (2) to the lateral constrain on the large-scale turbulent structures imposed by the limited lateral size of our computational domain.

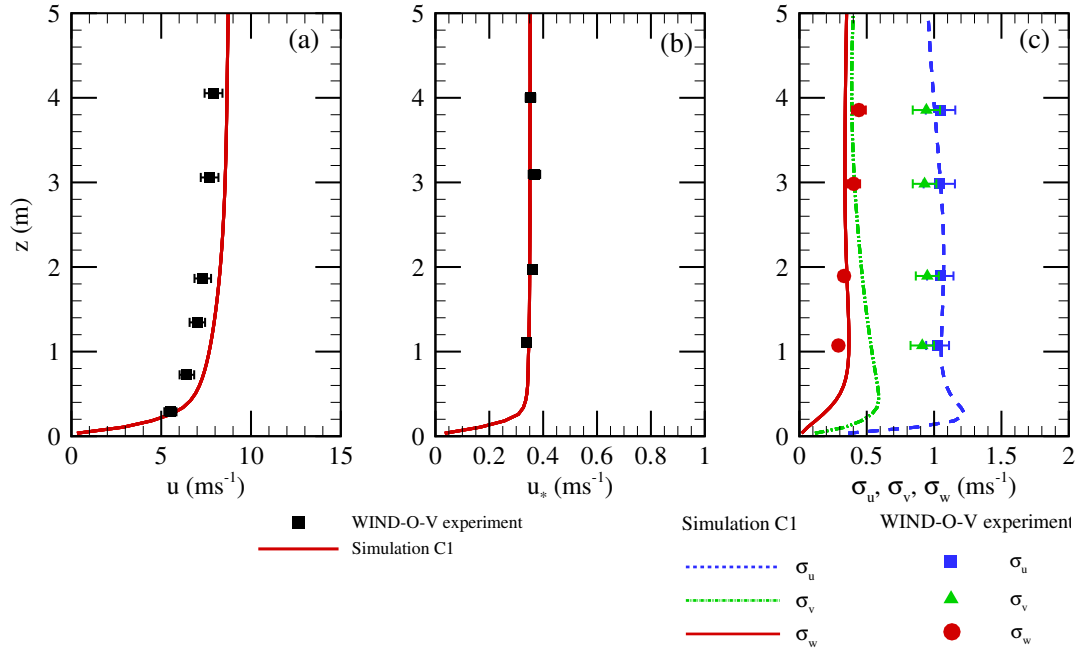


FIGURE 5.2: Comparison between the C1 simulation (lines) and the field measurements (symbols) on the mean vertical profiles of (a) the longitudinal wind velocity ( $u$ ), (b) the local friction velocity ( $u_*$ ), and (c) the standard deviations of the three velocity components ( $\sigma_u, \sigma_v, \sigma_w$ ). The error bars refer to the standard deviations of the experimental values for periods with similar wind intensity.

The partition of the momentum flux  $F_{uw}$  in quadrants is evaluated in Fig. 5.3a for the simulation C1. Fig. 5.3a presents the time variation of the quadrant contributions to the momentum flux, in magnitude ( $F_{Qi}^{uw}$ ) and in number of events ( $N_{Qi}^{uw}$ ), at four heights (0.4, 1.5, 2.0 and 4.0 m) and spatially averaged from  $x = 40$  to 60 m, corresponding to  $z/x_{fetch} = 0.01, 0.03, 0.04$  and 0.08, respectively. On the same figure, the quadrant contributions obtained at 3 m height during the field experiment ( $z/x_{fetch} = 0.02$ ) are compared. Like the experiment, the momentum flux is primarily driven by ejection (Q1) and sweep (Q3) motions with a domination of ejections in the magnitude of the flux and sweeps in the number of events. The quadrant partitioning of the momentum flux weakly changes with height. Close to the surface (0.4 m), ejections dominate both the flux magnitude and the number of events. Overall, the contributions across all heights of the ejection and sweep motions to  $F_{uw}$  average around 41% and 36% (32% and 32%) in magnitude (in number), which is consistent with the measurements, 41% and 36% (32% and 32%), respectively.

In conclusion, the mean wind flow and turbulence appear both well reproduced by the model. In particular, the simulated turbulent structures transport similarly the momentum as during the field experiment.

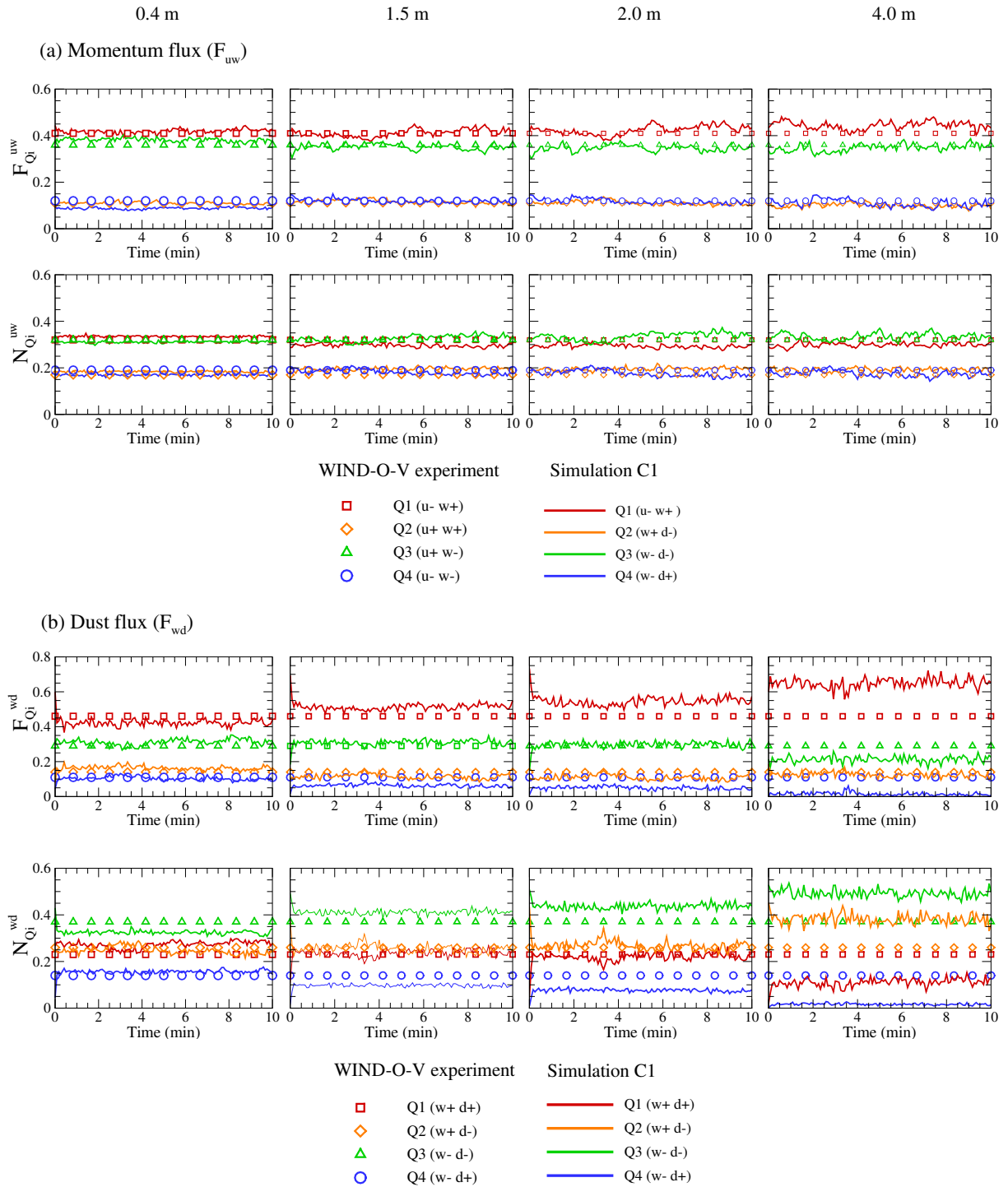


FIGURE 5.3: Time variation of the quadrant partitioning of the momentum flux  $F_{uw}$  (a) and dust flux  $F_{wd}$ , in magnitude ( $F_{Q_i}$ ) and in event number ( $N_{Q_i}$ ), as defined in equations 5.1 and 5.2, obtained from the 10-min simulated erosion event C1 at four heights (0.4, 1.5, 2.0 and 4.0 m) and compared with the mean fractions obtained at 3 m height from the WIND-O-V field experiment. The dust flux includes all particle sizes. Note that measurement data are averaged values with no time variation.

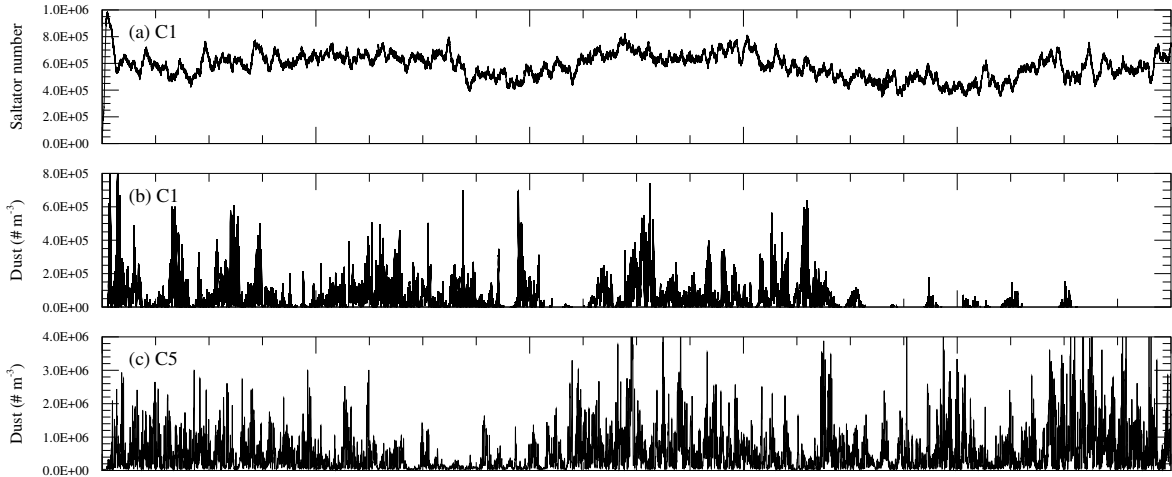


FIGURE 5.4: (a) Time variation of the total number of numerically resolved saltators within the computational domain during the 10-min simulated erosion event C1. (b-d) Time variation of the dust number concentration (including all particle sizes) at 1.0 m height and  $x_{fetch} = 50$  m during the 10-min simulated erosion events C1 and C5, respectively.

### 5.3.2 Saltation dynamics

In the simulation, saltation reaches an equilibrium state with the wind within the first minute of the erosion event. This is visible from the time variation of the total number of numerically resolved saltating particles (Fig. 5.4a). This result was observed in all simulations and is consistent with the simulation of Dupont *et al.* [2013]. The increase of the saltation flux  $F_{salt,tot}$  with  $u_{*0}$  is well reproduced by the model (Fig. 5.5a), with a behavior in agreement with existing parameterizations [Bagnold 1937; Kamawura 1951; Owen 1964]. However,  $F_{salt,tot}$  is about one order of magnitude larger than the flux obtained from the WIND-O-V experiment. These lower values of the WIND-O-V saltation fluxes compared to usual values reported in the literature are still under investigation. Here, we chose to not modify our saltation model to better fit the WIND-O-V values. This possible discrepancy is not expected to impact the comparison of the turbulent transport between momentum and dust.

The enhancement of the saltation flux with  $u_{*0}$  modifies the roughness length perceived by the flow, adding roughness induced by saltating particles. The variation of the simulated saltation roughness lengths ( $z_{0s}$ ) with  $u_{*0}$  is in agreement with the roughness values deduced from the WIND-O-V's experiment and within the range of values available in the literature [Owen 1964; Rasmussen *et al.* 1985] (Fig. 5.5b). This last result comforts us on the ability of our model to simulate the impact of the saltating particles on the flow and on the proper amplitude of the simulated saltation flux.

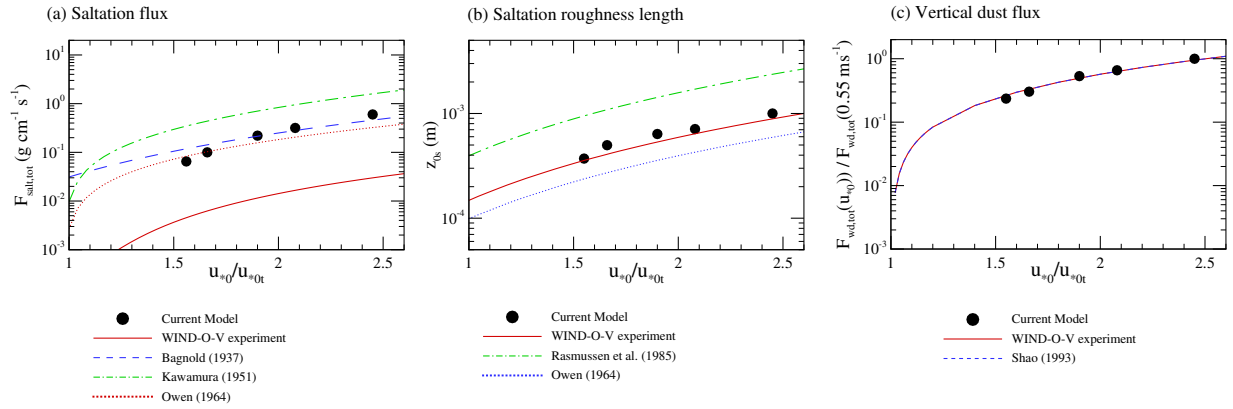


FIGURE 5.5: Comparison between simulated (dots), WIND-O-V field measurements (solid line) and semi-empirical parametrizations (broken lines) of (a) the saltation flux ( $F_{salt,tot}$ ), (b) the saltation roughness length ( $z_{0s}$ ), and (c) the turbulent diffusive dust flux including all particle sizes ( $F_{wd,tot}$ ) at  $z/x_{fetch} \sim 0.02$ , against the saltation friction velocity  $u_{*0}$  normalized by its threshold value  $u_{*t}$ . In (a) the simulated  $F_{salt,tot}$  is compared with the parametrizations of Bagnold [1937]:  $F_{salt,tot} = 1.5 \left( D/D_{ref} \right)^{1/2} \rho_a / g u_{*0}^3$  with  $D_{ref} = 250 \mu\text{m}$ ; Kamawura [1951]:  $F_{salt,tot} = 2.61 \rho_a / g (1 - u_{*t}/u_{*0}) (1 + u_{*t}/u_{*0})^2$ ; and Owen [1964]:  $F_{salt,tot} = (0.25 + 0.33v_{sed}/u_{*0}) \rho_a / g u_{*0}^3 (1 - u_{*t}^2/u_{*0}^2)$ , with  $D$  the saltating particle diameter,  $\rho_a$  the air density,  $g$  the gravitational acceleration and  $v_{sed}$  the settling velocity. In (b) the simulated  $z_{0s}$  is compared with the parametrizations of Rasmussen *et al.* [1985] and Owen [1964]:  $z_{0s} = C_c u_{*0}^2 / g$  with  $C_c = 0.08$  and  $0.02$ , respectively. In (c),  $F_{wd,tot}$  is compared with Shao *et al.* [1993]:  $F_{wd,tot} = C \rho_a (u_{*0}^2 - u_{*t}^2)$ , with  $C = 4$ . The dust fluxes have been normalized by their values at  $u_{*0}/u_{*t} = 2.5$ .

### 5.3.3 Dust dynamics

The wind erosion of our isolated erodible plot leads to the development of a dust internal boundary layer in simulations C1-C5 (Fig. 5.6a), comparable to the momentum internal boundary layer developing at a surface roughness transition [Kaimal *et al.* 1994]. The variation of the time-averaged depth  $z_d$  of this dust internal boundary layer with the fetch  $x_{fetch}$  is also presented in Fig. 5.6a according to the wind intensity ( $u_{*0}$ ). Here,  $z_d$  was estimated as the distance from the surface above which the dust concentration in number, including all particle sizes, represents less than 0.1% of the surface concentration. The depth of the internal boundary layer is enhanced with  $u_{*0}$ , reaching 6.0 m at  $x_{fetch} = 60$  m for  $u_{*0} = 0.54 \text{ ms}^{-1}$  (C5) against 4.5 m for  $u_{*0} = 0.34 \text{ ms}^{-1}$  (C1). This behavior with  $u_{*0}$  is explained by the stronger turbulence of the flow, enhancing the vertical turbulent diffusion of dust. The depth of the internal boundary layer is also particle-size dependent, decreasing with particle size as small particles are easier diffused in the above atmosphere (result not shown).

Within the dust internal boundary layer, the constant dust flux layer close to the surface develops slowly, reaching only 0.4 m height at  $x_{fetch} = 50$  m in simulation C1 (Fig. 5.6b). This value corresponds to the height above which the spatially average number dust flux  $F_{wd}$  represents less than 90% of the emission dust flux at the surface  $F_{emi,tot}$ , including all particle sizes (Fig. 5.6b). With increasing  $u_{*0}$ , the constant dust flux layer is better developed but still it only



reaches 0.6 m for  $u_{*0} = 0.54 \text{ ms}^{-1}$  (C5). Above this height, the ratio  $F_{wd}/F_{emi,tot}$  decreases exponentially with height. Like the dust internal boundary layer, the depth of the constant dust flux layer is particle size dependent, its depth being inversely proportional to the particle size (result not shown). Without fetch (simulation C6), the decrease of  $F_{wd}/F_{emi,tot}$  with height is less drastic, and the constant dust flux layer reaches 1.2 m height after 10 min of erosion. The absence of a larger constant flux layer in C6 is explained by the continuous enhancement of the dust concentration in the domain with time.

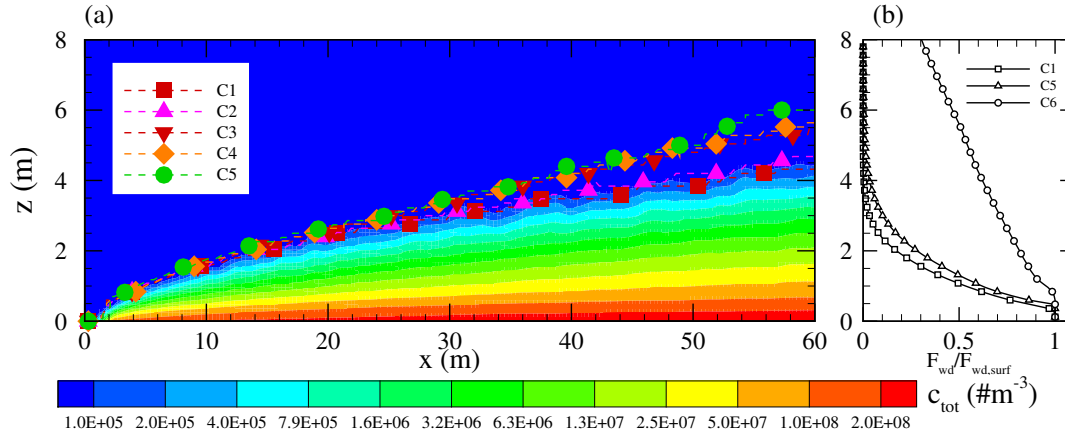


FIGURE 5.6: (a) Time-averaged dust number concentration field  $c_{tot}$  (including all particle sizes) as obtained from simulation C1. The depth of the dust boundary layer developing from the upwind edge of the erodible plot ( $x = 0 \text{ m}$ ) is also shown for simulations C1 to C5. This depth ( $z_d$ ) was defined as the distance above the surface from which the dust concentration reduces by 99.9% of the surface dust concentration. (b) Variation with height of the turbulent diffusive dust flux ( $F_{wd}$ ), including all particle sizes, normalized by the dust flux at the surface ( $F_{wd,surf}$ ) for simulations C1, C5 and C6, respectively.

The time series of the dust number concentration simulated near the surface,  $z/x_{fetch} = 0.02$  (simulation C1), shows a highly intermittent behaviour of the dust concentration (Fig. 5.4b). This intermittency is characterized by a kurtosis of 17, which is equivalent to the value observed during the WIND-O-V's experiment for the dust concentration of particles below  $4.0 \mu\text{m}$ . At the same location, the ratio between the dust concentration standard deviation and the mean dust concentration is also comparable with the experimental values: 1.3 against 1.4, respectively. Particle sizes above  $4.0 \mu\text{m}$  were not considered in our statistics due to the instrumentation limitation at measuring accurately the concentration of large particles.

The average dust flux including all particle sizes ( $F_{wd,tot}$ ) simulated at  $z/x_{fetch} = 0.02$  exhibits a similar trend with  $u_{*0}$  as the measured dust flux and as the dust flux parameterization of Shao *et al.* [1993] (Fig. 5.5c). The size-distribution of the dust flux is also comparable with that of the WIND-O-V's experiment (Fig. 5.1). This last result confirms the negligible impact of the dust deposition on the size-sorting of the dust flux between the surface and  $z/x_{fetch} = 0.02$ , given that the size-distribution of the available dust at the surface was taken equal to the size distribution of the measured dust flux.

The quadrant partitioning of the dust flux  $F_{wd}$  is evaluated for simulation C1 in Fig. 5.3b, similarly as in Fig. 5.3a for the momentum flux  $F_{uw}$  (section 5.3.1). Like momentum, the dust flux is dominated in magnitude by quadrants Q1 and Q3. At 1.5 m above the surface ( $z/x_{fetch} = 0.03$ ), the partitioning of  $F_{wd}$  is close to that observed during the WIND-O-V experiment for  $z/x_{fetch} = 0.02$ . Simulations show also that this partitioning evolves with height. Away from the surface and closer to the upper edge of the dust internal boundary layer (4.0 m height), the dust flux partitioning exhibits an increasing contribution of Q1 and Q3 to the flux, in magnitude and in number, respectively. Compared to the quadrant partitioning of  $F_{uw}$ , the near-surface Q1 contribution to  $F_{wd}$  in number of events ( $w^+d^+$ ) is lower than the equivalent Q1 contribution to  $F_{uw}$  ( $w^+u^-$ ), while Q2 and Q3 contributions are higher. This difference in partitioning between dust and momentum fluxes is consistent with the experimental observations [Dupont *et al.* 2019b], confirming the dissimilarity in turbulent transport between momentum and dust.

### 5.3.4 Instantaneous behavior

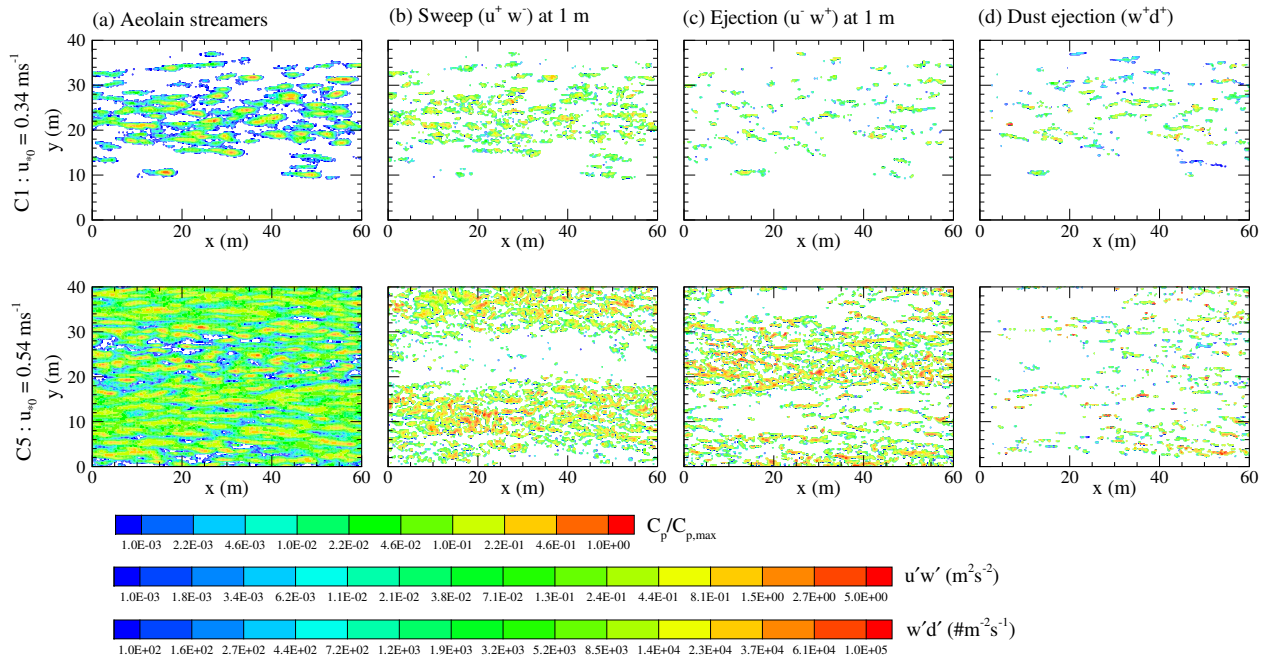


FIGURE 5.7: Snapshots of horizontal cross section ( $x - y$ ) of the (a) vertically integrated sand concentration ( $C_p$ ) normalized by its maximum value ( $C_{p,max}$ ), (b) 1-m high sweep motions ( $-u^+w^-$ ), (c) 1-m high ejection motions ( $-u^-w^+$ ), and (d) dust ejections ( $w^+d^+$ ) at the surface, for simulations C1 (top figures) and C5 (bottom figures), at the 7th minute of the erosion event. White areas represent regions with low intensity of the corresponding quantity.

We find it interesting to look at the instantaneous behaviour of the saltating and dust particles in relation to the wind dynamics. Hence, Figure 5.7 presents in horizontal sections  $x - y$ , the instantaneous spatial distributions of (a) the vertically integrated concentration of saltating particles, (b-c) the 1-m high momentum sweep and ejection motions, and (d) the surface dust

ejection motions, for simulations C1 and C5. The presence of aeolian streamers in our simulations is clearly visible, corresponding to elongated regions of high saltating particle concentration, surrounded by regions without saltation (Fig. 5.7a). In high wind conditions (C5), saltation becomes more spatially homogeneous with aeolian streamers embedded in large-scale saltation clouds. This result is consistent with previous simulations of Dupont *et al.* [2013]. Aeolian streamers appear well correlated with the near-surface momentum sweep motions (Fig. 5.7b), and much less with momentum ejection motions (Fig. 5.7c). An ensemble averaged view of the saltation flux during the passage of a near-surface momentum sweep motion ( $w^-u^+$ ) confirms this link between the downward transfer of high velocity fluid to the surface and saltation (Fig. 5.8a). A small spatial lag between the sweep and the peak in saltation is visible corresponding roughly to a time lag of about  $-0.5$  s. With increasing  $u_{*0}$ , the fluctuation of the saltation flux during the passage of the sweep motion is less significant. This may result from the more spatially homogeneous saltation field with increasing wind intensity (Fig. 5.7a). Conversely, the passage of a local ejection of low velocity fluid ( $w^+u^-$ ) precedes a peak in saltation and is followed by a minimum in saltation (Fig. 5.8b). The high concentration of sand particles at the saltation peak may reduce the longitudinal wind velocity  $u$ , favoring ejection.

Dust emission correlates well with the passage of aeolian streamers (Fig. 5.7d). Interestingly, not every passing streamers emit dust as dust emission depends on the balance between the energy provided by sandblasting and the energy required to release dust. The ensemble average two-dimensional  $x - z$  dust concentration field associated to the near-surface ejection motions confirms the importance of ejection motions in transporting dust particles upward, contributing to the dust emission-transfer toward the above atmosphere (Fig. 5.8b). This emission of dust follows the peak of saltation with a small lag that may correspond to the delay for released dust at the surface by sandblasting to be transported away from it through an ejection. With increasing wind speed, the dust plume appears more spatially correlated with the momentum ejection ( $w^+u^-$ ), indicating a better similarity between momentum and dust turbulent transports (Fig. 5.8b).

## 5.4 Sensitivity of the dust - momentum turbulent transport dissimilarity

In this section, the dissimilarity between momentum and dust turbulent transports is investigated numerically according to the wind intensity, the fetch length and the dust emission intermittency.

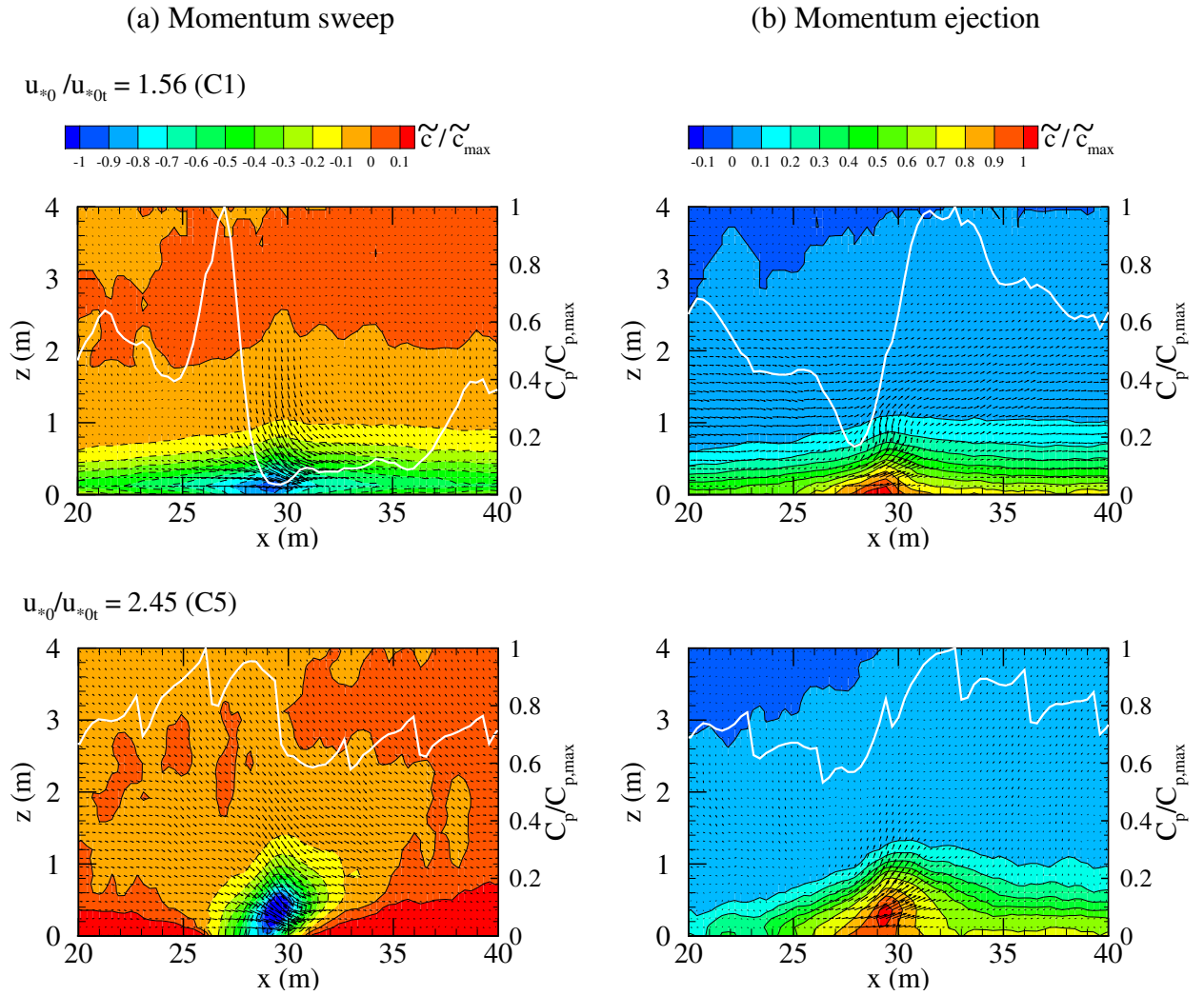


FIGURE 5.8: Ensemble-average dust concentration fluctuations  $\tilde{c}$  (background color), vertically integrated sand concentration  $C_p$  (white line), and wind vectors, associated with (a) sweep ( $u^+w^-$ ) and (b) ejection ( $u^-w^+$ ) motions at  $x = 30$  m and  $z = 0.4$  m, as obtained from simulations C1 (top) and C5 (bottom). Dust and sand concentrations have been normalized by their maximum values,  $\tilde{c}_{max}$  and  $C_{p,max}$ , respectively.

### 5.4.1 Influence of the wind intensity

Fig. 5.9 presents the variation with  $u_{*0}$  of the quadrant partitioning of the momentum  $F_{uw}$  and dust  $F_{wd}$  fluxes. As expected, the partitioning of  $F_{uw}$  is independent of  $u_{*0}$  (Fig. 5.9a), with a quadrant distribution similar to that obtained from the field experiment. On the other hand, the partitioning of  $F_{wd}$  changes with  $u_{*0}$ . At  $z = 0.4$  and  $1.5$  m, the Q2 ( $w^+d^-$ ) contribution to the dust flux magnitude decreases of about 10% with  $u_{*0}$ , in detriment of the Q3 ( $w^-d^-$ ) contribution. The contribution from the other quadrants remains relatively stable with  $u_{*0}$ . In number of events, the Q1 ( $w^+d^+$ ) contribution increases of about +10% in detriment of Q2, other quadrants remaining stable. Hence, upward motions of dusty air become more frequent and the magnitude of the upward motions of clean air is lower with increasing  $u_{*0}$ . Overall, the partitioning of  $F_{wd}$  becomes progressively closer to the partitioning of  $F_{uw}$ . In the upper

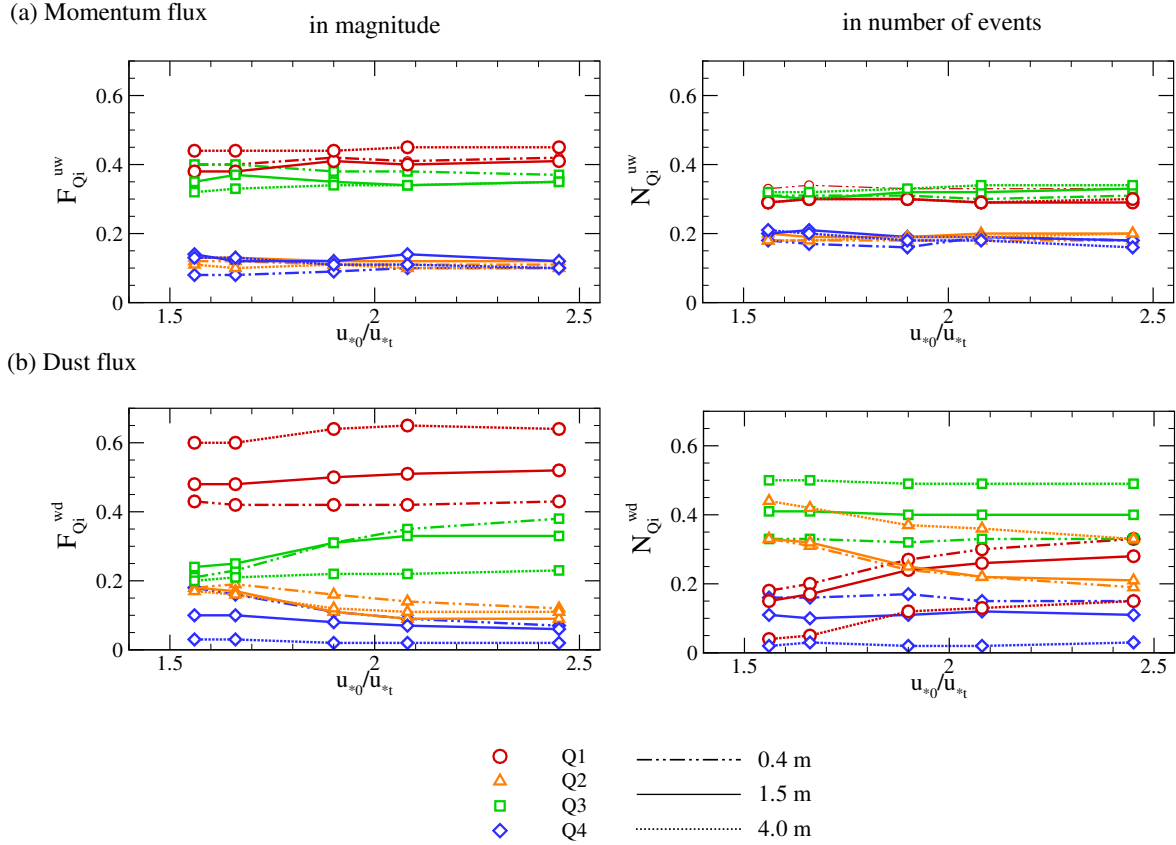


FIGURE 5.9: Variation with the normalized friction velocity  $u_{*0}$  of the quadrant partitioning in magnitude ( $F_{Qi}$ ) and in event number ( $N_{Qi}$ ) of the momentum flux  $F_{uw}$  (a) and dust flux  $F_{wd}$  including all particle size (b), at 3 heights (0.4, 1.5 and 4.0 m), obtained from simulations C1 to C5.

portion of the dust internal boundary layer ( $z = 4.0$  m), the same trend of the  $F_{wd}$  quadrant partitioning with  $u_{*0}$  is observed but in a lesser extent. At this height, the quadrant partitioning of  $F_{wd}$  still remains different from that of  $F_{uw}$  for the highest  $u_{*0}$ .

#### 5.4.2 Influence of the fetch length

Fig. 5.10 presents the time variation of the  $F_{wd}$  quadrant partitioning for the simulation C6 without fetch. The partitioning of  $F_{wd}$  appears similar to that of  $F_{uw}$  for  $z > 2$  m, while closer to the surface it differs with proportions close to those observed in simulation C1 (Fig. 5.3b). For example, at  $z = 0.4$  m, the Q3 contribution to the magnitude of  $F_{wd}$  is much lower ( $-20\%$ ) than that to  $F_{uw}$ , while the Q2 and Q4 contributions are higher,  $+10\%$  each. In number of events, Q1 and Q3 contribute less to  $F_{wd}$  than to  $F_{uw}$  while Q2 contributes more. This means that many ejection motions ( $w^+u^-$ ) carried low dust concentration ( $d^-$ ) close to the surface.

Note that during the first minute of the erosion event of simulation C6, the partitioning of  $F_{wd}$  at  $z = 2$  m is close to that observed during the field experiment (Fig. 5.3b). Indeed, the beginning of the event is equivalent to a short fetch, the fetch length increasing with time.

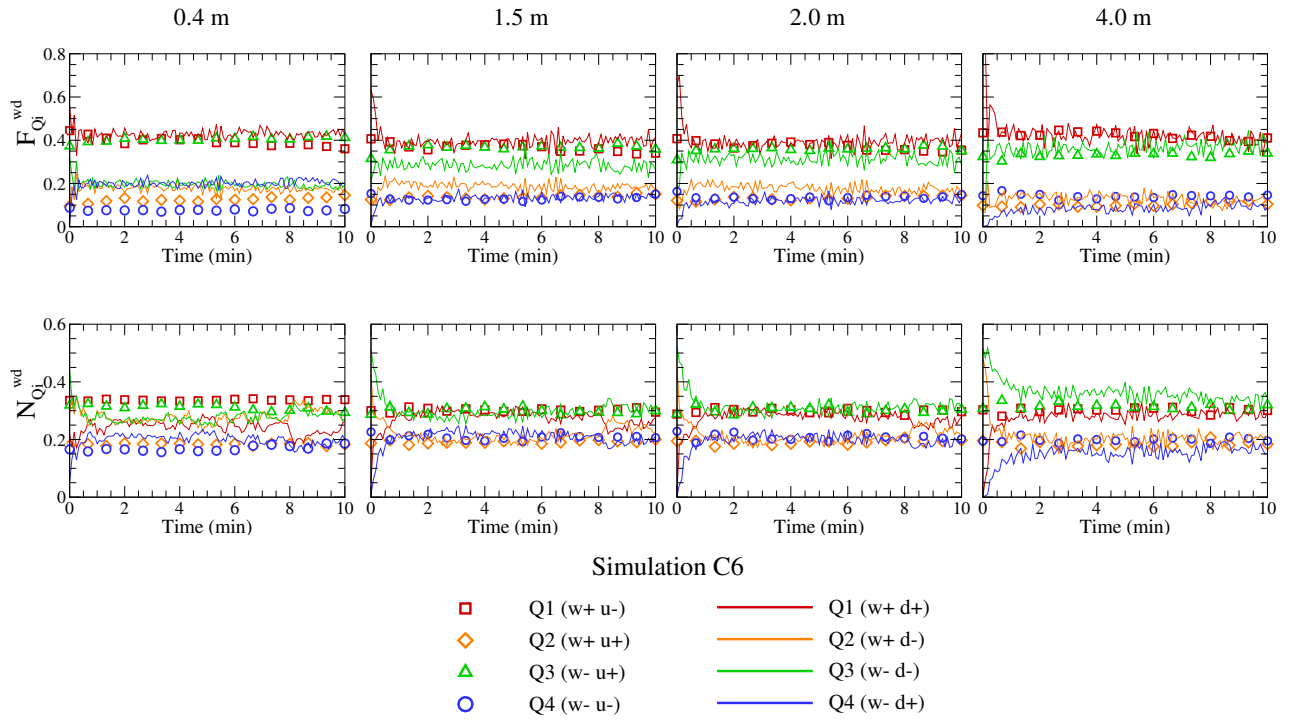


FIGURE 5.10: Time variation of the quadrant partitioning in magnitude ( $F_{Q_i}^{wd}$ ) and in event number ( $N_{Q_i}^{wd}$ ) of the dust flux  $F_{wd}$  compared to the quadrant partitioning of the momentum flux  $F_{uw}$ , at 4 heights (0.4, 1.5, 2.0 and 4.0 m) as obtained from simulation C6. The dust flux includes all particle sizes.

### 5.4.3 Influence of the dust emission intermittency

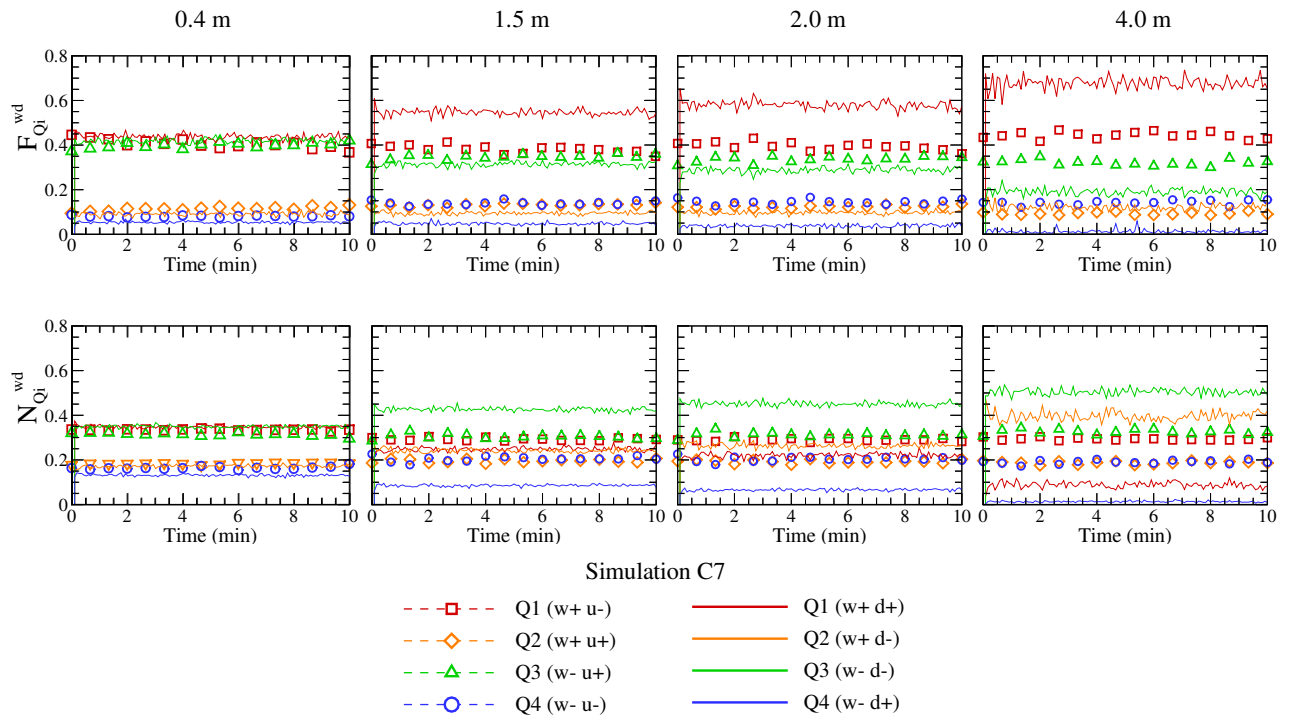


FIGURE 5.11: Same as Fig 5.10 but for simulation C7.

The time variation of the  $F_{wd}$  quadrant partitioning obtained from simulation C7 is presented in Fig. 5.11. This simulation is characterized by a continuous dust emission, independent of the wind intensity, conversely to the dust emission by sandblasting in other simulations. Unlike C1, the dust flux partitioning is close to the partitioning of the momentum flux near the surface ( $z = 0.4$  m). However, the partitioning of  $F_{wd}$  changes progressively with height, with an increasing contribution of Q1 ( $w^+d^+$ ) in the magnitude of the flux in detriment of Q3 ( $w^-d^-$ ) and Q4 ( $w^-d^+$ ). In number of events, Q2 ( $w^+d^-$ ) and Q3 contributions increase with height in detriment of Q1, meaning that downward motions of clean air becomes more frequent in the upper portion of the dust internal boundary layer.

## 5.5 Discussion

Dissimilarity in turbulent transport between momentum and dust has been observed during the WIND-O-V experiment on an isolated plot. This dissimilarity was in particular visible from the lower proportion of upward motions ( $w^+$ ) carrying dust ( $d^+$ ) than low momentum ( $u^-$ ) from the surface. This was explained by the intermittency of the dust emission as compared to the more continuous absorption of momentum at the surface. To analyse deeper the reasons of this dissimilarity, numerical simulations of the full erosion process with an explicit simulations of the main flow eddies were performed in this study for various erosion conditions.

Compared to the WIND-O-V experiment, the model was able to reproduce the main characteristics of the wind dynamics for the moderate erosive winds and the short fetch of the experiment ( $u_{*0}/u_{*t} \sim 1.5$  and  $z/x_{fetch} = 0.02$ ). The saltation process was also well reproduced with in particular the proper increase of the saltation roughness length with  $u_{*0}$  and the presence of aeolian streamers in the simulations surrounded by regions with little or no saltation, as usually observed over erodible surfaces [Carnerio *et al.* 2015; Baas *et al.* 2005; Stout *et al.* 1997]. The near-surface dust concentration exhibited the same level of intermittency as the observed one, with a kurtosis around 17. The trend of the dust flux with  $u_{*0}$  was also consistent with the measurements as well as its size distribution. Importantly, the quadrant distributions of the momentum and dust fluxes near the surface ( $z/x_{fetch} \sim 0.02$ ) were in good agreement with the observation. In particular, the number of upward events carrying positive fluctuations of dust ( $w^+d^+$ ) were lower than those carrying negative fluctuations of momentum ( $w^+u^-$ ), many of them carrying clean air, i.e. negative dust fluctuations ( $w^+d^-$ ). Hence, the model was able to reproduce the dissimilarity in turbulent transport between momentum and dust observed in the field experiment.

With increasing wind intensity ( $u_{*0}$ ), the dissimilarity in turbulent transport between momentum and dust decreases, confirming previous thought from Dupont *et al.* [2019b]. In particular, simulations predicted an increasing number of upward events carrying positive dust fluctuations ( $w^+d^+$ ) with  $u_{*0}$ , accompanied with an increase in magnitude of the downward motions



of clean air ( $w^- d^-$ ) (Fig. 5.9). Dupont *et al.* [2019b] estimated from an extrapolation of their field observation that similarity between momentum and dust should be reached for  $u_{*0}$  above 2.5 to 3.0 times  $u_{*t}$ . Here, the similarity was reached at  $u_{*0}/u_{*t} = 2.5$ , as shown from the comparable quadrant partitions of the dust and momentum fluxes at  $z = 0.4$  m. Dupont *et al.* [2019b] suggested that with increasing wind intensity, dust emission becomes less intermittent due to the more spatially homogeneous saltation. This was indeed confirmed from our simulations: (1) the kurtosis of the near-surface dust concentration reduced from 17 to 4 for  $u_{*0}/u_{*t} = 1.6$  to 2.5 (Fig. 5.4c), and (2) aeolian streamers became embedded in larger saltation structures (Fig. 5.7a), leading to dust emission less patchy in space or intermittent in time (Figs. 5.7c).

This shift toward similarity between momentum and dust turbulent transports with increasing wind intensity was not observed further away from the surface ( $z > 4.0$  m) due to the limited fetch of the erodible plot. Indeed, a dust internal boundary layer grows from the up-wind edge of the erodible plot where a mixing occurs in its upper part between the above and within dust particles. Hence, the dissimilarity in turbulent transport between momentum and dust is enhanced in the upper part of this internal layer due to the increasing number of downward events carrying clean air ( $w^- d^-$ ) from above, while upward motions of dusty air ( $w^+ d^+$ ) become less frequent but more significant in the magnitude of the dust flux. In this internal layer, a constant dust flux layer developed slowly near the surface. This constant layer was less than 1 m high at about  $x_{fetch} = 50$  m, which represents roughly the lower 10% of the dust internal boundary layer. It is probable that the dissimilarity in the upper internal layer and the weak constant dust flux layer were both accentuated in our simulations by the strong transition between the non-erosive and erosive surfaces, and by the air clean of dust reaching the erosive plot. During the WIND-O-V experiment, this transition was not as sharp although the surrounded plots were less erodible than the experimental plot.

The key role played by the dust emission intermittency on the dissimilarity in turbulent transport between momentum and dust was verified from a simulation performed with a continuous dust emission, independent of the wind intensity (simulation C7). Unlike simulations with dust emission by sandblasting, dust in C7 appeared similarly transported as momentum close to the surface ( $z/x_{fetch} < 0.03$ ), confirming that the dissimilarity observed in previous simulations was related to the difference between dust source and momentum absorption at the surface, with dust emission more intermittent than the momentum absorption at the surface due to the saltation threshold process. However, away from the surface, the turbulent transport of dust in C7 appeared increasingly dissimilar to that of the momentum due to the limited fetch of the erodible surface. This suggests that both dust emission intermittency and fetch limitation play on the dissimilarity between momentum and dust turbulent transports.

A simulation without fetch (C6) but with an intermittent emission of dust showed a dissimilar turbulent transport between momentum and dust near the surface ( $z \sim 0.36$  m) as in simulation C1. This confirms that the dissimilarity near the surface in C1 was driven by the dust emission intermittency and not by the limited fetch. The fetch was long enough at such height



to not perturb the flux partitioning. In other words, the footprint of the dust flux was only impacted by the local erodible plot. However, away from the surface ( $z \geq 2$  m), the dust turbulent transport became surprisingly similar to that of the momentum. At this height, the footprint of the dust flux integrates a larger upwind surface. We suspect that the intermittency of the dust emission flux is progressively lost as dust is transported-mixed away from the surface, dust particles spreading over weaker eddies than the ones initiating dust emission, attenuating the memory of the wind speed threshold mechanism of dust emission.

## 5.6 Conclusions

Our numerical experiment allowed us to confirm and further explain the dissimilarity in turbulent transport between dust and momentum observed during the WIND-O-V field experiment. Simulations revealed two reasons to observe this dissimilarity: (1) the intermittency of dust emission associated to moderate wind conditions, as opposed to the more continuous absorption of momentum at the surface, and (2) the limited development of the dust internal boundary layer from the upwind edge of the erodible surface, associated to a short fetch.

Dissimilarity due to dust emission intermittency was only observed close to the surface for moderate wind conditions. With increasing wind intensity, the dissimilarity between dust and momentum turbulent transports diminishes as dust emission becomes less intermittent, more spatially homogeneous, near-surface wind fluctuations exceeding most often the threshold value for initiating saltation. Dissimilarity due to a limited fetch increases with height as the upper edge of the dust internal boundary layer get closer. In this last case, the dissimilarity strength depends probably on the roughness and level of erodability of the upwind plots. Importantly, without fetch, dust becomes progressively transported by turbulence similarly as momentum with height, the intermittency of dust emission at the surface being progressively lost during the turbulent transport process.

In semiarid regions, the short fetch of erodible surfaces and the near-threshold wind conditions may stress the dissimilarity between dust and momentum turbulent transports. This should be considered when measuring dust emission flux.

## 6 A field investigation of sparse vegetation impact on dust suspension in a semi-arid environment

This chapter presents the results of the WIND-O-V's 2018 field experiment, designed to investigate the role of sparse vegetation on the quantity and size of the suspended dust during erosion events. This is achieved through a comparative analysis of the two WIND-O-V's field experiments, over bare and sparsely vegetated surfaces.

The findings of this chapter are intended to be published as a research paper.

**Keywords:** sparse vegetation, dust emission, dust size-distribution, semi-arid erosion, dust flux, dust flux PSD

**Abstract:** *This chapter presents the results of the WIND-O-V's 2018 field experiment in Tunisia designed to investigate the role of sparse vegetation on the quantity and size of the suspended dust flux in a semi-arid environment. The experiment featured continuous measurements of turbulence and dust fluxes, similar to the WIND-O-V's 2017 experiment and at the same site. The comparison between the 2018 and 2017 experiments, with and without vegetation, confirmed that sparse vegetation reduces erosion by increasing the erosion threshold friction velocity as a function of the vegetation height. The erosion threshold varied with wind direction, with winds parallel to the vegetation arrangement being most erosive. During the 2018 experiment, the size-distribution of the near-surface dust flux varied continuously, unlike the 2017 experiment, with a progressive impoverishment of coarse particles ( $1.50 \mu\text{m}$ ). The impoverishment of these particles was independent of vegetation, and caused by their depletion at the surface due to prolonged emissions without surface modification. Interestingly, rain and surface tillage events appeared to reboot the surface, making the coarser particles more readily available for emissions in 2017. Moreover, the size-distribution of the dust flux at the very beginning of the 2018 experiment, when the vegetation was at its maximum height, resembled closely that of 2017, showing the negligible role of vegetation on the size of the suspended dust.*

## 6.1 Introduction

Vegetation is known to influence wind-erosion dynamics by controlling the entrainment and near-surface transport of soil (sand) particles [Wiggs *et al.* 1994; Wolfe *et al.* 1993; Musick *et al.* 1990] and thereby dust emissions through sandblasting. Semi-arid environments being resource-limited are characterized by sparse vegetation that is highly variable in time and space [Bailey 2011]. In such regions, the impact of vegetation on dust emissions is still debated, with differences in dust aerosol concentrations often attributed to the seasonal variabilities in vegetation cover [Pierre *et al.* 2012; Evan *et al.* 2006; Zender *et al.* 2005; Wiggs *et al.* 1994]. The current understanding of aeolian-plant-soil interaction identifies five mechanisms through which scattered vegetation elements may modulate wind-erosion. Vegetation elements (1) extract momentum from the flow thereby reducing the shear stress acting on the surface [Wasson *et al.* 1986; Gillette *et al.* 1989; Dupont *et al.* 2014], (2) reduce the erodible surface area by covering the soil surface, (3) create wakes of reduced mean velocity discouraging particle entrainment [Leenders *et al.* 2007; Wolfe *et al.* 1993], (4) trap airborne soil particles by acting as islands for particle deposition [Gillies *et al.* 2014; Gillies *et al.* 2000; Lancaster *et al.* 1998; Ven *et al.* 1989], and (5) enhance the surface inter-particle cohesive bonds by trapping moisture [Kim *et al.* 2000]. Nevertheless, the true extent to which sparse vegetation regulates wind-erosion is still not clear.

Wolfe *et al.* [1993] were among the first to explore the protective role of sparse vegetation against wind-erosion (saltation). The experiments of Hagen [1994] demonstrated a high correlation between plant area index and surface sheltering by sparse vegetation. Later, Lancaster *et al.* [1998] observed that sand transport decreases exponentially with vegetation cover. Subsequent field experiments of Gibbens *et al.* [1983] and Brazel *et al.* [1987] showed that even partially defoliated or rooted dead vegetation elements act to reduce sand transport in semi-arid environments. Contrarily, Ash *et al.* [1983] and Logie [1982] suggested that isolated vegetation elements shed turbulent eddies by diverting the flow above and around them, inducing local surface shear stress peaks and thereby enhancing erosion locally. This was later supported by the wind-tunnel experiments of Sutton *et al.* [2008] who observed regions of elevated shear stress that enable the initiation of sand transport at wind speeds lower than those required for a bare surface. Further, Burri *et al.* [2011] demonstrated that in sparse grassland vegetation, the oscillating movements of the grass-blades brushing against the surface increased erosion. These opposing findings necessitate an improved understanding of the physical processes through which sparse semi-arid vegetation influences sand transport and thus dust emission.

Most existing research on vegetation-erosion dynamics in semi-arid environments centres around sand transport (saltation). The few studies on dust emission in such regions focussed on the airborne dust mass [Sofue *et al.* 2017; Cody *et al.* 2014; Urban *et al.* 2009; Gillette *et al.* 2004], with little attention to the role of vegetation on the relative sizes of the emitted dust, its near-surface

sorting, and transport. This lack of size-relative dust emissions data sets can lead to the inaccurate quantification of dust aerosols, especially from poor surface characterization [Pierre *et al.* 2012], thereby seeding unreliability in climate simulations and weather predictions. Furthermore, the simulations of the previous chapter demonstrated possible near-surface turbulent transport dissimilarity between momentum and dust in semi-arid regions, leading to dust flux overestimation by current schemes. Such dissimilarities are believed to increase with surface heterogeneities such as seasonally varying sparse vegetation common to semi-arid environments, and could contribute to model unreliability.

The goal of this study is to investigate sparse vegetation impact on the quantity and size of the emitted dust and its near-surface turbulent transport. To this end, we rely on the two novel field experiments of the WIND-O-V project (Sec. 3.2), the first over a bare isolated plot and the second over the same plot with sparse vegetation. From these, we hope to identify the role of scattered vegetation on dust emissions and the near-surface dust flux by comparing the flow and dust dynamics between the bare and vegetated surfaces.

## 6.2 Dust emission events of the 2018 campaign

The 2018 experiment featured many dust emission events with winds blowing along all directions eroding the experimental plot. Of these, only the winds that eroded the plot were considered, with the dust emitted by south-north winds not be measured due to the positioning of the measurement mast (Fig. 6.1) at the southern edge of the plot. Events with large variations in wind direction were also not considered due the errors induced while deducing the averaged quantities. Finally, for winds swaying close to eastern/western edges of the plot, only those that eroded the plot were considered.

Nine well-defined dust emission events ranging in duration between 2 to 8 hours were selected (Table 6.1). Similar to 2017, they were chosen based on a preferential wind direction ( $-80^\circ < \theta < 100^\circ$ ) ensuring dominant dust sourcing from the experimental plot, and were characterized by a near-constant mean wind direction and wind speed (Fig. 6.2a), positive dust flux (Fig. 6.2e), and a significant change in the number of particles measured by the EC OPC (Fig. 6.2f). These emission events occurred during the day, situated on the convective side of the near-neutral stability class  $-0.1 < z/L < 0.01$  (Fig. 6.2c). Overall, the 2018 experiment was characterized by a wind direction change from north-west to north-east between March and June, consistent with seasonal changes in south Tunisia and with the 2017 experiment.

The mean sensible heat flux  $H$  (Fig 6.2d) increased gradually between March and June, in two sets of comparable mean values consisting of the first five erosion events and the subsequent four. Of the first set, the April 07 event had low wind intensities (Fig 6.2a), weaker dust fluxes (Fig 6.2e) and lower dust concentrations (Fig 6.2f), while the April 17 and the May 02 events had the strongest wind peaks and thus, lower convective conditions (Fig 6.2c), stronger dust

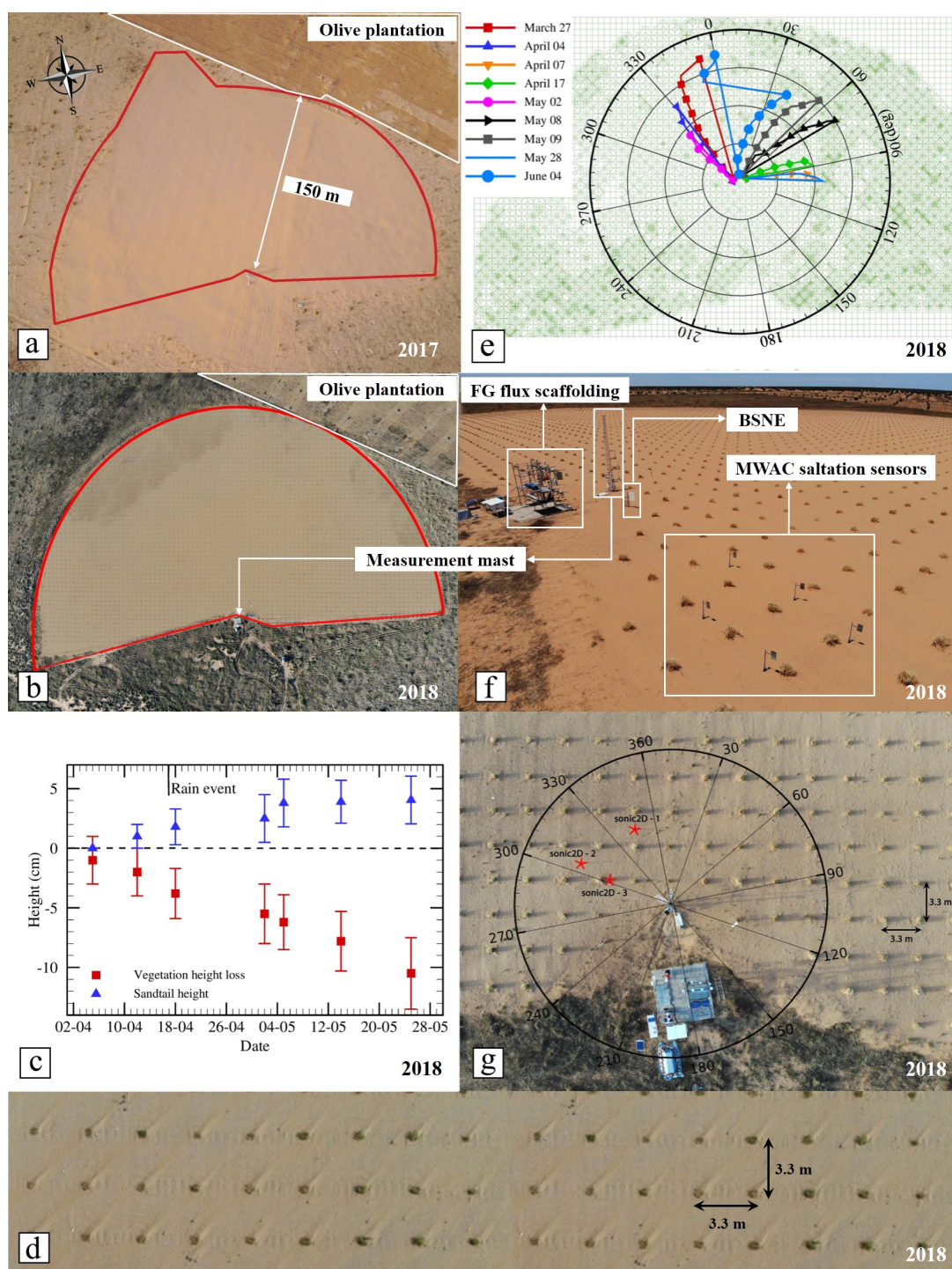


FIGURE 6.1: Plan-view images of the semi-circular 150 m radius WIND-O-V's site in South Tunisia during (a) the bare soil experiment of 2017, and (b) the 2018 experiment with sparse vegetation. (c) The time variation of the mean vegetation and sand-tail heights during the 2018 experiment, with the error bars indicating their standard deviations. (d) Top-view of the sand-tails in the lee of the barley tufts. (e) The representation of mean vegetation height as proportional to the intensity of the green markings. Superposed on it is the variation of the wind direction for the 9 erosion events of the 2018 experiment. (f) The main instrumentation mast, the flux-gradient scaffolding and the saltation sensors. (g) The positions of the 3 sonic-2D anemometers relative to the main mast. Source: Internal communication with Dr. Jean-Louis Rajot.



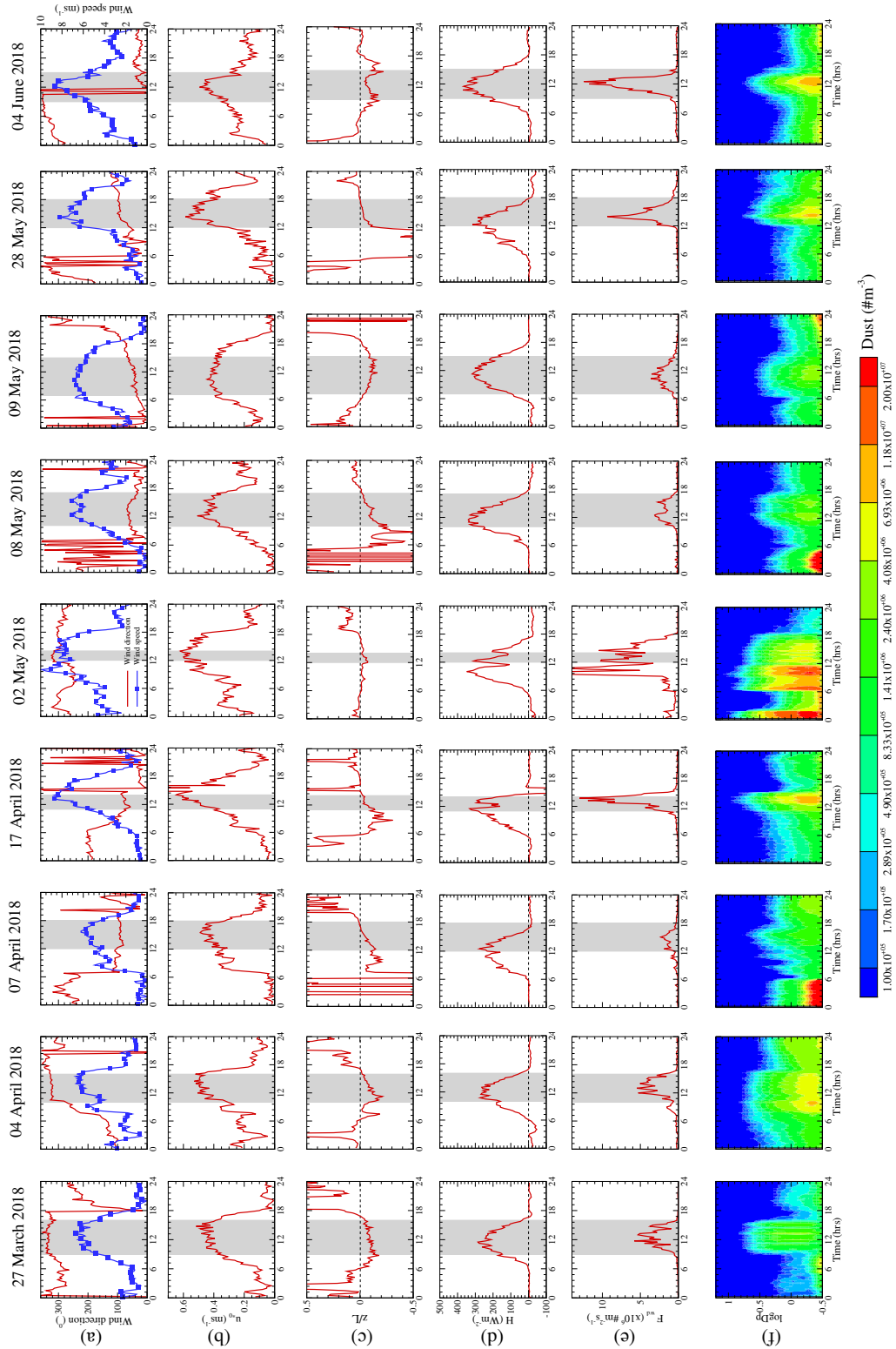


FIGURE 6.2: Main characteristics of the 9 erosion events: time variations of the (a) mean wind direction and the mean wind speed, (b) surface friction velocity ( $u_{*0}$ ) deduced from the sonic anemometers according to Dupont *et al.* [2018], (c) stability ( $z/L$ ), (d) sensible heat flux ( $H$ ), (e) dust number flux ( $F_{wd}$ ), and (f) mean size-resolved dust number concentration. All values, except  $u_{*0}$ , were measured at 3 m from the surface. The shaded areas highlight the selected erosion periods.

fluxes (Fig 6.2e) and higher dust concentrations (Fig 6.2f). Similarly for the second set, the May 28 and June 04 were stronger dust emission events. Overall, erosion with barley tufts was characterised by lower dust mass concentrations for comparable mean wind speeds (Table 7.1), giving a first insight into the possible influence of sparse vegetation on wind erosion.

Event date	$u_{*0}$ ( $\text{ms}^{-1}$ )	wind direction (deg)	$z/L$	$u$ ( $\text{ms}^{-1}$ )	Total Conc ( $\mu\text{gm}^{-3}$ )	Flux 0.60 $\mu\text{m}$ ( $\times 10^6 \text{ part m}^{-2}\text{s}^{-1}$ )	Flux 1.50 $\mu\text{m}$ ( $\times 10^6 \text{ part m}^{-2}\text{s}^{-1}$ )	Nb 15-min
<b>2018 events</b>								
27 March	0.40( $\pm 0.04$ )	- 27( $\pm 08$ )	- 0.07( $\pm 0.04$ )	6.50( $\pm 0.62$ )	304.91	0.2153	0.2046	28
04 April	0.43( $\pm 0.05$ )	- 37( $\pm 09$ )	- 0.09( $\pm 0.05$ )	6.63( $\pm 0.90$ )	311.41	0.3344	0.2251	24
07 April	0.42( $\pm 0.04$ )	89( $\pm 06$ )	- 0.08 ( $\pm 0.04$ )	6.36( $\pm 0.57$ )	97.84	0.0985	0.0580	24
17 April	0.60( $\pm 0.04$ )	80( $\pm 05$ )	- 0.03( $\pm 0.01$ )	9.14( $\pm 0.91$ )	808.20	0.7276	0.3026	12
02 May	0.58( $\pm 0.04$ )	- 46( $\pm 09$ )	- 0.04( $\pm 0.02$ )	8.87( $\pm 0.54$ )	525.92	0.6120	0.3100	16
08 May	0.47( $\pm 0.03$ )	58( $\pm 10$ )	- 0.08( $\pm 0.03$ )	7.09( $\pm 0.38$ )	94.67	0.2430	0.0895	20
09 May	0.45( $\pm 0.03$ )	42( $\pm 06$ )	- 0.10( $\pm 0.03$ )	6.87( $\pm 0.25$ )	70.39	0.1763	0.0603	32
28 May	0.53( $\pm 0.04$ )	92( $\pm 05$ )	- 0.03( $\pm 0.02$ )	8.57( $\pm 0.65$ )	286.14	0.3737	0.1151	20
04 June	0.47( $\pm 0.10$ )	14( $\pm 15$ )	- 0.09( $\pm 0.05$ )	6.64( $\pm 1.85$ )	165.82	0.3999	0.1176	24
<b>2017 events</b>								
07 March	0.33( $\pm 0.04$ )	- 43( $\pm 17$ )	- 0.14( $\pm 0.15$ )	6.18( $\pm 1.08$ )	633.75	0.3837	0.3229	32
08 March	0.36( $\pm 0.09$ )	- 17( $\pm 16$ )	- 0.05( $\pm 0.05$ )	7.21( $\pm 1.55$ )	1387.00	0.5147	0.5627	28
09 March	0.39( $\pm 0.05$ )	- 28( $\pm 07$ )	- 0.07( $\pm 0.03$ )	7.81( $\pm 0.75$ )	1191.40	0.7988	0.6527	32
14 April	0.35( $\pm 0.06$ )	- 75( $\pm 16$ )	- 0.07( $\pm 0.05$ )	6.48( $\pm 1.00$ )	600.11	0.2363	0.1971	28
16 April	0.40( $\pm 0.07$ )	19( $\pm 25$ )	- 0.09( $\pm 0.04$ )	7.77( $\pm 1.41$ )	900.64	0.5408	0.4131	28
20 April	0.32( $\pm 0.06$ )	50( $\pm 11$ )	- 0.07( $\pm 0.05$ )	8.03( $\pm 0.61$ )	642.34	0.5682	0.4763	53
02 May	0.34( $\pm 0.03$ )	64( $\pm 05$ )	- 0.16( $\pm 0.10$ )	6.70( $\pm 0.38$ )	286.71	0.2145	0.2242	32

TABLE 6.1: The main characteristics of the selected 2018 and 2017 erosion events: surface friction velocity ( $u_{*0}$ ), wind direction, stability ( $z/L$ ), 3 m high mean wind speed ( $u$ ), dust concentration from the EC OPC including all particle sizes, dust number flux from the 3 m high EC system for particle modes 0.60  $\mu\text{m}$  and 1.50  $\mu\text{m}$ , and the number of 15-minute averaging periods. The values presented are averages of all selected 15-minute time periods with the standard deviations within parentheses. The criteria to select the 15-minute time periods is described in Dupont *et al.* [2018].

## 6.3 Results

### 6.3.1 Wind dynamics during dust emission

For the selected 2018 erosion events, the wind velocity ( $\langle u \rangle$ ) from the 7 cup (squares) and 4 sonic anemometers (circles), exhibits a well-defined logarithmic profile (Fig. 6.3a), with the sonic and cup anemometers showing the same velocity amplitude and variation with height. The standard deviations of the horizontal velocity components ( $\langle \sigma_u \rangle, \langle \sigma_v \rangle$ ) in Fig. 6.3b) are comparable between events, with marginal variations with height. As expected, the standard deviation of the vertical velocity ( $\langle \sigma_w \rangle$ ) is lower and increases with height. The ratios of the velocity standard deviations and the friction velocity are:  $\langle \sigma_u \rangle / \langle u_* \rangle \approx 2.76$  and  $\langle \sigma_w \rangle / \langle u_* \rangle \approx 1.24$ , consistent with published values for bare surfaces [Kaimal *et al.* 1994], and that of the 2017 experiment [Dupont *et al.* 2018]. Interestingly, for the April 17, May 02 and May 28 events,  $\langle \sigma_u \rangle$  is slightly higher than  $\langle \sigma_v \rangle$ , most likely related to the increase in  $\langle \sigma_u \rangle$  with decreasing instability [Joffre *et al.* 1987]. The same was also observed for the 2017 experiment [Dupont *et al.* 2018] (Appendix A).

Flow with vegetation is generally associated with a displacement height ( $d$ ) where the mean fluid drag appears to act [Kaimal *et al.* 1994]. It is the distance from the surface where the



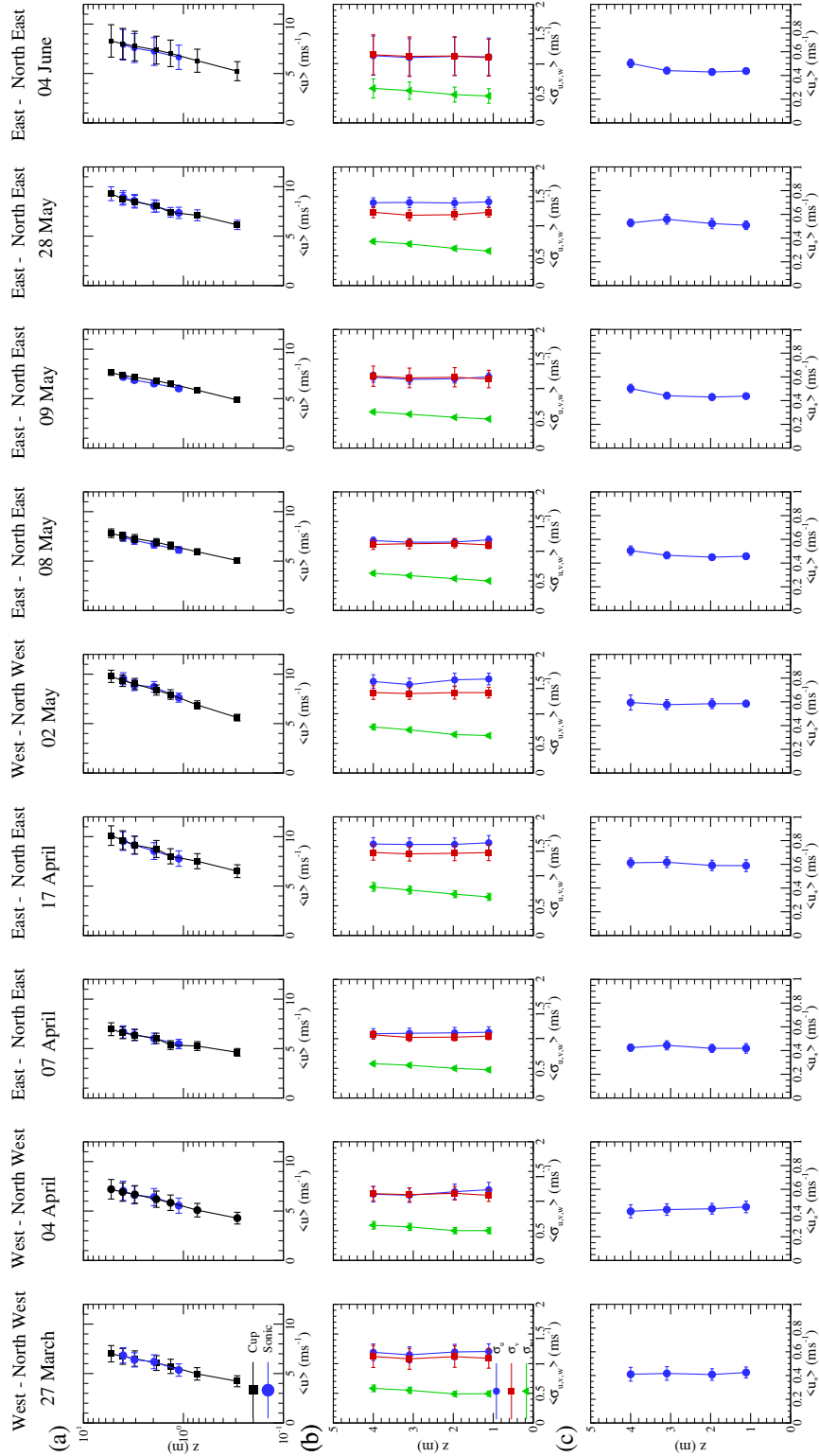


FIGURE 6.3: Vertical profiles of the (a) wind velocity deduced from the cup (square) and sonic (circle) anemometers, (b) standard deviations of the longitudinal (circle), lateral (square) and vertical (triangle) velocity components, and (c) friction velocity for the selected erosion events of the 2018 campaign. The error bars indicate the standard deviation of each variable.  $\langle \rangle$  denotes the ensemble average over all selected 15-minute time periods for each erosion event.

height-velocity curve deviates from the log-profile through an inflexion point. This extrapolation for the 2018 erosion events did not yield an inflexion point but rather led to zero velocity when  $z \rightarrow z_0$ , implying an insignificant displacement height. Further supporting this is (i) the closeness of the ratios between the velocity standard deviations and friction velocities ( $\langle \sigma_u \rangle / u_{*r}$ ,  $\langle \sigma_v \rangle / u_{*r}$ ,  $\langle \sigma_w \rangle / u_{*r}$ ) with those for bare surfaces [Dupont *et al.* 2018] (Appendix A), and (ii) the marginal deviation from the log-profile of the lowest cup anemometer ( $z \approx 0.2$  m) inside the vegetation layer (Fig. 6.3a).

The friction velocity ( $\langle u_* \rangle$ ) and thus the momentum flux ( $\langle u'w' \rangle$ ) appear almost constant with height across all events (Fig. 6.3c), with some deviation above 3 m for the easterly ones. This deviation is most probably linked to the shallow internal boundary layer developing over the experimental plot due to the rough to smooth surface roughness change [Kaimal *et al.* 1994] between the upwind olive plantations and the experimental plot, as against the minimal roughness change for the westerly winds (Fig. 6.1b). Similar deviations in the  $\langle u'w' \rangle$  profile were observed above 3 m for the easterly events of the 2017 experiment [Dupont *et al.* 2018], also due to the olive plantations (Fig. 6.1a).

Wind direction (deg)	Sonic2D-1 ( $\text{ms}^{-1}$ )	Sonic2D-2 ( $\text{ms}^{-1}$ )	Sonic2D-3 ( $\text{ms}^{-1}$ )
11 (N)	1.33( $\pm 0.85$ )	1.92( $\pm 1.30$ )	1.77( $\pm 1.11$ )
55 (NE)	2.56( $\pm 1.26$ )	1.94( $\pm 1.02$ )	2.14( $\pm 1.05$ )
102 (E)	2.70( $\pm 1.50$ )	2.66( $\pm 1.50$ )	2.48( $\pm 1.40$ )
-78 (W)	1.54( $\pm 1.85$ )	1.47( $\pm 1.80$ )	0.74( $\pm 0.93$ )

TABLE 6.2: Mean wind speed and the standard deviation (within parentheses) measured at 0.45 m from the surface at 3 different locations for four wind directions - north ( $11^\circ$ ), north-east ( $55^\circ$ ), east ( $102^\circ$ ) and west ( $-78^\circ$ ). The mean values are the average of all 15 minute time periods.

Individual barley tufts alter the wind field in their vicinity by acting as isolated wind-breaks creating triangular sheltered zones of reduced wind speed on their lee side [Judd *et al.* 1996] as explained in Chapter 2. This is seen for example for westerly ( $-78^\circ$ ) winds with the Sonic2D-3 recording a 50% drop in the mean wind speeds (Table 6.2) in comparison with the other anemometers that remain uninfluenced by vegetation (Fig. 6.1g). Sufficiently downwind of the leading Barley tuft, the mean wind speed resumes to its inter-row (between vegetation rows) levels, seen for the easterly ( $102^\circ$ ) winds for the Sonic2D-3, consistent with the observations of Mayaud *et al.* 2016b. The sheltered zones associated with such flows are known to encourage particle re-deposition as discussed in Chapter 2, and may explain the formation of sand-tails in the lee of the barley tufts (Fig. 6.1d).

### 6.3.2 Dust emission threshold

Thresholds of saltation and dust emission are generally assumed to be equivalent, with dust fluxes expressed in the form  $F_d = A(u_{*0} - u_{*t})^n$  [Shao 2008], where  $u_{*t}$  is the saltation threshold friction velocity,  $n \approx 3 - 5$  and  $A$  is a constant. During the WIND-O-V's experiment,

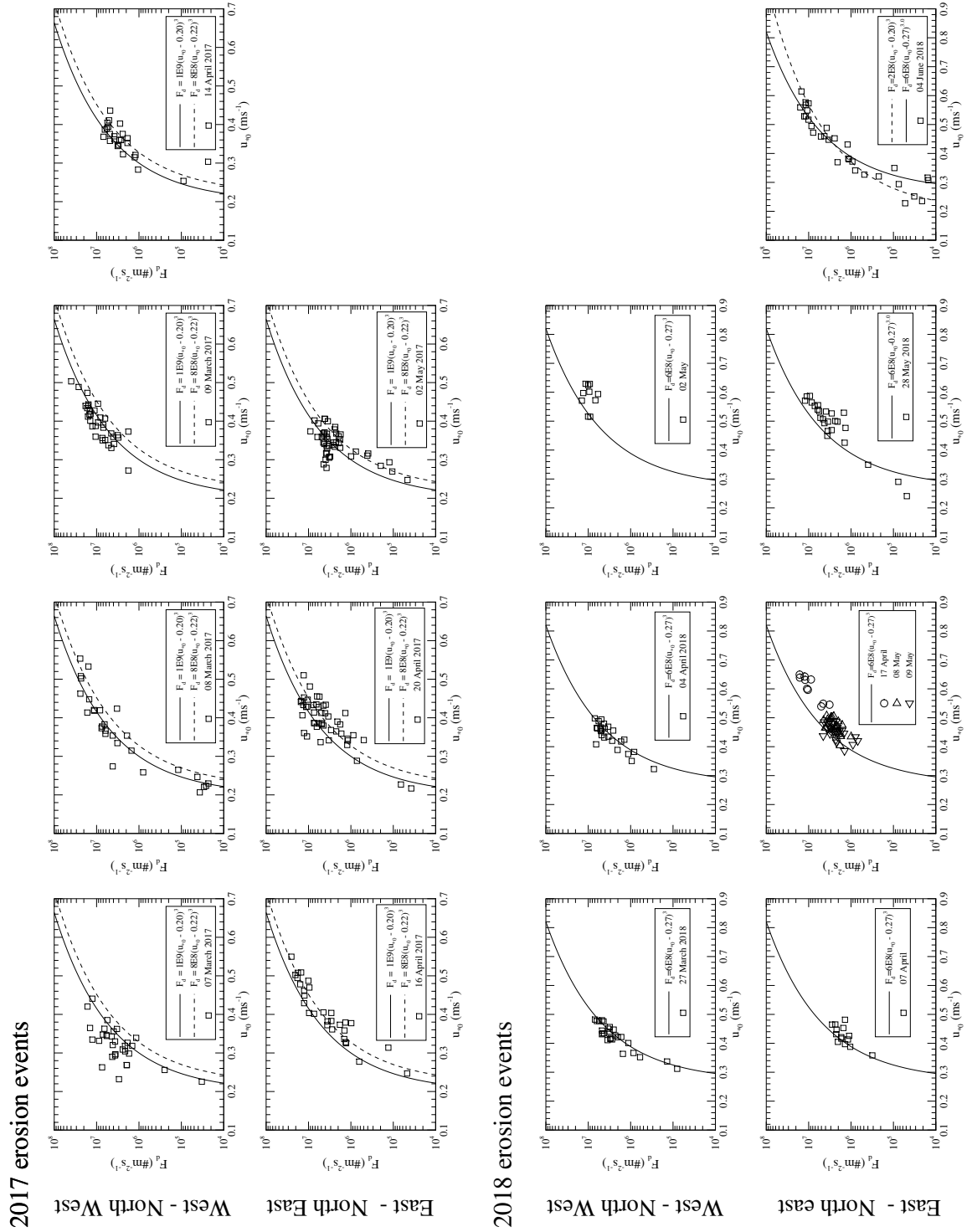


FIGURE 6.4: Variation of the dust number flux (including all particle sizes) with surface friction velocity ( $u_{*0}$ ) and wind direction for the 2017 and 2018 events of the WIND-O-V's campaign, along with the best fit in the form  $F_d = A(u_{*0} - u_{*0}^*)^3$ . Each point corresponds to a 15 minute time average.

unreliability in the saltation data set limited our reliance on the saltation threshold. Nevertheless, we assumed that the dust fluxes can be expressed in the above form, with a modified  $u_{*t}$  for dust emissions that may or may not be equivalent to the saltation threshold. For this we assume (i)  $F_d$  is sourced dominantly from the experimental plot, and (ii)  $F_d$  off-event is zero.

For erosion over the bare surface (2017 events in Figure 6.4), we fit the above equation for the first three erosion events of March 07-09 with  $n = 3$  and  $u_{*t} = 0.22 \text{ ms}^{-1}$ . It appears to be well correlated with the subsequent April 14 event. The following April 16 event deviates from it, and a second fit with  $u_{*t} = 0.22 \text{ ms}^{-1}$  is enabled, which remains in good agreement with the April 20 and May 02 events. This marginally varying dust emission threshold is closely comparable with the saltation threshold presented in Dupont *et al.* [2019b] for the bare surface. The threshold values appear to be functions of the wind direction, suggesting possible local differences in the soil characteristics of the plot.

Similarly for the 2018 events, we begin by fitting the above equation (retaining  $n = 3$ ) for the March 27 event with  $u_{*t} = 0.27 \text{ ms}^{-1}$ . The increase in the dust emission threshold from the bare soil values is due to the increase in the fluid momentum lost to the vegetation, thereby decreasing that available to drive erosion [Raupach 1992]. This first fit appears to be in good agreement with the April 04 event. All subsequent events, however, deviate from it. The lack of data points at lower friction velocities for the majority of events, due to the limitations in the wind direction range, limits our ability to suggest a reliable  $u_{*t}$ . Nevertheless, we suspect that the dust emission threshold decreases continuously with the mean vegetation height (Fig. 6.1c). This is supported by the fit for the June 04 event, with a dust emission threshold comparable with that of the bare soil ( $u_{*t} = 0.20 \text{ ms}^{-1}$ ). A similar decrease in (saltation) threshold with vegetation characteristics was observed by Wasson *et al.* [1986], Gillies *et al.* [2000], and Ven *et al.* [1989]. Furthermore, unlike for the bare surface, we believe that in 2018 the dust emission threshold was less influenced by the possible differences in soil characteristics between the two quarters (wind direction) and more by the differences in the local vegetation state (Fig. 6.1d).

### 6.3.3 Aerodynamic roughness length ( $z_0$ )

The barley tufts on the experimental plot (Fig. 6.1b) absorb momentum from the air flow, increasing the aerodynamic roughness length ( $z_0$ ) [Raupach 1992; Lancaster *et al.* 1998; Dupont *et al.* 2014], seen from the nearly two decade difference between the 2017 and 2018 experiments (Fig. 6.5a). As expected, the quantity of fluid momentum lost to the vegetation decreases with its mean height (Fig. 6.1c), reducing  $z_0$  by an order of magnitude between the March 27 and June 04 events. This is seen more clearly in Fig. 6.5c featuring additional data points corresponding to the non-erosive winds. Furthermore, unlike for the bare surface,  $z_0$  appears to be independent of wind intensity (Fig. 6.5a), and hence sand transport. This is due to the dominant vegetation effect on the fluid momentum change in comparison with saltation [Raupach 1992]. The same has also been observed in the field experiment of Lancaster *et al.* [1998] and the simulations of Dupont *et al.* [2014]. Interestingly,  $z_0$  in the presence of vegetation appears to be also a function of the wind direction, with a minimum when the wind flows along the vegetation rows ( $-80^\circ$ ,  $+10^\circ$ ,  $+100^\circ$ ) and maximum when diagonal ( $-35^\circ$ ,  $+55^\circ$ ) to

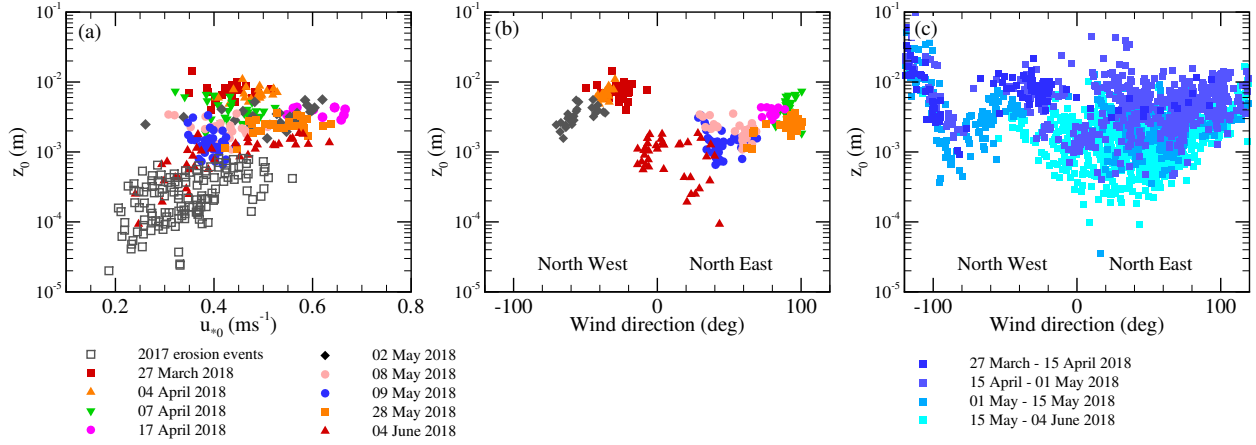


FIGURE 6.5: Variation of the aerodynamic roughness length ( $z_0$ ) as a function of (a) surface friction velocity ( $u_{*0}$ ) for 2017 and 2018 erosion events, and wind direction for the (b) selected 2018 erosion events, and (c) entire 2018 experimental duration. Each data point represents a 15 minute time period.

them (Fig. 6.5c). This is most likely due to the non-uniformity of vegetation frontal area as a function of wind direction leading to differences in the quantity of fluid momentum absorbed. Therefore, the significant differences between the  $z_0$  of the May 28 and June 04 events can be attributed to this wind direction effect (Fig. 6.5b). As expected, these results suggest that the erodability of the surface may be influenced by the vegetation density (surface cover), its height, and form.

### 6.3.4 Near-surface turbulent dust transport

Event date	Flux magnitude ( $F_{wd}^{Q_i}$ )				Event number ( $N_{wd}^{Q_i}$ )			
	Q1	Q2	Q3	Q4	Q1	Q2	Q3	Q4
	$w^+d^+$	$w^+d^-$	$w^-d^-$	$w^-d^+$	$w^+d^+$	$w^+d^-$	$w^-d^-$	$w^-d^+$
March 27	0.48	0.15	0.28	0.09	0.21	0.27	0.39	0.13
April 04	0.46	0.14	0.30	0.10	0.24	0.25	0.37	0.14
April 07	0.40	0.18	0.29	0.13	0.17	0.31	0.38	0.14
April 17	0.45	0.13	0.30	0.12	0.25	0.24	0.36	0.15
May 02	0.47	0.12	0.31	0.10	0.24	0.25	0.38	0.13
May 08	0.42	0.16	0.28	0.14	0.23	0.25	0.36	0.16
May 09	0.41	0.18	0.27	0.14	0.18	0.30	0.39	0.13
May 28	0.40	0.17	0.29	0.14	0.23	0.27	0.35	0.15
June 04	0.46	0.14	0.28	0.12	0.17	0.32	0.41	0.10
Mean 2017 values	0.49	0.12	0.30	0.09	0.24	0.25	0.40	0.12

TABLE 6.3: Mean fraction values in flux magnitude and in number of events of the 3 m high dust flux in each quadrant as defined in section 5.2.2 for the 9 selected dust emission events of the 2018 experiment for the  $2.5 \mu\text{m}$  dust particle. Also presented is the averaged values across all 2017 events.

Information regarding the turbulent transport of dust can be obtained from the quadrant partitioning of the dust flux, as explained in section 5.2.2. Table 6.3 presents the quadrant partitions

of the  $2.5 \mu\text{m}$  dust particle in magnitude of flux and in number of events for the 9 selected dust emission events of the 2018 experiment. Overall, the dust flux quadrant partitions are comparable with the 2017 experiment [Dupont *et al.* 2019b] (Appendix B), with ejections (Q1) dominating the flux magnitude and sweeps (Q3) the number of events. This suggests that the emitted dust was transported dissimilarly to momentum during the emission events, like in 2017 over the bare surface. With increasing wind speed, for example between April 07 ( $u_{*0} = 0.42 \text{ ms}^{-1}$ ) and April 17 ( $u_{*0} = 0.60 \text{ ms}^{-1}$ ), there is an increase in the Q1 contribution to the number of events and a decrease in Q2 contribution to both the flux magnitude and the number of events. This change in the quadrant partitions, towards the partitioning of the momentum flux (Fig. 5.9), was demonstrated in Chapter 5 to be consistent with an increase in the similarity between dust and momentum transports with increasing wind intensity. These observations suggest that the presence of sparse vegetation does not affect significantly the near-surface turbulent transport of dust during the emission events. This is further investigated in Chapter 7 from simulations using the 3D erosion model.

### 6.3.5 Particle Size Distribution (PSD) of the 3 m high EC dust flux

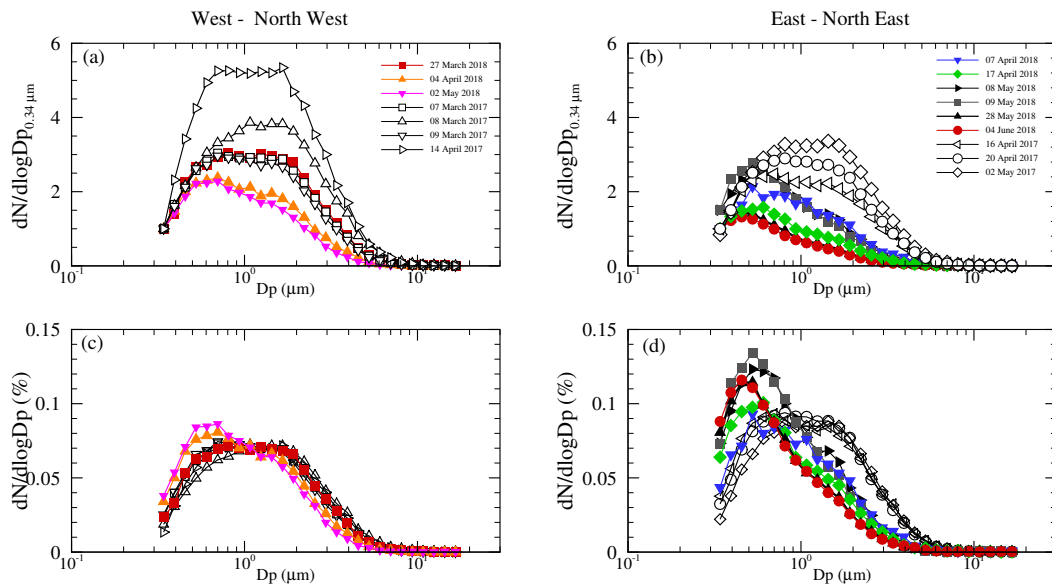


FIGURE 6.6: Particle size distribution (PSD) of the 3 m high EC dust number flux normalized by that of (a) the smallest bin and (b) all bins, for 2017 (unfilled symbols) and 2018 (filled symbols) erosion events, as a function of the wind direction. The PSD is the average of all 15 minute time periods for an event.

Figure 6.6 presents the particle size distribution (PSD) of the EC dust number flux as a function of wind direction for the 2017 (unfilled symbols) and 2018 (filled symbols) erosion events, normalized by the (a) flux of the smallest particles and (b) total dust flux. It shows that the dust flux PSD comprises of two principal modes -  $0.60 \mu\text{m}$  and  $1.50 \mu\text{m}$ . Compared to the 2018 events, the relative contribution of the two modes for the 2017 experiment show little variation

between events, with only a slightly higher contribution of the  $1.50 \mu\text{m}$  mode on March 08 and May 02 (Fig. 6.6a,b, Table 7.1).

Contrastingly, for the 2018 events, the dust flux PSD shows significant variations between events, with a more dominant contribution of the  $0.60 \mu\text{m}$  in the dust fluxes sourced from the eastern quarter (Fig. 6.6b). The dust emitted from the western quarter (Fig. 6.6a) has comparable modal contributions with the 2017 events, especially for the March 27 event, with a marginally higher contribution of the smaller mode for the April 04 and May 02 events. These variations between the two principal modes could be either due to an enrichment of the smallest particles ( $0.60 \mu\text{m}$  mode) or an impoverishment of the larger particles ( $1.50 \mu\text{m}$  mode). This is deciphered using Fig. 6.7 from the relative variations of the size-specific fluxes as a function of the surface friction velocity.

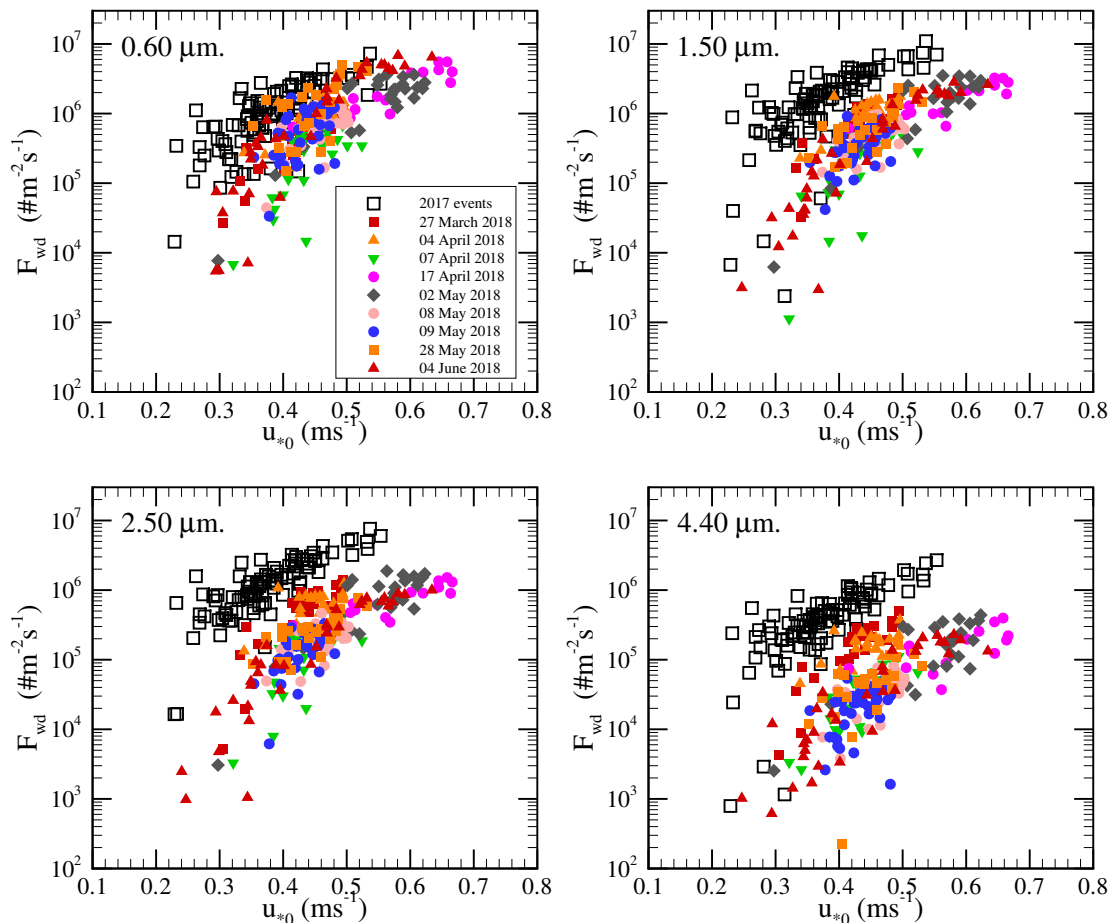


FIGURE 6.7: The variation with surface friction velocity ( $u_{*0}$ ) of the dust number flux for four particle sizes -  $0.60$ ,  $1.50$ ,  $2.50$  and  $4.40 \mu\text{m}$  for the 2017 (unfilled symbols) and 2018 (filled symbols) erosion events. Each data point represents a selected 15-minute time period.

For the smaller principal mode ( $0.60 \mu\text{m}$ ), the dust fluxes of the 2017 and 2018 events are closely comparable, with the 2018 events appearing to be slightly less emissive at lower wind speeds which could be related to the differences in the emission friction velocities. The dust number flux over the bare surface shows little variation with particle size up to  $2.50 \mu\text{m}$ , with

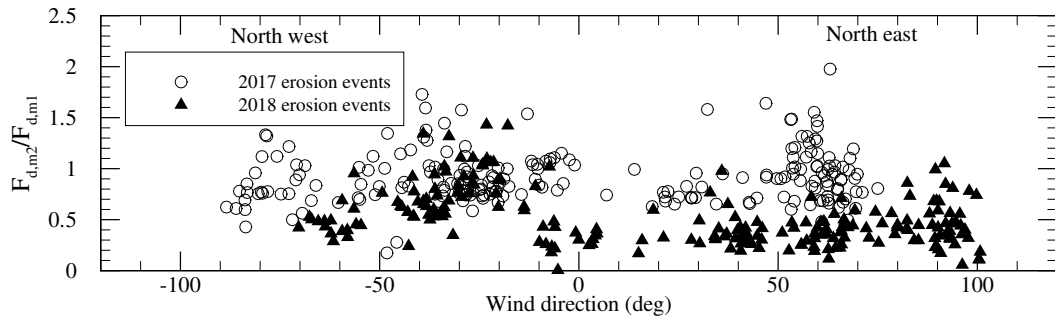


FIGURE 6.8: Variation of the ratio of the dust fluxes of the 2 principal modes ( $m_1 = 0.60 \mu\text{m}$  and  $m_2 = 1.50 \mu\text{m}$ ) as a function of wind direction for the 2017 (unfilled circles) and 2018 (filled triangles) erosion events. Each data point represents a selected 15-minute time period.

the flux of the  $4.40 \mu\text{m}$  bin being slightly lower than that of smaller particles. However in 2018, there is a decrease in the flux contribution with increasing size in comparison with the  $0.60 \mu\text{m}$  mode. This demonstrates that the observed PSD variability is due to an impoverishment of the dust flux in larger particles. Fig. 6.8 suggests that this impoverishment could be a function of the wind direction, with the dust fluxes emanating from the eastern quarter being more impoverished in comparison with those from the 2017 experiment.

Plausible reasons for this impoverishment are discussed in the next section.

## 6.4 Discussion on the dust flux PSD variability

### 6.4.1 Comparison of EC and FG dust fluxes

Prior to discussing the impoverishment of the dust flux in large particles, we find it important to verify the reliability of the EC dust flux by comparing it to the FG dust flux estimated from the vertical concentration gradient between 4.3 m and 2.0 m (Fig. 3.8b in chapter 3). The latter one is based on the FG similarity discussed in Chapter 2, assuming similarity in the turbulent transport of dust and momentum, and constant dust flux between the two measurement heights.

Figure 6.9 demonstrates that the variability in the dust flux PSD between the 2018 events, especially the dominant impoverishment from the eastern quarter, is visible in both the EC and FG fluxes. For the westerly events and the strong easterly event of April 17, the dust flux PSDs estimated using the 2 methods are closely comparable. For the weaker easterly events of April 07, May 08, and May 09, the FG method estimates an even higher contribution of the  $0.60 \mu\text{m}$  mode to the total dust flux. This may be related to the shallow internal dust boundary layer developing over the experimental plot, resulting in the upper FG spectrometer being outside of it and thereby measuring lower dust concentrations from the weaker upwind off-plot emissions (see section 6.4.5).



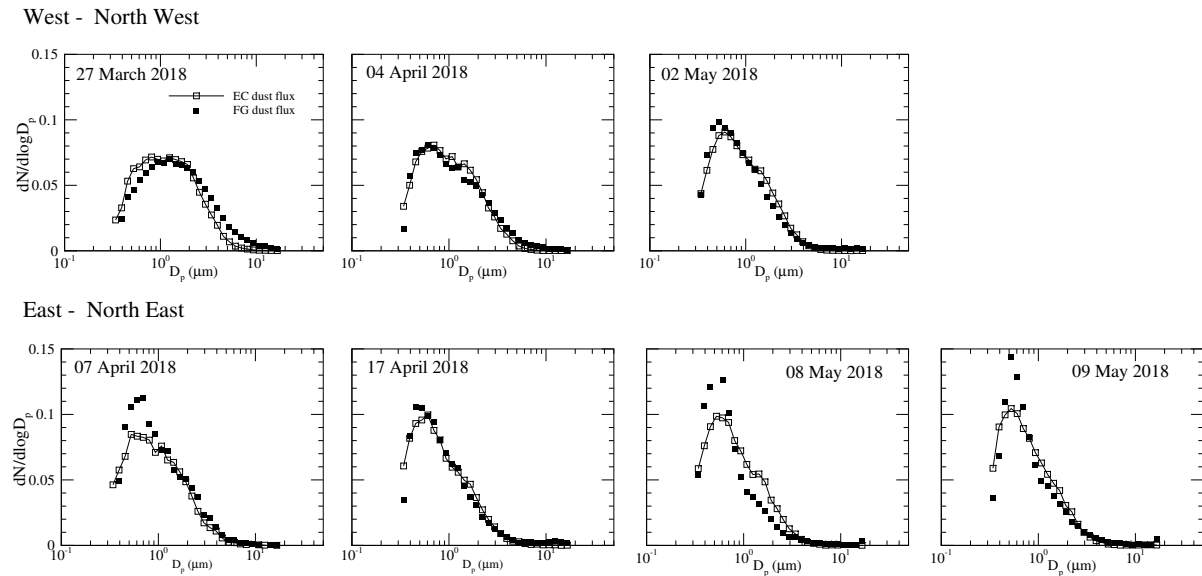


FIGURE 6.9: Comparison between the size-distributions of the dust fluxes estimated using the Eddy-Covariance (EC) and the Flux-Gradient (FG) methods for the first 7 erosion events of the 2018 campaign. During the May 28 and June 04 events, the 2 gradient spectrometers were placed at the same height for inter-comparison validations. The PSDs correspond to the average of all 15 minute periods for an event.

#### 6.4.2 Variability in soil characteristics

The emitted dust PSD is understood to be a function of the soil granulometry and the surface inter-particle cohesive bonding [Marticorena *et al.* 1995; Shao *et al.* 1993; Alfaro *et al.* 2001; Shao 2001]. Since the WIND-O-V's experiments were conducted on the same site (Fig. 6.1), in successive years, we suppose that the soil granulometry remained relatively stable.

Another possible explanation for the variability in dust flux PSD is the change in the inter-particle cohesive bonds due to differences in the soil humidity between the two years, with the 2018 campaign preceded by a more wetter climate. While this can explain the reduced emission of larger dust particles (as cohesive bond is proportional to size), it fails to justify the restriction of the impoverishment to the eastern quarter, and strongest impoverishment for the terminal events of May 28 and June 04 corresponding to less humid soils. The lack of soil humidity measurements during the WIND-O-V campaign limits any further exploration in this regard.

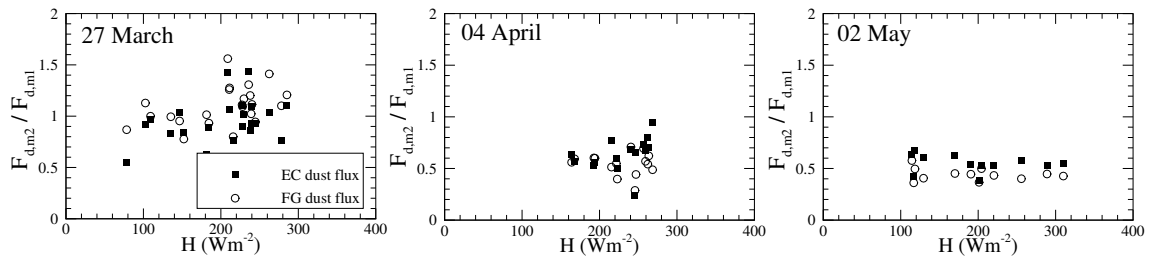
#### 6.4.3 Enhanced re-deposition with vegetation

Vegetation elements can increase re-deposition of the emitted dust particles of the coarser mode through interception, impaction, and sedimentation [Slinn 1982; Petroff *et al.* 2010], as discussed in Chapter 2. Furthermore, the increased occurrence of weak momentum sweeps in the lee of the vegetation elements [Mayaud *et al.* 2016b] may also encourage re-deposition. However, the negligible 2% vegetation cover (Fig. 6.1d) questions the extent of re-deposition

due to vegetation. Furthermore, (i) the similarity between the dust flux size-distribution at the beginning of the 2018 experiment, when the vegetation was at its maximum height, and that of 2017, and (ii) the increasing impoverishment (Fig. 6.6) of the  $1.50 \mu\text{m}$  mode with decreasing vegetation height (Fig. 6.1c), supports the hypothesis of negligible re-deposition on to vegetation elements. Moreover, the 150 m fetch, similar to the 2017 experiment, is too short for the deposition fluxes to reach levels equivalent to those of emission, and the emitted particles are quickly evacuated from the experimental plot as shown in the simulations of Chapter 5. Nonetheless, re-deposition effects are investigated using our 3D erosion model in Chapter 7.

#### 6.4.4 Thermal buoyancy effect on particle transport

West - North West



East - North East

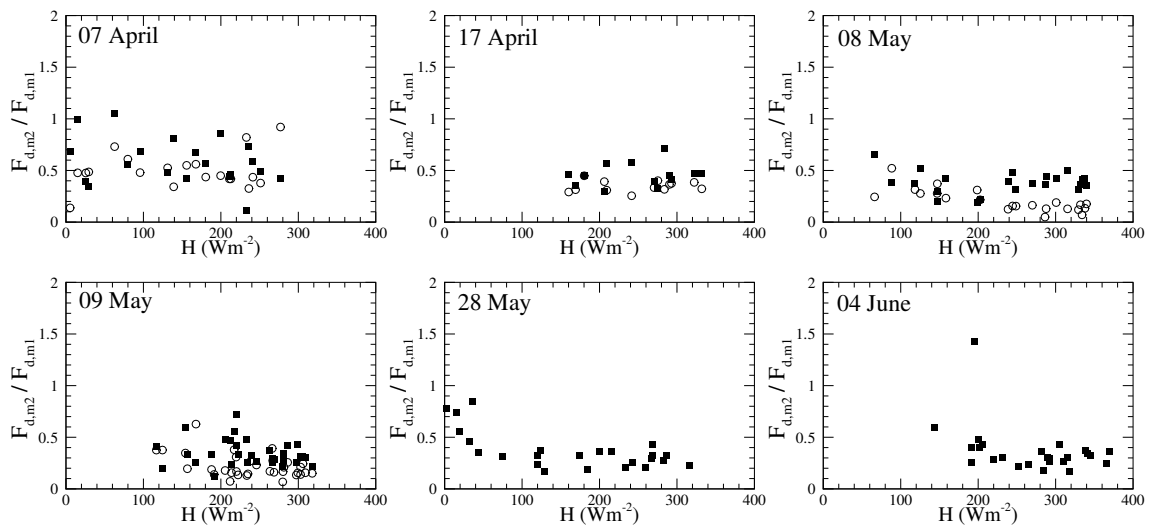


FIGURE 6.10: Variation of the ratio of the dust fluxes of the 2 principal modes ( $m1 = 0.60 \mu\text{m}$  and  $m2 = 1.50 \mu\text{m}$ ), estimated using the FG and EC methods, with the sensible heat flux. The FG dust flux for the last two events cannot be estimated as the two spectrometers were under inter-comparison at the same height. Each data point represents a 15 minute averaging period.

Recent field experiments of Li *et al.* [2011] and Smedman *et al.* [2007] suggest that under unstable atmospheric stratification the turbulent transfer of scalars (like dust) is dissimilar to momentum, with the former being more efficiently transported. Based on this, we question if the observed impoverishment of larger particles is related to a preferential transport of the smaller particles with increasing instability. To investigate this, we study the variation of the

ratio between the 2 principal modes of the dust flux ( $F_{d,1.50\mu\text{m}}/F_{d,0.60\mu\text{m}}$ ) as a function of the sensible heat flux. A more favourable transport of the smaller mode with increasing instability would result in the decrease in  $F_{d,1.50\mu\text{m}}/F_{d,0.60\mu\text{m}}$  with sensible heat flux. Figure 6.10 suggests that across all erosion events, both the EC and the FG dust flux show no clear trends of preferential small particle transport with sensible heat flux. Therefore, the observed impoverishment is most likely not related to atmospheric stratification.

#### 6.4.5 Fetch (foot-print) limitation

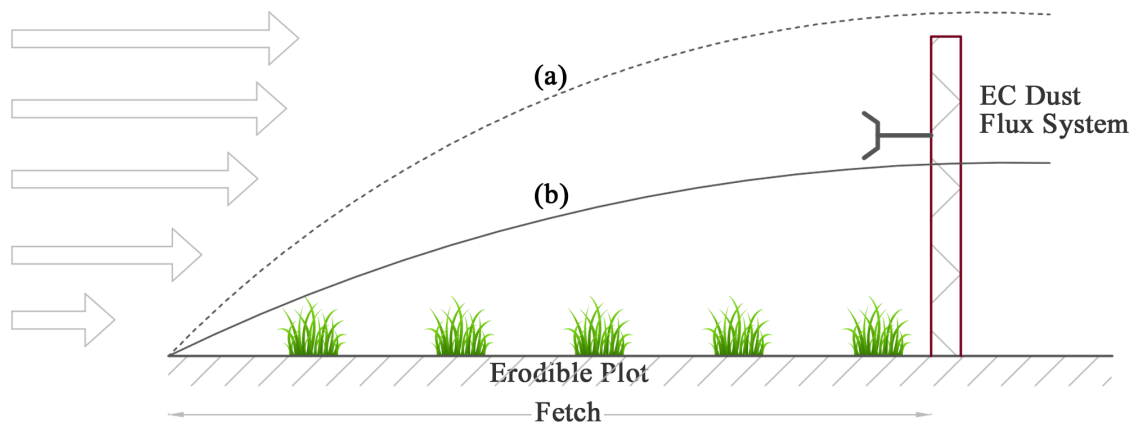


FIGURE 6.11: Schematic representation of the EC dust flux system (a) well within and (b) outside the internal dust boundary layer.

The variability in the dust flux PSD could also be due to fetch limitations associated with the development of an internal dust boundary layer, leading to possible contributions of the upwind off-plot emissions to the measured fluxes under weak erosive winds. As demonstrated in chapter 5, the quadrant partitioning of the dust flux provides information regarding the positioning of the dust flux measurement relative to the boundary layer, i.e. whether the measured flux is well within the boundary layer (Fig. 6.11a) and thus adequately representative of local emissions, or whether it is outside the boundary layer (Fig. 6.11b), incorporating fluxes emitted farther away (background dust fluxes).

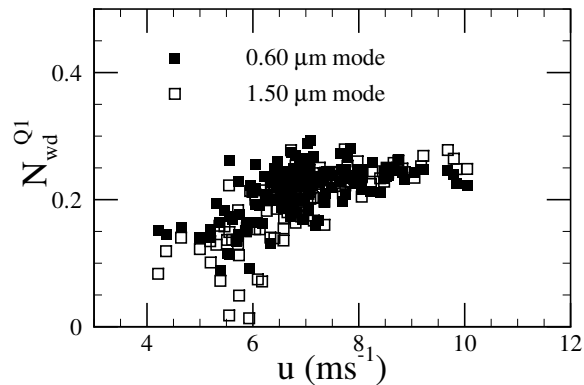
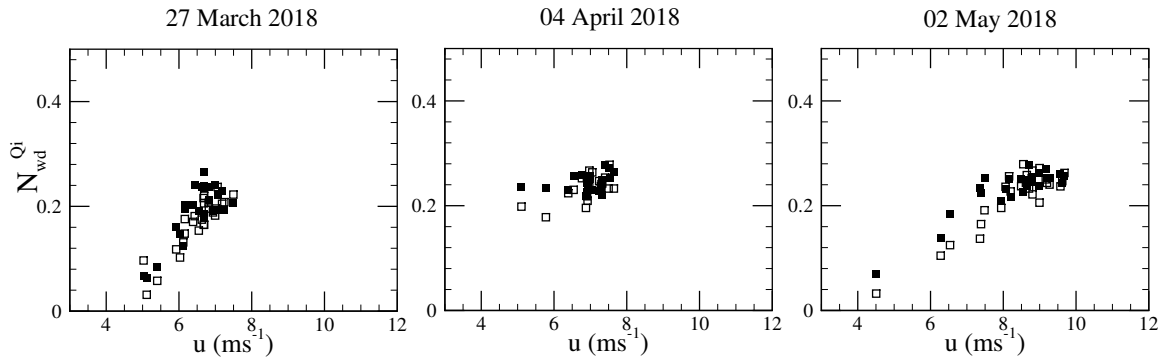


FIGURE 6.12: Variation with wind speed of the Q1 quadrant partition of the 15-minute averaged dust flux in event number ( $N_{wd}^{Q1}$ ) for the 2 principal modes,  $0.60\ \mu\text{m}$  (filled squares) and  $1.50\ \mu\text{m}$  (unfilled squares), for the 2017 experiment. Each data point represents a 15 minute averaging period.

For erosion over the bare surface (Figure 6.12), the number of ejection events carrying particles ( $N_{wd}^{Q1}$ ) of the two principal modes are closely comparable, regardless of the wind direction, increasing simultaneously, as expected, with wind speed. This quadrant partition resembles

the simulated ones (see section 5.4) for fluxes estimated well within the dust boundary layer, suggesting that the measured flux is dominated by local emissions, and implying that the particles of the 2 modes are fed equally-intermittently [Dupont *et al.* 2019b] to the near-surface turbulent eddies transporting them.

### West - North West



### East - North East

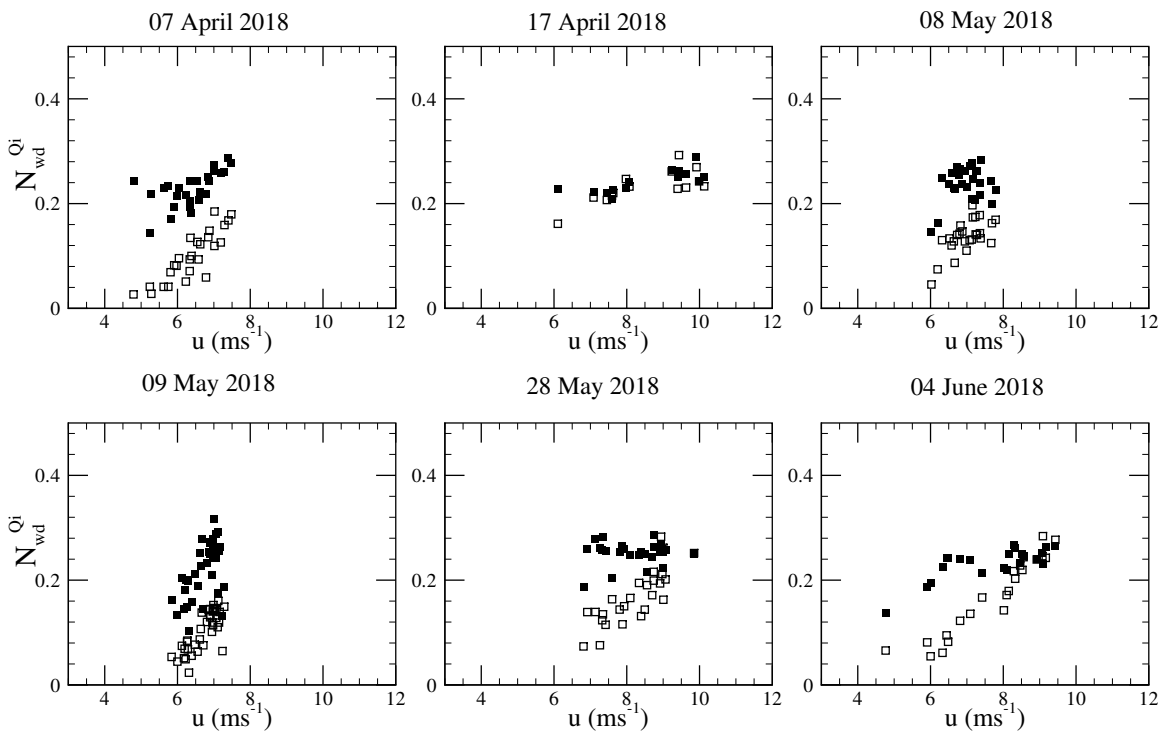


FIGURE 6.13: Same as figure 6.12 for the 9 selected emission events of the 2018 experiment.

In 2018 (Fig. 6.13), the quadrant partitions of the 2 principal modes for the westerly events are comparable with those of the 2017 experiment, with a similar decrease in  $N_{wd}^{Q1}$  of the two modes at very low wind speeds. On the contrary, we observe a marked difference between the ejection events of the two modes for the easterly events, except for April 17. The sharper decrease in  $N_{wd}^{Q1}$  of the  $1.50 \mu\text{m}$  mode indicates the scarcity of these larger particles available to be carried away by the turbulent eddies. This is comparable to the simulated fluxes at the edge of the dust boundary layer (see section 5.4). Therefore, we suspect that the easterly events, except the

strong April 17 event, were characterized by a shallow internal dust boundary layer resulting in the EC OPC measurements possibly contaminated (as mentioned for the 4.3 m high FG OPC in section 6.4.1) by weaker emissions from the off-plot upwind surfaces. This is further supported by the differences in the EC and FG dust flux PSDs for these events, as against a strong resemblance in the PSDs for the April 17 event with a well developed internal dust boundary layer (Fig.6.9).

Fetch limitation could lead to an impoverishment of dust flux in larger particles during relatively weak emission events. However, it cannot explain the strong impoverishment on April 17, as this event was characterized by a well developed internal dust boundary layer seen from the similarities between the EC and FG dust flux PSDs (Fig.6.9). This shows that fetch limitation is not the main reason for the dust flux impoverishment.

#### 6.4.6 Source depletion

As mentioned in section 6.2, our field experiments featured many erosion events, some of which could not be considered before due to measurement or averaging limitations. In this section, we consider all erodible winds that emitted dust from the plot, irrespective of the wind direction.

Figure 6.14a shows the reduction in the ratio between the 2 principal modes ( $F_{wd,1.5\mu m} / F_{wd,0.6\mu m}$ ) of the 3 m high dust flux during the 2018 field experiment from about 1.0 on March 21 to 0.2 on June 04. This reduction features three trends - (Z1) an initial sharp reduction to  $F_{wd,1.5\mu m} / F_{wd,0.6\mu m} = 0.8$  between March 21 and March 27, (Z2) a subsequent, relatively slower reduction to about  $F_{wd,1.5\mu m} / F_{wd,0.6\mu m} = 0.4$  by April 17, and (Z3) an increase to  $F_{wd,1.5\mu m} / F_{wd,0.6\mu m} = 0.6$  on April 27, followed by a slow reduction to 0.2 by June 04. The change from Z1 to Z2 coincides with the surface tillage on March 26. The increase in  $F_{wd,1.5\mu m} / F_{wd,0.6\mu m}$  on April 27 (Z3) follows the April 17 rain event and the April 26 surface tillage. This indicates that the impoverishment of the dust flux in large particles is related to the nature of the surface rather than to the vertical transport of the emitted particles. This is confirmed by the absence of a similar trend in the ratio of the transfer velocities  $V_{t,1.5\mu m} / V_{t,0.6\mu m}$  (Figs. 6.14b).

Likewise, the 2017 campaign (Fig. 6.15a) shows a reduction in  $F_{wd,1.5\mu m} / F_{wd,0.6\mu m}$  from 0.8 to 0.5 from March 07 to March 11 (Z1). But the subsequent dust emission periods (Z2, Z3, and Z4), characterized by frequent rain-tillage events, display no trend in  $F_{wd,1.5\mu m} / F_{wd,0.6\mu m}$ .

During both experiments, the study site was continuously eroded irrespective of the wind direction. This continuous surface emission can be quantified roughly by the cumulative sum of the wind speed or the surface friction velocities, for  $u_{*0} > u_{*t}$  (Figs. 6.14c and 6.15c), as dust emission fluxes can be expressed as a function of one of these quantities (section 2.2.5). For the 2018 campaign, the first reduction in  $F_{wd,1.5\mu m} / F_{wd,0.6\mu m}$  up to March 27 (Z1) corresponds

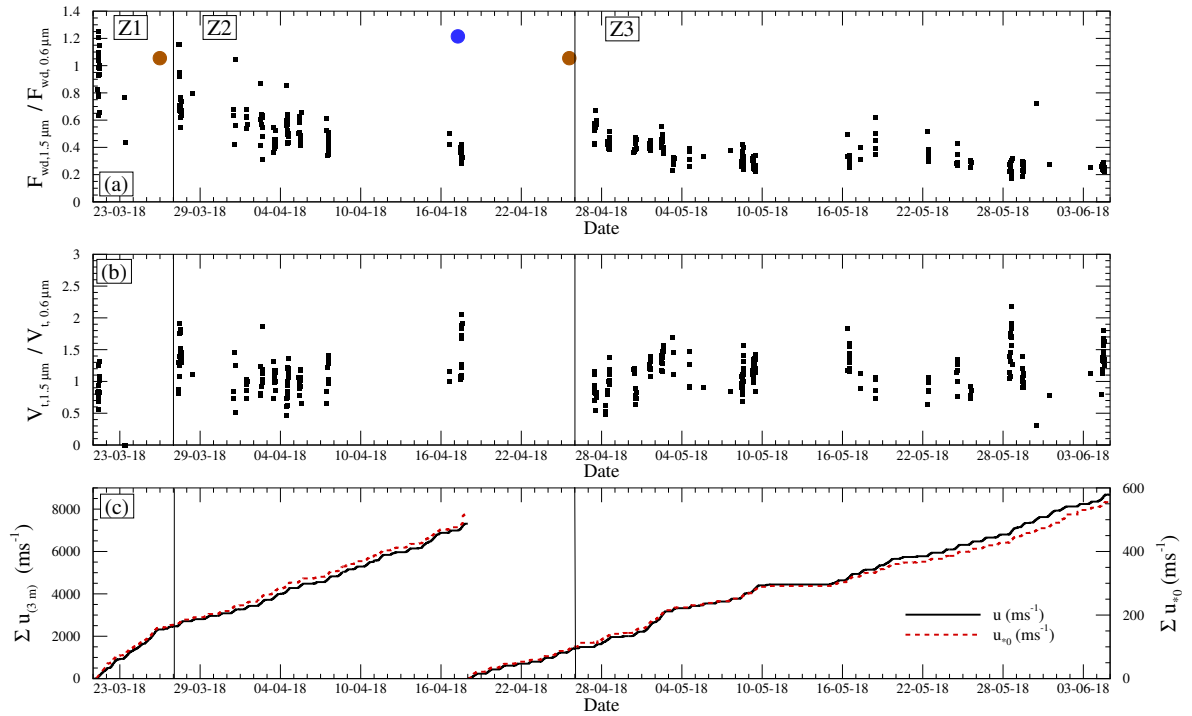


FIGURE 6.14: Time variation of (a) the ratio of the dust fluxes of the  $1.5\ \mu\text{m}$  and  $0.6\ \mu\text{m}$  modes, (b) the ratio of the transfer velocities of the  $1.5\ \mu\text{m}$  and  $0.6\ \mu\text{m}$  modes, and (c) the cumulative wind speed (solid line) and surface friction velocity (dotted line) during the WIND-O-V's 2018 field experiment. The fluxes and transfer velocities correspond to emission events with the wind blowing along  $100^\circ < \theta < 270^\circ$ . The cumulative values in (c) cover the entire duration of the experiment, regardless of the wind direction, for winds stronger than the bare soil threshold ( $u_{*t} > 0.22\ \text{ms}^{-1}$ ). The blue circles correspond to rain events and the brown circles to tilling operation (surface preparation). Z1, Z2, and Z3 are the three emission periods.

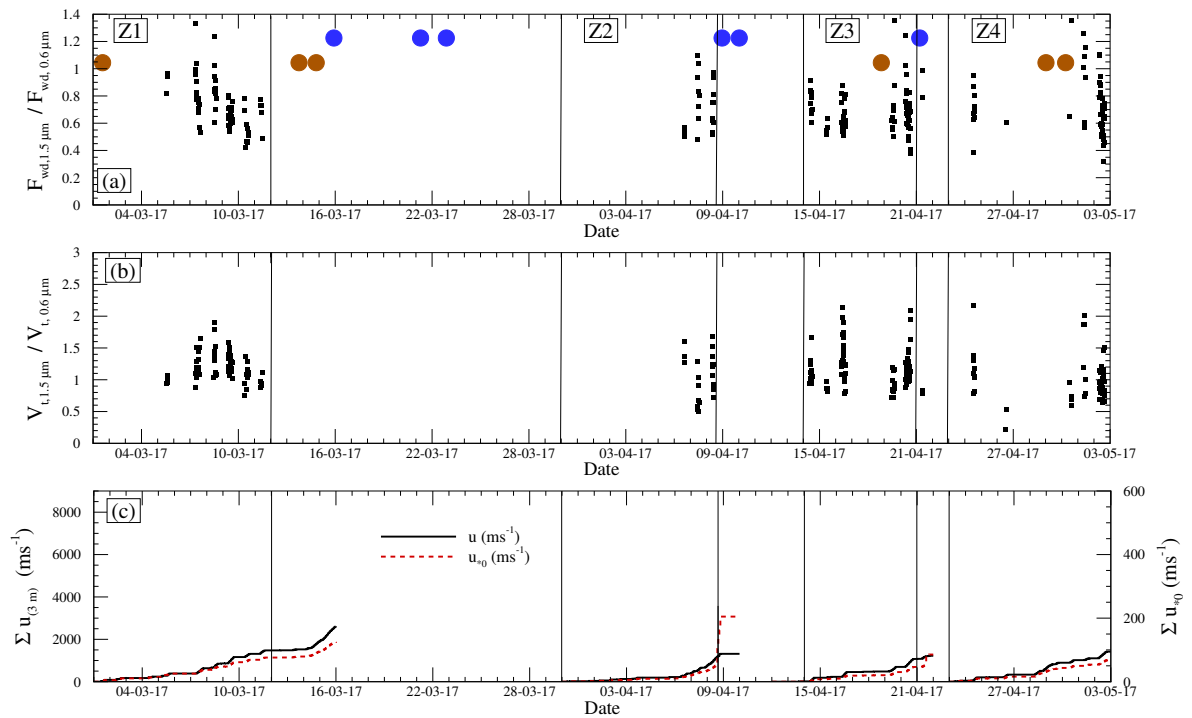


FIGURE 6.15: Same as Fig 6.14 for the WIND-O-V's 2017 field experiment.

to a sharp increase in the cumulative sum of the 3 m high mean wind (or surface friction velocity) with a slope of about  $464 \text{ ms}^{-1}/\text{day}$  ( $40 \text{ ms}^{-1}/\text{day}$ ), without any surface modifications from rainfall or tillage. The subsequent reduction in  $F_{wd,1.5\mu\text{m}}/F_{wd,0.6\mu\text{m}}$  from 0.8 to 0.6 between March 27 and April 17 (Z2) corresponds to a lesser slope of the cumulative mean wind (friction velocity) of about  $215 \text{ ms}^{-1}/\text{day}$  ( $16 \text{ ms}^{-1}/\text{day}$ ), before the interruption of emission by a strong rain event. The final trend after April 17 corresponds to a slope of  $166 \text{ ms}^{-1}/\text{day}$  ( $13 \text{ ms}^{-1}/\text{day}$ ). The four 2017 erosion periods (Z1 to Z4) were generally characterized by lesser mean wind (or surface friction velocity) slopes, except for the last 5 days of Z1 where we observed the only impoverishment in coarse particles of this year.

Figs. 6.14 and 6.15 illustrate an important difference between the 2017 and 2018 experimental campaigns. The 2018 experiment was marked by two periods of dust emissions, ranging over 28 and 48 days, respectively, whereas the 2017 experiment had four dust emission sets of shorter duration ranging between 8 to 12 days, interrupted by rain events. This shows that the impoverishment of the coarser particles ( $> 1.5 \mu\text{m}$ ) seen during the 2018 experiment is due to their depletion at the source resulting from prolonged periods of wind erosion. The three trends of the 2018 experiment suggest that the source depletion is both a function of the wind intensity and emission duration, with the short stronger emissions of the first 7 days (March 21 to March 27) causing the same level of depletion as the weaker but longer emissions of the next 22 days (March 27 to April 17), and the much weaker and more longer emissions over the subsequent 39 days (April 27 to June 04). A similar depletion was not observed for the 2017 experiment due to the short emission periods, except for the initial 5-day long emission period (March 07 and March 11).

During both experiments, rain and surface tillage events altered the dust emission trend. These events appear to reset the surface, increasing the availability of the coarser  $1.5 \mu\text{m}$  mode for emissions. This is clearly seen after the April 26 tillage event of the 2018 experiment, and also explains the continuous availability of the larger mode during the 2017 experiment marked by a greater frequency of rain-tillage events. The physics of source depletion or the mechanism through which the rain and tillage events increase the emissions of the coarse dust particles still eludes us and needs to be further investigated, especially soil granulometry analysis.

## 6.5 Conclusions

The WIND-O-V's field experiments aspired to investigate the role of sparse vegetation on the quantity and size of the emitted dust in semi-arid regions. The comparison between the 2018 and 2017 experiments, with and without vegetation, confirmed that sparse vegetation reduces dust emission by reducing the flow energy available to drive erosion. Our results showed that the erosion threshold varied as a function of the wind direction, with winds parallel to the vegetation arrangement being most erosive, and further decreased with the vegetation height.

Comparison between dust fluxes from the 2017 and 2018 experiments revealed differences in their size distributions characterized by the progressive impoverishment in coarse particles in 2018. This impoverishment appeared not related to differences in soil properties, re-deposition over vegetation, the preferential turbulent transport of the smaller particles, or fetch limitations. Interestingly, the impoverishment was found to be independent of vegetation, and caused by the depletion of coarser particles ( $1.5 \mu\text{m}$ ) at the surface due to stronger winds and longer erosion periods without rain-tillage events as compared to 2017. During both experiments, the rain and tillage events appeared to reset the surface, increasing the availability of the coarser particles, with these events being less frequent in 2018. These results suggest the possibility of a continuous evolution in the availability of erodible dust particles at the surface, influenced in part by meteorological or human interventions. This should be considered in large-scale dust dispersion modelling.

Overall, sparse vegetation reduces the quantity of the dust emitted but does not affect the size of the near-surface dust flux in comparison with the bare surface. This is supported by the similarity between the dust flux size-distribution at the beginning of the 2018 experiment, when the vegetation was at its maximum height, and those of 2017. This investigation is extended over larger surfaces in the next chapter using the 3D erosion model.





# 7 Investigating sparse vegetation impact on the suspended dust during emission events

The investigations of the previous chapter are continued here, focussing on the role of near-surface turbulence and the deposition process on the suspended dust flux during emission events over sparsely vegetated surfaces. This is achieved through numerical experiments using the 3D erosion model presented in Chapter 3, evaluated here against the WIND-O-V's 2018 field experiment.

**Keywords:** 3D erosion model, LES model, sparse vegetation, dust emission, dust size-distribution, semi-arid erosion, dust flux, dust flux PSD

**Abstract:** *The WIND-O-V's field experiment demonstrated a negligible impact of vegetation on the size-distribution of the 3 m high dust flux during emission events. This is further investigated in this chapter using the 3D erosion model, described in Chapter 3, and evaluated here over sparsely vegetated surfaces against the WIND-O-V's 2018 field experiment. Our simulations illustrate differences in the near-surface turbulence between bare and sparsely vegetated surfaces, especially close to the surface, influencing saltation and dust emission patterns. They show that sparse vegetation promotes a more similar transport between momentum and dust close to the surface in comparison with the bare surface. This turbulence transport difference, however, does not affect the size-distribution of the dust flux. Furthermore, a sensitivity analysis of the deposition processes indicates little impact of vegetation on the size-distribution of the suspended dust, independent of the fetch, vegetation density, and wind intensity. Finally, this last result suggests that the deposition process only influences the size-distribution of the dust flux when the emission and deposition fluxes are of the same order of magnitude, an extension of the inferences of Chapter 4*

## 7.1 Introduction

Quantifying dust emissions, especially their size-distribution, from semi-arid regions in climate models remains challenging due to large seasonal and geographical variations in surface properties [Pierre *et al.* 2012] such as vegetation, surface moisture, land-use patterns etc.. The size-distribution of the airborne dust matters due to its influence on weather and climate, among other Earth system processes [EEA 2014; Weuve *et al.* 2012; Derbyshire 2007; Griffin *et al.* 2001; Swap *et al.* 1992]. The representation of airborne dust-size in large-scale models has evolved from a single particle size in Jousaume [1990] to 12 bins in Zhao *et al.* [2003]. Recent experimental campaigns like JADE - with measurements of atmospheric and surface properties, and saltation and dust fluxes in Australia [Ishizuka *et al.* 2008] and AMMA - with continental scale dust flux measurements and ocean deposition along West Africa [Lebel *et al.* 2010], have helped improve regional-scale modelling of dust dispersion [Menut *et al.* 2009], particularly the representation of the airborne dust-size. Nevertheless, the size-distribution of the dust flux, i.e. the size-relative contribution of the individual bins to the total dust flux, remains challenging. This is explained by the (i) limited understanding of the role of surface properties, especially sparse vegetation, on the quantity and size of the suspended dust, and (ii) lack of a comprehensive local mapping of surface properties. In this regard, dust emissions from arid regions are relatively easier to characterize, aided by a certain regional homogeneity in surface properties. However, dust emissions over semi-arid regions are less understood due to influences of seasonal vegetation, land-use patterns, and weather conditions on their quantity and size.

Field experiments in different semi-arid environments have been extensively used to understand erosion (saltation) patterns. They have led to the development of large-scale semi-empirical erosion models such as Wind Erosion Equation [Woodruff *et al.* 1965], the Revised Wind Erosion Equation [Fryrear *et al.* 2000], the Wind Erosion Prediction System [Tatarko *et al.* 2007] etc., capable of incorporating local surface properties. However, proportionality factors between the emitted dust and saltation fluxes vary by many orders of magnitude [Shao 2008], partly due to variations in surface characteristics. Therefore, the linking of dust emissions to saltation schemes could be erroneous due to (i) differences in the intermittency and spatial heterogeneities of saltation and dust emission patterns related to surface properties, and (ii) differences between the near-surface sorting of the emitted dust / saltators in the presence of vegetation and that over a bare surface.

At the plant-scale, there exists substantial experimental data, both on the field and inside wind tunnels, demonstrating a reduction in erosion (saltation) with sparse vegetation [Wolfe *et al.* 1993; Hagen 1994; Lancaster *et al.* 1998; Sutton *et al.* 2008; Burri *et al.* 2011, etc. ]. These experiments, however, focussed mainly on the study of sand transport, and paid little attention to dust emissions. In this regard, the recent experimental work of Mayaud *et al.* [2016a], examining flow patterns around typical semi-arid vegetation, attempts to provide some insight

into the near-surface transport of the emitted dust. Adding to this, is the WIND-O-V's field experiment, that demonstrated a reduction in the quantity of dust emitted, and a negligible impact of vegetation on the dust flux size-distribution in comparison with bare surface emissions. Such field experiments, provide important information on the dust emission process, but can often be limited in their observational range. For example, the WIND-O-V's field experiment was limited by dust flux measurements at 3 m from the surface, and therefore was unable to observe dust transport within the vegetation layer and dust emissions at the surface. Furthermore, such experiments can also be limited by instrument range concerning frequency of acquisition, the size-range of dust measured etc. As demonstrated in Chapter 5, such limitations can be overcome through numerical experiments. Furthermore, numerical models can help map dust suspensions covering all semi-arid regions, an otherwise expensive and laborious physical (in-situ) process, and thereby contribute to better dust representation in climate models.

Shao *et al.* [1999], Dupont *et al.* [2013], Klose *et al.* [2013], and Dupont *et al.* [2015] were among the first to showcase the reliability of numerical models to reproduce wind erosion, coupling flow turbulence, erosion intermittency, and dust dispersion over bare surfaces. Later Dupont *et al.* [2014] extended the scope of such modelling to erosion (saltation) over sparsely vegetated surfaces. The advantage of such numerical modelling is the ability to reproduce (i) commonly occurring dust emission scenarios that may be difficult to be explicitly observed in nature, (ii) erosion scenarios with varying surface properties and wind conditions, and (iii) examine erosion processes at the finest of scales difficult to be seen on the field. These advantages have been previously demonstrated in Chapter 5 wherein our 3D erosion model was used to reproduce and investigate the turbulent dust transport dissimilarity with momentum observed during the WIND-O-V's 2017 experiment.

In this chapter, this 3D erosion model is extended to sparsely vegetated surfaces, following Dupont *et al.* [2014], and evaluated against the WIND-O-V's 2018 field experiment detailed Chapter 6. Thereafter, this model is used to investigate the role of near-surface turbulence and deposition onto vegetation on the size-distribution of the suspended dust. Here, our investigations focus on dust dispersion over very large erodible surfaces with homogeneous sparse vegetation, unlike the short 150 m fetch of the field experiment. This is because the fetch effects have already been evaluated in Chapter 5. Finally, we intend to present a reliable numerical tool to quantify dust emissions over different semi-arid environments, thereby contributing to the development of a regional scale dust emission model over semi-arid regions and improving dust representation in climate models.

## 7.2 Material and method

The 3D erosion model used here is described in Section 3.3.

### 7.2.1 Simulation details

Wind erosion was simulated under neutral stratification over a flat, dry surface with sparse vegetation in conditions similar to the first three erosion events (March 27, April 04, and April 07) of the WIND-O-V's 2018 field experiment (detailed in Chapters 3 and 6). The computational domain extended over  $20 \times 15 \times 10$  m, corresponding to  $200 \times 150 \times 100$  grid points in the  $x$ ,  $y$  and  $z$  directions, respectively. The domain was discretized with a 0.1 m resolution along the horizontal and 0.01 m grid spacing at the surface along the vertical and stretched above. This fine resolution was chosen to simulate the main turbulent exchanges close to the surface where the concentration of dust particles is very high.

The lateral boundary conditions were periodic for both wind flow and sand-particle motion. As previously mentioned in Chapter 5, this enabled the simulation of a very large erodible surface, with a regular vegetation arrangement, and a well-developed saltation layer. Dust dispersion condition was different from the WIND-O-V's 2018 experiment and the numerical experiment in Chapter 5, with a periodic lateral boundary condition that ignores fetch effects. This was chosen to study dust dispersion over large erodible surfaces, i.e independent of the fetch. The effects of fetch on the near-surface dust flux were not considered due to the similarities between the 2017 and 2018 experiments, in particular the turbulent dust transport over short erodible plots, already explored in Chapter 5.

The surface soil was comprised of a unimodal log-normal size-distribution of the saltating particles  $p_s(D)$  having a mean diameter  $100 \mu\text{m}$  and a geometric standard deviation of 1.2 (Fig. 5.1). The dust size-distribution available in the surface soil ( $p_d(d_b)$ ) was divided into ten bins between  $0.45 \mu\text{m}$  and  $10.00 \mu\text{m}$ .  $p_d(d_b)$  was taken differently from that for the bare surface, with a strong concentration (in number) of the  $1.50 - 2.50 \mu\text{m}$  mode (Fig. 7.1), the progressively varying mode during the 2018 experiment. This distribution was chosen to investigate the influence of deposition on the size-distribution of the dust flux during emission events.

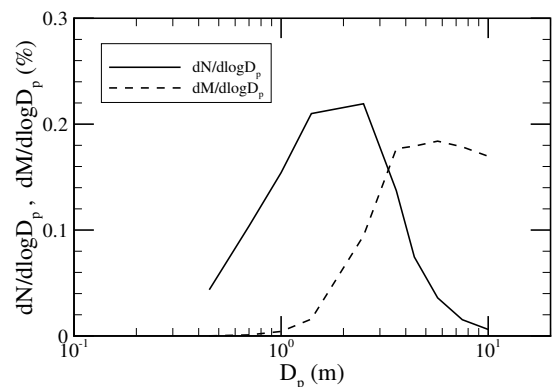


FIGURE 7.1: Particle size distribution (PSD) of the surface dust as the percentage contribution of the individual bins in number ( $dN/d\log D_p$  - solid line) and mass ( $dM/d\log D_p$  - dotted line).

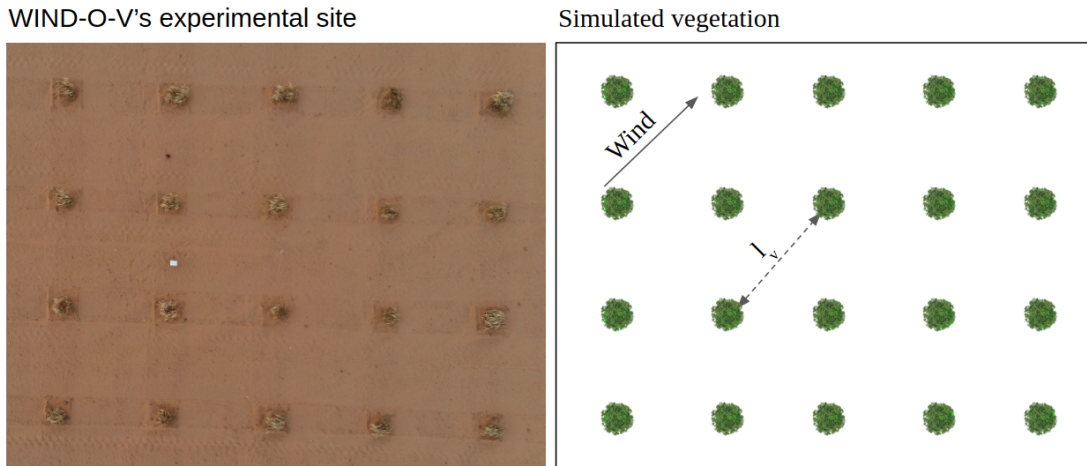


FIGURE 7.2: The plan-view of the vegetation on the WIND-O-V's experimental site in 2018 and the schematic of the simulated vegetation. Here  $l_v$  represents the inter-plant distance along the mean wind direction.

Vegetation effects, representative of the barley tufts during the WIND-O-V's 2018 experiment (Fig. 7.2), were incorporated by modelling shrubs as half-ellipsoids of height  $h_v = 0.5$  m, width  $d_v = 0.9$  m and a leaf area index of about 0.1. This configuration (L1 in Fig. 7.3) provided a surface cover ( $c_v$ ) of 6.5 % and was used in evaluation cases C1 and C2 (Table 7.1), and the subsequent case C3. Two more vegetation configurations, L2 and L3 (Fig. 7.3), were then evaluated with plant widths  $d_v = 0.7$  m and 0.5 m, and surface cover of 25 % and 18 %, corresponding to simulations C4 and C5, respectively.

In addition to  $h_v$ ,  $d_v$ , and  $c_v$ , another parameter defining the vegetation arrangement is  $l_v$  - the distance between two successive vegetation elements along the mean wind direction. For example, Fig. 7.2 illustrates the  $l_v$  for a wind blowing at  $45^\circ$  to the vegetation arrangement. This  $l_v$  is higher than that when the wind blows at  $0^\circ$  or  $90^\circ$  to the vegetation arrangement, but lower than that when the wind is at  $30^\circ$  or  $60^\circ$  to it. Therefore,  $l_v$  accounts for the inter-plant surface area available for the mean wind to erode. In this study, simulations C1, C2, and C3 (Table 7.1) with the same vegetation configuration L1, differed solely by the mean wind direction relative to the vegetation arrangement, leading to  $l_v = 2.5$  m ( $45^\circ$ ), 3.5 m ( $0^\circ$ ), and 6.8 m ( $60^\circ$ ). For cases C4 and C5,  $l_v$  changed to 1.1 m and 0.8 m due to the higher number density of the vegetation configurations L2 and L3 (Fig. 7.3).

Like in Chapter 5, soil erosion was simulated following Dupont *et al.* [2013], through a two-step procedure. First, the flow dynamics was simulated without erosion with an air free of dust until the flow reaches equilibrium with the surface. Then, 10,000 initially resolved saltating particles were released randomly within 0.3 m from the surface, and the erosion modules were activated. Erosion events were then simulated for 10 minutes with a time step of  $\Delta t = 400 \mu s$ .

Twelve simulations of 10 minute wind erosion were performed. The first two simulations (cases C1 with  $u_{*sb} = 0.33 \text{ ms}^{-1}$  and C2 with  $u_{*sb} = 0.32 \text{ ms}^{-1}$ ) were used to evaluate the 3D erosion model. They were characterized by the same vegetation configuration (L1) featuring

Simulation	$c_v$ (%)	$l_v$ (m)	Configuration	Wind direction (°)	$u_{*sb}$ ( $\text{ms}^{-1}$ )	Deposition parametrization
C1	6.5	2.5	L1	45	0.27, 0.33, 0.60	Section 3.3
C2	6.5	3.5	L1	0, 90	0.35	Section 3.3
C3	6.5	6.8	L1	30, 60	0.26, 0.32	Section 3.3
C4	25	1.1	L2	45	0.54	Section 3.3
C5	18	0.8	L3	45	0.54	Section 3.3
C1-M1	6.5	2.5	L1	45	0.33	altered: M1
C4-M1	25	1.1	L2	45	0.54	altered: M1
C4-M2	25	1.1	L2	45	0.54	altered: M2
C1-M3	6.5	2.5	L1	45	0.33	altered: M3

TABLE 7.1: Main characteristics of the twelve simulations: the vegetation surface cover ( $c_v$ ), inter-plant distance along the mean wind direction ( $l_v$ ), vegetation layout, wind direction, and the equivalent bare surface friction velocity ( $u_{*sb}$ ). Simulations C1 and C2 are comparable with the WIND-O-V's 2018 field experiment detailed in Chapter 6. The first set of simulations (C1 - C5) have deposition parametrized as detailed in Chapter 3, and the second set (C1-M1, C4-M1, C4-M2, and C1-M3) feature modified deposition parameterized - detailed later in this chapter. The estimation of  $u_{*sb}$  is detailed in section 7.2.2

different wind intensities and wind directions, comparable with the first three erosion events



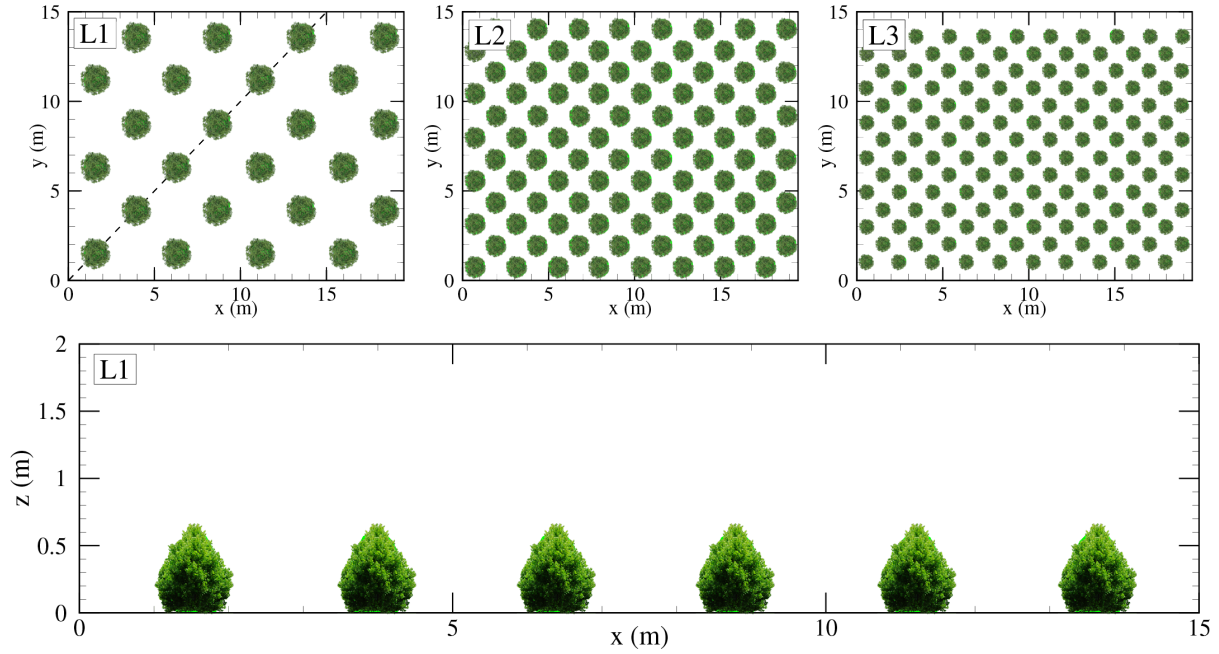


FIGURE 7.3: Schematic representation of the plan-view of the simulated vegetation layouts L1, L2, and L3 (top figures) and the diagonal cross section of L1 (bottom figure).

(March 27, April 04, and April 07) of the 2018 experiment. Two additional simulations for case C1 with  $u_{*sb} = 0.27 \text{ ms}^{-1}$  and  $0.60 \text{ ms}^{-1}$  were then simulated to study the role of wind intensity on dust emissions. Next, two simulations (C3 with  $u_{*sb} = 0.26$  and  $0.33 \text{ ms}^{-1}$ ) similar to C1 and C2, differing only with the wind aligned at  $60^\circ$  to the vegetation arrangement were executed. Finally, two more cases, C4 and C5 (both with  $u_{*sb} = 0.54 \text{ ms}^{-1}$ ), with vegetation configurations L2 and L3 were simulated to evaluate the effects of vegetation density on the wind flow, saltation, and dust dispersion. Thereafter, the role of deposition on the size-distribution of the dust flux during emission events was investigated through four cases, C1-M1, C4-M1, C4-M2, and C1-M3, with M1, M2 and M3 referring to modifications of the dust deposition parametrization.

## 7.2.2 Data analysis

Wind dynamics, saltation, and dust quantities have been horizontally averaged over the entire domain since periodic conditions were considered for all simulations.

To compare the vegetation cases between themselves and with the bare surface, the surface friction velocity  $u_{*sv}$  observed over the vegetation surface is converted to an equivalent bare surface friction velocity  $u_{*sb}$  following Dupont *et al.* [2014]. This is enabled by assuming that the mean velocity profiles above both the equivalent bare and vegetated surfaces are equal at a reference altitude  $z_{ref}$ , taken here to be 50 m. Assuming both profiles are logarithmic, we get

$$u_{*sb} = u_{*sv} \log\left(\frac{z_{ref}}{z_{0sv}}\right) / \log\left(\frac{z_{ref}}{z_{0sb}}\right), \quad (7.1)$$

where  $z_{0sv}$  is the roughness length of the vegetated surface and  $z_{0sb}$  is the saltation roughness length over the bare surface expressed as,

$$z_{0sb} = \left( \frac{Au_{*sb}}{2g} \right)^{1-r} z_0^r, \quad (7.2)$$

where  $A = 0.21$ ,  $r = u_{*t}/u_{*sb}$  with  $u_{*t}$  the saltation threshold friction velocity over bare soil equal to  $0.22 \text{ ms}^{-1}$  in this study. The bare surface roughness is taken to be  $z_0 = 100 \mu\text{m}$ , equivalent to the WIND-O-V's field site [Dupont *et al.* 2018] and  $z_{0sv}$  is estimated from the log profile of the simulated wind velocity.

In addition to quadrant analysis (Sec. 5.2.2), dust and momentum transports are investigated here using octant analysis. Here, the quadrant decomposition of the momentum flux is further decomposed based on the sign of the dust fluctuations. For this, the momentum flux in quadrant  $Q_i$  ( $\langle u'w' \rangle_{Q_i}$ ) is decomposed as,

$$\langle u'w' \rangle_{Q_i} = \langle u'w' \rangle_{Q_i}^{d^+} + \langle u'w' \rangle_{Q_i}^{d^-}, \quad (7.3)$$

and the number of events responsible for the flux is decomposed as,

$$n_{Q_i}^{uw} = n_{Q_i}^{uw,d^+} + n_{Q_i}^{uw,d^-}, \quad (7.4)$$

where  $d^+$  and  $d^-$  refer to positive or negative dust fluctuations. The magnitude percentages of momentum flux in quadrant  $Q_i$  coincident with  $d^+$  or  $d^-$  are estimated as,

$$F_{Q_i}^{uw,d^+} = 100 \times \frac{|\langle u'w' \rangle_{Q_i}^{d^+}|}{\sum_{Q_i} |\langle u'w' \rangle_{Q_i}|}, \quad (7.5)$$

and

$$F_{Q_i}^{uw,d^-} = 100 \times \frac{|\langle u'w' \rangle_{Q_i}^{d^-}|}{\sum_{Q_i} |\langle u'w' \rangle_{Q_i}|}, \quad (7.6)$$

Similarly, the event number percentages coinciding with  $d^+$  or  $d^-$  are estimated as,

$$N_{Q_i}^{uw,d^+} = 100 \times \frac{n_{Q_i}^{uw,d^+}}{\sum_{Q_i} n_{Q_i}^{uw}}, \quad (7.7)$$

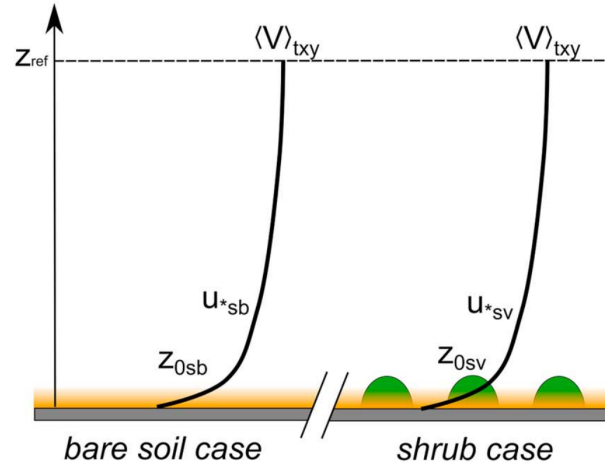


FIGURE 7.4: Schematic representation of the calculation of the equivalent saltation friction velocity  $u_{*sb}$  over bare sand from the wind profiles simulated over vegetated surfaces composed of shrubs. Source: Dupont *et al.* [2014]

and

$$N_{Q_i}^{uw,d^-} = 100 \times \frac{n_{Q_i}^{uw,d^-}}{\sum_{Q_i} n_{Q_i}^{uw,d^-}} \quad (7.8)$$

### 7.3 Model evaluation

The 3D erosion model is first evaluated on its ability to simulate both the wind dynamics during erosion events, and the average and instantaneous characteristics of saltation and dust dispersion, using data from the WIND-O-V's 2018 experiment (Chapter 6) and published literature.

#### 7.3.1 Flow dynamics

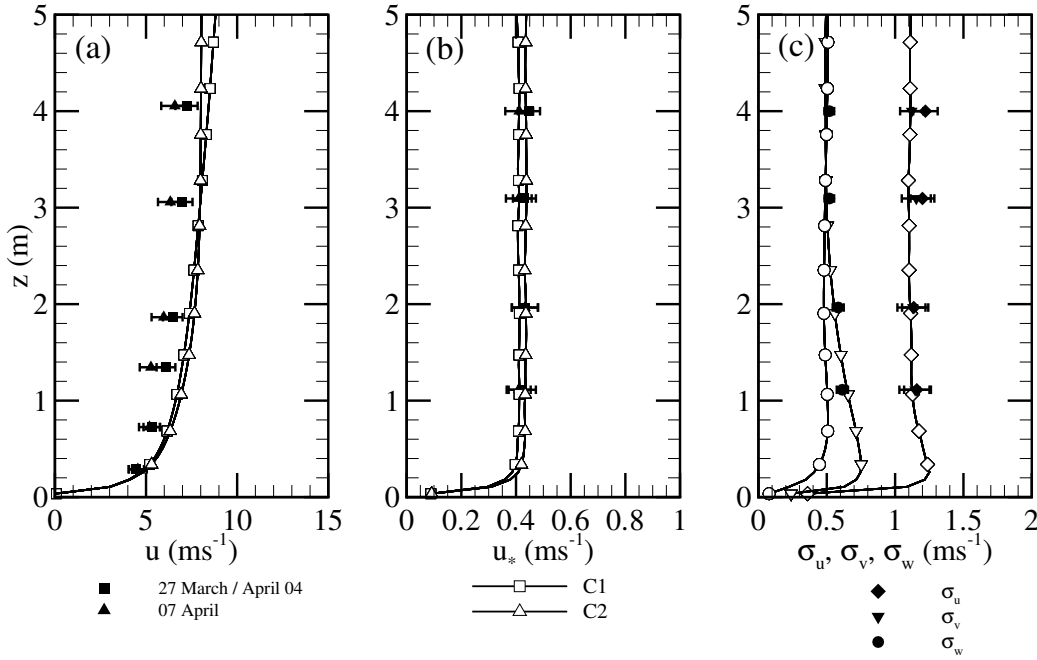


FIGURE 7.5: Comparison between simulations (lines with unfilled symbols) C1 (squares) and C2 (triangles) and the field measurements (filled symbols) on the mean vertical profiles of (a) the longitudinal wind velocity ( $u$ ), (b) the local friction velocity ( $u_*$ ), and (c) the standard deviations of the three velocity components ( $\sigma_u, \sigma_v, \sigma_w$ ) for C1. The error bars refer to the standard deviations of the experimental values for periods with similar wind intensity.

The mean vertical profiles of the wind velocity ( $u$ ), local friction velocity ( $u_* = \sqrt[4]{\langle u'w' \rangle^2 + \langle v'w' \rangle^2}$ ), and standard deviations of the three velocity components ( $\sigma_u, \sigma_v, \sigma_w$ ), obtained from simulations C1 and C2 are compared with the corresponding profiles from the WIND-O-V's 2018 experiment, for a similar surface friction velocity  $u_{*sv}$  (Fig. 7.5). Here C1 is compared with the March 27 and April 04 events having a mean wind at about  $45^\circ$  to vegetation arrangement, and C2 with the April 07 event with mean wind along the vegetation inter-rows. These first three

experimental events were characterized by a relatively constant surface roughness (section 6.3.3) that diminished thereafter. Similar to the bare surface, our model reproduces well the expected logarithmic velocity profile (Fig. 7.5a) and the constant momentum flux layer (Fig. 7.5b). Consistent with the field experiment, the sparse vegetation does not affect the wind profile within the vegetation layer ( $z < 0.5$  m). The overestimation of  $u$  could be explained by the strict neutral stratification in our simulation as opposed to the slightly unstable stratification during the experiment (Fig. 6.2), similar to the bare surface simulations (Section 5.3.1). Both  $\sigma_u$  and  $\sigma_w$  fit also well the experimental values, only  $\sigma_v$  appears underestimated (Fig. 7.5c for C1) like the bare soil simulations.

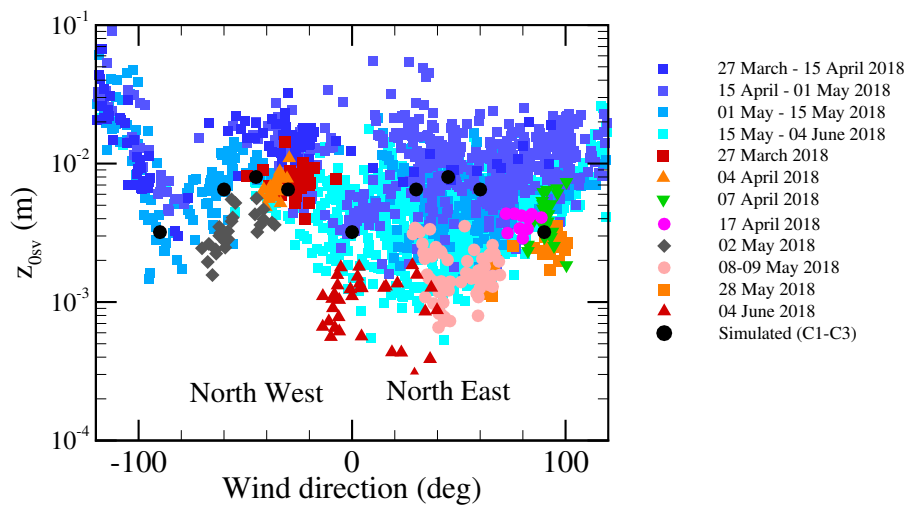


FIGURE 7.6: Variation with wind direction of the simulated aerodynamic roughness length  $z_{0sv}$  (filled circles) in comparison with the observations from the 2018 field experiment. Similar to Fig. 6.5.

During the WIND-O-V's 2018 field experiment, the aerodynamic roughness length ( $z_{0sv}$ ) varied with wind direction with a maximum when the wind was diagonal to the vegetation rows and minimum when parallel to them (Fig. 6.5). This was verified in our simulations by first considering case C1 with  $u_{*0sb} = 0.33 \text{ ms}^{-1}$  and mean wind blowing at  $45^\circ$  to the  $x$ -axis. This configuration yielded  $z_{0sv} = 0.008$  m. Next, two erosive winds were simulated in cases C2 and C3 by merely changing the mean wind direction to  $0^\circ$  and  $60^\circ$ , respectively, relative to the  $x$ -axis. For these cases, our model simulated the change in the mean  $z_{0sv}$  similar to the average trend of the field experiment. The symmetrical nature of our model and the periodic conditions for wind flow imply that a wind blowing at  $60^\circ$  is equivalent to that blowing at  $30^\circ$  to the  $x$ -axis, and so on for other wind directions. The decrease in  $z_{0sv}$  during the experimental duration related to changing vegetation characteristics was not considered in this study. Nevertheless, our model is capable of reproducing differences in  $z_{0sv}$  as a function of the vegetation characteristics. This has also been demonstrated in the previous simulations of Dupont *et al.* [2014].

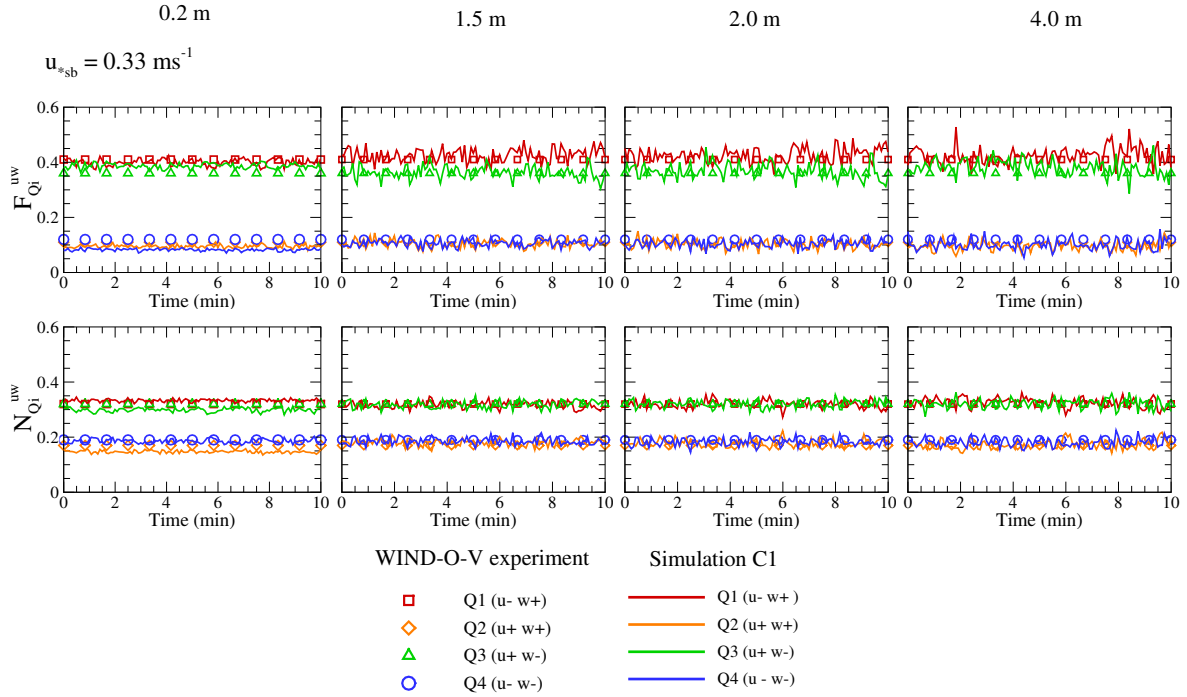


FIGURE 7.7: Time variation of the quadrant partitioning of the momentum flux  $F_{uw}$  in magnitude ( $F_{Q_i}$ ) and in event number ( $N_{Q_i}$ ), as defined in equations 5.1 and 5.2, obtained from the 10-min simulated erosion event C1 at four heights (0.2, 1.5, 2.0 and 4.0 m) and compared with the mean fractions obtained at 3 m height from the WIND-O-V's 2018 field experiment.

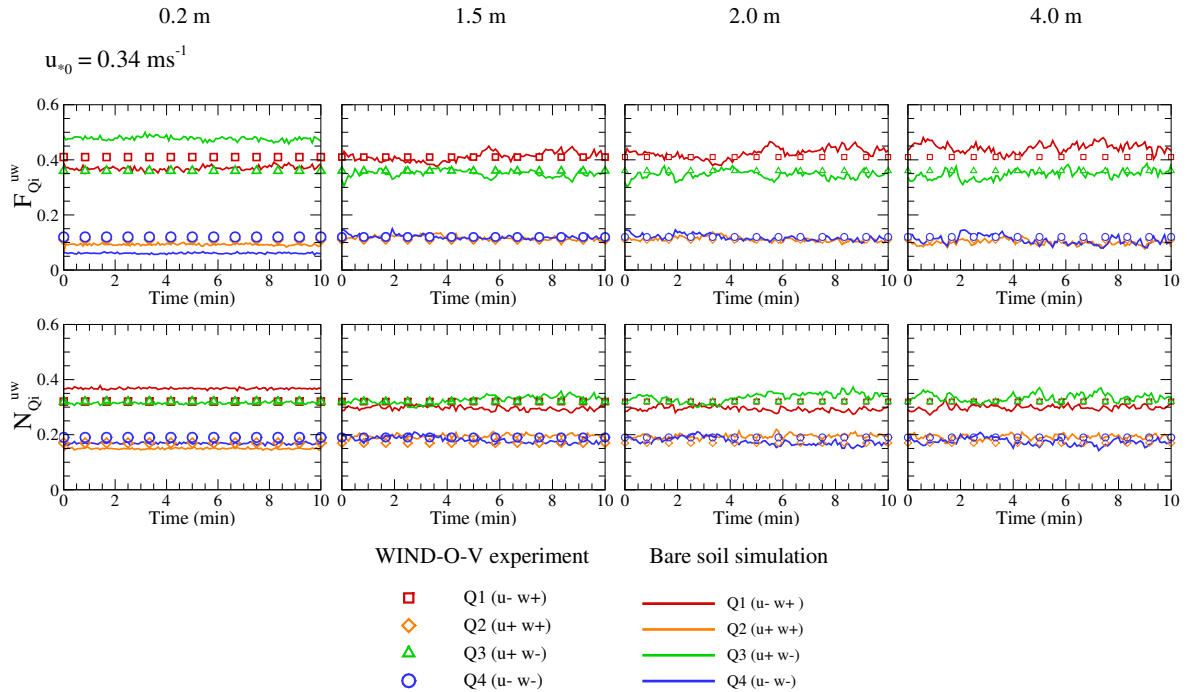


FIGURE 7.8: Same as Fig. 7.7 for the bare surface with  $u_{*0} = 0.34 \text{ ms}^{-1}$ .

Information on the turbulent structures simulated by our model can be obtained from the quadrant partitioning of the momentum flux, like in Chapter 5. At heights well above the vegetation layer ( $z > 0.5$  m in Fig. 7.7), the quadrant partitioning of the simulated momentum flux ( $F_{uw}$ ) is closely comparable to the experimental observations ( $z = 3$  m) and the bare surface simulations (Fig. 7.8), with  $F_{uw}$  primarily driven by ejection (Q1) and sweep (Q3) motions both in event number and flux magnitude. Within the vegetation layer ( $z \approx 0.2$  m), ejection (Q1) and sweep (Q3) motions continue to dominate the momentum flux, unlike over the bare surface ( $z \approx 0.2$  m) where sweeps (Q3) dominate the flux magnitude and ejections (Q1) in event number. Therefore, in comparison with the bare surface, the turbulent transport of momentum over a sparsely vegetated surface appears to be more uniform across all heights. This difference in the momentum transport manifests as a sharp decrease in the contribution of sweep (Q3) motions to the dust flux magnitude, accompanied by small changes in the contribution of other motions, within the vegetation layer in comparison with the bare surface. This may be due to the absorption of momentum by the vegetation elements, and implies a reduction in the efficiency of sweep motions to carry high velocity fluid to the surface, a key driver of saltation. Overall, these results indicate that vegetation elements alter the near-surface turbulence in comparison with that over the bare surface, and were observed independent of the wind intensity.

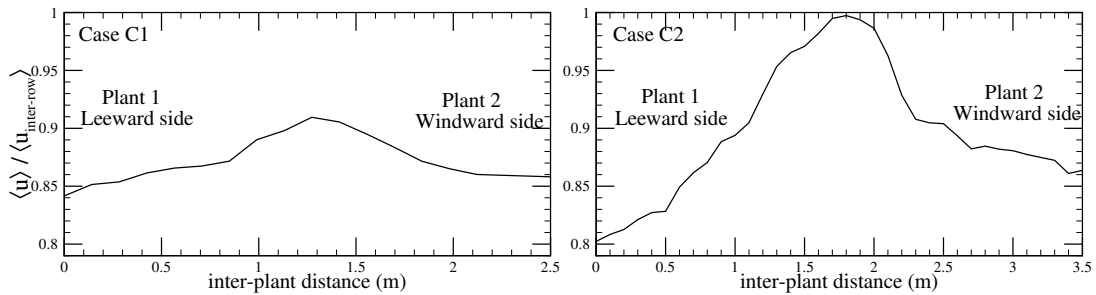


FIGURE 7.9: Variation of the ratio between the velocity in the lee of the vegetation element and the averaged velocity of inter-row region for cases C1 and C2 with inter-plant distances  $l_v = 2.5$  and  $3.5$  m respectively.

Wind measurements around the barley tufts during the WIND-O-V's experiment (Sec. 6.3.1) and around grassy elements in the field measurements of Mayaud *et al.* [2016a] suggested a decrease in wind intensity in the lee of the vegetation elements. This was verified in our simulations through the time average of wind speeds at  $z = 0.2$  m along the vegetation rows in the mean wind direction for Case C1 with  $u_{*0sb} = 0.33 \text{ ms}^{-1}$  and C2 with  $u_{*0sb} = 0.32 \text{ ms}^{-1}$ . In the lee of the barley tufts, our model simulates about a 15-20 % decrease in the mean wind speed in comparison with that in the inter-row region, independent of the wind direction (Fig. 7.9). Overall, our model underestimates the decrease in the wind intensity in the lee of the vegetation in comparison with the 2018 field experiment and may be due to differences in the plant morphology between the experiment and the model which influences the flow characteristics around the vegetation elements [Judd *et al.* 1996]. As expected, the wind speed

increases away from the lee of the vegetation element, towards the inter-row mean value, before decreasing again at the windward edge of the next vegetation element. For case C1, the smaller inter-plant distance ( $l_v$ ) of 2.5 m is insufficient for the flow to fully develop to the inter-row values, unlike that in C2 with a higher  $l_v$  of 3.5 m. This variation in the mean wind speed in the vegetation layer is consistent with the previous simulations of Dupont *et al.* [2014], and the observations of Mayaud *et al.* [2016a] and the WIND-O-V's field experiment.

Altogether, these results demonstrate that our 3D erosion model simulates relatively well the mean wind flow and turbulence characteristics representative of sparsely vegetated surfaces.

### 7.3.2 Erosion dynamics

The simulated saltation reaches an equilibrium state with the wind within the first minute of erosion for all simulations of this study. This was verified similarly to the bare surface simulations (section 5.3.2) from the time variation of the total number of numerically resolved saltating particles (result not shown, but similar to Fig. 5.4a). As expected, the saltation flux including all particle sizes ( $F_{salt,tot}$ ) over the vegetated surface is lower than that over the bare surface, consistent with the observations of Leenders *et al.* [2007] and the simulations of Dupont *et al.* [2014].

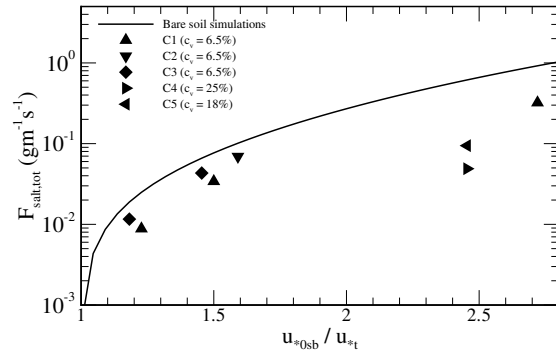


FIGURE 7.10: Simulated saltation fluxes as a function of the equivalent bare friction velocity ( $u_{*sb}$ ) normalized by the saltation threshold ( $u_{*t}$ ) for erosion over the bare surface (solid line) and with vegetation (filled symbols).

Simulation	$u_{*sb}$	$r_{salt}(\%)$
C1	0.27	64
C3	0.26	37
C1	0.33	56
C2	0.35	31
C3	0.32	24
C1	0.60	65
C4	0.54	92
C5	0.54	83

TABLE 7.2: Saltation flux reduction due to vegetation as against that over a bare surface.

For a given vegetation configuration and wind direction, our model reproduces well the increase with wind speed of  $F_{salt,tot}$  in agreement with the previous simulations of Dupont *et al.* [2014] (Fig. 7.10). Table 7.2 presents the reduction of  $F_{salt,tot}$ , evaluated similarly to Dupont *et al.* [2014], by defining a reduction factor  $r_{salt} = 100 \times (F_{salt,tot,bare} - F_{salt,tot,veg}) / F_{salt,tot,bare}$ . It demonstrates that sparse vegetation covering just  $c_v \approx 6.5\%$  of the erodible surface (cases C1 to C3) significantly reduces sand transport up to 56% under moderate erosive winds ( $u_{*sb} \approx 0.33\text{ms}^{-1}$ ). For a given wind intensity ( $u_{*sb}$ ) and surface cover, erosion reduction is a function of wind direction, decreasing with increasing inter-plant distance along the mean wind direction ( $l_v$ ). This is seen from the 32 percentage point change in the

sand transport reduction when  $l_v$  changes from 2.5 m to 6.8 m for the same vegetation configuration (C1 to C3) and at comparable wind intensities ( $u_{*sb} \approx 0.33 \text{ ms}^{-1}$ ). This is explained by the larger apparent erodible surface area available with increasing  $l_v$ . For a given wind speed and wind direction, the reduction in sand transport increases with the surface cover, as seen with the  $r_{salt} = 92\%$  for C4 ( $c_v = 25\%$ ) as against the  $r_{salt} = 83\%$  for C5 ( $c_v = 18\%$ ).

Fig. 7.11 presents the the simulated 3 m high total dust flux ( $F_{wd,tot}$ ) as a function of wind intensity in comparison with that simulated over the bare surface and the observations of the 2018 experiment. Here, the estimated  $F_{wd,tot}$  is restricted to  $d_{p,b} \leq 7.5 \mu\text{m}$  to enable a reliable comparison with that simulated over the bare surface. This comparison remains qualitative due to the differences in the surface dust size-distributions between simulations with and without vegetation, and with the field experiment. The figure shows that our model simulates well the variation with wind intensity and vegetation density of the total dust flux in comparison with the bare surface simulations and the 2018 field experiment. The similarities in the variations between  $F_{wd,tot}$  and  $F_{salt,tot}$  as a function of wind intensity is because dust emissions were driven purely by sandblasting (Sec. 3.3) in our simulations.

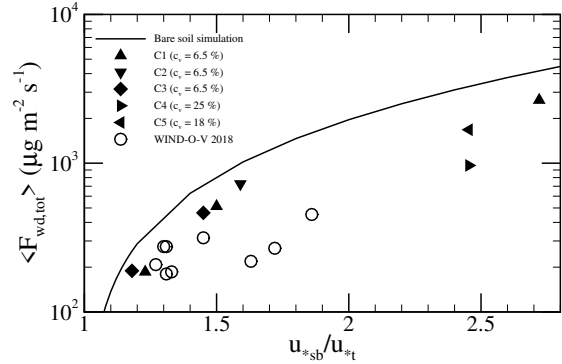


FIGURE 7.11: Simulated 3 m high dust fluxes as a function of the equivalent bare friction velocity for erosion over the bare surface (solid line) and with vegetation (filled symbols). The unfilled circles represent the selected events of the WIND-O-V 2018 experiment.

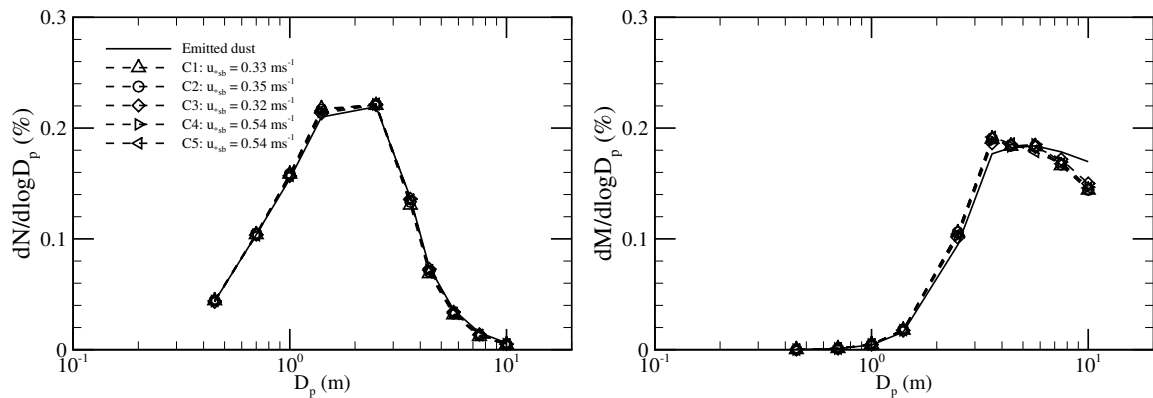


FIGURE 7.12: Particle size distribution (PSD) of the 3 m high dust flux after 10 minutes of simulated erosion for cases C1, C2, C3, C4, and C5 in comparison with that emitted dust at the surface.

The particle size distribution (PSD) of the 3 m high dust flux after 10 minutes of simulated erosion remains close to the surface emission flux across all simulations (Fig. 7.12). In mass, the PSD demonstrates a slight decrease in the contribution of the largest particles, which is due to their high deposition probabilities.



As discussed in Chapter 4, the near-surface dust flux PSD is influenced by the surface dust size-distribution, the cohesive bond parameter  $\beta$ , and the re-deposition during emissions, with the first two remaining constant across all simulations. This implies that re-deposition during emissions in the presence of vegetation remained minimal even under high wind speeds and a relatively high frontal area density ( $c_v = 25\%$  for C4). This last result is most probably due to the channelization of dust emissions and its transport (Fig. 7.13), reducing the probability of deposition on to vegetation.

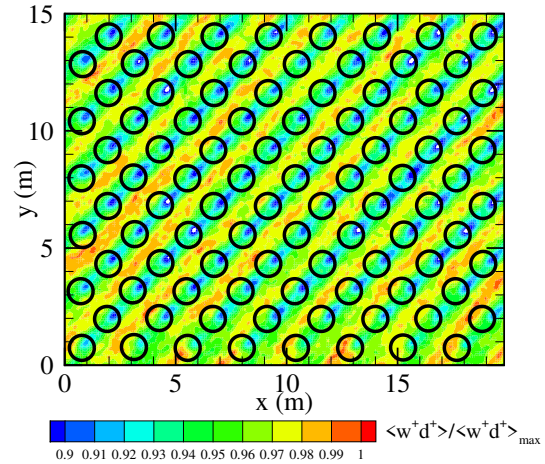


FIGURE 7.13: Time-averaged horizontal cross section ( $x - y$ ) of the dust emissions for case C4 at  $z = 0.1$  m.

### 7.3.3 Near-surface dust turbulent transport

The turbulent transport of the emitted dust is evaluated, similarly to the momentum flux ( $F_{uw}$ ) using quadrant partitioning. Here, the simulated  $F_{wd}$  partitions are not compared to that of the 2018 experiment because our model can reproduce the dissimilarity in the turbulent transport between dust and momentum observed during WIND-O-V's experiments as demonstrated in Chapter 5. The  $F_{wd}$  partitions are instead compared with the  $F_{uw}$  partitions to investigate the degree of similitude between the turbulent transports of dust and momentum during erosion events.

The dust flux ( $F_{wd}$ ) well above the vegetation layer ( $z \geq 2.0$  m in Fig. 7.14) is dominated by ejections (Q1) and sweeps (Q3), with the partitioning of  $F_{wd}$ , in flux magnitude and in number of events, comparable in proportions to those simulated over the bare surface (Fig. 7.15) and the 3 m high experimental momentum flux ( $F_{uw}$ ). This indicates that dust and momentum are transported similarly, i.e. by the same turbulent eddies, at these heights. Immediately above the vegetation layer ( $z \approx 1.5$  m), the quadrant partitions show that dust transport remains similar to momentum. This differs from that at an equivalent height over the bare surface, where dust and momentum transport appear dissimilar, with a decrease in  $F_{wd}^{Q3}$  (sweeps) and an increase in  $F_{wd}^{Q2}$  in comparison with that of  $F_{uw}$ . At the very beginning of the simulation, the  $F_{wd}$  partitions over the vegetation layer deviate from those of the  $F_{uw}$ , similar to the bare surface simulations under periodic dust dispersion condition (Fig. 7.15).

Within the vegetation layer ( $z \approx 0.2$  m), the  $F_{wd}$  partitions are closely comparable to those of  $F_{uw}$  in flux magnitude, but deviate slightly in event number with a marginal decrease in  $N_{wd}^{Q1}$  and a similar increase in  $N_{wd}^{Q2}$ . This last one is most likely associated with intermittent emissions at the surface, leading to the non-availability of dust particles to be associated with

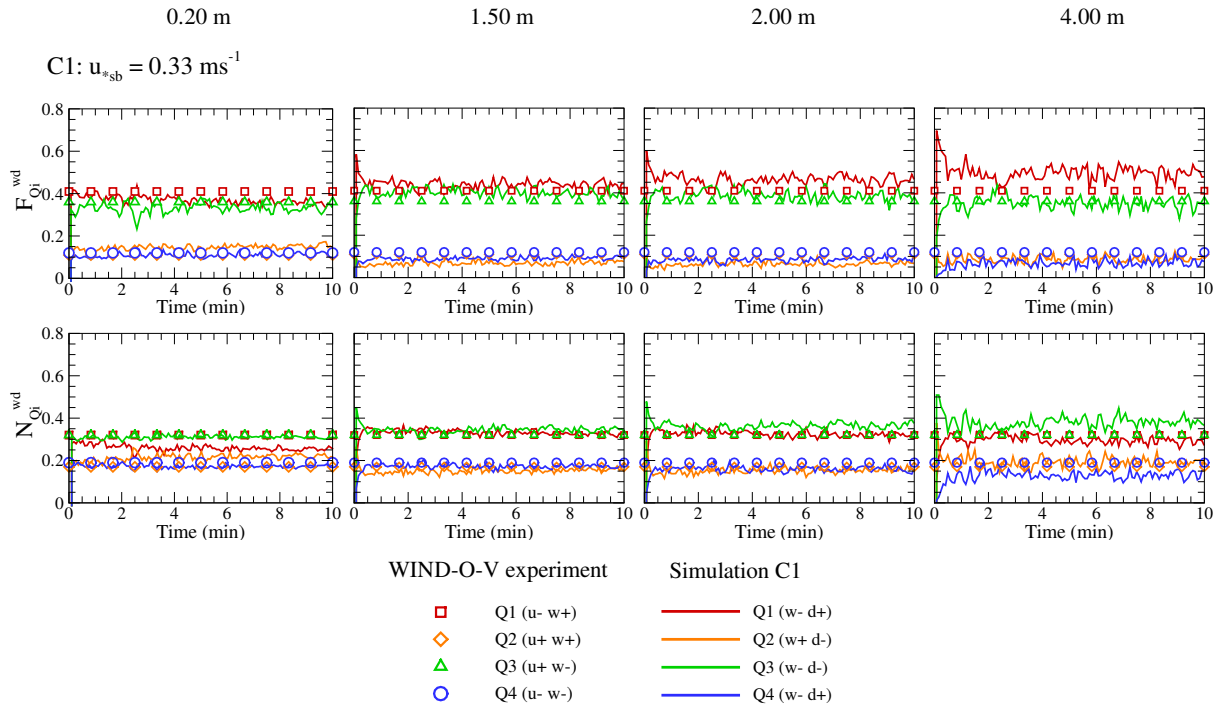


FIGURE 7.14: Time variation of the quadrant partitioning of the dust flux  $F_{wd}$  in magnitude ( $F_{Qi}$ ) and in event number ( $N_{Qi}$ ), as defined in equations 5.1 and 5.2, obtained from the 10-min simulated erosion event C1 at four heights (0.2, 1.5, 2.0 and 4.0 m) and compared with the mean fractions of the momentum flux  $F_{uw}$  obtained at 3 m height from the WIND-O-V’s 2018 field experiment. The quadrants correspond to the  $1.5 \mu\text{m}$  dust size.

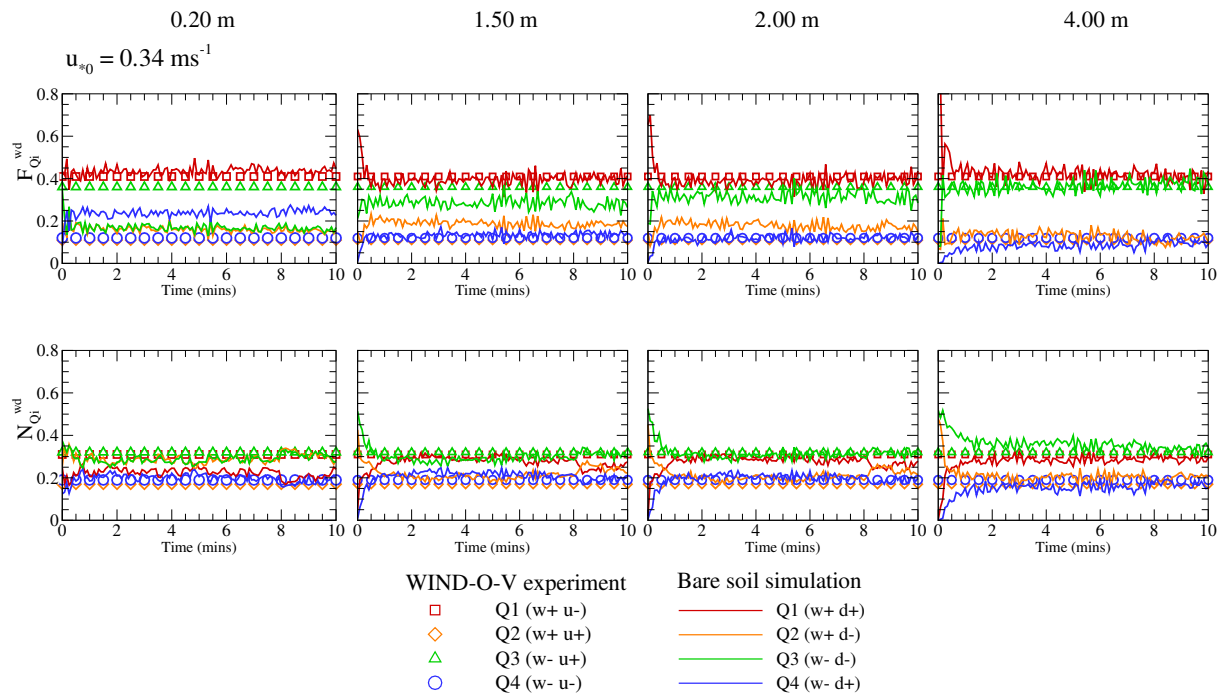


FIGURE 7.15: Same as Fig. 7.14 but for periodic dust dispersion over the bare surface (C6 in Chapter 5).

every momentum ejection. Nevertheless, in comparison with the bare surface, dust appears to be transported more similarly to momentum. This is seen from an approximately 15% increase in the Q3 contribution and an equivalent decrease in the Q4 contribution to the dust flux magnitude, in comparison with the bare surface.

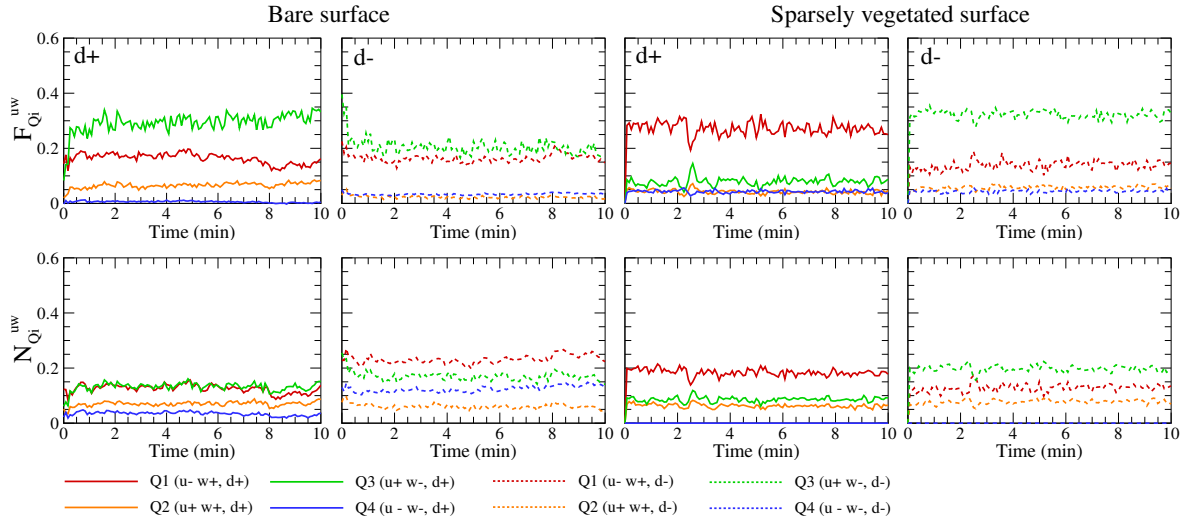


FIGURE 7.16: Time variation of the fractions in magnitude ( $F_{Qi}$ ) and in event number ( $N_{Qi}$ ) of the momentum flux in each quadrant, at  $z = 0.2$  m, associated with positive or negative dust concentration ( $d^+$ ,  $d^-$ ) fluctuations for the bare soil simulations and the sparsely vegetated case C1, both with comparable wind intensities  $u_{*sb} \approx 0.33 \text{ ms}^{-1}$ . The solid lines correspond to positive dust fluctuations  $d^+$  and the dotted lines to  $d^-$ .

The differences in the dust transport within the vegetation layer and at equivalent heights over bare surfaces is further investigated through octant analysis, described in section 7.2.2, by dividing the quadrant partitions of the momentum flux into those corresponding to positive or negative dust fluctuations,  $d^+$  or  $d^-$  (Fig 7.16). The figure shows that over bare surfaces, sweep (Q3) motions associate more strongly with positive dust fluctuations  $d^+$  as against ejection (Q1) motions, seen from  $F_{uw}^{Q3} > F_{uw}^{Q1}$  and equivalent contributions in event number at  $z = 0.2$  m. At a similar height within the vegetation layer,  $d^+$  are associated more favourably with ejection (Q1) motions both in frequency of occurrence and flux magnitude. Similarly, in the presence of vegetation,  $d^-$  are associated more strongly with sweep (Q3) motions in frequency of occurrence and flux magnitude, as against over the bare surface where they coincide with greater number of ejection (Q1) motions. This comparison clearly illustrates that the presence of vegetation encourages the evacuation of the emitted dust towards the upper atmosphere, as against the bare surface wherein the tendency of their deposition through sweep motions is higher. It also confirms that dust and momentum turbulent transport is more similar inside the vegetation layer as against that over a bare surface at an equivalent height.

A similar trend within the vegetation layer is observed for the smaller dust particles up to  $7 \mu\text{m}$  (Fig 7.17). Above this size, there is an increase in the Q2 contribution and a decrease in the Q3 contribution to the dust flux magnitude. Thereby, the larger dust particles are transported

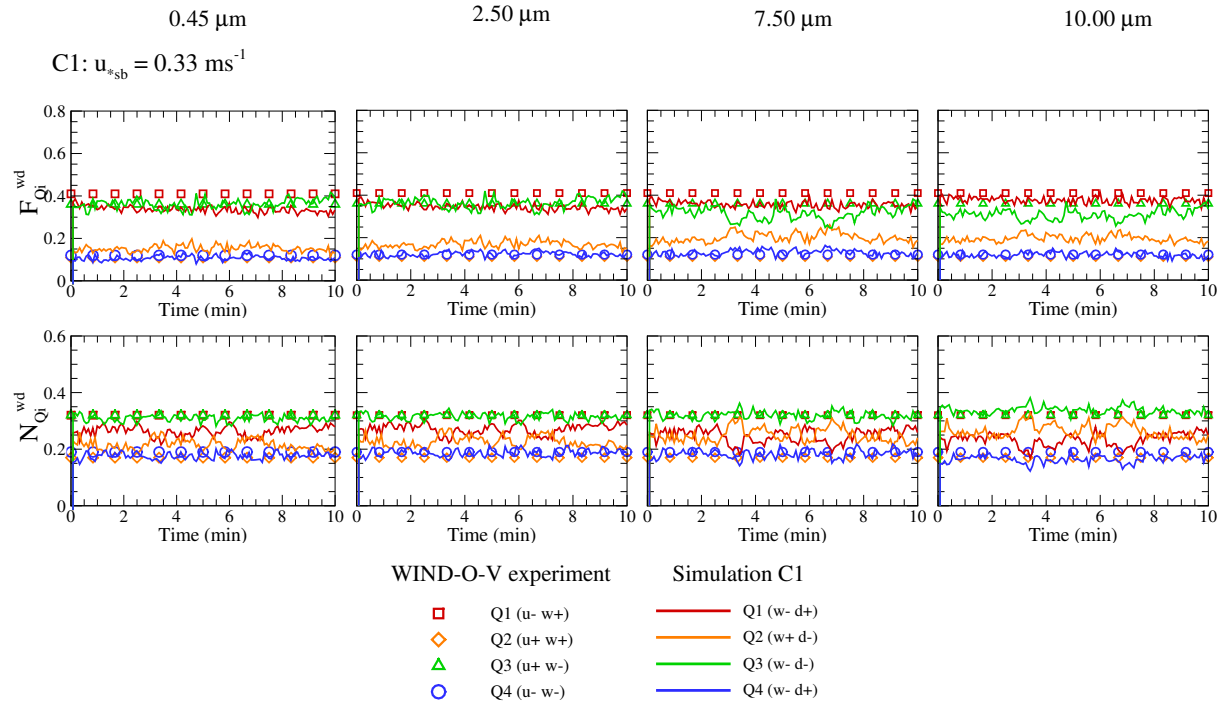


FIGURE 7.17: Time variation of the quadrant partitioning of the dust flux  $F_{wd}$  in magnitude ( $F_{Q_i}$ ) and in event number ( $N_{Q_i}$ ), as defined in equations 5.1 and 5.2, obtained from the 10-min simulated erosion event C1 at 0.2 m height for 4 dust particle sizes ( $d_{p,b} = 0.45, 2.50, 7.50,$  and  $10.00 \mu\text{m}$ ) and compared with the mean fractions of the momentum flux  $F_{uw}$  obtained at 3 m height from the WIND-O-V's 2018 field experiment.

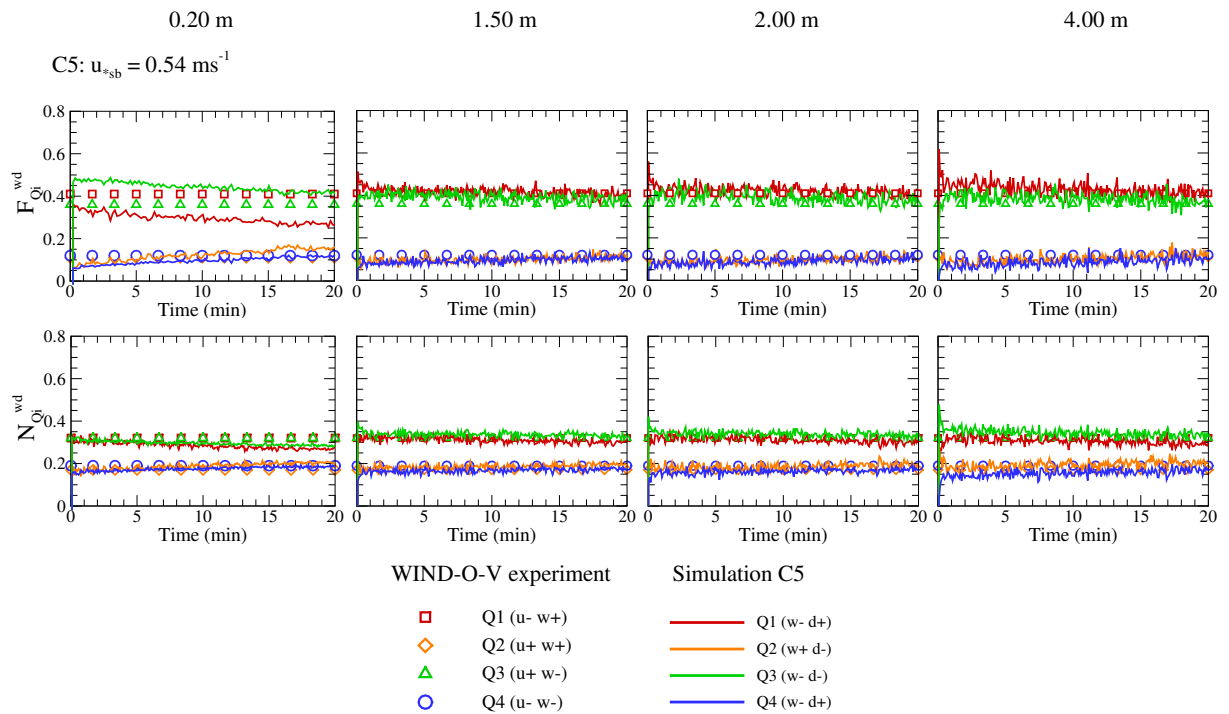


FIGURE 7.18: Same as Fig. 7.14 for simulation C5 with 20 minutes of erosion.

less similarly to momentum, similarly to that over an isolated bare plot of short fetch (Chapter 5). The source of this dissimilarity is, however, not in the intermittency of dust emissions, as the same was not observed for the  $0.45 \mu\text{m}$  particles emitted with a similar probability as the  $7.5 \mu\text{m}$  particles (Fig. 7.1). It is most likely due to the dominant deposition of the coarser dust particles (Fig. 2.16) in the presence of vegetation. This was not observed over the bare surface because of the relatively weaker deposition of the largest particles (Fig. 4.2), thereby leading to size-independent transport dissimilarity below  $8 \mu\text{m}$ .

The turbulent transport of dust above the vegetation layer remains independent of the vegetation configuration (Fig. 7.18), with quadrant partitions for C5 comparable with the less denser case C1 (Fig. 7.14). Within the vegetation layer, dust transport changes in comparison with the C1, with an initial increase in the Q3 contribution and a decrease in the Q1 contribution to the flux magnitude, thereby deviating from those of the momentum flux. This implies that dust transport is less similar to momentum within the vegetation layer of denser canopies, as against that within sparsely vegetated ones. However, this dissimilar dust transport is different from that over bare surfaces at a similar height.

Overall, our results suggest that the turbulent transport of the emitted dust close to the surface is different in the presence of vegetation as against that over the bare surface. The presence of vegetation, however, does not significantly influence the dust transport above the canopy.

## 7.4 Instantaneous behaviour

Figure 7.19 presents the instantaneous view of saltation (vertically integrated sand concentration field normalized by its maximum) for cases (a) C1 ( $u_{*sb} = 0.33 \text{ ms}^{-1}$ ), (b) C3 ( $u_{*sb} = 0.32 \text{ ms}^{-1}$ ), (c) C4 ( $u_{*sb} = 0.54 \text{ ms}^{-1}$ ), and (d) C5 ( $u_{*sb} = 0.54 \text{ ms}^{-1}$ ). At moderate wind intensities ( $u_{*sb} \approx 0.33 \text{ ms}^{-1}$ ), the simulated saltation field comprises of regions of strong sand transport surrounded by regions of little or no saltation, similar to the aeolian streamers simulated over a bare surface (section 5.3.4). As expected, the streamers are aligned along the mean wind direction, meandering or even merging with other streamers as they move forward. This behaviour is consistent with the field experiments of Baas *et al.* [2005] over a sandy beach (bare surface) and Baas *et al.* [2007] with sparse vegetation.

With increasing vegetation cover, sand transport becomes characteristically different from that with sparse vegetation, with the saltation featuring narrow streamers (Fig. 5.7), restricted to the inter-row regions between the vegetation. This channelization of sand transport is seen more clearly for C5 (Fig. 7.19d). A similar behaviour was previously observed by Dupont *et al.* [2014], who questioned the nomenclature of 'streamers' because they do not meander much, and are driven by the turbulent flow structures of the size of the inter-row width. In such high density vegetation cases, the saltation along the vegetation rows remains lower because of the lower wind speeds and the trapping of sand particles by the vegetation. Furthermore,



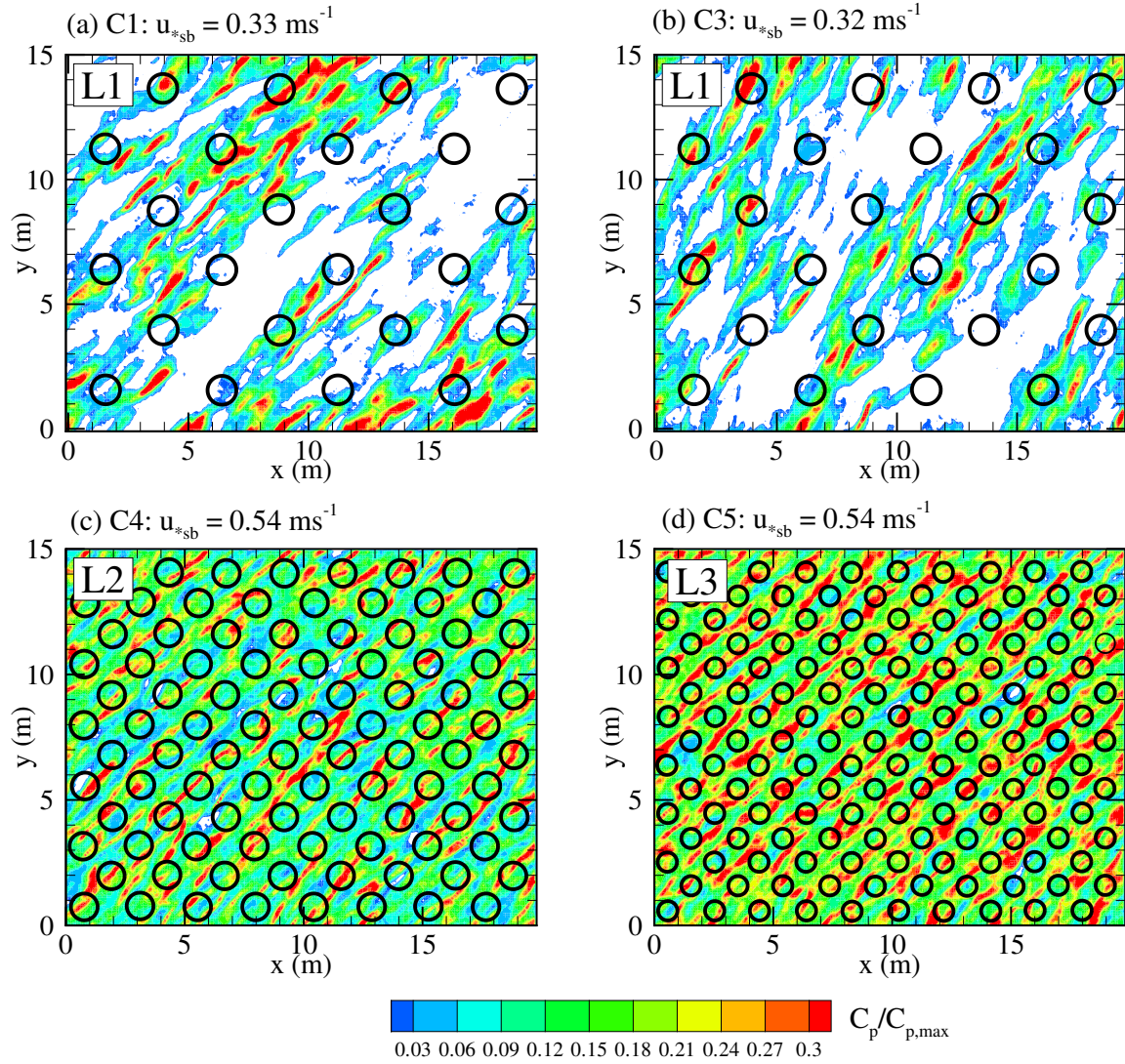


FIGURE 7.19: Instantaneous snapshots of horizontal cross section ( $x - y$ ) of the vertically integrated sand concentration ( $C_p$ ) normalized by its maximum value ( $C_{p,max}$ ) for cases (a) C1 ( $u_{*sb} = 0.33 \text{ ms}^{-1}$ ), (b) C3 ( $u_{*sb} = 0.32 \text{ ms}^{-1}$ ), (c) C4 ( $u_{*sb} = 0.54 \text{ ms}^{-1}$ ), and (d) C5 ( $u_{*sb} = 0.54 \text{ ms}^{-1}$ ). The circles represent the vegetation elements. White areas represent regions with low intensity of the corresponding quantity.

this distinction between row and inter-row regions changes with the wind direction, i.e. with inter-plant distance [Dupont *et al.* 2014], thereby changing the quantity of sand transported.

Similarly to over the bare surface, the simulated surface dust ejections ( $w^+ d^+$  at  $z \approx 0.1 \text{ m}$ ) correlate well with the passage of aeolian streamers (Fig. 7.20). As discussed in section 5.3.4, not every passing streamer emits dust particles, as the emission process depends on the balance between the energy provided by sandblasting and that required to break the inter-particle cohesive bonds. The small difference in the peak of the dust emissions and the sand concentrations (dotted box in Fig. 7.20a) is due to the time lag ( $-0.2 \text{ s}$ ) between the release of dust by sandblasting and the passage of momentum ejections to carry them away from the surface. This time lag is however much shorter than that over a bare surface ( $-0.5 \text{ s}$ ), most probably

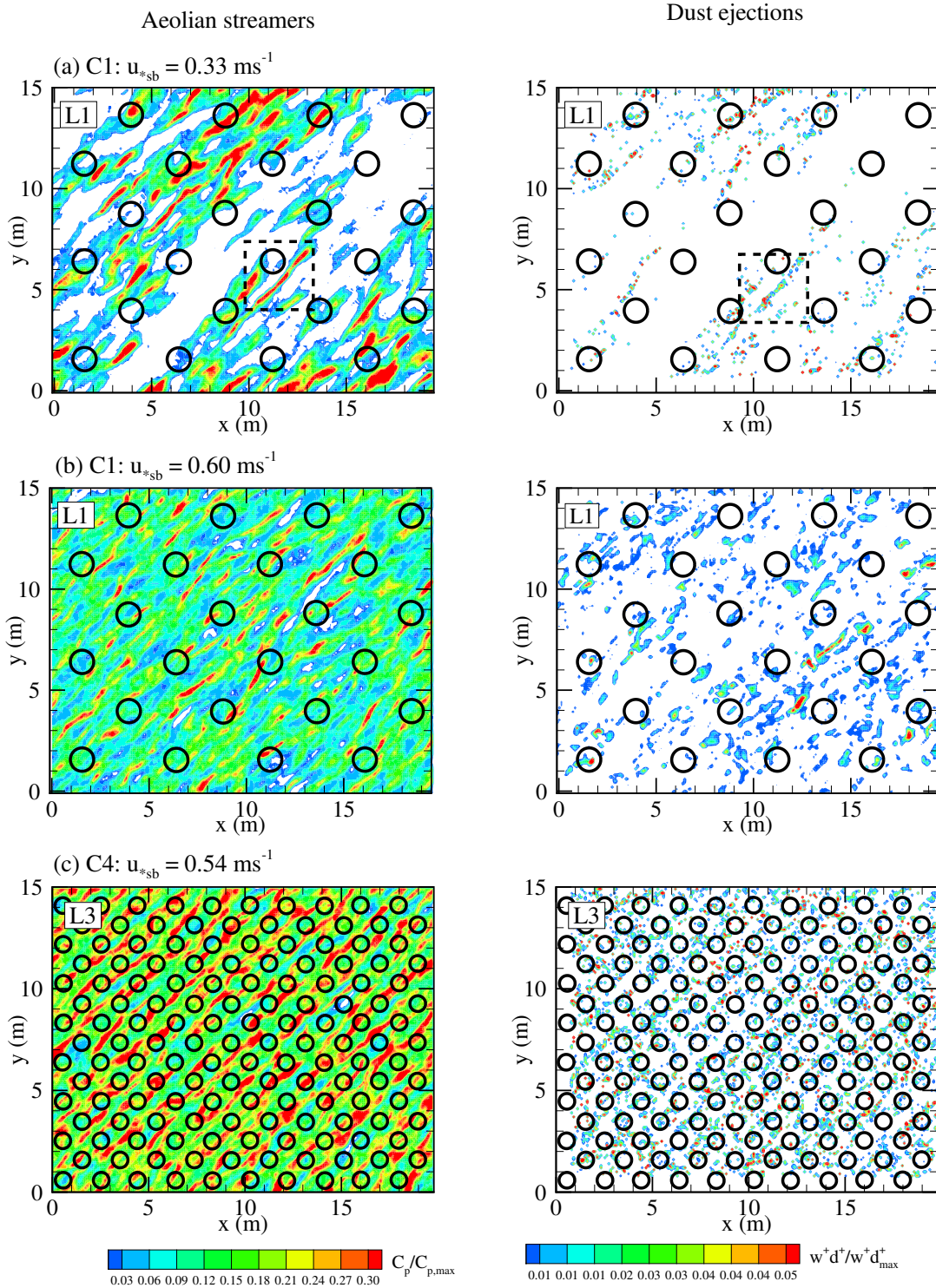


FIGURE 7.20: Instantaneous snapshots of horizontal cross section ( $x - y$ ) of the vertically integrated sand concentration ( $C_p$ ) normalized by its maximum value ( $C_{p,max}$ ) and the surface dust ejections ( $w^+ d^+$  at  $z \approx 0.1 \text{ m}$ ) normalized its maximum value for cases (a) C1 with  $u_{*sb} = 0.33 \text{ ms}^{-1}$ , (b) C2 with  $u_{*sb} = 0.60 \text{ ms}^{-1}$  and (c) C5 with  $u_{*sb} = 0.54 \text{ ms}^{-1}$ . The circles represent the vegetation elements. White areas represent regions with low intensity of the corresponding quantity.

due to the better mixing between momentum and dust in vegetation layer. The dust emissions continue to be correlated with streamers with increasing wind intensity (Fig. 7.20b) and

vegetation density (Fig. 7.20c). Moreover, dust emission patterns appear to be spatially more homogeneous with increasing vegetation density. These differences in dust emission patterns as a function of vegetation layout are related to the differences in the near-surface turbulence affecting sand transport and therefore dust emissions.

## 7.5 Evaluating deposition over vegetation

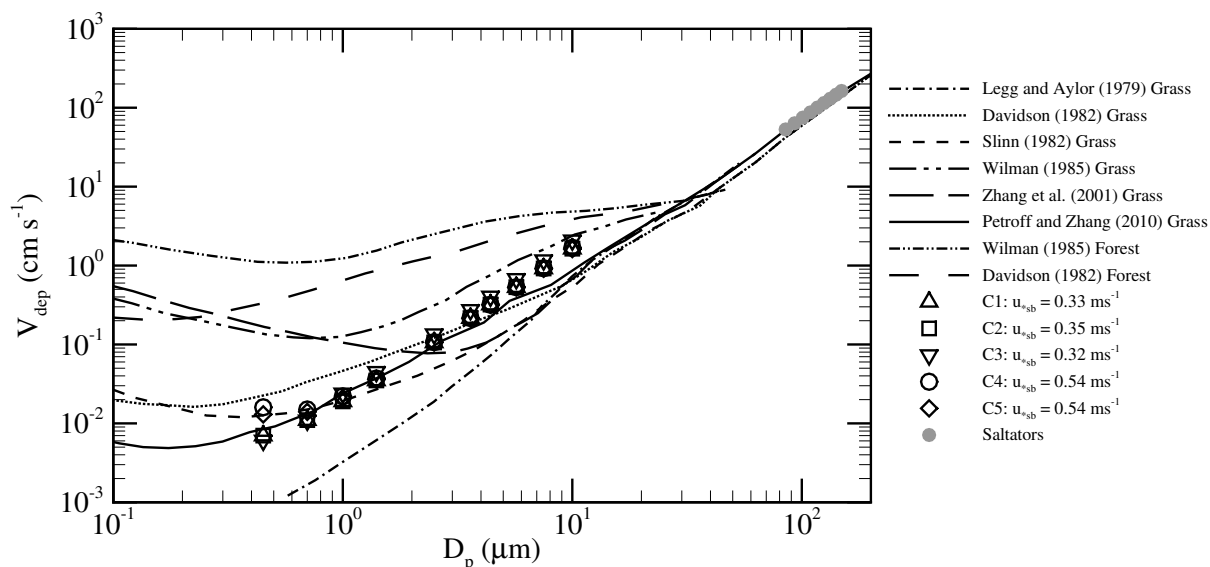


FIGURE 7.21: Variation with particle size of the simulated deposition velocity ( $V_{dep}$ ) in the presence of vegetation in comparison with published literature (over grass and forest canopies).

The simulated deposition velocities ( $V_{dep}$ ) of dust particles as a function of particle size (Fig. 7.21) are comparable with those proposed by Petroff *et al.* [2010] for a uniform grass canopy, remaining close to the lower limits of  $V_{dep}$  over grass canopies and higher than those over a bare surface (Fig. 4.2). Similarly,  $V_{dep}$  for the larger saltating particles is consistent with published results, with the saltators primarily deposited by gravitational settling. Here, the deposition velocities were calculated as the ratio of the deposition flux at the surface to the concentration of particles deposited.

The contribution of the deposition process to the impoverishment of the 3 m high dust flux during the WIND-O-V's 2018 experiment (Chapter 6) could not be estimated due to the absence of dust measurements close to the surface. This is investigated here through a sensitivity analysis of the size-distribution of the near-surface dust flux to deposition on to vegetation during emission events using our 3D erosion model. Fig. 7.21 demonstrates that published  $V_{dep}$  of dust particles differ by more than an order of magnitude for a given vegetation canopy and by nearly two decades between grass and forest canopies. Moreover, these published  $V_{dep}$  values are for continuous canopies as against the scattered vegetation in our simulations. Differences



also exist in the size-relative deposition velocities, i.e. between the smallest and largest particles, seen for example from the small variation in the Davidson *et al.* [1982] scheme as against a two decade variation proposed by Petroff *et al.* [2010], both over grass canopies. Furthermore, these schemes differ in the range of  $V_{dep}$  for a given particle size, with uncertainty increasing with decreasing particle size. The agreement across models for the saltating particles is due to the more dominant influence of gravitational settling on the total deposition flux.

Such large variations in the  $V_{dep}$  parametrizations imply that the contribution of the different deposition processes to the total deposition flux is still not fully understood. This, along with the lack of a comprehensive data set of dust deposition over sparsely vegetated surfaces allows for some experimentation of the dust deposition parametrizations within the range between deposition over a bare surface and over a forest canopy. Thereby, the analysis presented here focuses on the sensitivity of the dust flux PSD on the (i) brownian deposition of the finest dust particles, and (ii) inertial impaction and interception of the coarser particles. Dust particles larger than  $10 \mu\text{m}$  are not considered in this study as they deposit primarily through gravitational settling.

### 7.5.1 Sensitivity of $F_{wd}$ PSD to brownian deposition due to vegetation

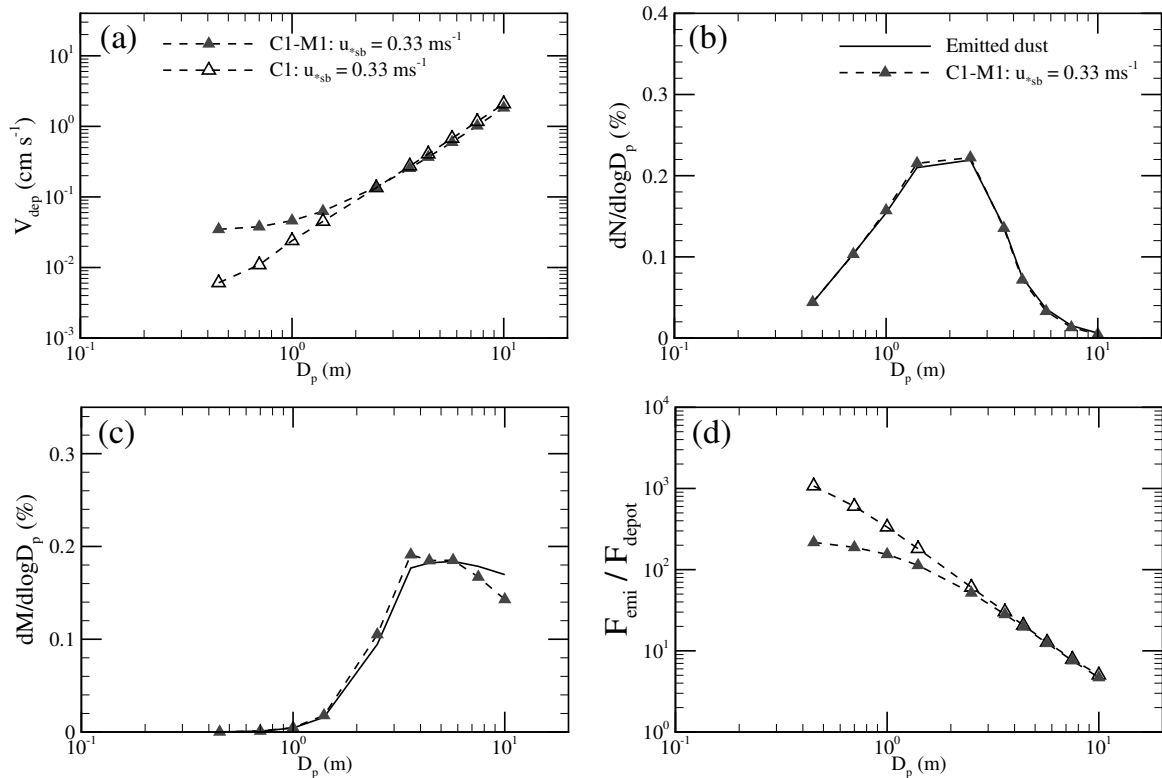


FIGURE 7.22: Variation with particle size of (a) the deposition velocity ( $V_{dep}$ ), (b-c) the percentage contribution to the 3 m high dust flux in number and mass, respectively, and (d) the ratios of the emission and deposition fluxes for cases C1 and C1-M1.

First, the role of brownian deposition on the PSD of the near-surface dust flux ( $F_{wd}$ ) is examined. To this end, the current parametrization of brownian deposition velocity, detailed in Chapter 3, was modified using a multiplication factor  $\zeta = 10$  (Eq. 2.32). This modification was first evaluated for case C1 with  $u_{*sb} = 0.33 \text{ ms}^{-1}$  (C1-M1). It resulted in an increase in the  $V_{dep}$  of the particles smaller than  $2 \mu\text{m}$  with no change in that of the larger particles (Fig. 7.22a). This increase in  $V_{dep}$ , however, did not influence any significant variation in the 3 m high  $F_{wd}$  PSD after 10 minutes of simulated erosion (Fig. 7.22b,c). This last result can be explained by the emission fluxes ( $F_{emi}$ ) remaining much stronger, across all particle sizes, compared to the deposition fluxes ( $F_{dep}$ ), with the former being nearly 100 times that of  $F_{dep}$  for the smallest particles (Fig. 7.22d) and about 10 times for the largest particles. Furthermore, the actual deposition on to vegetation remains negligible at less than 0.5% of the total mass deposited due to the low frontal area density and surface cover for case C1.

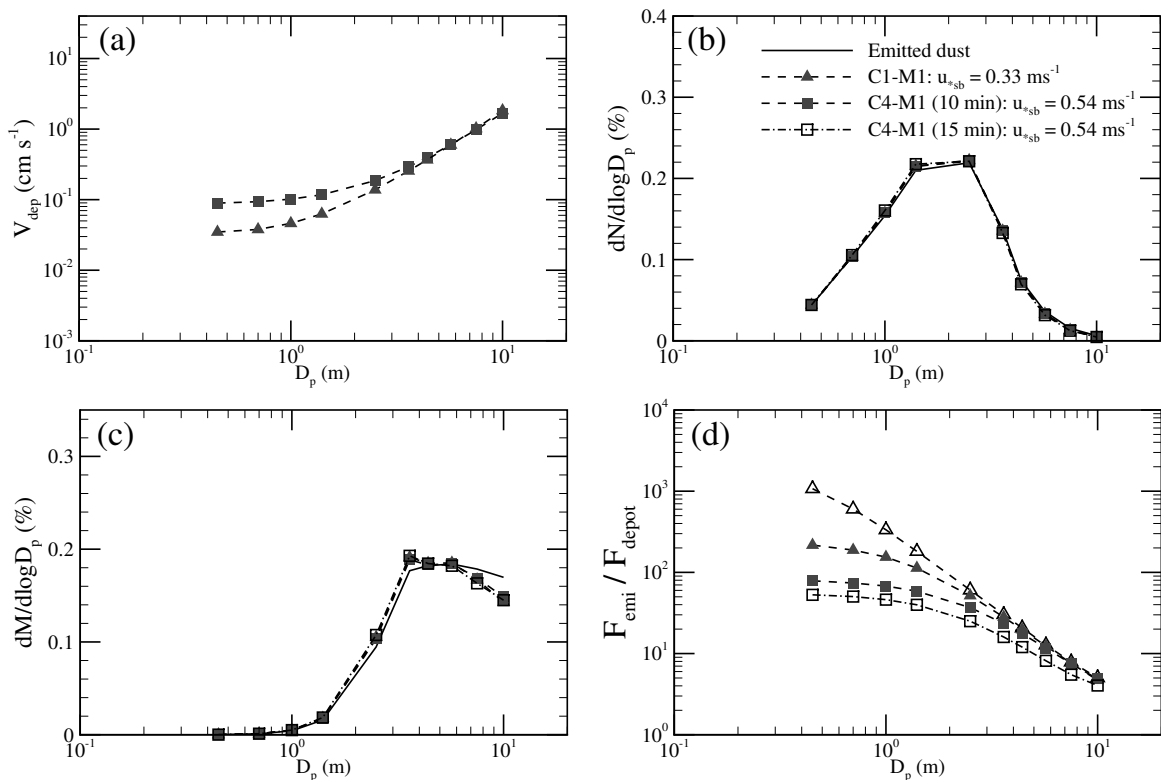


FIGURE 7.23: Similar to Fig. 7.22 for cases C1-M1 and C4-M1.

To investigate the role of vegetation density, the above modification of brownian deposition was then evaluated for case C4 with  $u_{*sb} = 0.54 \text{ ms}^{-1}$ . Fig. 7.23a shows that the  $V_{dep}$  of the finest particles increases for case C4 as against C1, most probably due to the higher frontal area density of the vegetation. However, even after 20 minutes of erosion, equivalent to a fetch of several hundred kilometres, the increased deposition of fine particles does not alter significantly the PSD of the near surface dust flux (Figs. 7.23b,c). Here too, the relatively strong emission fluxes, at about 50 times higher than the deposition fluxes of the smallest particles (Fig. 7.23d), explains the little change in the dust flux PSDs.

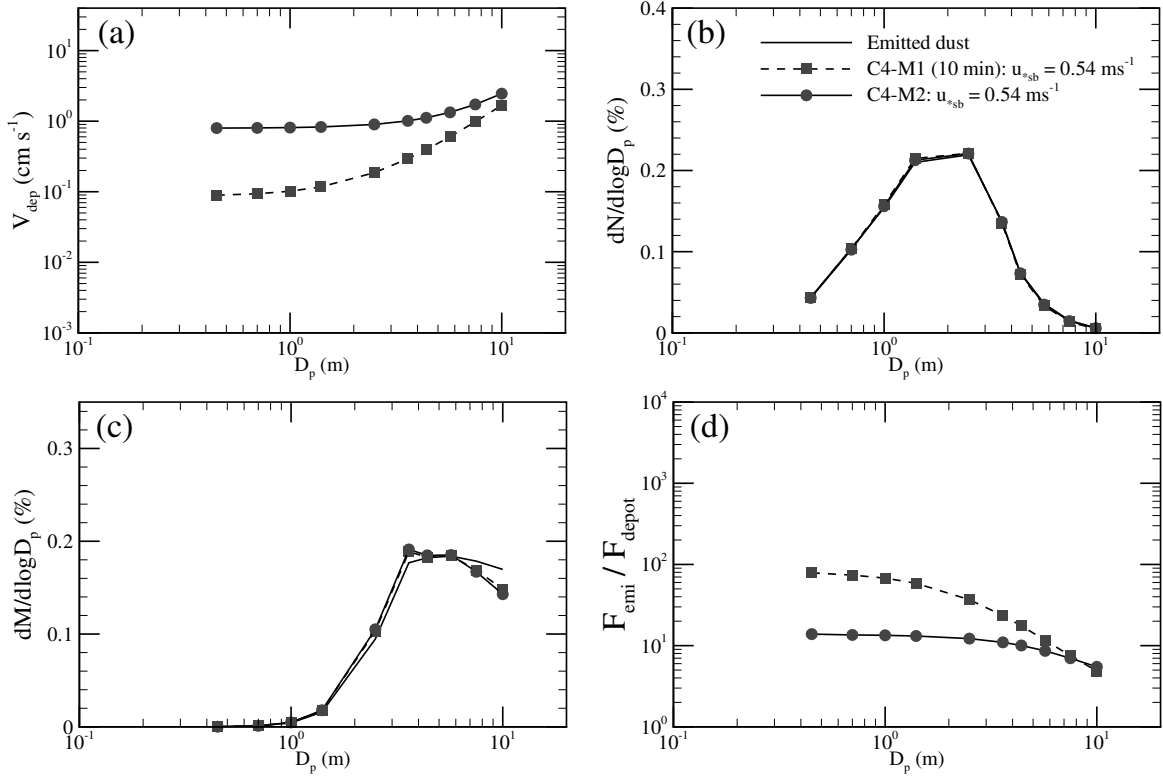


FIGURE 7.24: Similar to Fig. 7.22 for cases C4-M1 and C4-M2.

The parametrization of brownian deposition velocity was further modified using  $\zeta = 100$  for case C4 with  $u_{*sb} = 0.54 \text{ ms}^{-1}$ . This resulted in simulated  $V_{dep}$  of the order of  $1 \text{ cms}^{-1}$  across all particle sizes (Fig. 7.24a), higher by two decades for the smallest particles in comparison with C4, and close to that over a forest canopy as proposed by Wiman *et al.* [1985] (Fig. 7.21). However, the increased deposition of the smallest particles resulted in no significant change in the  $F_{wd}$  PSD (Fig. 7.24b,c) as  $F_{emi}$  remained nearly 10 times that of  $F_{dep}$  across all particle sizes (Fig. 7.24d).

These results suggest that the increased brownian deposition of the fine particles due to vegetation does not influence the size-distribution of the suspended dust flux during emission events, remaining independent of the wind intensity and vegetation configuration.

### 7.5.2 Sensitivity of $F_{wd}$ PSD to interception and impaction due to vegetation

A third modification was experimented upon by retaining the original parametrization of brownian deposition and altering interception and impaction of the largest particles by the vegetation using a multiplication factor  $\zeta = 10$  for case C1 with  $u_{*sb} = 0.33 \text{ ms}^{-1}$ . It resulted in an increase in  $V_{dep}$  for particles larger than  $1 \mu\text{m}$  and a very large (three decade) variation within dust particle size range (Fig. 7.25a). The relatively faster deposition of the coarse particles was reflected in the PSD of the near-surface dust flux, with an impoverishment in the number of particles larger than  $3 \mu\text{m}$  (Fig. 7.25b) and a dominant mode along  $1.5 \mu\text{m}$  (Fig.

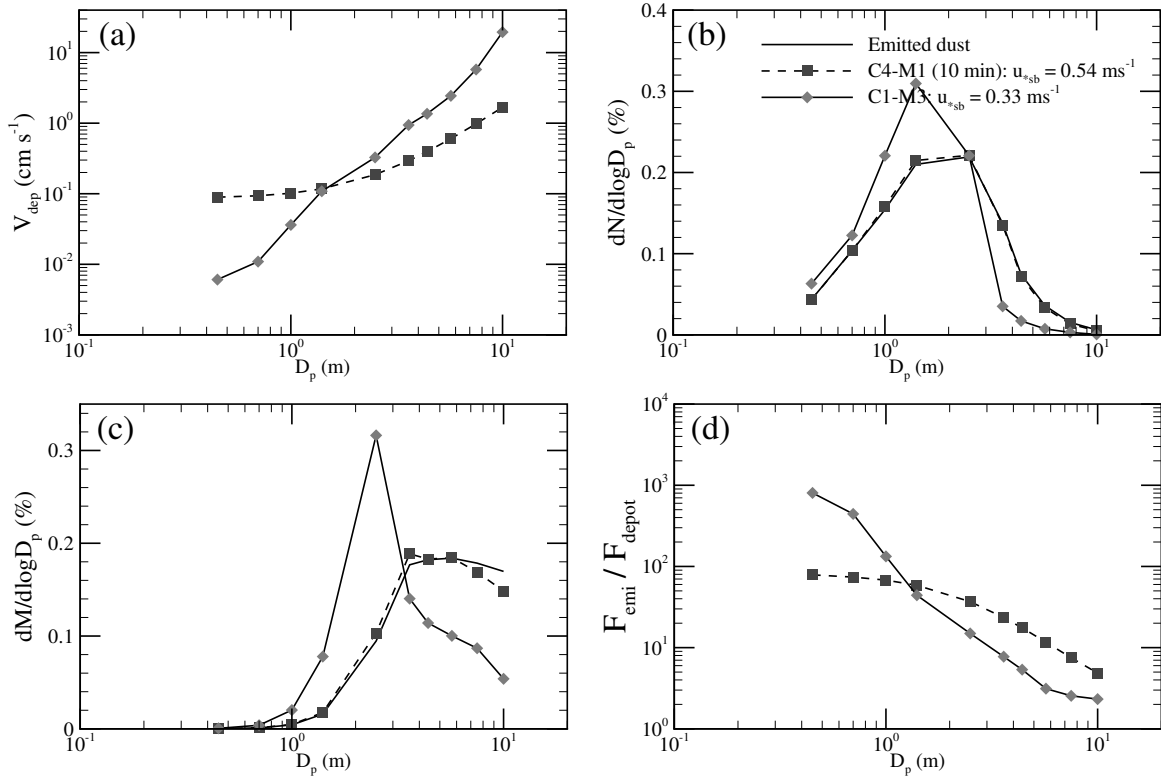


FIGURE 7.25: Similar to Fig. 7.22 for cases C4-M1 and C1-M3.

7.25b,c). This change in  $F_{wd}$  PSD as against the surface emission flux can be explained by the size-relative  $F_{emi}/F_{dep}$  in Fig. 7.25d. In comparison with M1 and M2, the strong impoverishment of the larger dust particles in simulation C1-M3 can be traced to their stronger deposition with  $F_{dep}$  of the same order of magnitude as  $F_{emi}$  (Fig. 7.25d).

## 7.6 Conclusion

The full erosion process, including saltation and dust dispersion, over a sparsely vegetated surface was simulated for the first time using a 3D erosion model. The simulation results were consistent with the observations from the WIND-O-V's 2018 field experiment, and previously published data, demonstrating a reduction in the flow energy available to drive erosion due to its greater absorption by vegetation as against a bare surface.

Our numerical experiments illustrated differences in the surface turbulence between bare and sparsely vegetated surfaces, leading to variations in saltation and dust emission patterns. Close to the surface, i.e. within the vegetation layer, vegetation elements appeared to encourage a better turbulent mixing between momentum and dust, leading to a more similar turbulent transport of the two quantities in comparison with that over a bare surface. At distances well above the vegetation layer, dust transport appeared not influenced by the presence of vegetation, appearing similar to over bare surfaces at equivalent heights.

Our simulations showed that the impact of near-surface turbulence and deposition on the size-distribution of the suspended dust remains negligible, independent of fetch and wind intensity. A sensitivity analysis of the role of the deposition process on the size-distribution of the suspended dust during emission events revealed a negligible impact within the two-decade range of published dust deposition velocities. This further confirms the negligible role of deposition on the size-distribution of the dust flux measured during the WIND-O-V's 2018 experiment. Furthermore, our results suggest that the deposition process can influence the size of the suspended dust only when both deposition and emission fluxes are of the same order of magnitude. This inference is an extension of Chapter 4 which demonstrated the importance of the deposition process relative to the differences between the peak of the emitted dust flux and the minimum of the dust deposition velocity curve, and the fetch of the erodible surface. Finally, this study encourages a better characterization of the deposition process over sparsely vegetated surfaces.

## 8 Conclusions and perspectives

### 8.1 Conclusions

The central problem addressed in this thesis is the impact of sparse vegetation on the size-distribution of the suspended dust in semi-arid environments. It was explored through a combination of numerical and field experiments, starting with dust emissions over bare surfaces and then over sparsely vegetated surfaces. These investigations were streamlined by three key questions:

1. What is the impact of surface properties, the surface wind and the re-deposition process on the size-distribution of the suspended dust during emission events?
2. Is the emitted dust transported similarly to momentum near the surface, i.e. by the same turbulent eddies?
3. How does the dust emission process differ in the presence of sparse vegetation as against that over the bare surface?

Here, each of these questions is responded to through a summary of conclusions emerging from this doctoral work.

The first question was explored, partly, through a sensitivity analysis, using a 1D dust dispersion model in Chapter 4, of the various processes and parameters influencing the size-distribution of the suspended dust during emission events. It demonstrated differences between existing emission schemes in the quantification of the influences of surface properties, the surface wind and the deposition process on the emitted dust. Furthermore, it exposed an ambiguity between the emitted dust flux ( $F_{emi}$ ) at the surface and the net emitted dust flux ( $F_{wd}$ ) within the first few meters from the surface (Fig. 8.1).  $F_{wd}$  is commonly measured during field experiments and is often erroneously used to evaluate  $F_{emi}$  in dust emission schemes. The sensitivity analysis revealed that the  $F_{emi}$  size-distribution depends on the size of the dust available in the surface soil ( $p_d$ ) and the surface inter-particle cohesive bond coefficient ( $\beta$  in Fig. 8.1). The variation of  $\beta$  between existing models results in varying  $F_{emi}$  size-distributions for the same surface soil ( $p_d$ ). Away from the surface, the  $F_{wd}$  size-distribution differs from that of  $F_{emi}$  with the former influenced by the near-surface size-sorting processes due to turbulence and deposition, with deposition effects increasing with fetch length. Moreover, the extent of deposition induced size-sorting is related to differences between peaks of the size-distribution of  $F_{emi}$  and the size-relative dust deposition velocity ( $V_{dep,min}$  in Fig. 8.1). In summary, the size-distribution of the suspended dust is strongly influenced by the cohesive bond

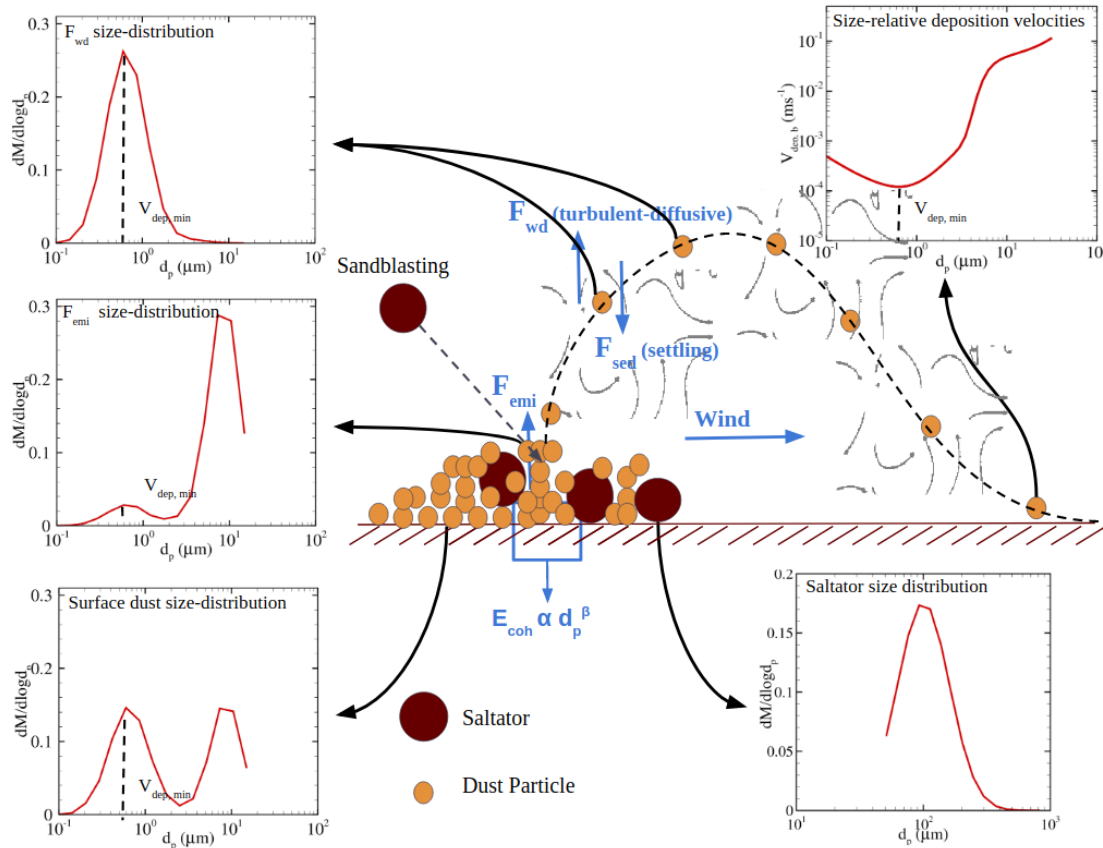


FIGURE 8.1: Schematic representation of the different dust size-distributions including that of the emitted dust flux ( $F_{emi}$ ) and the net-emitted ( $F_{wd}$ ) dust flux.

parametrization and the size-relative deposition effects, both acting according to surface soil dust availability. This needs to be considered while evaluating dust emission schemes from field experiments.

The WIND-O-V's 2017 field experiment, that examined dust emissions over an isolated bare erodible plot in south Tunisia prior to this doctoral work, showcased that the near-surface turbulent transport of dust and momentum was dissimilar, implying that the same eddies did not always carry dust and momentum simultaneously. Investigations in Chapter 5, using a 3D erosion model, revealed that this dissimilar dust transport was caused by (i) the intermittency of dust emissions as against the continuous absorption of momentum at the surface, and (ii) the short fetch (150 m) of the WIND-O-V's experiment, leading to the limited development of the internal dust boundary layer from the upwind edge of the erodible plot. The dissimilarity due to dust emission intermittency was observed only close to the surface for moderate wind conditions, diminishing with increasing wind intensity as the dust emissions become more spatially homogeneous (less intermittent). The dissimilarity due to short fetch increases with height, closer to the upper edge of the internal dust boundary layer, and is most probably influenced by the roughness and erodability of the upwind surface. Furthermore, with increasing fetch, dust is progressively transported similarly to momentum as a function of height, with the emission intermittency progressively lost during turbulent transport. Overall, in semi-arid

regions, the short fetch of erodible plots, due to heterogeneous surface properties (vegetation patches, cultivation etc.), and the near-threshold wind conditions may promote dissimilarity between dust and momentum turbulent transports.

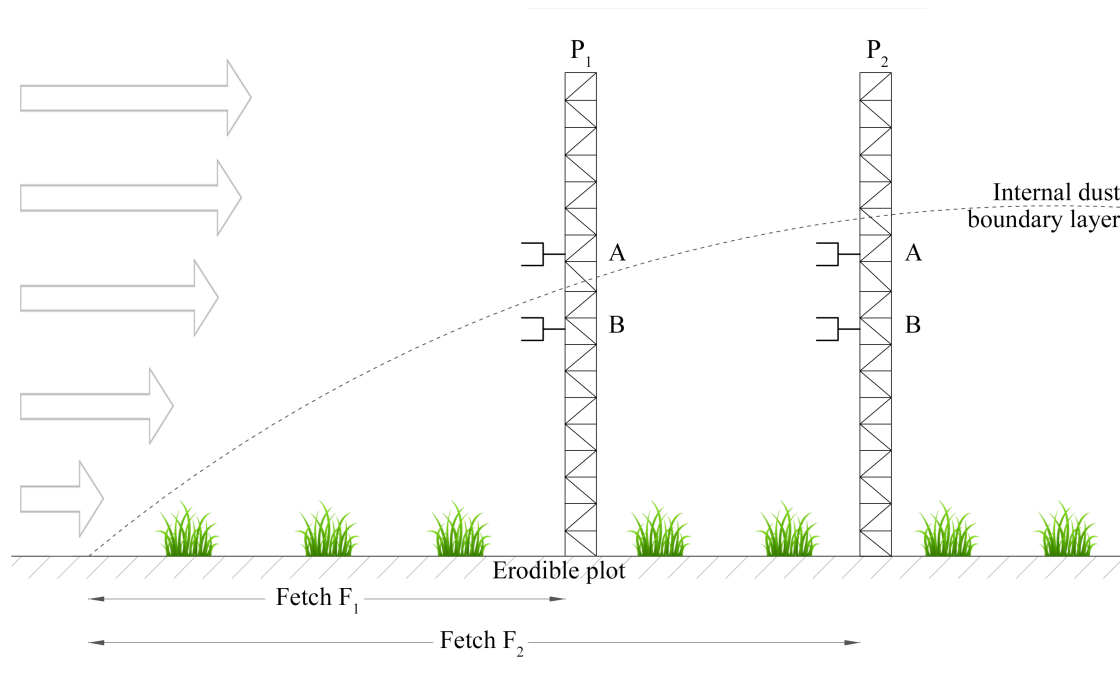


FIGURE 8.2: Schematic representation of the positioning of dust flux measurement sensors relative to the internal boundary layer as a function of the fetch length.

The numerical experiments in Chapter 5 have interesting implications on the design of field experiments, concerning the formation of internal dust boundary layers during emissions over short fetch erodible plots and the positioning of the dust sensors relative to this boundary layer. Over short fetch lengths ( $F_1$  in Fig. 8.2), sensor B is well within the internal boundary layer as against sensor A. Therefore the measurements of A are not representative of the local emissions as against those of B. Moreover, if A and B are two sensors of a flux-gradient dust flux system, then the resulting flux will be erroneous, and could even falsely indicate at a deposition event if the background dust concentration (above the internal boundary layer) is larger than the local emissions. Furthermore, the depth of the internal boundary layer increases with wind intensity, and this may lead to differences in the accuracies of the measured dust flux especially at moderate winds close to the erosion threshold. Additionally, the internal boundary layer depth decreases with increasing dust particle size, leading to a situation wherein the sensor is outside the boundary layer of the largest dust particles to be measured. These measurement problems diminish with increasing fetch ( $F_2$  in Fig. 8.2), as over large erodible surfaces the near-surface measurements are adequately representative of the local emissions.

The WIND-O-V's 2018 field experiment, conducted as part of this doctoral work over the same site as the 2017 experiment, confirmed that sparse vegetation reduced the quantity of the eroded soil material by absorbing a portion of the flow energy and thereby reducing that available for erosion. The comparison between the 3 m high dust fluxes between the 2017 and



2018 experiments in Chapter 6, i.e. over bare and vegetated surfaces, revealed the negligible impact of vegetation on the size-distribution of the suspended dust. Subsequent numerical experiments, using a 3D erosion model in Chapter 7, demonstrated that even over very large surfaces the influence of vegetation on the size-distribution of the suspended dust ( $< 10 \mu\text{m}$ ), through deposition and near-surface turbulent size-sorting, remains negligible. Erosion simulations over bare and vegetated surfaces demonstrated differences in the near-surface turbulence as a function of the vegetation density, influencing the saltation and dust emission patterns. Moreover, very close to the surface, dust and momentum appeared to be transported more similarly by the turbulence in the presence of sparse vegetation as against that over the bare surface.

Interestingly, the WIND-O-V's experiments illustrated the possibility of a progressive variation in the size-distribution of the emitted dust due to changes in the surface dust availability over prolonged erosion periods, with a combination of rain and surface tillage appearing to reset the surface. This has implications on the modelling of airborne dust in climate models in semi-arid regions, wherein the unpredictability of meteorological events and seasonal human intervention may lead to large differences in the size-distributions of the suspended dust.

Finally, this doctoral work resulted in a reliable 3D erosion model capable of reproducing dust emissions in semi-arid environments. This model can therefore be used to quantify the suspended dust and its size-distribution over different arid/semi-arid environments, and contribute towards the better representation of airborne mineral dust in climate models - the larger goal of the WIND-O-V project.

## 8.2 Direction for future work

Despite the many interesting results of this thesis, our understanding of the dust suspension process remains incomplete. One such limitation is the inadequate understanding of the saltation process, and thereby dust emissions, at moderate winds closer to the erosion threshold. Indeed, existing erosion models, including the one used in this thesis, simulate the saltation process only at high wind speeds, i.e in an equilibrium state where saltation is driven primarily by the splash process. However, experimental observations indicate that quite often erosive winds fluctuate close to the erosion threshold, resulting in highly intermittent non-equilibrium erosion conditions wherein the saltation is driven by a combination of aerodynamic entrainment and splash. Such non-equilibrium erosion conditions are encouraged over heterogeneous surfaces with vegetation or humidity patches, like those in semi-arid environments. This problem can be summed up through two questions, (i) How does the partitioning of the saltation flux between aerodynamic entrainment and splash evolve under erosive winds close to the threshold?, and (ii) How does the erodability of the surface, controlled by surface moisture and vegetation, influence the saltation process and its threshold? The investigation of

non-equilibrium saltation and the subsequent extension of the 3D erosion model of this thesis to such erosion conditions would improve the accuracy of dust representation in climate models and may help reduce the large variations of the sandblasting efficiencies between existing dust emission schemes near the erosion threshold.

Another perspective arising from this thesis is the verification of the constant dust flux layer during erosion experiments. Most often, dust emission experiments are conducted assuming a well-developed dust boundary layer with a constant dust flux layer over several meters from the surface. This assumption also forms the basis of the flux-gradient method, the most commonly used dust flux measurement technique. However, our simulations suggest the possibility of a shallow constant dust flux layer due to landscape-scale surface heterogeneities in semi-arid regions. This could be verified experimentally through a profile of Eddy-Covariance dust flux measurements, leading to the quantification of the vertical divergence of the dust flux as a function of the fetch, wind intensity and particle size.



**A Appendix A: Aerodynamic  
Parameters Over an Eroding Bare  
Surface: Reconciliation of the Law of  
the Wall and Eddy Covariance  
Determinations**

RESEARCH ARTICLE

10.1029/2017JD027984

Key Points:

- Conversely to previous studies, friction velocities obtained from the law of the wall and eddy covariance approaches are found similar
- The von Karman's constant is found independent of wind soil erosion intensity
- Several recommendations are proposed to estimate aerodynamic parameters over bare surface in order to evaluate saltation and dust fluxes

Correspondence to:

S. Dupont,  
sylvain.dupont@inra.fr

Citation:

Dupont, S., Rajot, J.-L., Labiadh, M., Bergametti, G., Alfaro, S. C., Bouet, C., et al. (2018). Aerodynamic parameters over an eroding bare surface: Reconciliation of the law of the wall and eddy covariance determinations. *Journal of Geophysical Research: Atmospheres*, 123, 4490–4508. <https://doi.org/10.1029/2017JD027984>







Received 30 OCT 2017

Accepted 3 APR 2018

Accepted article online 16 APR 2018

Published online 10 MAY 2018

## Aerodynamic Parameters Over an Eroding Bare Surface: Reconciliation of the Law of the Wall and Eddy Covariance Determinations

S. Dupont<sup>1</sup> , J.-L. Rajot<sup>2,3,4</sup> , M. Labiadh<sup>3</sup>, G. Bergametti<sup>4</sup> , S. C. Alfaro<sup>4</sup>, C. Bouet<sup>2,4</sup> , R. Fernandes<sup>1</sup> , B. Khalfallah<sup>4</sup>, E. Lamaud<sup>1</sup>, B. Marticorena<sup>4</sup> , J.-M. Bonnefond<sup>1</sup>, S. Chevaillier<sup>4</sup>, D. Garrigou<sup>1</sup>, T. Henry-des-Tureaux<sup>2</sup>, S. Sekrafi<sup>3</sup>, and P. Zapf<sup>4</sup>

<sup>1</sup>ISPA, INRA, Bordeaux Sciences Agro, Villenave d'Ornon, France, <sup>2</sup>iEES Paris (Institut d'Ecologie et des Sciences de l'Environnement de Paris), UMR IRD 242, Université Paris Est Créteil-Sorbonne Université-CNRS-INRA-Université Paris Diderot, Bondy, France, <sup>3</sup>IRA-Médénine, Médénine, Tunisia, <sup>4</sup>LISA (Laboratoire Interuniversitaire des Systèmes Atmosphériques), UMR CNRS 7583, Universités Paris Est Créteil et Paris Diderot, IPSL, Créteil, France

**Abstract** Assessing accurately the surface friction velocity is a key issue for predicting and quantifying aeolian soil erosion. This is usually done either indirectly from the law of the wall (LoW) of the mean wind velocity profile or directly from eddy covariance (EC) of the streamwise and vertical wind velocity fluctuations. However, several recent experiments have reported inconsistency between friction velocities deduced from both methods. Here we reinvestigate the determination of aerodynamic parameters (friction velocity and surface roughness length) over an eroding bare surface and look at the possible reasons for observing differences on these parameters following the method. For that purpose a novel field experiment was performed in South Tunisia under the research program WIND-O-V (WIND erOsion in presence of sparse Vegetation). We find no significant difference between friction velocities obtained from both law of the wall and EC approaches when the friction velocity deduced from the EC method was extrapolated to the surface. Surface roughness lengths show a clear increase with wind erosion, with more scattered values when deduced from the EC friction velocity. Our measurements further suggest an average value of the von Karman constant of  $0.407 \pm 0.002$ , although individual wind events lead to different average values due probably to the definition of the ground level or to the stability correction. Importantly, the von Karman constant was found independent of the wind intensity and thus of the wind soil erosion intensity. Finally, our results lead to several recommendations for estimating the aerodynamic parameters over bare surface in order to evaluate saltation and dust fluxes.

### 1. Introduction

The friction velocity  $u_*$  (or shear velocity) is one of the primary scaling parameters involved in aeolian soil erosion. It represents a velocity scale characterizing the surface wind shear stress. Under high-Reynolds-number flow, the surface wind shear induces mechanically turbulent eddies, which are responsible under strong wind for sediment entrainment and turbulent dispersal of dust in the lower atmosphere. As a consequence, existing parameterizations of saltation and dust fluxes usually scale as the second or third power of  $u_*$ , and the initiation of soil erosion is defined from a threshold friction velocity above which erosion starts (e.g., Bagnold, 1941; Shao, 2008). Additionally, dust fluxes are usually estimated from the flux-gradient relationship, which also depends on  $u_*$  through the diffusion coefficient (e.g., Gillette et al., 1972). Hence, an accurate estimation of  $u_*$  is crucial in order to compare erosion flux parameterizations obtained from different field or laboratory experiments or to quantify accurately dust fluxes in field experiments.

The friction velocity has been often estimated indirectly by the erosion community from the law of the wall (LoW) approach, that is, the mean wind velocity profile within the surface layer (e.g., Marticorena et al., 2006; Shao et al., 2011). The LoW states that this velocity profile has a logarithmic form, or pseudo logarithmic for nonneutral thermal stratification, where the von Karman constant ( $\kappa$ ) relates the surface wind shear stress to the near-surface wind velocity profile (Andreas et al., 2006). This indirect evaluation of  $u_*$  was justified by the use of cup anemometers measuring wind speed at low frequency (<1 Hz). Hence, most wind erosion

flux parameterizations derived from field experiments have been deduced from an indirect evaluation of  $u_*$ , assuming  $\kappa = 0.40$  or  $0.41$  (Li et al., 2010).

Nowadays, the more affordable access to high-frequency anemometers ( $\geq 10$  Hz) has led to a growing number of field experiments where  $u_*$  is estimated directly from the correlations between the measured horizontal and vertical wind velocity fluctuations, also known as the eddy covariance (EC) approach, without requiring any assumption on the value of  $\kappa$  and on the state of the atmosphere (e.g., Li et al., 2010; Lee & Baas, 2016). This direct evaluation of  $u_*$  is often considered as more reliable than the LoW approach. However, the direct evaluation of  $u_*$  from a single-height measurement without controlling for the presence of a constant momentum flux layer may be critical (Lee & Baas, 2016).

The few comparisons presented in the literature on the friction velocity obtained from the above direct and indirect methods were unsuccessful (e.g., Biron et al., 2004; King et al., 2008; Li et al., 2010; Lee & Baas, 2016). They all reported differences of more than 20 to 35% on  $u_*$ . No clear explanations were reported in these studies to explain these significant differences in  $u_*$  evaluation. Li et al. (2010) justified this difference from a modification of the von Karman constant in presence of windblown particles, while Lee and Baas (2016) observed later no link between the magnitude of their  $u_*$  difference and the presence of windblown particles, which contradicts a modification of the  $\kappa$  value. These latter authors suggested that  $u_*$  obtained from the logarithmic wind profile is more representative of a flow ensemble while  $u_*$  obtained from eddy covariance is more impacted by coherent eddy structures. This questions the range of eddy scales that should be considered in  $u_*$  determination. Hence, an accurate evaluation of  $u_*$  appears problematic, while a precise value of  $u_*$  is crucial for establishing universal parameterizations of erosion fluxes or estimating dust fluxes.

The von Karman constant used in the LoW has been debated for years by the meteorological and fluid mechanic communities regarding its value and its constancy. Most of the studies suggest that  $\kappa$  ranges from 0.35 to 0.45 (Högström, 1985; Oncley et al., 1996). The most recent study performed from field measurements in the atmospheric surface layer indicated a value closer to 0.37 than the usual values of 0.40–0.41 (Andreas et al., 2006), but with always a large variability of values around the mean due to measurement uncertainty. Frenzen and Vogel (1995) and Oncley et al. (1996) suggested that  $\kappa$  is a function of the roughness Reynolds number ( $Re_* = u_* z_0 / \nu$ , where  $z_0$  is the surface roughness length and  $\nu$  the fluid kinematic viscosity). However, later, Andreas et al. (2006) showed that this dependence on  $Re_*$  was due to an artificial correlation from shared variables used in the calculation of  $\kappa$  and  $Re_*$ . In presence of aeolian soil erosion, the constant value of  $\kappa$  has been questioned. Li et al. (2010) observed values of  $\kappa$  decreasing with increasing soil erosion by wind. They found values as low as 0.264. By analogy with previous hydrodynamic research on river flow with suspended particles (e.g., Wright & Parker, 2004), they explained this decrease by the presence of saltating particles. Following these authors, in addition to increasing the surface roughness, the vertical concentration gradient of saltating particles may also increase the velocity gradient by damping the turbulence, leading to an “apparent” von Karman parameter. Since  $\kappa$  intervenes in the evaluation of  $u_*$  from the LoW approach, uncertainty or modification of the value of  $\kappa$  could significantly impact the value of  $u_*$  and could explain differences observed with the direct estimation of  $u_*$ .

Previous field experiments comparing LoW and EC approaches faced the absence of a constant flux layer and neglected stability correction in the LoW. Lee and Baas (2016) never observed a constant flux layer with height, and Li et al. (2010) were unable to verify its existence due to a single-height high-frequency anemometer. Both studies also neglected the stability correction of the LoW wind velocity profile, while the stability correction may be significant for assessing aerodynamic parameters, even in near-neutral conditions. These limitations could explain some of the discrepancies observed between LoW and EC approaches on the determination of the friction velocity and cancel the apparent decrease of the von Karman constant  $\kappa$  with aeolian soil erosion suggested by Li et al. (2010).

This study ambitions to reconcile the determination of aerodynamic parameters ( $u_*$  and  $z_0$ ) from both, LoW and EC approaches, over an eroding bare surface. The main goal is to investigate the possible reasons for observing differences in aerodynamic parameters between both approaches such as the state of the constant flux layer, the value of the von Karman constant, the stability correction, or the impact of soil erosion, in order to suggest recommendations for evaluating saltation and dust fluxes. For that purpose, a novel field experiment was performed in South Tunisia under the research program WIND-O-V (WIND erOsion in presence of sparse Vegetation), where wind velocity and turbulence were measured at several heights using

vertical profiles of both cup and sonic anemometers. This experimental design allowed us to acquire wind velocity and friction velocity profiles, to compare  $u_*$  and  $z_0$  obtained from both EC and LoW approaches, and to estimate  $\kappa$ .

## 2. Background

In atmospheric surface layers, the logarithmic region of the wind velocity above a bare surface starts around a few millimeters height. This logarithmic region is located above the buffer layer that marks the transition between the viscous layer at the surface and the turbulent layer above. During an erosion event, the presence of saltating particles near the surface shifts the logarithmic layer to the upper saltation layer as saltating particles absorb momentum from the wind flow. The top of the logarithmic region depends on the extent of the surface. For a homogeneous and infinite surface, the top layer reaches a few hundred meters height in near-neutral conditions, while for limited surface extent the top layer matches the depth of the internal boundary layer developing from the upwind edge of the surface of interest (e.g., Kaimal & Finnigan, 1994).

In the logarithmic region, the mean wind velocity profile is expressed as

$$\langle u(z) \rangle = \frac{u_{*0}}{\kappa} \left[ \log \left( \frac{z}{z_0} \right) - \Psi_m \left( \frac{z}{L} \right) + \Psi_m \left( \frac{z_0}{L} \right) \right], \quad (1)$$

where the symbol  $\langle \rangle$  denotes the time average,  $z$  is the vertical coordinate,  $u_{*0}$  is the friction velocity at the surface,  $\Psi_m$  is the stability function accounting for the thermal stratification of the surface layer (e.g., Höögström, 1988), and  $L$  is the Monin-Obukhov length that compares the turbulence generated by buoyancy and wind shear. During wind erosion, (1)  $u_{*0}$  accounts for both surface wind shear and momentum flux absorbed by near-surface saltating particles (e.g., Raupach, 1991) and (2)  $z_0$  is known as the saltation roughness length, integrating the surface roughness length and the additional roughness induced by saltating particles (Owen, 1964).

With the LoW approach,  $u_{*0}$  is deduced indirectly from the linear regression of  $\langle u \rangle$ , usually taking  $\kappa = 0.40$  and knowing  $L$  independently. By neglecting  $\Psi_m(z_0/L)$ , the linear regression of equation (1) leads to

$$\langle u(z) \rangle = A \left[ \log(z) - \Psi_m \left( \frac{z}{L} \right) \right] + B, \quad (2)$$

where  $A$  and  $B$  are the slope and intercept of the regression, respectively. Hereafter, the friction velocity deduced from this approach will be referred to as  $u_{*0LoW}$ . Hence,  $u_{*0LoW} = \kappa A$ . If  $L$  is unknown (not in this study), an iterative procedure is usually performed to deduce  $u_{*0}$ ,  $\theta_{*0}$  (surface temperature scale) and  $z_0$  from wind velocity and air temperature profiles (e.g., Frangi & Richard, 2000; Marticorena et al., 2006). The surface roughness length  $z_{0LoW}$  is deduced from the slope  $A$  and intercept  $B$  of the regression, independently of  $\kappa$ :  $z_{0LoW} = \exp(-B/A)$ .

With the EC approach, the local friction velocity  $u_*(z)$  is estimated directly at the heights of the sonic anemometers from the correlations between the horizontal and vertical wind velocity fluctuations such as  $u_* = (\langle u'w' \rangle^2 + \langle v'w' \rangle^2)^{1/4}$ , where the prime denotes the deviation from the averaged value and  $u$ ,  $v$ , and  $w$  are the streamwise, spanwise, and vertical wind velocity components, respectively. In an ideal surface layer, the shear stress (or momentum flux) is constant with height, leading to  $u_* = u_{*0}$ . However, in a real atmospheric surface layer, it is often difficult to observe a perfect constant flux layer (Andreas et al., 2006; Haugen et al., 1971; Höögström, 1985). A surface friction velocity comparable to  $u_{*0LoW}$  is then deduced by extrapolating the vertical distribution of  $u_*(z)$  to the surface (Biron et al., 2004). A linear extrapolation is often used such as (Andreas et al., 2006)

$$u_*(z) = az + u_{*0}. \quad (3)$$

In an ideal surface layer the slope  $a$  would be zero. Hereafter, the friction velocity deduced at the surface ( $z = 0$ ) from this approach will be referred to as  $u_{*0EC}$ . The surface roughness length  $z_{0EC}$  is deduced from the intercept  $B$  of the regression of  $\langle u \rangle$  knowing  $u_{*0EC}$  and considering  $\kappa = 0.40$ :  $z_{0EC} = \exp(-\kappa B/u_{*0EC})$ . This represents the only way to estimate the roughness length from  $u_{*0EC}$ .

A direct estimation of  $u_{*0}$  allows us to evaluate the von Karman constant from the logarithmic form of the wind velocity profile. Hence,  $\kappa$  can be deduced from the slope  $A$  of the regression of  $\langle u \rangle$  knowing  $u_{*0EC}$ :  $\kappa = u_{*0EC}/A$ .

### 3. The WIND-O-V's 2017 Experiment

#### 3.1. Site

The WIND-O-V's 2017 experiment took place from 1 March to 15 May 2017 in South Tunisia, in the experimental range (Dar Dhaoui) of the Institut des Régions Arides of Médenine close to Médenine/Zarzis (Figures 1a and 1b). The site approximates a flat half-circle plot of 150-m radius where measurements were performed at the center of the circle in order to ensure a fetch of at least 150 m for westerly, northerly to easterly winds (Figure 1c). In the north, the fetch was slightly longer, about 200 m. The ground surface was flat with a slope less than  $0.3^\circ$  (0.6%) in all directions. The plot was surrounded by small bushes in the northwest ( $0.34 \pm 0.08$ -m height and  $0.58 \pm 0.20$ -m diameter) and young olive trees arranged in a square pattern (about  $1.7 \pm 0.3$ -m height,  $1.5 \pm 0.4$ -m diameter, and 26 m spaced) in the northeast. The soil is typical of the Jeffara basin with a loamy sand layer very prone to wind erosion. Before the experiment, the surface had been tilled with a disk plough and leveled with a wood board in order to meet the conditions of an ideal flat bare soil without soil crust or ridges.

#### 3.2. Measurements

A 9-m high lattice mast was erected at the center of the half-circle plot (Figure 1d). The mast was well anchored in the ground to remove any possibility of mast motion with wind. On this mast, turbulent velocity components and air temperature fluctuations were measured simultaneously at 1.0, 1.9, 3.0, and 4.1 m above the surface using four ultra sonic anemometers (one Campbell Scientific CSAT3, two Gill R3, and one Gill WindMaster) sampling at 60, 50, 50, and 20 Hz, respectively. These four sonic anemometers allowed us in particular to estimate a vertical profile of friction velocities and thus to verify the presence of a constant flux layer. On the same mast, seven cup anemometers (0.2, 0.6, 1.3, 1.8, 3.0, 4.0, and 5.2 m) and four thermocouples (0.4, 1.6, 3.7, and 5.0 m) were also installed to measure simultaneously at 0.1 Hz the mean horizontal wind velocity and temperature profiles, respectively. These additional anemometers were used to characterize the logarithmic wind profile. Sonic anemometers were oriented toward the north and cup anemometers toward the northwest. All anemometers on the tower were intercalibrated prior to the experiment.

Among several instrumentations installed on the site for characterizing saltation and dust fluxes, one vertical array of five sediment traps like Big Spring Number Eight (BSNE) (Fryrear, 1986) was deployed to quantify the saltation flux, and two Saltiphones (Eijkelkamp<sup>®</sup>, Giesbeek, the Netherlands) were positioned close to the surface (about 7-cm height) and near the mast to follow at 0.1 Hz the dynamics of erosion events (beginning, end, and intensity). The principle of the Saltiphone is to count the impacts of saltating particles on a microphone surface (Spaan & Van den Abeele, 1991). The sediment traps had 0.10 m and 0.05 m horizontal and vertical openings, respectively, and were positioned vertically at 0.10, 0.25, 0.40, 0.60, and 0.90 m above the surface (using the middle of the opening as a reference). For this study, we focus solely on data from both BSNE and Saltiphones to identify the periods of aeolian soil erosion and to quantify the related windblown sediment fluxes, respectively.

#### 3.3. Data Processing

A 15-min averaging time was chosen for computing all statistics characterizing the wind dynamics. This value was deduced from the point of convergence of the cumulative  $u$ - $w$  cospectrum to an asymptote (Oncley et al., 1996). Figure 2 presents the average ogives  $Og_{uw}$  of the momentum flux  $\langle u'w' \rangle$  obtained from the four sonic anemometers during three wind erosion events. As a reminder,  $Og_{uw}$  is the cumulative integral of the  $u$ - $w$  cospectrum  $S_{uw}$ :  $Og_{uw}(f) = \int_{\infty}^f S_{uw}(s) ds$ , where the integration starts from the highest frequencies and  $f$  is the frequency. For all events, the four ogives converge nicely to 1 around  $fz / \langle u \rangle \approx 5 \times 10^{-4}$ , which corresponds to 15 min. This averaging time ensures that (1) all significant turbulent structures carrying momentum flux are included in the statistics and (2) estimated first- and second-order statistical moments reach reasonable uncertainty levels (see Appendix A). Considering a lower averaging time would underestimate the momentum flux, and thus the friction velocity, and increase its uncertainty level.

The wind velocity components recorded from the sonic anemometers were rotated horizontally so that  $u$  represents the horizontal component along the mean wind direction  $x$  and  $v$  the horizontal component along the transverse direction  $y$ . In order to account for possible errors in the vertical orientation of the sonic anemometers, a second rotation was performed at every height around the  $y$  axis. Note that the vertical velocity recorded by the Gill WindMaster (sonic anemometer located at 4.1-m height) has been corrected following the Technical Key Note KN1509v3 published by Gill Instruments in February 2016, due to a bug in the firmware of the instrument. Periods with southerly winds were discarded to remove data with possible wake effect



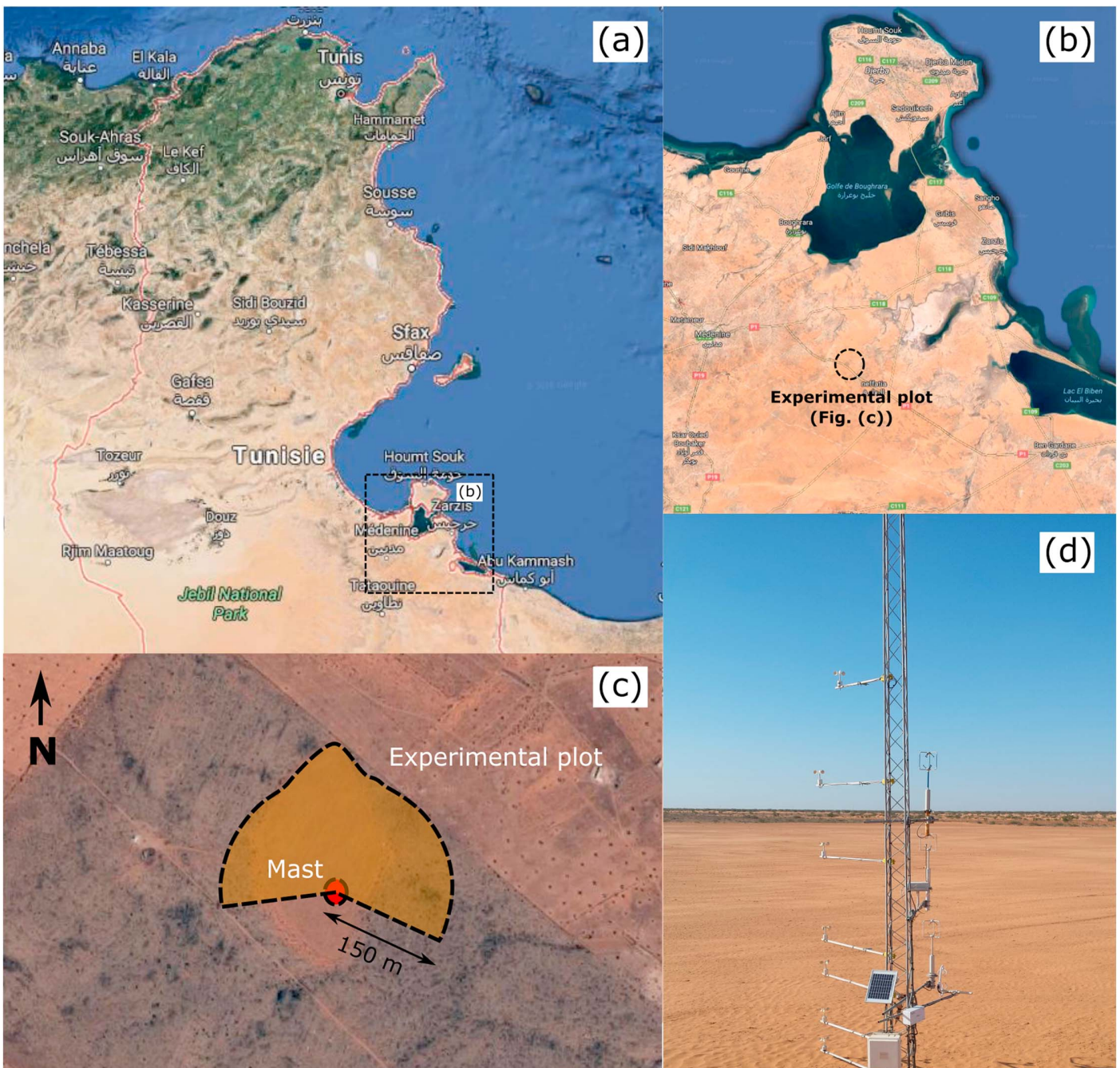


**Figure 1.** WIND-O-V (WIND erOSion in presence of sparse Vegetation)'s 2017 experimental site. (a and b) Localization of the site in Tunisia (Google Maps). (c) Schematic representation of the near-half-circle experimental plot where the measurement mast was located at its center. (d) North view of the plot from the back of the mast where cup and ultrasonic anemometers were mounted.

from the mast. Finally, quality controls of turbulence measurements were performed by testing for flow steadiness for each 15-min period using the criterion given by Foken et al. (2004) and time series were visualized in order to detect occasional instrument failures.

To delineate the near-neutral stability class from our data, we looked at the behavior of the vertical heat flux and the local friction velocity as a function of the stability parameter  $z/L$  during the whole experiment (Figure 3). Here the heat flux  $\langle w'\theta' \rangle$  (where  $\theta'$  is the fluctuation of the air temperature) and the local friction velocity  $u_*$  were deduced from the sonic anemometer at 3-m height. With the same approach as in

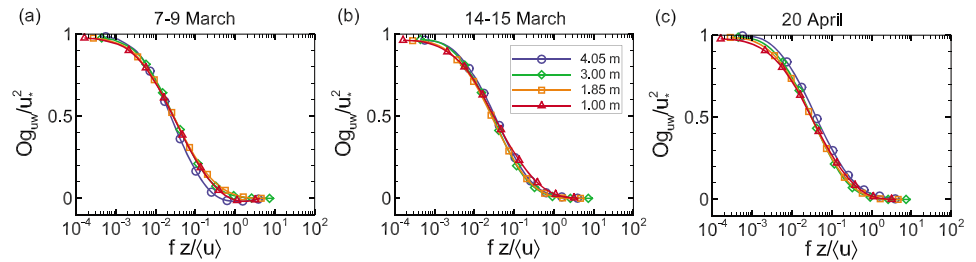


**Figure 2.** Ensemble-averaged normalized ogives  $Og_{uw}$  of the momentum flux obtained from the four sonic anemometers, for the 7–9 March (a), 14–15 March (b), and 20 April (c) events. The frequency  $f$  is normalized by the mean wind speed  $\langle u \rangle$  and the anemometer height  $z$ .

Dupont and Patton (2012), we found four stability regimes: forced convection, near-neutral, transition to stable, and stable. The near-neutral regime was defined as  $-0.2 < z/L < 0.01$  where the heat flux is usually low and the momentum flux is significant enough to induce soil erosion.

For this study, we only focused on 15-min time periods with windy conditions and computed for each of them the aerodynamic parameters (surface friction velocities and roughness lengths) using both LoW and EC approaches, as well as computed the von Karman constant following the methods described in section 2. To make sure that the differences in dynamic parameters between EC and LoW approaches are not related to a mean wind velocity difference between sonic and cup anemometers, we corrected the mean wind velocities obtained from all cup anemometers using the ratio of the mean velocities between the sonic and cup anemometers at 4-m height. Hence, at 4 m the mean wind speed from sonic and cup anemometers are made equal. This correction represented only  $\pm 2\%$  of the mean wind speed following the wind event and did not impact our results as both type of anemometers gave most often close mean wind speeds. For one wind event (7–9 March event, see next section), we also applied a +3% correction to the instantaneous horizontal wind velocity components recorded by the sonic anemometer at 3.0-m height as this anemometer was slightly underestimating the mean wind speed for northwesterly winds. We have no clear explanation for this underestimation. This wind attenuation may be explained by a piece of element of our installation, located

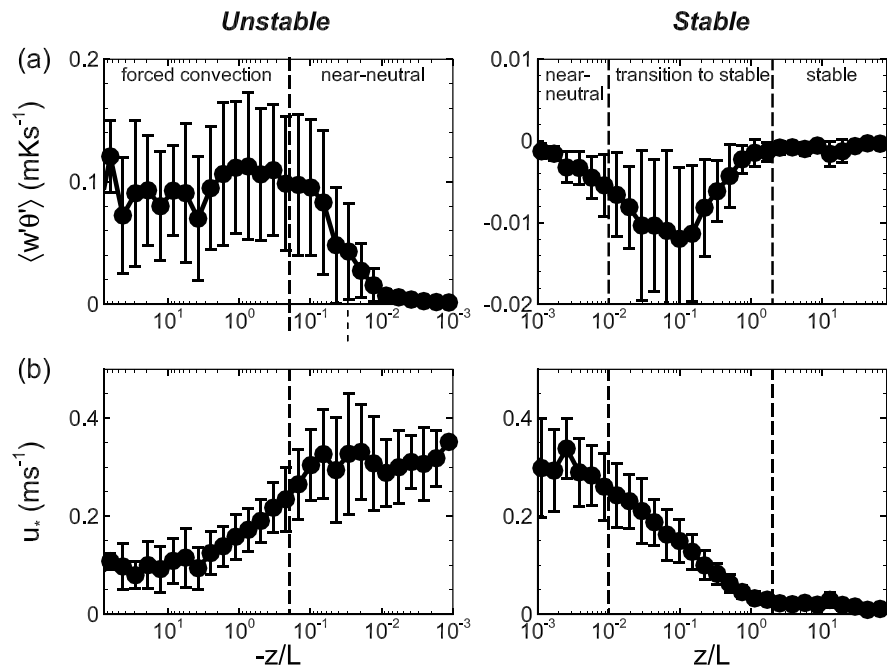


**Figure 3.** (a) Heat flux  $\langle w'\theta' \rangle$  and (b) friction velocity  $u_*$  as a function of stability  $z/L$  obtained from the sonic anemometer at 3-m height during the whole experiment. The long-dashed vertical lines delimit the four stability regimes: forced convection, near-neutral, transition to stable, and stable. The error bars show the standard deviation.

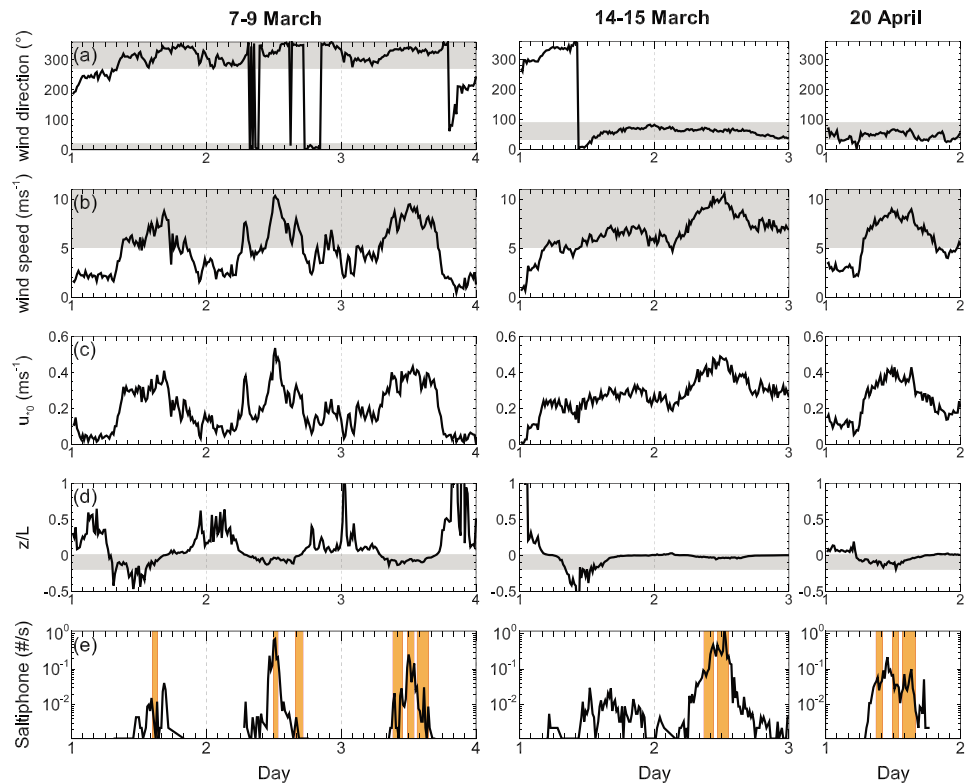


**Figure 4.** Main characteristics of the 7–9 March, 14–15 March, and 20 April events (left, middle, and right columns, respectively): time variations of the (a) mean wind direction, (b) mean wind speed at 3-m height, (c) surface friction velocity, (d) stability, and (e) mean impact number of saltating particles recorded by one of the Saltiphone. The shaded areas delimit the values considered for selecting the 15-min time periods in our analysis. The orange vertical areas in (e) correspond to the sampling periods of the Big Spring Number Eight.

a few tens of centimeters downwind from the anemometer, that could have perturbed the measurement for this specific wind direction. However, no flow distortion was observed in our data set in terms of tilt angle and modified wind direction. This correction improved the continuity at 3-m height of the mean velocity profiles and of the horizontal velocity variance profiles obtained from the sonic anemometers. Importantly, we carefully checked that this correction has a limited impact on the momentum flux at 3-m height and has overall no consequences on the main results obtained in this study.

Finally, in both EC and LoW approaches, the Monin-Obukhov length  $L$  involved in the wind velocity profile (equation (1)) has been simply deduced from  $\langle w'\theta' \rangle$  and  $\langle u'w' \rangle$  obtained from the sonic anemometers (e.g., Dupont & Patton, 2012).

### 3.4. Wind Events

Among the several strong wind events recorded during the experiment, we selected three main events well established for several hours with constant mean wind direction and with 15-min average wind speed higher than  $5 \text{ ms}^{-1}$  at 3.0-m height. The main characteristics of these three wind events are presented in Figure 4 and summarized in Table 1. The first event corresponds to three consecutive daytime events that occurred on 7–9 March, and those were characterized by northwesterly winds. The second event started on 14 March around noon, finished at the end of 15 March, with a lower intensity early on 15 March and was characterized by a constant northeasterly wind. The third event occurred on 20 April during daytime and was characterized by northeasterly winds. Hereafter, these three events will be referred to as either the 7–9 March, 14–15 March, and 20 April events or the first, second, and third wind events, respectively.

The three wind events were associated with soil erosion as shown by the Saltiphone's recording in Figure 4e. Both Saltiphone's recording and saltation fluxes  $Q$  show a clear increase of soil erosion with the surface friction velocity  $u_{*0}$  (Figures 5a and 5b). The best fit of the Saltiphone's recording as a function of  $u_{*0}$  leads to a

**Table 1**

Main Characteristics of the Selected Wind Events: Surface Friction Velocity Deduced From the Eddy Covariance Approach ( $u_{*0}$ ), Wind Direction, Stability ( $z/L$ ), and Number of Selected 15-Min Time Periods (Nb 15 Min)

Events	$u_{*0}$ ( $\text{ms}^{-1}$ )	Wind direction (deg)	$z/L$	Nb 15 min
7–9 March	0.33 ( $\pm 0.07$ )	322 ( $\pm 50$ )	-0.07 ( $\pm 0.05$ )	94
14–15 March	0.32 ( $\pm 0.07$ )	60 ( $\pm 11$ )	-0.02 ( $\pm 0.04$ )	131
20 April	0.32 ( $\pm 0.06$ )	50 ( $\pm 11$ )	-0.07 ( $\pm 0.05$ )	53

Note. Between parentheses are indicated the standard deviations. The criteria chosen to select the 15-min time periods are presented in section 3.4.

threshold friction velocity  $u_{*0t}$  around  $0.22 \text{ ms}^{-1}$  (Figure 5a). The increase of  $Q$  fits well with the third power of  $u_{*0}$  (Figure 5b), in particular the parametrization of Lettau and Lettau (1978):  $Q = c \sqrt{d_p/D} \rho u_{*0}^2 (u_{*0} - u_{*0t}) / g$ , where  $D$  is a reference grain diameter ( $= 250 \mu\text{m}$ ),  $d_p$  the mean grain diameter ( $= 102 \mu\text{m}$  here), and  $\rho$  the air density. We obtained a coefficient  $c$  near 0.5, which is smaller than the value of 4.2 proposed by Lettau and Lettau (1978). This lower value may be explained by the smaller impact velocity of saltating particles during our experiment due to their small size. A similar magnitude of saltating flux was observed by Zhang et al. (2016) from a wind tunnel experiment with a single mode of soil grain diameter around  $100 \mu\text{m}$ . Their coefficient  $c$  ranged from 0.27 to 0.86, following their soil configuration.

For all events, we only selected 15-min periods with near-neutral conditions ( $-0.2 < z/L < 0.01$ ), significant wind speed ( $\geq 5 \text{ ms}^{-1}$  at 3-m height), and wind directions  $\leq 20^\circ$  or  $\geq 270^\circ$  for the 7–9 March event and between  $30^\circ$  and  $90^\circ$  for the 14–15 March and 20 April events (see the shaded areas in Figure 4).

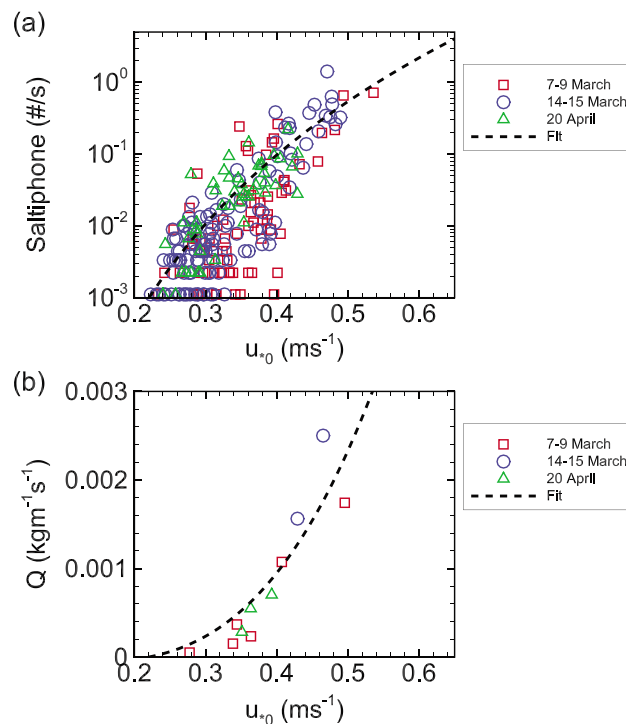


**Figure 5.** Mean impact number of saltating particles recorded by the Saltiphone (a) and saltation flux  $Q$  (b) against the surface friction velocity ( $u_{*0}$ ) obtained for the 7–9 March, 14–15 March, and 20 April events. Saltiphone’s values have been averaged over 15-min periods while saltation fluxes have been averaged over 1 to 4 hours depending on the Big Spring Number Eight collecting time period. The best fit in (a) was obtained for  $110.4u_{*0}^{7.7}$ , which leads to a threshold friction velocity  $u_{*0t}$  near  $0.22 \text{ ms}^{-1}$  below which the Saltiphone did not detect particle impactation. The fitted curve in (b) corresponds to the parametrization of Lettau and Lettau (1978) with  $c = 0.5$  (see the text). The mean square error between this parametrization and the observations is  $\pm 40\%$ , with a coefficient of determination  $r^2 = 0.80$ .



Periods with mean square deviations between measured and fitted wind velocities higher than 5% were discarded. Table 1 gives the number of 15-min periods considered for each wind event considering the above screening criteria.

## 4. Results

### 4.1. Wind Dynamics

We found it important to first control the main characteristics of the wind dynamics during the selected events before evaluating the aerodynamic parameters (friction velocity and roughness length) and the von Karman constant.

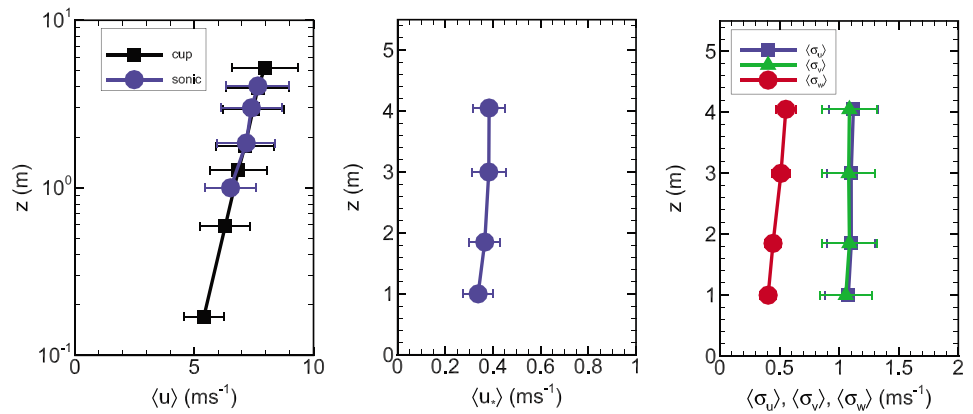
For the three wind events, the mean wind velocity ( $\langle u \rangle$ ) exhibits a well-defined logarithmic profile along the vertical profile (Figure 6). Sonic and cup anemometers show the same velocity amplitude and variation with height (Figure 6, left column). Both standard deviations of the horizontal wind velocity components ( $\langle \sigma_u \rangle$ ,  $\langle \sigma_v \rangle$ ) appear close to each other, the streamwise component being slightly higher for the second event, and both appear almost constant with height (Figure 6, right column). As expected, the standard deviation of the vertical wind velocity component ( $\langle \sigma_w \rangle$ ) is lower and increases with height. The ratios between the velocity standard deviations and the friction velocity are consistent with known values observed in the turbulent surface layer:  $\langle \sigma_u \rangle / \langle u_* \rangle \approx 2.75$  and  $\langle \sigma_w \rangle / \langle u_* \rangle \approx 1.25$  against 2.50 and 1.25, respectively (Raupach et al., 1996).

The mean local friction velocity ( $u_*$ ), and thus the mean momentum flux ( $\langle u'w' \rangle$ ), appears almost constant with height (Figure 6, middle); it decreases slightly near the surface (1-m height) and remains constant above for the 7–9 March event, while it slightly increases with height above 2 m for the 14–15 March and 20 April events. This increase with height could be related to the limited fetch in the northeast direction, the top of the profile being possibly contaminated by turbulence established with the rougher upwind surface outside the plot. This limited fetch does not seem to occur for the 7–9 March event as the plot is longer in the northwest direction (see Figure 1c). Overall, the average mean square deviations between  $u_*$  and the median value of the four anemometer heights ( $u_{*mEC}$ ) are below 10% of  $u_{*mEC}$  (about 6%, 8%, and 9% for the first, second, and third events, respectively), which remains quite reasonable.

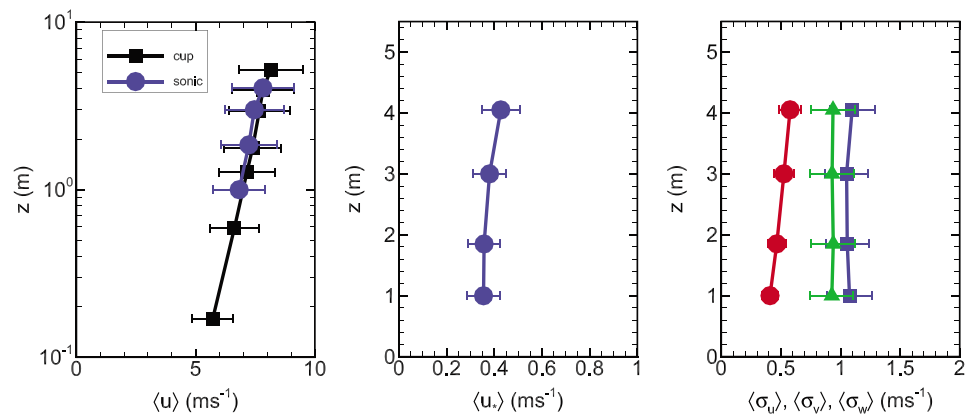
To identify the eddy scales of the main turbulent structures contributing to the velocity variances and to the turbulent transport of momentum ( $u$ - $w$  correlation), Figure 7 presents for all events the ensemble-averaged spectra of the streamwise and vertical velocity components ( $S_u$  and  $S_w$ ) and  $u$ - $w$  cospectrum ( $S_{uw}$ ) obtained at four heights above the surface from the four sonic anemometers. The frequency  $f$  has been normalized using the measurement height  $z$  and the mean wind speed at the same height ( $\langle u(z) \rangle$ ). The normalized wind spectra at the four heights match nicely together. They display the familiar shape of atmospheric surface layer spectra with a well-defined  $-2/3$  power law in the inertial subrange and  $+1$  power law in the energy-containing range for the  $w$  spectra. The peak positions of the  $u$  and  $w$  spectra are distant from each other, 0.008 and 0.32, respectively. The  $w$  peak position is close to the referenced value of 0.28 usually observed in the surface layer (Kaimal et al., 1972), while the  $u$  spectrum peaks at a lower frequency than the value of 0.045 reported in Kaimal et al. (1972). This lower frequency of the main  $u$  fluctuations observed here could be explained by the lower roughness of our bare surface compared to the crop surface covered with wheat stubble of Kaimal et al., 1972's experiment. This distance between  $u$  and  $w$  spectrum peaks reflects the longitudinal elongated shape of turbulent structures near the surface. Our lower surface roughness length ( $<10^{-3}$  m) may have accentuated this elongated shape of turbulent structures. The scale of the main turbulent structures transporting momentum is intermediate between the scales of the eddies contributing the most efficiently to longitudinal and vertical wind fluctuations. The peak of the  $u$ - $w$  cospectrum is around 0.03, which is near the value of 0.07 reported in Kaimal et al. (1972). These results confirm that the length of our averaging procedure (15 min) and frequency of measurements (even close to the surface, at 1-m height) include all the main turbulent structures contributing to the wind turbulence and momentum transport.

To summarize, the wind dynamics observed during our experiment are consistent with usual observations in the surface layer in terms of mean profiles and main turbulent structures. The slight increase of the momentum flux at the top of the profile during the 14–15 March and 20 April events may indicate a shorter fetch at 4-m height for northeasterly winds although the mean velocity profile exhibits a perfect logarithmic form along the whole vertical profile.

(a) 7-9 March



(b) 14-15 March



(c) 20 April

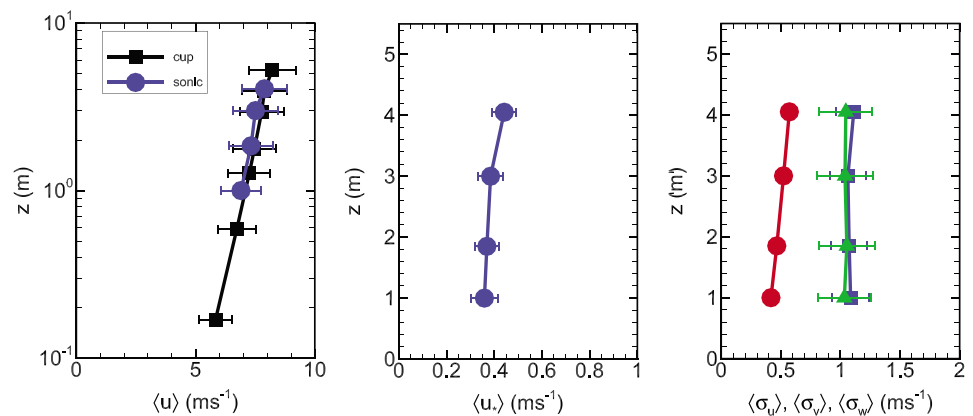


**Figure 6.** Mean vertical profiles of the wind velocity deduced from cup and sonic anemometers (left column), local friction velocity (middle column), and standard deviations of the longitudinal (blue line with squares), lateral (green line with triangles), and vertical (red line with circles) velocity components (right column), obtained for the 7–9 March (a), 14–15 March (b), and 20 April (c) events. The error bars show the standard deviation of each variable. The symbol  $\langle \rangle$  denotes the average over all selected 15-min time periods of each wind events.

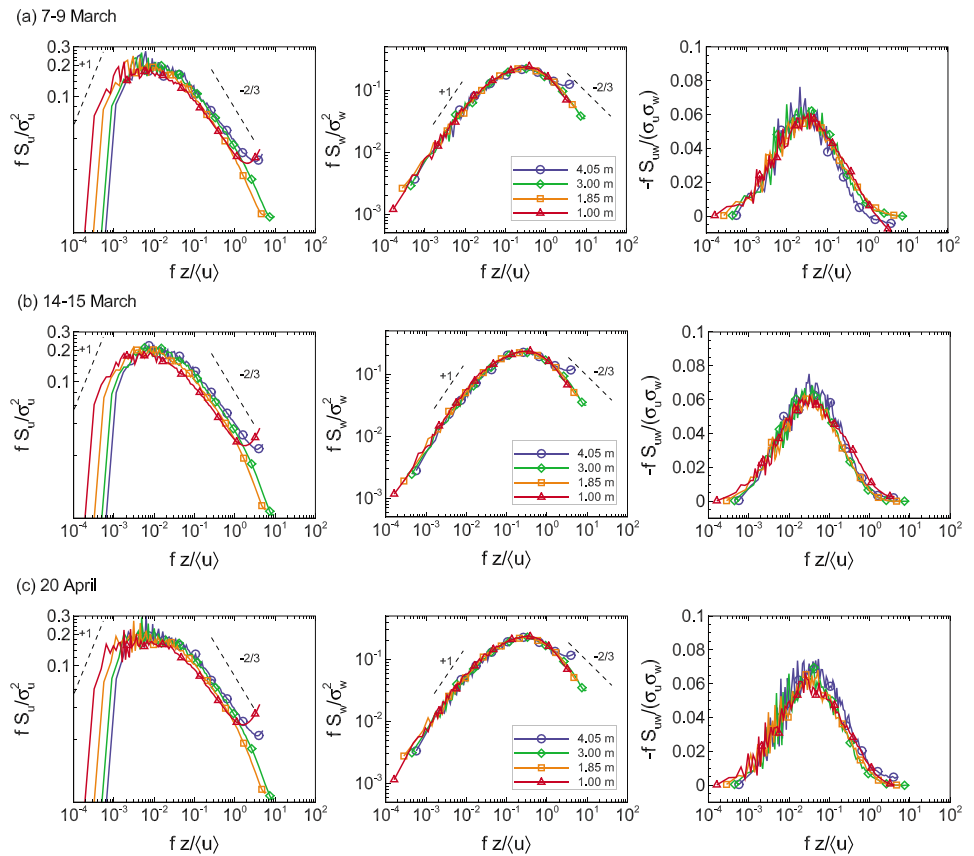


**Figure 7.** Ensemble-averaged normalized spectra of the longitudinal and vertical wind velocity components (left and middle columns) and  $u$ - $w$  cospectra (right column) obtained at four levels above the surface, for the 7–9 March (a), 14–15 March (b), and 20 April (c) events. The frequency  $f$  is normalized by the mean wind speed  $\langle u \rangle$  and the height  $z$ .

#### 4.2. Friction Velocity

The median value of the friction velocities  $u_{*mEC}$  obtained by eddy covariance from the 4 sonic anemometers is compared in a scatter plot with the friction velocity  $u_{*0LoW}$  obtained from the LoW approach (Figure 8a). The friction velocities deduced from the EC approach appear larger than the ones deduced from the LoW approach, especially for the second and third events:  $+0.02 \text{ ms}^{-1}$  for the 7–9 March event and  $+0.07 \text{ ms}^{-1}$  for the 14–15 March and 20 April events.

The agreement between both approaches is improved when substituting for  $u_{*mEC}$  with the extrapolated value at the surface of the friction velocity obtained by eddy covariance  $u_{*0EC}$  (equation (3) and Figure 8b). Only a small bias is perceptible between  $u_{*0LoW}$  and  $u_{*0EC}$ :  $u_{*0EC}$  is slightly underestimated during the first wind event ( $-0.02 \text{ ms}^{-1}$ ) and overestimated during the second ( $+0.02 \text{ ms}^{-1}$ ) and third ( $+0.01 \text{ ms}^{-1}$ ) events. The mean square errors between  $u_{*0EC}$  and  $u_{*0LoW}$  are only  $\pm 0.04$ ,  $\pm 0.02$ , and  $\pm 0.03 \text{ ms}^{-1}$  for the first, second, and third events, respectively. Most of the variability between  $u_{*0LoW}$  and  $u_{*0EC}$  is random and could be attributed to measurement uncertainty,  $\pm 6\%$  for  $u_{*0LoW}$  and  $\pm 14\%$  for  $u_{*0EC}$  (see Appendix A).

Neglecting the stability correction in the evaluation of  $u_{*0LoW}$ , that is,  $\Psi_m = 0$  in equation (2), leads to different biases between  $u_{*0LoW}$  and  $u_{*0EC}$ , but the mean square errors remain similar (Figure 8c). The biases become  $+0.01$ ,  $+0.02$ , and  $+0.03 \text{ ms}^{-1}$  for the first, second, and third events, which indicates an average modification of  $u_{*0LoW}$  going up to 10% for the first event. This highlights the sensitivity of  $u_{*0LoW}$  to  $\Psi_m$  and thus the importance of accounting for stability correction in the LoW, even in near-neutral conditions.

A small difference in height of the anemometer profile significantly changes  $u_{*0LoW}$  through the slope  $A$  of the velocity profile against  $\left[ \log(z) - \Psi_m \left( \frac{z}{L} \right) \right]$ , while the evaluation of  $u_{*0EC}$  is less affected. For a demonstration, the mean bias between  $u_{*0LoW}$  and  $u_{*0EC}$  in Figure 8b was removed by subtracting 3 cm from all anemometer heights for the 7–9 March event and by adding 3 cm and 2 cm to all anemometer heights for the 14–15 March

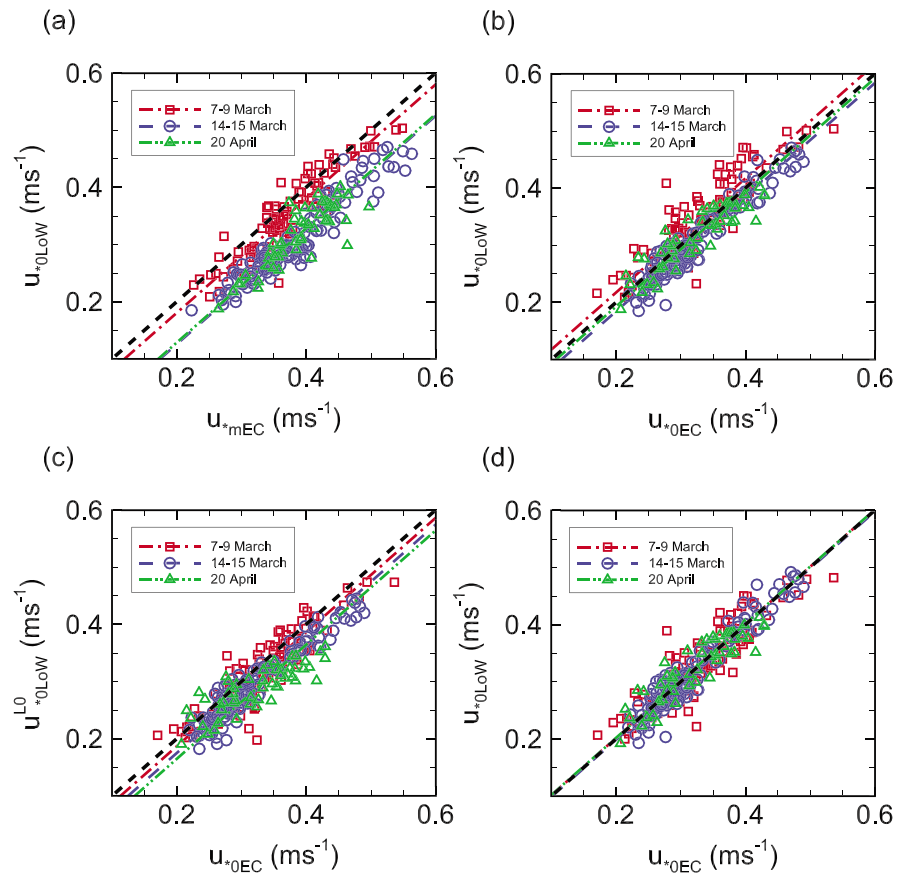


**Figure 8.** Comparison of the friction velocities obtained from the eddy covariance (EC) and law of the wall (LoW) approaches for 7–9 March, 14–15 March, and 20 April events. (a) The friction velocity from the EC approach corresponds to the median value of local friction velocity obtained from the four sonic anemometers ( $u_{*mEC}$ ). (b) The friction velocity from the EC approach corresponds to the extrapolated value at the surface of the local friction velocities obtained from the four sonic anemometers ( $u_{*0EC}$ ). (c) The friction velocity from the LoW approach has been deduced by neglecting the stability function  $\Psi_m$  in equation (2) ( $u_{*0LoW}^{L0}$ ) and the friction velocity from the EC approach corresponds to  $u_{*0EC}$ . (d) Same as (b) but by removing (adding) 3 cm (3 and 2 cm) to all anemometer heights for the 7–9 March event (14–15 March and 20 April events, respectively). The black dashed line indicates the 1:1 relationship; the dash-dotted red line represents the linear regression of the 7–9 March event dots; the long-dashed blue line represents the linear regression of the 14–15 March event dots; the dash-dotted-dotted green line represents the linear regression of the 20 April event dots.

and 20 April events, respectively. With this correction on the ground level ( $z_{surf}$ ), the agreement between  $u_{*0LoW}$  and  $u_{*0EC}$  is improved (Figure 8d). A difference in  $z_{surf}$  between the three events could be explained by the modification of the surface during soil erosion or by a difference in horizon following the wind direction, although our site was relatively flat. Both reasons add to uncertainties in our measurements of anemometer heights at the beginning of the experiment. However, a difference of 6 cm in ground level between northwest and northeast directions appears quite large and thus may not explain the whole bias observed between  $u_{*0LoW}$  and  $u_{*0EC}$ . Furthermore, applying such a correction on  $z_{surf}$  would mean to consider as true the von Karman constant of 0.40 chosen in the LoW approach. This is why we preferred to not consider hereafter any correction on  $z_{surf}$ .

In conclusion, the mean biases observed between  $u_{*0LoW}$  and  $u_{*0EC}$  in Figure 8b remain small for all wind events. These biases could be explained by different combined effects such as (1) the value of the von Karman constant that was fixed at 0.40 in the LoW approach, (2) the stability function  $\Psi_m$ , or (3) the definition of the ground level ( $z_{surf} = 0$ ) used to define the heights of the anemometers. It is difficult to estimate which part of the bias between  $u_{*0LoW}$  and  $u_{*0EC}$  is due to one of these possible reasons.



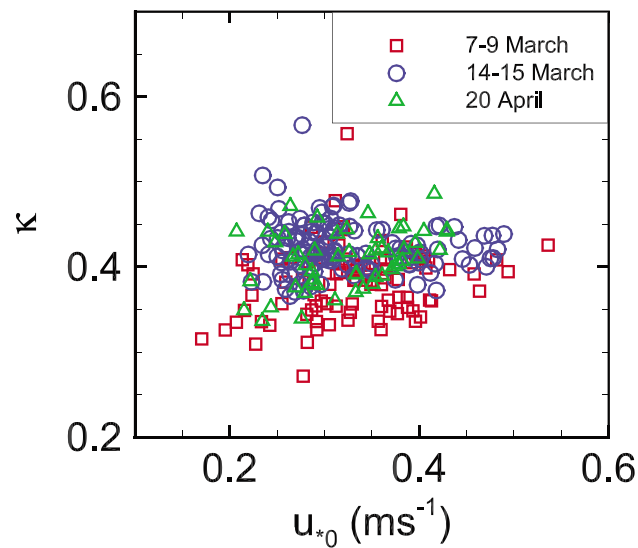


**Figure 9.** The von Karman constant ( $\kappa$ ) against the surface friction velocity ( $u_{*0}$ ) obtained for the 7–9 March, 14–15 March, and 20 April events.

#### 4.3. Von Karman Constant

Including all wind events, we obtained a von Karman constant  $\kappa$  close to 0.407, with a 68.3% confidence interval on this mean value of  $\pm 0.002$  (Figure 9). This value is close to the usual values considered in the literature (0.40–0.41) and thus comforts us in choosing  $\kappa = 0.40$  for estimating  $u_{*LoW}$ . The random variability in  $\kappa$  depicted in Figure 9 is characterized by a standard deviation of  $\pm 0.039$  ( $\pm 10\%$ ), which is similar to the variability usually observed in studies quantifying  $\kappa$  (e.g., Andreas et al., 2006, 1996; Andreas et al., 2006). This variability is mainly explained by uncertainties of measurements. Our uncertainty analysis led to an expected error on  $\kappa$  of around  $\pm 15\%$  (see Appendix A).

However, a significant difference in  $\kappa$  mean value exists between wind events. Our measurements lead to  $\kappa = 0.382 \pm 0.004$ ,  $0.423 \pm 0.003$ , and  $0.409 \pm 0.005$  for the first, second, and third events, respectively. As for the friction velocity, we suspect that a part of this difference between events could come from variations of  $z_{surf}$  or the stability function.

Importantly,  $\kappa$  exhibits no dependence on the surface friction velocity for each event (Figure 9), and therefore no dependence on wind erosion intensity since saltation increases with surface friction velocity (Figure 5).

#### 4.4. Roughness Length

The roughness lengths obtained from the EC and LoW approaches ( $z_{0EC}$  and  $z_{0LoW}$ ) show on average a similar behavior with  $u_{*0}$  (Figure 10). They both increase with  $u_{*0}$ , especially for  $z_{0LoW}$ , which is consistent with the general picture of enhancement of the apparent surface roughness due to the presence of saltating particles that absorb momentum from the flow. Without wind erosion,  $z_{0EC}$  and  $z_{0LoW}$  should only represent the roughness length of the surface and remain constant for  $u_{*0}$  lower than the threshold value  $u_{*0t} = 0.22 \text{ ms}^{-1}$  (horizontal lines in Figure 10). However, it is difficult to find sufficient 15-min periods with  $u_{*0}$  lower than  $u_{*0t}$  to confirm this tendency as for such low wind condition, the thermal stratification deviates from the near-neutral conditions. As in several previous observations (Farrell, 1999; Gillette et al., 1998; Owen, 1964; Rasmussen et al., 1985),  $z_0$  seems to scale with the square of  $u_{*0}$ , in the presence of wind erosion ( $u_{*0} \geq u_{*0t}$ ),  $z_0 \approx C_c u_{*0}^2 / g$ , where  $g$  is the gravitational acceleration. For the first event, both LoW and EC approaches lead to  $C_c = 0.03$  although  $z_{0EC}$  points appear quite scattered, while for the second and third events the LoW approach leads to  $C_c = 0.01$  and the EC approach to  $C_c = 0.02$ . Overall, these  $C_c$  values are close to the value of 0.02 obtained by Owen (1964).

The difference in  $z_0$  between the first and the two others wind events, for the same values of  $u_{*0}$ , is certainly explained by the difference in wind sector, and thus a difference in surface influencing the anemometer measurements. The bias between  $z_{0EC}$  and  $z_{0LoW}$ , especially for the last two events, may have the same origin

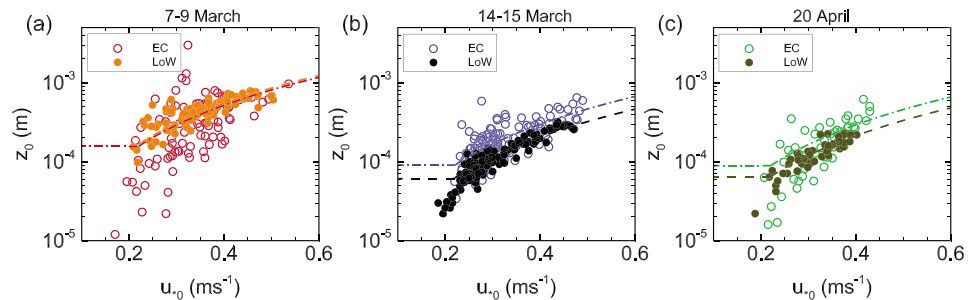


**Figure 10.** Variation of the surface roughness length ( $z_0$ ) as a function of the surface friction velocity ( $u_{*0}$ ) deduced from the eddy covariance (EC) and law of the wall (LoW) approaches, and obtained for the 7–9 March (a), 14–15 March (b), and 20 April (c) events. The lines represent the best fit of  $z_0$  to  $C_c u_{*0}^2 / g$ . In (a),  $C_c = 0.03$  for both EC and LoW approaches (dash-dotted and dashed lines, respectively). In (b) and (c),  $C_c = 0.02$  and  $0.01$  for EC and LoW approaches (dash-dotted and dashed lines, respectively). For friction velocities lower than the threshold value of  $0.22 \text{ ms}^{-1}$  deduced from Figure 5, the average behavior of roughness lengths has been assumed constant.

as the bias between  $u_{*0\text{EC}}$  and  $u_{*0\text{LoW}}$ : the fixed value of the von Karman constant in the EC approach ( $\kappa = 0.40$ ) while  $z_{0\text{LoW}}$  is estimated independently of  $\kappa$ , the definition of  $z_{\text{surf}}$  and/or the parameterization of the stability function  $\Psi_m$ .

The random variability around the mean  $z_0$  values depicted in Figure 10 appears larger for  $z_{0\text{EC}}$  than for  $z_{0\text{LoW}}$ . The mean square errors between  $z_0$  and  $C_c u_{*0}^2 / g$  obtained with the EC are  $\pm 94\%$ ,  $\pm 42\%$ , and  $\pm 45\%$  for the first, second, and third events, against  $\pm 23\%$ ,  $\pm 19\%$ , and  $\pm 18\%$ , respectively, with the LoW approach. Most of this variability on the roughness length values reported in Figure 10 is explained by uncertainties of the measurements. Our uncertainty analysis shows that the 68.3% confidence interval is wider for  $z_{0\text{EC}}$  than  $z_{0\text{LoW}}$ :  $0.6z_{0\text{LoW}} \leq z_{0\text{LoW}} \leq 1.6z_{0\text{LoW}}$  and  $0.3z_{0\text{EC}} \leq z_{0\text{EC}} \leq 2.6z_{0\text{EC}}$  (Appendix A). This larger uncertainty of  $z_{0\text{EC}}$  is explained by the larger uncertainty of  $u_{*0\text{EC}}$  than of  $u_{*0\text{LoW}}$ . Importantly, our uncertainty analysis shows that the LoW approach is more appropriate to estimate the surface roughness length than the EC approach since  $z_{0\text{LoW}}$  depends only on first-order moment and  $\kappa$  does not have to be predefined.

## 5. Discussion and Conclusion

Two friction velocities have been deduced from the EC approach, the mean friction velocity within the surface layer ( $u_{*m\text{EC}}$ ) and the extrapolated friction velocity at the surface ( $u_{*0\text{EC}}$ ). Both were obtained from the four sonic anemometers located between 1.0- and 4.1-m height. Compared to the friction velocity obtained from the LoW approach ( $u_{*0\text{LoW}}$ ),  $u_{*m\text{EC}}$  was 20% larger, while  $u_{*0\text{EC}}$  was in good agreement with  $u_{*0\text{LoW}}$ , regardless of the wind intensity. The mean square error between  $u_{*0\text{LoW}}$  and  $u_{*0\text{EC}}$  was only  $\pm 0.04 \text{ ms}^{-1}$ , and no significant bias was observed. Hence, extrapolating the local friction velocities obtained by EC to the surface instead of averaging them seems to solve most of the discrepancy in  $u_*$  between LoW and EC approaches. This result was obtained after carefully checking the main characteristics of the wind dynamics and turbulent structures by comparison with expected behavior in the surface layer. This result confirms that the friction velocity appearing in the logarithmic form of the velocity profile is representative of the shear stress at the surface, and not of the average shear stress in the surface layer.

Although  $u_*$  should be constant with height in an ideal surface layer, in reality a perfect constant flux layer is rarely observed. In our measurements, the average mean square deviations between local  $u_*$  and  $u_{*m\text{EC}}$  were lower than 10%. As discussed in Andreas et al. (2006), the variability of  $u_*$  with height could be explained by the imperfect stationarity of the surface layer compared to flows in a wind tunnel. This, however, should not lead to a specific trend of the mean  $u_*$  with height as observed in some of our wind events. We suspect that the slight increase with height of the mean  $u_*$  observed in particular for northeasterly winds was a consequence of a limited fetch, the upper profile being possibly contaminated by turbulence established with the rougher upwind surface outside the plot. Despite this imperfect constant flux layer, the mean velocity profile was always logarithmic (mean square deviations  $< 5\%$ ). Observing a logarithmic velocity profile does not necessarily mean a constant flux layer.

Our measurements suggest an average value of the von Karman constant  $\kappa$  of  $0.407 \pm 0.002$ . This mean value is remarkably close to the value of 0.40–0.41 usually taken in the literature. Importantly,  $\kappa$  was found independent of the wind intensity (Figure 9) and thus, independent of the soil erosion intensity since the saltation flux was clearly increasing with wind intensity (Figure 5). Although individual wind events exhibits small differences in average values of  $\kappa$ :  $\kappa = 0.382 \pm 0.004$ ,  $0.423 \pm 0.003$ , and  $0.409 \pm 0.005$  for the 7–9 March, 14–15 March, and 20 April events, respectively, these differences appear uncorrelated with the saltation intensity. We do not have a clear explanation for these small differences in  $\kappa$  between events. The intraday variability of  $\kappa$  during the first and second events does not exhibit any particular tendency or difference (result not shown). The high uncertainty of individual 15-min values of  $\kappa$  ( $\pm 15\%$ ) makes it harder to explain small differences on  $\kappa$  mean values between events. We suspect that a part of these differences could be related to uncertainty associated with the stability correction or the variability in ground level ( $z_{\text{surf}}$ ) between erosion events since the first wind event did not have the same wind directions as the two others and since the last wind event was more than 1 month later than the first two.

The observed independence of  $\kappa$  to wind erosion intensity contradicts the reduction of  $\kappa$  with saltation observed by Li et al. (2010). They explained their  $\kappa$  reduction with the decrease of the turbulent mixing efficiency in presence of sediments in the flow although their measurements were above the saltation layer. Compared to Li et al. (2010), our saltation fluxes were lower by a factor of 10, while our friction velocities normalized by the threshold friction velocity ( $u_{*0}/u_{*0t}$ ) were higher, ranging from 0.8 to 2.5 against 0.9 to 1.8 in Li et al. (2010). Two main reasons could explain this apparent contradictory behavior. First, the lower median grain diameter of our soil, 102  $\mu\text{m}$  against 300  $\mu\text{m}$  in Li et al., 2010, decreases  $u_{*0t}$  and also the particle impact velocity, which consequently reduced the saltation flux. A similar reduction of saltation flux with particle size was observed by Zhang et al. (2016) from a wind tunnel experiment. Second, our sampling periods for collecting sediments with the BSNE were much longer than in Li et al. (2010) (1 to 4 hr compared to 2 to 5 min). Hence, our sampling periods may have included periods of low saltation due to both saltation intermittency and wind variability. Overall, the nonsensitivity of  $\kappa$  value to wind erosion in our experiment may suggest that the apparent increase of  $\kappa$  suggested by Li et al. (2010) could simply be due to a nonconstant flux layer. Indeed, Li et al., 2010's experiment was limited by only one eddy covariance level at 1-m height, making it impossible to verify the presence of a constant flux layer. This led them to assume equality between the friction velocity obtained at this height and the surface friction velocity and thus to assume that the difference in  $u_*$  between LoW and EC approaches was due to a modification of  $\kappa$ . Our findings on the nonsensitivity of  $\kappa$  to wind erosion are also confirmed by the conclusion of Lee and Baas (2016) who observed no dependence on wind erosion of their difference in  $u_*$  between LoW and EC approaches, meaning that the  $\kappa$  value was independent of the wind erosion intensity.

Overall, several reasons could explain the difference in  $u_*$  between EC and LoW approaches observed in previous field experiments (Lee & Baas, 2016; Li et al., 2010). Some of them have been already discussed by these authors. We would like here to highlight four of them. First, the hypothesis of equality between  $u_*$  at the surface and above the surface could be the main reason for the observed differences, in particular because previous studies never observed a constant flux layer or were unable to verify its existence due to an unique sonic anemometer. Second, neglecting the stability correction function  $\Psi_m$  in the logarithmic wind velocity profile (equation (1)) can significantly modify the estimated value of  $u_{*0\text{LoW}}$ , even in near-neutral conditions. In our experiment, although  $\Psi_m$  represented only 3% of  $\log(z/z_0)$  in the wind velocity profile (equation (1)), neglecting  $\Psi_m$  could have led to a difference in  $u_{*0\text{LoW}}$  of up to 10%. Third, an accurate definition of the ground level ( $z_{\text{surf}}$ ) used to define the anemometer heights appears crucial for estimating  $u_{*0\text{LoW}}$ . Our analysis highlighted that a difference of a couple of centimeters can lead to a few  $0.01 \text{ ms}^{-1}$  bias between  $u_{*0\text{EC}}$  and  $u_{*0\text{LoW}}$  (see section 4.2). Fourth, the sampling frequency of sonic anemometers in Li et al. (2010) and Lee and Baas (2016), 32 and 50 Hz, respectively, may have been too low for measurements below 1-m height, down to 0.115-m height in Lee and Baas (2016). These small sampling frequencies may have missed a portion of the high-frequency fluctuations of  $w$  and thus underestimated the friction velocity by not accounting for the momentum transport by the smallest eddies near the surface. Unfortunately, Li et al. (2010) and Lee and Baas (2016) did not present any spectra of their vertical wind velocity component or cospectra of their momentum flux to verify the adequacy of their anemometer sampling frequency. Additionally, the 2- to 5-min averaging time chosen by Li et al. (2010) to derive the friction velocity from their sonic anemometer may also have been too low, missing the contribution from large eddies to the momentum transport. Our analysis showed that 15 min was the lowest limit for an averaging time at 1-m height in order to account for all eddies contributing

to the momentum flux (Figure 2), and a sampling frequency of 60 Hz at 1-m height was a minimum to obtain the inertial range of the  $w$  spectrum (Figure 7).

To conclude, surfaces subject to aeolian soil erosion in semiarid regions often do not respond to the ideal characteristics of application of the LoW, in particular regarding the surface flatness and extent. Even in optimal conditions, accurately estimating a friction velocity above these surfaces is challenging. This needs to be remembered when using the friction velocity to scale erosion fluxes or to estimate dust flux from the flux-gradient relationship. The present study leads to the following recommendations:

1. The surface friction velocity has to be deduced either from a vertical profile of several eddy covariance measurements or from the LoW with a good resolution of the wind starting from the upper saltation layer. Estimating the surface friction velocity from only one level of eddy covariance measurement is inaccurate, even for an apparently homogeneous surface, and thus less accurate for inhomogeneous sites.
2. Aerodynamic parameters ( $u_*$  and  $z_0$ ) would be better deduced independently of  $\kappa$  because of the variability of  $\kappa$  values at the scale of the erosion event. This means to deduce  $z_0$  from the regression of the logarithmic wind speed profile and  $u_*$  from the eddy covariance approach.
3. Neglecting the stability correction in the LoW could lead to significant differences in the estimated values of the aerodynamic parameters, even in near-neutral conditions.
4. Aerodynamic parameters are sensitive to the ground level definition, especially when deduced from the LoW approach. Consequently, the ground level surrounding the measurement mast has to be carefully assessed in all wind directions and reassessed during the field experiment to account for surface modification due to soil erosion.
5. When deducing a friction velocity from the EC approach, the spectra of the wind velocity components and momentum cospectrum have to be checked in order to verify that the choice of the averaging time and sampling frequency of the sonic anemometers is adequate to account for the main eddies responsible for the momentum flux.
6. Since the friction velocity deduced from the LoW approach is representative of the surface wind shear stress,  $u_{*0LoW}$  appears appropriate for scaling saltation fluxes or for defining the threshold friction velocity above which erosion starts. However, as a consequence of the imperfect constant flux layer,  $u_{*0LoW}$  may not be appropriate for estimating dust fluxes at a few meters height ( $z$ ) above the surface from the flux-gradient relationship as  $u_{*0LoW}$  may not accurately represent the velocity scale of the turbulent diffusivity at this level. A local evaluation of the friction velocity from the eddy covariance approach may be more accurate in that case.

## Appendix A: Uncertainty Analysis

The uncertainties on friction velocities ( $u_{*0LoW}$ ,  $u_{*0EC}$ ), roughness lengths ( $z_{0LoW}$ ,  $z_{0EC}$ ), and von Karman constant ( $\kappa$ ) were evaluated by means of Monte Carlo simulations. The approach used to estimate these variables was reproduced in multiple simulations ( $10^5$ ) from typical wind event values of the mean wind speeds ( $\langle u \rangle$ ), momentum fluxes ( $\langle u'w' \rangle$ ), and stability function ( $\Psi_m$ ) where random variabilities were added to their mean values in order to simulate the propagation of prescribed individual uncertainties to the final results. Monte Carlo simulation method was preferred from the conventional uncertainty analysis method as it allows to quantify more accurately the propagation of uncertainties in complex nonlinear systems (Herrador & González, 2004; Papadopoulos & Yeung, 2001).

### A1. Sources of Uncertainty

We identified four sources of uncertainty: (1) the mean wind speed deduced from cup anemometers and used to fit the LoW, (2) the momentum flux estimated by eddy covariance from the sonic anemometers, (3) the origin of the ground surface defining the heights of the cup and sonic anemometers, and (4) the stability function used in the LoW. All four quantities ( $\alpha$ ) were characterized by their own uncertainty  $\Delta_\alpha$  assuming a normal distribution of their values. Their uncertainties  $\Delta_\alpha$  were defined as the percentage of their standard deviation  $\sigma_{(\alpha)}$  of the mean value  $\langle \alpha \rangle$  relative to  $\langle \alpha \rangle$ :  $\Delta_\alpha = \sigma_{(\alpha)} / \langle \alpha \rangle$ . This means that there is a 68.3% probability of having a value between  $\langle \alpha \rangle - \Delta_\alpha \langle \alpha \rangle$  and  $\langle \alpha \rangle + \Delta_\alpha \langle \alpha \rangle$ .

The main source of uncertainty for  $\langle u \rangle$  and  $\langle u'w' \rangle$  is related to sampling error due to the limited number of independent samples contributing to the mean during the chosen averaging time  $T$  (15 min) (Businger, 1986). Increasing the averaging time would reduce the uncertainty, but the condition of stationarity of the

**Table A1**

Summary of the Considered Sources of Uncertainties and the Resulting Propagated Uncertainties Obtained From the Monte Carlo Simulations

Variables	Denomination	Uncertainty
<i>Sources of uncertainty</i>		
$z_{\text{surf}}$	Ground surface origin	$\pm 1$ cm
$\langle u \rangle$	Mean wind speed obtained from cup anemometers	$\pm 2\%$
$u_*$	Local friction velocity deduced from sonic anemometers	$\pm 10\%$
$\Psi_m$	Stability function	$\pm 2\%$
<i>Resulting propagated uncertainty</i>		
$u_{*0\text{LoW}}$	Surface friction velocity obtained from the LoW approach	$\pm 6\%$
$u_{*0\text{EC}}$	Surface friction velocity obtained from the EC approach	$\pm 14\%$
$z_{0\text{LoW}}$	Surface roughness length obtained from the LoW approach	$0.6z_{0\text{LoW}} \leq z_{0\text{LoW}} \leq 1.6z_{0\text{LoW}}$
$z_{0\text{EC}}$	Surface roughness length obtained from the EC approach	$0.3z_{0\text{EC}} \leq z_{0\text{EC}} \leq 2.6z_{0\text{EC}}$
$\kappa$	von Karman constant	$\pm 15\%$

Note. The uncertainties correspond here to the 68.3% confidence interval over the 15-min average values. LoW = law of the wall; EC = eddy covariance.

sampling period may be less verified (Finkelstein & Sims, 2001). The error level of a turbulent quantity  $\alpha$  can be expressed as  $\Delta_\alpha = (\sigma_\alpha / \langle \alpha \rangle) \sqrt{2\tau_\alpha / T}$ , where  $\sigma_\alpha$  and  $\langle \alpha \rangle$  are the standard deviation and the mean of  $\alpha$ , and  $\tau_\alpha$  is the integral time scale of  $\alpha$  (scale of independent measure) (Kaimal & Finnigan, 1994). The integral time scale can be deduced either from the spectrum peak or from the autocorrelation function.

For  $\langle u \rangle$ , the ratio  $\sigma_u / \langle u \rangle$  is typically around 0.14 and  $\tau_u$  is about 5 s during our wind events. This leads to a  $\pm 2\%$  uncertainty on  $\langle u \rangle$ . For  $\langle u'w' \rangle$ ,  $\sigma_{u'w'} / \langle u'w' \rangle$  is around 4 and  $\tau_{u'w'}$  is about 1 s, leading to a  $\pm 20\%$  uncertainty, and thus a  $\pm 10\%$  uncertainty on the local friction velocity  $u_*$ . This large uncertainty on the momentum flux is typical of eddy covariance fluxes (see, e.g., Kaimal & Finnigan, 1994; Rannik et al., 2016). For the same averaging period, higher moments have lower accuracy than lower moments due to increasing variability compared to mean value ( $\sigma_\alpha / \langle \alpha \rangle$ ) with the order of the moment (Kaimal & Finnigan, 1994).

We estimated the uncertainty on the origin of the ground surface as  $\pm 1$  cm. This value includes error in measurements and variability of the surface during the experiment as the surface changed with soil erosion.

Since all our selected measurement periods were in near-neutral conditions, we applied a  $\pm 2\%$  uncertainty on  $\Psi_m$  as proposed by Andreas et al. (2006) based on the variability of the multiplicative constant in  $\Psi_m$  reported in the literature.

## A2. Friction Velocity Uncertainty

Error on  $u_{*0\text{LoW}}$  is related to the uncertainty of the slope  $A$  of the regression of  $\langle u \rangle$  on  $\left[ \log(z) - \Psi_m \left( \frac{z}{L} \right) \right]$  (see equation (2)). In our Monte Carlo trials, the mean wind speed profile was characterized by a mean friction velocity of  $0.32 \text{ ms}^{-1}$ , a roughness length of  $5 \times 10^{-4} \text{ m}$ , a Monin-Obukhov length of  $-43 \text{ m}$ , and with the anemometer heights given in section 3. The simulations led to a range of  $u_{*0\text{LoW}}$  values normally distributed from which we identified an uncertainty of  $\pm 6\%$  (68.3% confidence interval).

Error on  $u_{*0\text{EC}}$  depends on the uncertainty of the intercept of the regression of  $u_*$  on  $z$  (see equation (3)). The mean profile of  $u_*$  was chosen as  $0.0164z + 0.3431$ , which fits the mean profile of Figure 6a. The simulations led to  $u_{*0\text{EC}}$  with also a normal distribution from which we identified an uncertainty of  $\pm 14\%$ .

Note that the uncertainty of  $u_{*0\text{EC}}$  is more important than that of  $u_{*0\text{LoW}}$ . This is explained by the evaluation of  $u_{*0\text{LoW}}$  from a first-order moment ( $\langle u \rangle$ ) while  $u_{*0\text{EC}}$  is deduced from a second-order moment ( $\langle u'w' \rangle$ ), the former moment having higher accuracy than the later one for the same averaging period, as explained in section A1.

## A3. Roughness Length Uncertainty

Error on  $z_{0\text{LoW}}$  depends on the uncertainty of the slope  $A$  and intercept  $B$  of the regression of  $\langle u \rangle$  on  $\left[ \log(z) - \Psi_m \left( \frac{z}{L} \right) \right]$ , while error on  $z_{0\text{EC}}$  depends on the uncertainty of the slope  $A$  and on the uncertainty of



$u_{*0EC}$  estimated in the previous section. The simulations led to  $z_{0LoW}$  and  $z_{0EC}$  values with a gamma distribution. We obtained the following 68.3% confidence interval:  $0.6z_{0LoW} \leq z_{0LoW} \leq 1.6z_{0LoW}$  and  $0.3z_{0EC} \leq z_{0EC} \leq 2.6z_{0EC}$ .

For the same reasons as for the friction velocity, the uncertainty of the roughness length estimated indirectly from the EC approach appears more important than that obtained from the LoW approach.

### Von Karman Constant Uncertainty

Error on  $\kappa$  depends on the uncertainties of the slope  $A$  and of  $u_{*0EC}$ . The simulations led to  $\kappa$  values normally distributed from which we identified an uncertainty of  $\pm 15\%$ .

Table A1 summarizes all uncertainties considered and deduced in this study.

### Acknowledgments

We acknowledge the support of the French National Research Agency (ANR) under the grant ANR-15-CE02-0013 (project WIND-O-V). We would like to thank the following: (i) Houcine Khatteli, Director of the Institut des Régions Arides (IRA) of Médenine, for the constant support of IRA in all research related to wind erosion and in particular for giving us access to the Dar Dhaoui's experimental range and for the IRA's logistic help during the all experiment to ensure the success of the campaign, (ii) the guards of the experimental stations (Noureddine Boukhli, Mokhtar Elghoul, and Mousbah Elghoul) for their constant help and surveillance of the experimental system, and (iii) Mark R. Irvine and Christophe Chipeaux for their help with the data acquisition setup from Raspberry Pi. Finally, we thank the three anonymous reviewers for their helpful comments. The processed data used in this study are available at the WIND-O-V Web site (<https://www6.inra.fr/anr-windov/>).

### References

- Andreas, E. L., Claffey, K. J., Jordan, R. E., Fairall, C. W., Guest, P. S., Persson, P. O. G., & Grachev, A. A. (2006). Evaluations of the von Kármán constant in the atmospheric surface layer. *Journal of Fluid Mechanics*, 559, 117–149. <https://doi.org/10.1017/S0022112006000164>
- Bagnold, R. (1941). *The physics of blown sand and desert dunes*. Methuen, London: Springer Netherlands.
- Biron, P. M., Robson, C., Lapointe, M. F., & Gaskin, S. J. (2004). Comparing different methods of bed shear stress estimates in simple and complex flow fields. *Earth Surface Processes and Landforms*, 29(11), 1403–1415. <https://doi.org/10.1002/esp.1111>
- Businger, J. A. (1986). Evaluation of the accuracy with which dry deposition can be measured with current micrometeorological techniques. *Journal of Climate and Applied Meteorology*, 25, 1100–1124. [https://doi.org/10.1175/1520-0450\(1986\)025<1100:EOTAWW>2.0.CO;2](https://doi.org/10.1175/1520-0450(1986)025<1100:EOTAWW>2.0.CO;2)
- Dupont, S., & Patton, E. G. (2012). Influence of stability and seasonal canopy changes on micrometeorology within and above an orchard canopy: The CHATS experiment. *Agricultural and Forest Meteorology*, 157, 11–29. <https://doi.org/10.1016/j.agrformet.2012.01.011>
- Farrell, E. (1999). An investigation of surface-wind systems for aeolian saltation: Field and laboratory experiments (Master's thesis). Dept. of Geogr. Univ. of S. Calif. Los Angeles.
- Finkelstein, P. L., & Sims, P. F. (2001). Sampling error in eddy correlation flux measurements. *Journal of Geophysical Research*, 106(D4), 3503–3509. <https://doi.org/10.1029/2000JD900731>
- Foken, T., Göockede, M., Mauder, M., Mahrt, L., Almiro, B., & Munger, J. (2004). Post-field data quality control. In X. Lee, W. Massman, & B. Law (Eds.), *Handbook of micrometeorology: A guide for surface flux measurement and analysis* (Vol. 29, pp. 181–208). Dordrecht: Springer.
- Frangi, J.-P., & Richard, D. C. (2000). The WELSONS experiment: Overview and presentation of first results on the surface atmospheric boundary-layer in semiarid Spain. *Annales Geophysicae*, 18, 365–384. <https://doi.org/10.1007/s005850050895>
- Frenzen, P., & Vogel, C. A. (1995). On the magnitude and apparent range of variation of the von Kármán constant in the atmospheric surface layer. *Bound-Layer Meteorol*, 72(4), 371–392. <https://doi.org/10.1007/BF00709000>
- Fryrear, D. W. (1986). A field dust sampler. *Journal of Soil and Water Conservation*, 41(2), 117–120.
- Gillette, D. A., Blifford Jr., I. H., & Fenster, C. R. (1972). Measurements of aerosol size distributions and vertical fluxes of aerosols on land subject to wind erosion. *Journal of Applied Meteorology*, 11(6), 977–987. [https://doi.org/10.1175/1520-0450\(1972\)011<0977:MOASDA>2.0.CO;2](https://doi.org/10.1175/1520-0450(1972)011<0977:MOASDA>2.0.CO;2)
- Gillette, D. A., Marticorena, B., & Bergametti, G. (1998). Change in the aerodynamic roughness height by saltating grains: Experimental assessment, test of theory and operational parameterization. *Journal of Geophysical Research*, 103(D6), 6203–6209.
- Haugen, D. A., Kaimal, J. C., & Bradley, E. F. (1971). An experimental study of Reynolds stress and heat flux in the atmospheric surface layer. *Quarterly Journal of the Royal Meteorological Society*, 97, 168–180. <https://doi.org/10.1002/qj.49709741204>
- Herrador, M. A., & González, A. G. (2004). Evaluation of measurement uncertainty in analytical assays by means of Monte-Carlo simulation. *Talanta*, 64, 415–422. <https://doi.org/10.1016/j.talanta.2004.03.011>
- Högström, U. (1985). Von Kármán's constant in atmospheric boundary layer flow: Reevaluated. *Journal of the Atmospheric Sciences*, 42(3), 263–270. [https://doi.org/10.1175/1520-0469\(1985\)042<0263:VKCIAB>2.0.CO;2](https://doi.org/10.1175/1520-0469(1985)042<0263:VKCIAB>2.0.CO;2)
- Högström, U. (1988). Non-dimensional wind and temperature profiles in the atmospheric surface layer: A re-evaluation. *Boundary-Layer Meteorology*, 42(1–2), 55–78. <https://doi.org/10.1007/BF00119875>
- Kaimal, J. C., & Finnigan, J. J. (1994). *Atmospheric boundary layer flows. Their structure and measurements*. New-York: Oxford University Press.
- Kaimal, J. C., Wyngaard, J. C., Izumi, Y., & Coté, O. R. (1972). Spectral characteristics of surface-layer turbulence. *Quarterly Journal of the Royal Meteorological Society*, 98, 563–589. <https://doi.org/10.1002/qj.49709841707>
- King, J., Nickling, W. G., & Gillies, J. A. (2008). Investigations of the law-of-the-wall over sparse roughness elements. *Journal of Geophysical Research*, 113, F02S07. <https://doi.org/10.1029/2007JF000804>
- Lee, Z. S., & Baas, A. C. W. (2016). Variable and conflicting shear stress estimates inside a boundary layer with sediment transport. *Earth Surface Processes and Landforms*, 41(4), 435–445. <https://doi.org/10.1002/esp.3829>
- Lettau, K., & Lettau, H. (1978). Experimental and micro-meteorological field studies of dune migration. In *Exploring the worlds driest climate* (pp. 110–147). Madison: Institute for Environmental Studies University of Wisconsin.
- Li, B., Sherman, D. J., Farrell, E. J., & Ellis, J. T. (2010). Variability of the apparent von Kármán parameter during aeolian saltation. *Geophysical Research Letters*, 37, L15404. <https://doi.org/10.1029/2010GL044068>
- Marticorena, B., Kardous, M., Bergametti, G., Callot, Y., Chazette, P., Khatteli, H., et al. (2006). Surface and aerodynamic roughness in arid and semiarid areas and their relation to radar backscatter coefficient. *Journal of Geophysical Research*, 111, F03017. <https://doi.org/10.1029/2006JF000462>
- Oncley, S. P., Friehe, C. A., Larue, J. C., Businger, J. A., Itsweire, E. C., & Chang, S. S. (1996). Surface-layer fluxes, profiles, and turbulence measurements over uniform terrain under near-neutral conditions. *Journal of Atmospheric Sciences*, 53(7), 1029–1044.
- Owen, P. R. (1964). Saltation of uniform grains in air. *Journal of Fluid Mechanics*, 20(2), 225–242. <https://doi.org/10.1017/S0022112064001173>
- Papadopoulos, C. E., & Yeung, H. (2001). Uncertainty estimation and Monte Carlo simulation method. *Flow Measurement and Instrumentation*, 12, 291–298. [https://doi.org/10.1016/S0955-5986\(01\)00015-2](https://doi.org/10.1016/S0955-5986(01)00015-2)
- Rannik, U., Peltola, O., & Mammarella, I. (2016). Random uncertainties of flux measurements by the eddy covariance technique. *Atmospheric Measurement Techniques*, 9(10), 5163–5181. <https://doi.org/10.5194/amt-9-5163-2016>

- Rasmussen, K. R., Sorensen, M., & Willetts, B. B. (1985). Measurement of saltation and wind strength on beaches, *Proceedings of International Workshop on the Physics of Blown Sand* (Vol. 8, pp. 301–326). Aarhus, Denmark: Dept. of Theor. Stat., Aarhus Univ.
- Raupach, M. R. (1991). Saltation layers, vegetation canopies and roughness lengths. *Acta Mechanica*, *1*, 83–96. [https://doi.org/10.1007/978-3-7091-6706-9\\_5](https://doi.org/10.1007/978-3-7091-6706-9_5)
- Raupach, M. R., Finnigan, J. J., & Brunet, Y. (1996). Coherent eddies and turbulence in vegetation canopies: The mixing-layer analogy. *Boundary-Layer Meteorology*, *78*(3–4), 351–382. <https://doi.org/10.1007/BF00120941>
- Shao, Y. (2008). *Physics and modelling of wind erosion*. Heidelberg, Germany: Springer.
- Shao, Y., Ishizuka, M., Mikami, M., & Leys, J. F. (2011). Parameterization of size-resolved dust emission and validation with measurements. *Journal of Geophysical Research*, *116*, D08203. <https://doi.org/10.1029/2010JD014527>
- Spaan, W. P., & Van den Abeele, G. D. (1991). Windborne particle measurements with acoustic sensors. *Soil Technology*, *4*, 51–63.
- Wright, S., & Parker, G. (2004). Density stratification effects in sand-bed rivers. *Journal of Hydraulic Engineering ASCE*, *130*(8), 783–795. [https://doi.org/10.1061/\(ASCE\)0733-9429\(2004\)130:8\(783\)](https://doi.org/10.1061/(ASCE)0733-9429(2004)130:8(783))
- Zhang, J., Teng, Z., Huang, N., Guo, L., & Shao, Y. (2016). Surface renewal as a significant mechanism for dust emission. *Atmospheric Chemistry and Physics*, *16*, 15,517–15,528. <https://doi.org/10.5194/acp-16-15517-2016>

# **B Appendix B: Dissimilarity Between Dust, Heat, and Momentum Turbulent Transports During Aeolian Soil Erosion**





## Dissimilarity Between Dust, Heat, and Momentum Turbulent Transports During Aeolian Soil Erosion

**Key Points:**

- The near-surface size-resolved dust flux is estimated using the eddy covariance technique
- Dissimilarity between dust, heat, and momentum turbulent transports is observed due to the large intermittency of the dust emission
- Our findings have implications on the evaluation of dust flux using techniques based on similarity with momentum-heat turbulent transport

**Supporting Information:**

- Supporting Information S1

**Correspondence to:**

S. Dupont,  
sylvain.dupont@inra.fr

**Citation:**

Dupont, S., Rajot, J.-L., Labiadh, M., Bergametti, G., Lamaud, E., Irvine, M. R., et al. (2019). Dissimilarity between dust, heat, and momentum turbulent transports during aeolian soil erosion. *Journal of Geophysical Research: Atmospheres*, 124, 1064–1089. <https://doi.org/10.1029/2018JD029048>

Received 22 MAY 2018

Accepted 21 DEC 2018

Accepted article online 7 JAN 2019

Published online 25 JAN 2019

S. Dupont<sup>1</sup> , J.-L. Rajot<sup>2,3,4</sup> , M. Labiadh<sup>3</sup>, G. Bergametti<sup>4</sup> , E. Lamaud<sup>1</sup>, M. R. Irvine<sup>1</sup> , S. C. Alfaro<sup>4</sup>, C. Bouet<sup>2,4</sup> , R. Fernandes<sup>1</sup> , B. Khalfallah<sup>4</sup>, B. Marticorena<sup>4</sup> , J. M. Bonnefond<sup>1</sup>, S. Chevaillier<sup>4</sup>, D. Garrigou<sup>1</sup>, T. Henry-des-Tureaux<sup>2,3</sup>, S. Sekrafi<sup>3</sup>, and P. Zapf<sup>4</sup>

<sup>1</sup>ISPA, INRA, Bordeaux Sciences Agro, Villenave d'Ornon, France, <sup>2</sup>IEES Paris (Institut d'Ecologie et des Sciences de l'Environnement de Paris), UMR IRD 242, Université Paris Est Créteil-Sorbonne Université-CNRS-INRA-Université Paris Diderot, Bondy, France, <sup>3</sup>IRA-Médenine, Médenine, Tunisia, <sup>4</sup>LISA (Laboratoire Interuniversitaire des Systèmes Atmosphériques), UMR CNRS 7583, Universités Paris Est Créteil et Paris Diderot, IPSL, Créteil, France

**Abstract** Measuring accurately size-resolved dust flux near the surface is crucial for better quantifying dust losses by semiarid soils. Dust fluxes have been usually estimated from the flux-gradient approach, assuming similarity between dust and momentum turbulent transport. This similarity has, however, never been verified. Here we investigate the similarity between dust (0.3 to 6.0  $\mu\text{m}$  in diameter), momentum, and heat fluxes during aeolian erosion events. These three fluxes were measured by the Eddy Covariance technique during the WIND-O-V (WIND erOsion in presence of sparse Vegetation's) 2017 field experiment over an isolated erodible bare plot in South Tunisia. Our measurements confirm the prevalence of ejection and sweep motions in transporting dust as for heat and momentum. However, our measurements also reveal a different partition of the dust flux between ejection and sweep motions and between eddy time scales compared to that of momentum and heat fluxes. This dissimilarity results from the intermittency of the dust emission compared to the more continuous emission (absorption) of heat (momentum) at the surface. Unlike heat emission and momentum absorption, dust release is conditioned by the wind intensity to initiate sandblasting. Consequently, ejection motions do not carry dust as often as heat and low momentum from the surface. This dissimilarity diminishes with increasing wind intensity as saltation patterns, and thus dust emission through sandblasting, become spatially more frequent. Overall, these findings may have implications on the evaluation of dust flux from techniques based on similarity with momentum or heat turbulent transport.

### 1. Introduction

Aeolian soil erosion is responsible for about 32% of the annual natural mass emission of aerosols in the atmosphere (IPCC, 2013). Desert regions are the main source of mineral dust in the atmosphere, followed by semiarid regions. Mineral dust in the atmosphere has environmental and climatic implications (Mahowald, 2011; Shao, Wyrwoll, et al. 2011; Yin et al., 2002; Yu et al., 2015) as well as health impacts related to air quality deterioration and inhalation of minute particles (Bonasoni et al., 2004; Derbyshire, 2007). Compared to desert regions, semiarid regions are characterized by a mix of bare and vegetated surfaces going from grassland, crop, shrubland, to woodland, with different erodible levels. This complex arrangement of surfaces complicates the estimation of dust emission from these regions (Pierre et al., 2018).

One of the key issues for quantifying dust emission lies on estimating the near-surface dust flux. Dust production and transport within the first meters of the surface atmospheric layer is conditioned by the near-surface turbulence. While the mechanism of dust production at the surface through sandblasting (e.g., Alfaro et al., 1997; Gomes et al., 1990) and, to a lesser extent, through direct liftoff by dust devils (Neakrase et al., 2016) has been subject to several researches, the mechanism of dust turbulent transport within the first meters above the surface has received less attention. This is why dust is usually simply assumed as passive scalars (diameter lower than 20  $\mu\text{m}$ ), transported as the momentum by near-surface turbulence. This hypothesis is especially used when assessing dust flux using the flux-gradient relationship, assuming equivalence between momentum and dust eddy diffusivity coefficients (Gillette et al., 1972; Ishizuka et al., 2014; Nickling & Gillies, 1993; Shao, Ishizuka, et al., 2011; Sow et al., 2009).

This similarity in dust and momentum transports was justified by the assumption that both dust and momentum are carried by the same eddies. This analogy in turbulent transport between momentum and scalars is often referred to as the Reynolds analogy (Li & Bou-Zeid, 2011). The specific eddies responsible for momentum and scalar transport are known as coherent eddy structures (Robinson, 1991). Such structures have a certain coherence in space and time compared to the random background turbulence. In near-neutral conditions such as during a synoptic-scale dust storm, turbulence is mostly shear-driven. Here the coherent structures in the near-surface layer include different nested structures (e.g., Adrian, 2007; Hutchins et al., 2012): (1) very large-scale elongated structures scaling with the boundary layer thickness and corresponding to juxtaposed meandering regions of low- and high-speed streaks, (2) inclined hairpin vortices arranged into packets resulting from the ejection of low speed from the surface, and (3) local sweeps and ejections constituting the primary motions of hairpin vortices. These last two motions, sweeps and ejections, are responsible for most of the turbulent transport of momentum and scalars in the near-surface boundary layer (e.g., Katul et al., 1997). The importance of ejections and sweeps in moving particles such as dust, away and toward the surface, respectively, has been demonstrated from Direct Numerical Simulations (e.g., Vinkovic et al., 2011) but has never been verified from field experiment.

Heat also has long been considered as transported as momentum under the same argument as for dust that both momentum and heat are carried by the same eddies. However, many studies observed a dissimilarity between heat and momentum turbulent transport, in particular with increasing instability conditions (Dupont & Patton, 2012; Li & Bou-Zeid, 2011). This dissimilarity results from the enhancement of buoyancy-driven turbulence (buoyant-thermal motions) with increasing instability and consequently the reduction of shear-driven turbulence, the former turbulence type optimizing heat transport (Li & Bou-Zeid, 2011; Salesky et al., 2017). The turbulent Prandtl number, which characterizes the ratio of turbulent diffusivities between momentum and heat, is thus often lower than one and increases with stability (Businger et al., 1971; Kays, 1994). This means that heat is transported by turbulence more efficiently than momentum, even in near-neutral conditions, although the Prandtl number exhibits large scatter for this stability condition. Similarly, differences in transport between heat and gas such as water vapor or CO<sub>2</sub> have also been reported due mainly to difference in distribution of sources and sinks between these scalars as well as due to the scalar gradient across the top of the boundary layer's entrainment zone, especially in convective conditions (e.g., Cava et al., 2008; Dupont & Patton, 2012; Katul et al., 2008; Lamaud & Irvine, 2006; Moene et al., 2006; Williams et al., 2007). There are therefore reasonable arguments to challenge the assumption that dust turbulent transport is in analogy to that of momentum and heat.

Dissimilarity in atmospheric turbulent transport between particles in general and momentum or heat has been less investigated. This is partly due to the difficulty of measuring directly particle fluxes using the eddy covariance technique as it requires to measure simultaneously high-frequency wind velocity components and particle concentration. Most studies having measured particle flux from this technique focused on the quantification of the flux itself and not on its analogy with momentum or heat fluxes. These studies were mainly performed over urban areas (Deventer, El-Madany, et al., 2015; Dorsey et al., 2002; Mårtensson et al., 2006), vegetated surfaces (Damay et al., 2009; Deventer, Held, et al., 2015), and much less over desert areas (Fratini et al., 2007; Porch & Gillette, 1977). The only studies comparing particle and heat turbulent transports either observed similarity between both scalars (Fratini et al., 2007; Mårtensson et al., 2006) or assumed similarity to correct their particle flux from the heat flux due to the slow response time of their particle counter (Damay et al., 2009; Deventer, Held, et al., 2015). Hence, in these studies particles are usually considered as passive scalars with the same source/sink distributions as heat. With increasing particle size, particle inertia and gravity cannot be neglected, and dissimilarity with momentum and heat is expected as particle trajectories do not follow exactly the carrier eddy (Fratini et al., 2007; Shao, 2008). These inertia and gravity effects are neglected for dust particles smaller than 10 μm in diameter (Fratini et al., 2007; Shao, 2008).

To our knowledge, only two field experiments measured dust flux by the eddy covariance technique and compared the turbulent transport of dust with that of momentum or heat. First, Porch and Gillette (1977) observed similarity between dust and momentum turbulent exchange coefficients (eddy diffusivity coefficients). Their result was, however, limited to a dust deposition period. More recently, Fratini et al. (2007) observed under strong wind conditions (friction velocity around 0.60 ms<sup>-1</sup>) that dust particles (0.26–7.00-μm diameter range) act as a passive scalar and are transported as heat. This similarity between dust and heat was less verified under low wind conditions (friction velocity around 0.40 ms<sup>-1</sup>); this was attributed by

Fratini et al. (2007) to an underestimation of the dust concentration due to dilution performed by their counter system. Their measurements were performed far from the surface (12 m) as compared to usual dust flux measurement height (only a few meter height), and above an extended desert region of northern China, as opposed to isolated erodible plots in semiarid regions.

We argue here that dissimilarity in turbulent transport between dust and momentum (and heat) is possible near the surface as observed for gas because of the different physics in source/sink between dust and momentum (and heat). Indeed, the absorption (emission) of momentum (heat) at the surface is dominated by convective turbulent transport, while the emission of dust is conditioned by the breakage of cohesion forces of dust particles on soil aggregates by impaction of saltating particles (sandblasting) and, less common, through direct lift force from strong wind gusts. If this dissimilarity exists, it should be accounted for in parametrizations and estimations of dust fluxes in, respectively, models and field measurements using the flux-gradient relationship. The goal of this study is to verify this dissimilarity between dust, heat, and momentum fluxes in the near-surface atmospheric layer (3-m height) during the wind erosion of an isolated bare plot in a fragmented cultural landscape, typical of semiarid regions. To that purpose, a novel field experiment was performed in South Tunisia under the research program WIND-O-V (WIND erOsion in presence of sparse Vegetation) (Dupont et al., 2018). During this experiment, wind velocity components, air temperature, and size-resolved dust concentration were measured simultaneously at high frequency at 3-m height over a flat bare soil under soil erosion conditions. The turbulent transports of momentum, heat, and dust are compared from quadrant, octant, cospectral, and multiresolution analyses.

## 2. The WIND-O-V's 2017 Experiment

### 2.1. Site

The WIND-O-V's 2017 experiment took place from 1 March to 15 May 2017 in South Tunisia, in the experimental range (Dar Dhaoui) of the Institut des Régions Arides of Médenine close to Médenine/Zarzis (Figures 1a and 1b). The site approximates a flat half-circle plot of 150-m radius where measurements were performed at the center of the circle in order to ensure a fetch of at least 150 m for westerly, northerly to easterly winds (Figure 1c). In the north, the fetch was slightly longer, about 200 m. The ground surface was flat (slope less than  $0.3^\circ$  in all directions). The plot was surrounded by less erodible plots with small bushes in the northwest ( $0.34 \pm 0.08$  m height and  $0.58 \pm 0.20$  m diameter) and young olive trees arranged in a square pattern (about  $1.7 \pm 0.3$  m height,  $1.5 \pm 0.4$  m diameter, and 26 m spaced) in the northeast. The soil is typical of the Jeffara basin with a surface loamy sand layer very prone to wind erosion. Before the experiment and after the main rainfall events, the surface had been tilled with a disc plow and leveled with a wood board in order to meet the conditions of an ideal flat bare soil without soil crust nor ridges.

### 2.2. Measurements

A 9-m-high lattice mast was erected at the center of the half-circle plot (Figure 1d). On this mast, turbulent velocity components and air temperature fluctuations were measured simultaneously at 1.0, 1.9, 3.0, and 4.1 m above the surface using four 3-D ultrasonic anemometers (one Campbell Scientific CSAT3, two Gill R3, and one Gill WindMaster) sampling at 60, 50, 50, and 20 Hz, respectively. On the same mast, seven cup anemometers (0.2, 0.6, 1.3, 1.8, 3.0, 4.0, and 5.2 m) and four thermocouples (0.4, 1.6, 3.7, and 5.0 m) were also installed to measure simultaneously at 0.1 Hz the mean horizontal wind velocity and temperature profiles, respectively. All anemometers on the tower were intercalibrated prior to the experiment.

Airborne dust concentration per size class was measured at 1 Hz from three PALAS WELAS-2300 particle spectrometers, covering 0.3–17- $\mu$ m diameter range particles and with 16 intervals per decade. The spectrometers determined the size and number of particles in sampled air in the optical chamber, delivered by a pump with a flow rate of 5 L/min. Before the experiment, the spectrometers were calibrated from monodisperse dust particles of silicon dioxide (1.28  $\mu$ m in diameter) as recommended by the manufacturer. Equivalence between the refractive indices of silicon dioxide and mineral dust particles was assumed. One of the spectrometers was coupled to the 3-m height sonic anemometer in order to deduce size-resolved number dust fluxes using the eddy covariance technique. A specific small sampling head was built for this particle spectrometer in order to not disturb the measurements of the 3-m-height anemometer. This head was simply constituted of a 25-cm-long and 1-cm-diameter tube with a drilled cover letting particles entering while protecting from the rain (see Figure 1e). This sampling head was positioned about 20 cm south from the head of the sonic anemometer. This head was made in order to minimize disruption of the air while sampling dust particle within the air. The two other spectrometers were used stand-alone at 2- and 4-m height



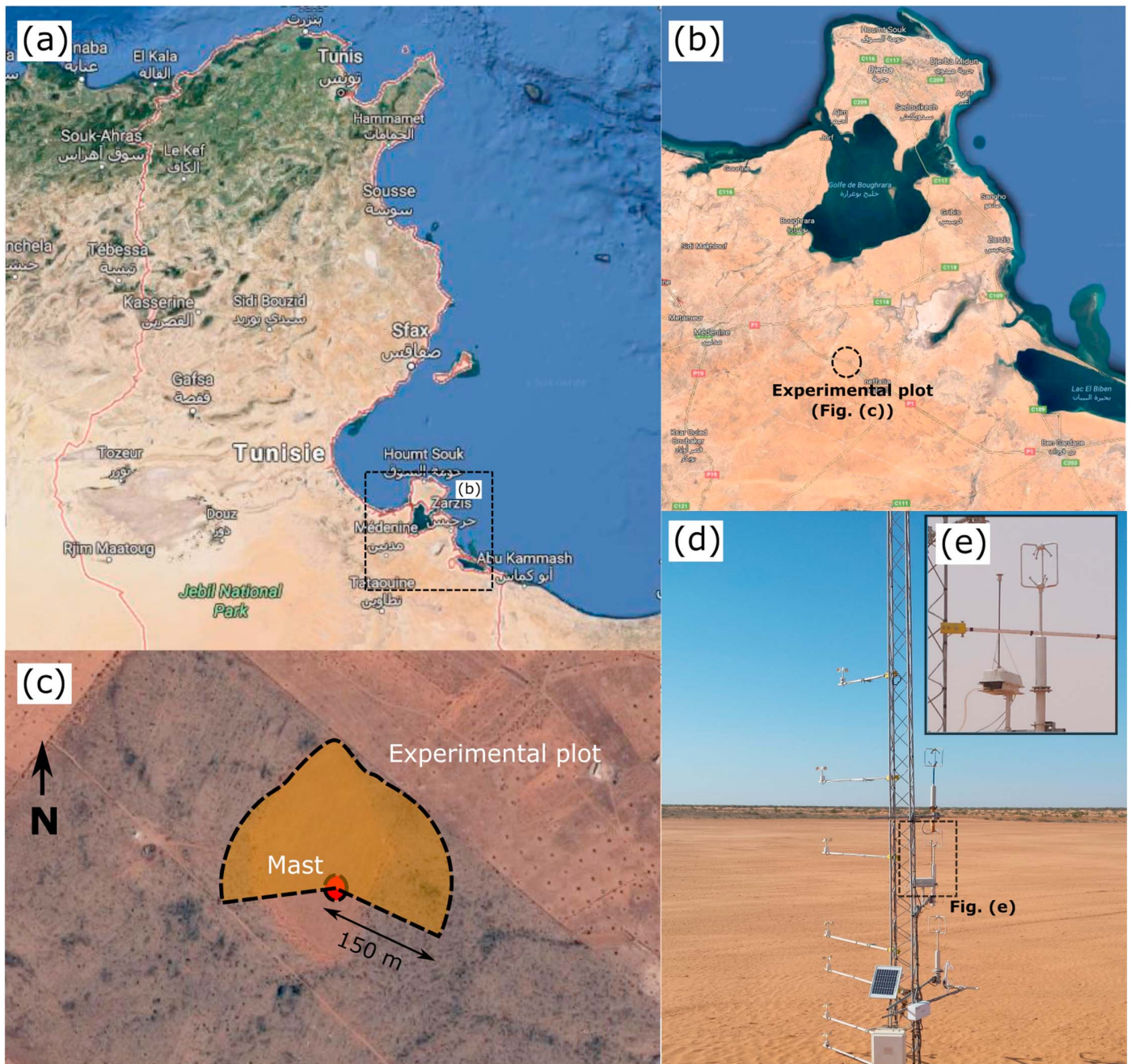


**Figure 1.** WIND-O-V (WIND erOsion in presence of sparse Vegetation's) 2017 experimental site. (a and b) Localization of the site in Tunisia (Google Map). (c) Schematic representation of the near-half-circle experimental plot where the measurement mast was located at its center. (d) North view of the plot from the back of the mast where cup and ultrasonic anemometers were mounted. (e) Sampling head of the particle spectrometer located downwind the 3-m-height ultrasonic anemometer.

on an other mast. Since these two spectrometers were not coupled to a sonic anemometer, they could be equipped with a standard Total Suspended Particles sampling head (BGI by Mesa Labs, Butler, NJ, United States). The particle size distribution measured by the three spectrometers was similar for particles smaller than  $4 \mu\text{m}$ , confirming the negligible impact of the sampling head for such particle size range. Above  $4 \mu\text{m}$ , the spectrometer equipped with the small sampling head started to underestimate the number of particles as compared to the two other spectrometers. Nonetheless, the dust concentration fluctuations of particles larger than  $4 \mu\text{m}$  could still be considered valid for estimating the dust flux by eddy covariance provided

that the dust spectra still respond to the expected shape. For this study, we focus solely on data from the spectrometer coupled to the sonic anemometer.

Saltation was also followed from two Saltiphones (Eijkelkamp<sup>®</sup>, Giesbeek, the Netherlands) positioned close to the surface and several sediment traps like Big Spring Number Eight (BSNE) (Fryrear, 1986), allowing to characterize the erosion dynamics and to quantify the saltation flux and particle size distribution, respectively (see Dupont et al., 2018).

Data from all anemometers and particle spectrometers were acquired and stored simultaneously from several synchronized Raspberry Pi's assembled in a local network.

### 2.3. Data Processing

A 15-min averaging time was chosen for computing all statistics characterizing the wind and dust dynamics. This value was deduced in Dupont et al. (2018) from an ogive analysis, which consists in searching for the point of convergence of the cumulative momentum cospectrum to an asymptote (e.g., Oncley et al., 1996). This averaging time ensures that all significant turbulent structures carrying momentum flux, and thus other fluxes, are included in the statistics. On each 15-min period, a Reynolds decomposition was applied to all variables of interest such as wind velocity components, air temperature, or dust concentration. Hence, a variable  $\alpha$  was decomposed into  $\alpha = \langle \alpha \rangle + \alpha'$ , where the symbol  $\langle \rangle$  denotes the time average and the prime the deviation from the averaged value. Prior to this decomposition, the large-scale trend on  $\alpha$  with period larger than 15 min was simply removed from a sixth-order polynomial fit.

The wind velocity components recorded from the sonic anemometers were rotated horizontally so that  $u$  represents the horizontal component along the mean wind direction  $x$  and  $v$  the horizontal component along the transverse direction  $y$ . In order to account for possible errors in the vertical orientation of the sonic anemometers, a second rotation was performed at every height around the  $y$  axis.

Dust concentration fluctuations were compared-correlated with the fluctuations of the wind velocity components reduced to the frequency of the particle spectrometer (1 Hz). A time-lag correction was applied on the dust fluctuations for each averaging time (15 min). This time lag was deduced by maximizing the covariance between the dust concentration and vertical wind velocity fluctuations. Overall, this time lag remained small, varying between  $-1$  and  $+2$  s, as the dust sensor was very close to the sonic anemometer. To simplify the analysis, size-resolved dust concentration was also synthesized in seven bins between  $0.3$  and  $17 \mu\text{m}$  by aggregating by four the intervals of the particle spectrometer and by removing the first interval, which is insufficiently accurate following the spectrometer constructor.

Quality controls of turbulence and particle measurements were performed. In particular, flow steadiness was tested for each 15-min period using the criterion given by Foken et al. (2004) in order to verify the low impact of mesoscale variability on the 15-min averaging periods. This steadiness test was not applied to dust concentration due to the intermittency of the time series (see section 4.1). This apparent nonstationarity of dust concentration was not related to mesoscale variability nor to nonphysical extreme values (spikes) but to the intermittent nature of dust emission. Since dust emission depends on wind turbulence, we considered that a 15-min averaging time was a good compromise to apply Reynolds decomposition as the flow is stationary at this scale and as all significant turbulent structures carrying flux are included in the statistics at this scale. Finally, the time series were also visualized in order to detect occasional instruments failures.

### 2.4. Erosion Events

Two well-defined erosion events occurred during the experiment (9 March and 20 April events), with constant mean wind direction, high wind speed, and significant levels of dust concentration in the air during several hours. Other events occurred with less ideal characteristics in term of dust concentration magnitude, wind direction constancy, or erosion duration (7 and 8 March and 14 and 16 April events). These events were, however, included in our study in order to support the findings deduced from the two main events (9 March and 20 April). Note that the 14–15 March event presented in Dupont et al. (2018) was not considered in this study as the particle spectrometer coupled to the sonic anemometer was not working during this event. Overall, this study will, therefore, focus on six events.

The main meteorological and dust concentration characteristics of these six events are presented in Figure 2. All events occurred during daytime; they are thus mainly located on the convective side of the near-neutral stability conditions ( $-0.2 < z/L < 0.01$ , as defined in Dupont et al., 2018; Figure 2d). The events exhibit

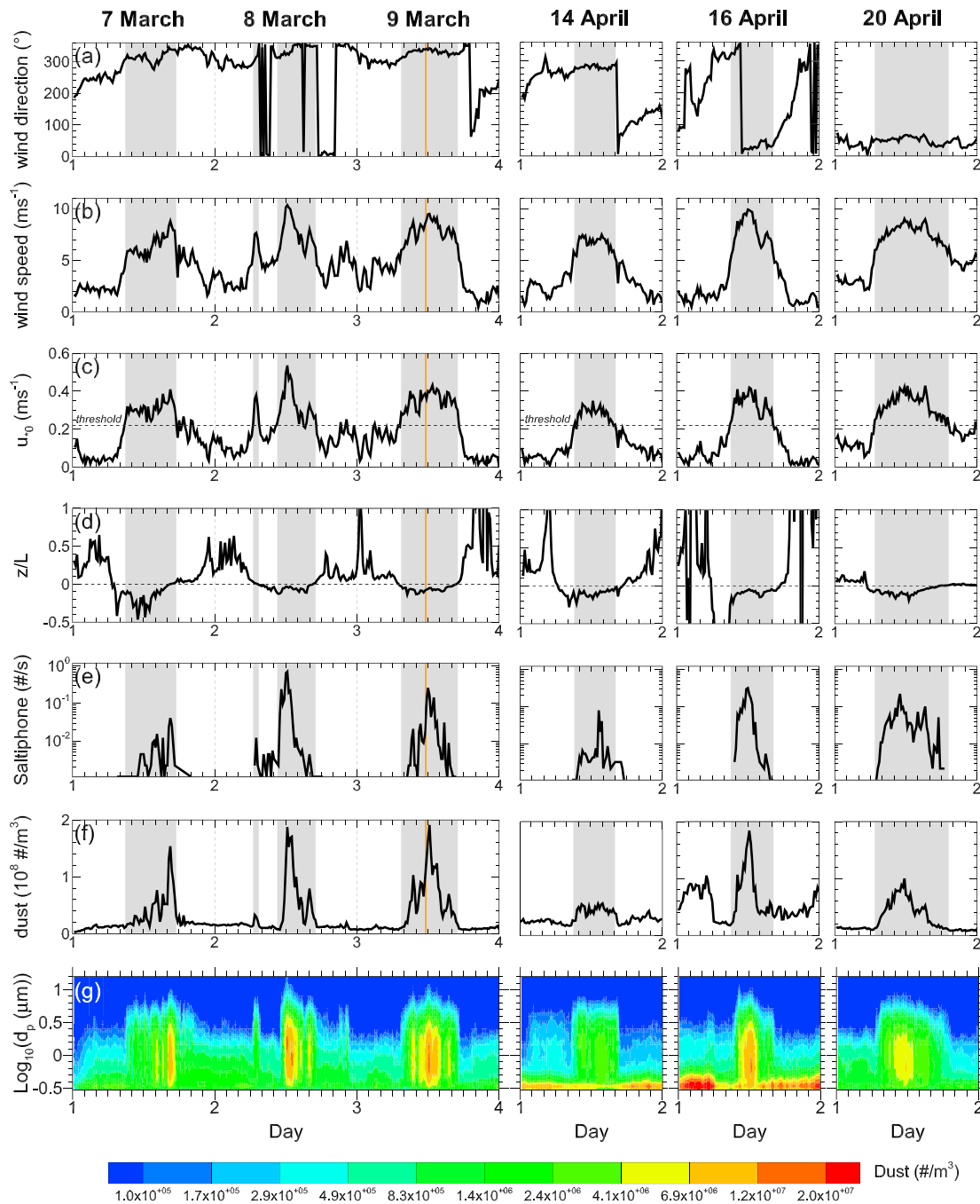


**Figure 2.** Main characteristics of the six erosion events: time variations of the (a) mean wind direction, (b) mean wind speed at 3-m height, (c) surface friction velocity ( $u_{*0}$ ) deduced from the sonic anemometers according to Dupont et al. (2018), (d) stability, (e) mean impact number of saltating particles recorded by one of the Saltiphone, (f) total mean dust concentration in number measured at 3-m height, and (g) mean size-resolved dust concentration in number. The shaded areas highlight the erosion periods defined as  $u_{*0} \geq 0.22 \text{ ms}^{-1}$ , where  $0.22 \text{ ms}^{-1}$  is the threshold friction velocity deduced in Dupont et al. (2018). The orange vertical line indicates the position of the time series presented in Figure 4.



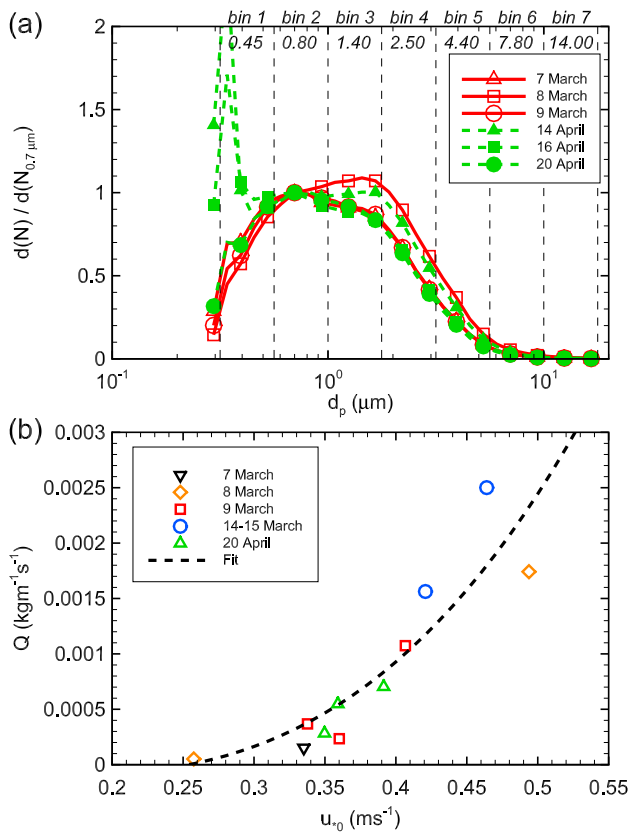


**Figure 3.** (a) Ensemble-averaged size-resolved dust concentration in number measured by the spectrometer at 3-m height during the six erosion events and normalized by the 0.7- $\mu\text{m}$  dust concentration. The seven bins considered in our analysis are indicated with their mean particle size. (b) Saltation flux  $Q$  against the surface friction velocity ( $u_{*0}$ ) obtained for the 7–9 March, 14 and 15 March, and 20 April events. The fitted curve in (b) corresponds to the parameterization of Lettau and Lettau (1978) with  $c = 0.7$  (see Dupont et al., 2018). The saltation flux was not measured during the 14 and 16 April events. The 14 and 15 March event was not considered in this study (see section 2.4).

different wind directions (Figure 2a): west for the 14 April event, northwest for the 7–9 March events, and northeast for the 16 and 20 April events. During the 16 April event, the wind turned from north to northeast. The 7 March and 14 April events exhibit the lowest wind intensity (Figure 2b), and thus, the highest convective conditions and the lowest dust concentration (Figures 2f and 2g). The 8 March event presents the strongest wind peak, followed by the 16 April event. The 9 March and 20 April events exhibit similar wind intensities. Importantly, an intense rain event occurred between 9 and 10 April, before the three April wind events, with a cumulated rain of about 30 mm. This rain event formed a small surface crust that was weakened on 19 April by the passage of a wood board on the surface.

As expected, the number of impacting saltating particles recorded by the Saltiphone (Figure 2e) and the size-resolved particle number concentration measured by the particle spectrometer (Figure 2f) vary both as the wind speed (Figure 2b) for surface friction velocity  $u_{*0}$  higher than the threshold friction velocity ( $0.22 \text{ ms}^{-1}$  as deduced in Dupont et al., 2018; Figure 2c). Hence, particles detected by the spectrometer are most likely mineral dust resulting from wind erosion. From now on, when performing ensemble average at the event scale, only 15-min periods with  $u_{*0} \geq 0.30 \text{ ms}^{-1}$  will be considered in order to account only for well-established erosion periods.

During erosion events, the size range of particles detected by the spectrometer increased from a background concentration (Figure 2g). The mean size-resolved dust number concentrations measured by the particle spectrometer exhibit a similar distribution for all events, with a maximum around  $0.7 \mu\text{m}$ , except for the strongest event (8 March event) and, in a lesser extent, for the 14 April event, where a peak around  $1.7 \mu\text{m}$  is visible (Figure 3a). Note that the large peaks around  $0.3 \mu\text{m}$  for the 14 and 16 April events are more likely related to air pollution than dust particles. During both days, a large concentration of particles smaller than about  $0.7 \mu\text{m}$  was always present, even without dust erosion (Figure 2g). Interestingly, the dust number concentration during the 20 April event is lower than during the 9 March event, while both events had similar surface friction velocities and saltation fluxes (Figures 2c and 3b).

The wind dynamics of 7–9 March and 20 April events were previously analyzed in Dupont et al. (2018). The wind was found consistent with usual observations in surface boundary layer in terms of mean turbulent velocity profiles and main turbulent structures. This was also verified for the 14 and 16 April events (result not shown). A slight increase of the momentum flux at the top of the profile (4-m height) during the 20 April event was observed. We suspected that it was due to the shorter fetch of our experimental site for northeasterly winds compared to the northwesterly winds of the 7–9 March event. For northeasterly winds, the top of the profile was possibly contaminated by turbulence established with the rougher upwind surface outside the plot, although the mean velocity profile was well approximated by a logarithmic function. During the 14 and 16 April events, the 4-m-height level may have also been contaminated by turbulence established with the surface outside the plot due to shorter fetch for westerly and northeasterly winds, respectively (results not shown). Nevertheless, this shorter fetch for westerly and northeasterly winds is unlikely to impact our results here as our analysis focuses exclusively on measurements performed at 3-m height.

### 3. Method for Analyzing Similarity in Turbulent Transport

Different methods exist to investigate the similarity between the transport of quantities such as momentum, heat, and scalar (dust here), with different assumptions and different degree of details. The most general approach looks at the correlation between quantities, integrating all motion frequencies present in the time

series (correlation coefficient), while the most detailed approaches look at the flux partition according to the type (quadrant-octant analysis), the frequency (Fourier spectral analysis), or the scale (wavelet analysis) of turbulent structures composing the signal. All four methods will be used here and are detailed below. The wavelet approach used in this study is based on the Haar multiresolution flux decomposition (Howell & Mahrt, 1997).

### 3.1. Correlation Coefficients

Correlation coefficients between variables or fluxes represent a first simple approach to look at the similarity between quantities transported by the turbulent flow by integrating the whole frequency range of eddies. The correlation coefficient  $r_{\alpha,\beta}$  between quantities  $\alpha$  and  $\beta$  is defined as

$$r_{\alpha,\beta} = \frac{\langle(\alpha - \langle\alpha\rangle)(\beta - \langle\beta\rangle)\rangle}{\sigma_{\alpha} \sigma_{\beta}}, \quad (1)$$

where  $\alpha$  and  $\beta$  are either the streamwise or vertical wind velocity components ( $u$  and  $w$ ), air temperature ( $\theta$ ), dust concentration ( $d$ ), momentum flux ( $uw$ ), heat flux ( $w\theta$ ), or dust flux ( $wd$ ), and  $\sigma_{\alpha}$  and  $\sigma_{\beta}$  are the standard deviations of  $\alpha$  and  $\beta$ , respectively.

### 3.2. Quadrant Analysis

The quadrant analysis highlights turbulent structures associated with the complete flow (no time scale decomposition) at a specific time. The turbulent flux  $\langle\alpha'\beta'\rangle$  is split into four quadrants depending on the sign of the fluctuations  $\alpha'$  and  $\beta'$ , irrespective of their duration or frequency. Here  $\beta$  is either  $w$  or  $u$  for vertical or horizontal fluxes, respectively. For simplicity when discussing the quadrants, we will refer to them as Q1, Q2, Q3, and Q4.

The flux  $\langle\alpha'\beta'\rangle$  is decomposed such as  $\langle\alpha'\beta'\rangle = \sum_{Qi} \langle\alpha'\beta'\rangle_{Qi}$ , where  $\langle\alpha'\beta'\rangle_{Qi}$  is the magnitude of the flux in quadrant  $Qi$ . Similarly, the number of events responsible for the flux is decomposed such as  $n^{\alpha\beta} = \sum_{Qi} n_{Qi}^{\alpha\beta}$ , where  $n^{\alpha\beta}$  is the total number of events (here the number of points of the time series) and  $n_{Qi}^{\alpha\beta}$  is the number of events in quadrant  $Qi$  contributing to the flux.

The magnitude percentage of the flux within quadrant  $Qi$  is computed as

$$F_{Qi}^{\alpha\beta} = 100 \times \left| \langle\alpha'\beta'\rangle_{Qi} \right| / \left| \sum_{Qi} \langle\alpha'\beta'\rangle_{Qi} \right|, \quad (2)$$

and the event number percentage within quadrant  $Qi$  is computed as

$$N_{Qi}^{\alpha\beta} = 100 \times n_{Qi}^{\alpha\beta} / n^{\alpha\beta}. \quad (3)$$

Similarity between fluxes will be characterized by a similar distribution of the flux between quadrants.

The criteria defining each of the four quadrants are presented in Table 1. For the momentum flux ( $\langle u'w' \rangle$ ), Q1 and Q3 correspond to  $uw$ -ejection ( $u' < 0$  and  $w' > 0$ ) and  $uw$ -sweep ( $u' > 0$  and  $w' < 0$ ) motions, that is, slow momentum fluid transported upward and fast momentum fluid transported downward, respectively. For the heat flux ( $\langle w'\theta' \rangle$ ), Q1 and Q3 events refer to as  $w\theta$  ejections and  $w\theta$  sweeps (warm upward and cool downward plumes, respectively) since most of erosion events occurred during daytime (positive heat flux coming from the surface). For the dust flux ( $\langle w'd' \rangle$ ), Q1 and Q3 events refer to as  $wd$  ejections and  $wd$  sweeps (dusty upward [emission] and clean downward plumes, respectively).

### 3.3. Octant Analysis

In an octant analysis, the quadrant decomposition of the momentum flux is further decomposed following the sign of the temperature or scalar fluctuations in order to establish whether temperature and scalar are transported similarly as momentum (Dupont & Patton, 2012). Hence, the momentum flux in quadrant  $Qi$  ( $\langle u'w' \rangle_{Qi}$ ) can be decomposed as

$$\langle u'w' \rangle_{Qi} = \langle u'w' \rangle_{Qi}^{\varphi^+} + \langle u'w' \rangle_{Qi}^{\varphi^-}, \quad (4)$$

and the number of events responsible for the flux is decomposed as



**Table 1**

Mean Fraction Values, in Event Number and in Magnitude, of the Momentum ( $\langle u'w' \rangle$ ), Heat ( $\langle w'\theta' \rangle$ ), and Number Size-Resolved Dust ( $\langle w'd' \rangle$ ) Fluxes in Each Quadrant as Defined in Equations (2) and (3), Respectively, for the 9 March and 20 April Events

	9 March				20 April			
	Q1	Q2	Q3	Q4	Q1	Q2	Q3	Q4
	Ejection		Sweep		Ejection		Sweep	
	$w'+, u'-$	$w'+, u'+$	$w'-, u'+$	$w'-, u'-$	$w'+, u'-$	$w'+, u'+$	$w'-, u'+$	$w'-, u'-$
$w'+, \theta'+$	$w'+, \theta'-$	$w'-, \theta'-$	$w'-, \theta'+$	$w'+, \theta'+$	$w'+, \theta'-$	$w'-, \theta'-$	$w'-, \theta'+$	
$w'+, d'+$	$w'+, d'-$	$w'-, d'-$	$w'-, d'+$	$w'+, d'+$	$w'+, d'-$	$w'-, d'-$	$w'-, d'+$	
In number								
$N_{Qi}^{uw}$	0.32	0.17	0.32	0.19	0.31	0.17	0.32	0.20
$N_{Qi}^{w\theta}$	0.31	0.18	0.35	0.16	0.32	0.17	0.36	0.15
$N_{Qi}^{wd}$ (0.45 $\mu\text{m}$ )	0.23	0.26	0.37	0.14	0.24	0.25	0.36	0.15
$N_{Qi}^{wd}$ (0.80 $\mu\text{m}$ )	0.23	0.26	0.39	0.12	0.24	0.25	0.39	0.12
$N_{Qi}^{wd}$ (1.40 $\mu\text{m}$ )	0.24	0.25	0.39	0.12	0.24	0.25	0.40	0.11
$N_{Qi}^{wd}$ (2.50 $\mu\text{m}$ )	0.24	0.25	0.39	0.12	0.23	0.25	0.40	0.12
$N_{Qi}^{wd}$ (4.40 $\mu\text{m}$ )	0.23	0.27	0.38	0.12	0.21	0.28	0.39	0.12
$N_{Qi}^{wd}$ (7.80 $\mu\text{m}$ )	0.10	0.39	0.44	0.07	0.07	0.41	0.47	0.05
$N_{Qi}^{wd}$ (14.00 $\mu\text{m}$ )	0.02	0.47	0.49	0.02	0.02	0.47	0.49	0.02
In magnitude								
$F_{Qi}^{uw}$	0.41	0.11	0.36	0.12	0.41	0.11	0.36	0.12
$F_{Qi}^{w\theta}$	0.46	0.09	0.36	0.09	0.48	0.07	0.37	0.08
$F_{Qi}^{wd}$ (0.45 $\mu\text{m}$ )	0.46	0.14	0.29	0.11	0.45	0.14	0.29	0.12
$F_{Qi}^{wd}$ (0.80 $\mu\text{m}$ )	0.49	0.12	0.30	0.09	0.49	0.12	0.30	0.09
$F_{Qi}^{wd}$ (1.40 $\mu\text{m}$ )	0.49	0.12	0.30	0.09	0.49	0.12	0.30	0.09
$F_{Qi}^{wd}$ (2.50 $\mu\text{m}$ )	0.49	0.12	0.30	0.09	0.49	0.12	0.30	0.09
$F_{Qi}^{wd}$ (4.40 $\mu\text{m}$ )	0.45	0.15	0.29	0.11	0.45	0.16	0.28	0.11
$F_{Qi}^{wd}$ (7.80 $\mu\text{m}$ )	0.39	0.21	0.25	0.15	0.38	0.22	0.24	0.16
$F_{Qi}^{wd}$ (14.00 $\mu\text{m}$ )	0.34	0.23	0.23	0.20	0.32	0.24	0.24	0.20

$$n_{Qi}^{uw} = n_{Qi}^{uw|\varphi^+} + n_{Qi}^{uw|\varphi^-}, \quad (5)$$

where  $\varphi$  is either  $\theta$  or  $d$ , and  $\varphi^+$  or  $\varphi^-$  refers to whether the instantaneous momentum flux coincides with positive or negative  $\varphi$  fluctuations.

The magnitude percentages of momentum flux in quadrant  $Qi$  coincident with positive and negative  $\varphi$  fluctuations are calculated using

$$F_{Qi}^{uw|\varphi^+} = 100 \times \left| \langle u'w' \rangle_{Qi}^{\varphi^+} \right| / \sum_{Qi} \left| \langle u'w' \rangle_{Qi} \right|, \quad (6)$$

and

$$F_{Qi}^{uw|\varphi^-} = 100 \times \left| \langle u'w' \rangle_{Qi}^{\varphi^-} \right| / \sum_{Qi} \left| \langle u'w' \rangle_{Qi} \right|, \quad (7)$$

and the event number percentage of momentum flux in quadrant  $Qi$  coincident with positive and negative  $\varphi$  fluctuations are calculated using

$$N_{Qi}^{uw|\varphi^+} = 100 \times n_{Qi}^{uw|\varphi^+} / n^{\alpha\beta}, \quad (8)$$

and

$$N_{Qi}^{u|w|\varphi^-} = 100 \times n_{Qi}^{u|w|\varphi^-} / n^{\alpha\beta}. \quad (9)$$

### 3.4. Fourier Spectral Analysis

The Fourier analysis provides information on the partition of the variance of  $\alpha$  or of the flux  $\langle \beta' \alpha' \rangle$  ( $\beta$  is either  $u$  or  $w$ ) following the frequency of the turbulent structures. The Fourier analysis presumes that the flow is composed of a superposition of periodic turbulent structures with specific frequencies that can be separated one from the other. Hence, a time series  $\alpha(k)$  over a time period  $T$  is decomposed into a finite number of sine and cosine terms such as

$$\alpha(k) = \sum_{n=0}^{N-1} \frac{S_{\alpha}(n)}{N} \exp(i2\pi nk/N), \quad (10)$$

where  $k = t/\Delta t$  with  $t$  the time and  $\Delta t$  the time step,  $n$  is the number of cycles per time period  $T$ ,  $N$  the number of data points ( $T/\Delta t$ ), and  $S_{\alpha}(n)$  the discrete Fourier transform. The portion of the signal variance explained by waves of frequency  $f = n/T$  is represented by  $|S_{\alpha}(n)|^2$ . Hence, the total variance is  $\sigma_{\alpha}^2 = \sum_{n=1}^{N-1} |S_{\alpha}(n)|^2$  (Stull, 1988).

Similarly, the flux  $\langle \beta' \alpha' \rangle$  can be decomposed following turbulent structure frequency such as  $\langle \beta' \alpha' \rangle = \sum_{n=1}^{N-1} S_{\alpha}(n)^* \cdot S_{\beta}(n)$ , where  $S_{\alpha}(n)^*$  is the complex conjugate of  $S_{\alpha}(n)$  and  $S_{\alpha}(n)^* \cdot S_{\beta}(n)$  represents the portion of the flux explained by waves of frequency  $f$ . Similarity between the turbulent transport of two quantities  $\alpha$  will be characterized by the same distribution of their fluxes  $\langle \beta' \alpha' \rangle$  according to the frequency.

### 3.5. MRD

The multiresolution decomposition (MRD) represents a simple discrete orthogonal decomposition of a signal or a flux, providing information on the eddy scale responsible for the signal fluctuations or for the flux. Unlike the Fourier decomposition, MRD satisfies Reynold's averaging at all scales and does not assume periodicity (Howell & Mahrt, 1997; Vickers & Mahrt, 2003). Hence, turbulent structures are defined in time as opposed to in frequency with the Fourier spectral analysis.

MRD consists in partitioning a time series  $\alpha(t)$  of  $2^M$  points into simple block averages on different scales  $m$  of dyadic width  $2^m$ , starting from  $m = M$  to  $m = 0$ . Hence, the first partition corresponds to the largest scale  $2^M$  and is the simple average of  $\alpha$ , which is then removed from the initial signal. The second partition averages the two halves of the residual signal resulting from the first partition, which are then removed, and so on (Vickers & Mahrt, 2003). The  $\alpha$  mean value at scale  $m$  and for the  $n$ th segment is given by

$$\bar{\alpha}_n(m) = \frac{1}{2^m} \sum_{i=(n-1)2^m+1}^{n2^m} \alpha r_i(m), \quad (11)$$

where  $\alpha r_i(m)$  is the signal residual after removing the block averages from scales greater than  $2^m$  points. The number of segment at scale  $m$  is  $2^{M-m}$ , and the length of the segments is  $2^m$ . Nilsson et al. (2014) interpreted  $\bar{\alpha}_n(m)$  as the eddy fluctuation of  $\alpha$  at scale  $m$  from the average at scale  $m + 1$ , calculated from the  $2^m$  points belonging to segment  $n$  of the  $\alpha$  time series ( $2^M$  points).

Nilsson et al. (2014) introduced the mapped time series  $\bar{\alpha}(k, m)$  which consists of mapping  $\bar{\alpha}_n(m)$  on the  $2^M$  grid points of the  $\alpha$  time series. Hence, the  $\alpha$  time series is the sum over all scales of the mapped time series:

$$\alpha(k) = \sum_m \bar{\alpha}(k, m). \quad (12)$$

The value of the MRD spectrum ( $D_{\alpha}$ ) at scale  $m + 1$  is simply the variance of the mapped signal  $\bar{\alpha}(t, m)$  at scale  $m$ :

$$D_{\alpha}(m+1) = \frac{1}{2^M} \sum_{k=1}^{2^M} \bar{\alpha}^2(k, m), \quad (13)$$

where the sum of  $D_{\alpha}$  on all scales is equal to the  $\alpha$  variance:  $\sigma_{\alpha}^2 = \sum_m D_{\alpha}$ .

Similarly, the value of the MRD cospectrum ( $D_{\beta\alpha}$ ) between two signals  $\alpha$  and  $\beta$  at scale  $m + 1$  is given by

$$D_{\beta\alpha}(m+1) = \frac{1}{2^M} \sum_{k=1}^{2^M} \bar{\alpha}(k, m) \bar{\beta}(k, m), \quad (14)$$

where the sum of  $D_{\beta\alpha}$  on all scales is equal to the flux:  $\langle \beta' \alpha' \rangle = \sum_m D_{\beta\alpha}$ .

One interesting feature of MRD cospectra is the possibility to decompose the flux  $D_{\beta\alpha}(m+1)$  at scale  $m+1$  between the positive and negative fluctuating quantities  $\bar{\alpha}(k, m) \bar{\beta}(k, m)$  contributing to the flux at this scale. The positive contribution to the flux at scale  $m+1$  is calculated as

$$D_{\beta\alpha}^+(m+1) = \frac{1}{2^M} \sum_{k=1}^{2^M} \bar{\alpha}(k, m) \bar{\beta}(k, m) I^+, \quad (15)$$

and the negative contribution as

$$D_{\beta\alpha}^-(m+1) = \frac{1}{2^M} \sum_{k=1}^{2^M} \bar{\alpha}(k, m) \bar{\beta}(k, m) I^-, \quad (16)$$

where  $I^+$  and  $I^-$  define the sign of the flux such as when  $\bar{\alpha}(k, m) \bar{\beta}(k, m)$  is positive  $I^+ = 1$  and  $I^- = 0$  and the opposite when  $\bar{\alpha}(k, m) \bar{\beta}(k, m)$  is negative. Hence,  $D_{\beta\alpha}(m+1) = D_{\beta\alpha}^+(m+1) + D_{\beta\alpha}^-(m+1)$ .

Similarly, the percentage of event number responsible at scale  $m+1$  for positive and negative fluxes are, respectively,

$$ND_{\beta\alpha}^+(m+1) = 100 \times nD_{\beta\alpha}^+(m+1) / 2^M, \quad (17)$$

and

$$ND_{\beta\alpha}^-(m+1) = 100 \times nD_{\beta\alpha}^-(m+1) / 2^M, \quad (18)$$

where  $nD_{\beta\alpha}^+$  and  $nD_{\beta\alpha}^-$  are the number of events at scale  $m+1$  inducing positive and negative fluxes, respectively ( $nD_{\beta\alpha}^+ + nD_{\beta\alpha}^- = 2^M$ ).

## 4. Results

Before presenting the average turbulent transport behavior of momentum, heat, and dust, from the different methods listed in section 3, we find it important to have a qualitative look at the instantaneous behavior of these variables, as measured during wind events (section 4.1), as well as to verify the distribution of their variance according to the eddy frequency (section 4.2).

As already indicated, our analysis will mainly focus on the two main events, 9 March and 20 April, which represent two different wind directions. Figures from the other events are only presented as supporting information S1 as they confirm the findings from the two main events.

### 4.1. Instantaneous Behavior

Overall, the instantaneous fluctuations of dust number concentration (including all particle sizes) appear much more intermittent, with sharper peaks, than those of meteorological variables (Figure 4). Here “intermittency” is defined as the non-Gaussian aspect of variable time derivative, that is, increments (e.g., Warhaft, 2000). Fluctuations of meteorological variables appear less intermittent and more symmetrically distributed between their mean tendency, that is, lower skewness and kurtosis. The 15-min time series presented in Figure 4 occurred a few hours after the beginning of the 9 March event, when the wind erosion is well established (orange vertical line in Figure 2). Other periods show similar behavior.

Looking more particularly at specific local events, highlighted in gray in Figure 4, we can identify different behaviors between momentum, heat, and dust transports. Event A corresponds to an  $uw$ -ejection event (negative fluctuation of  $u$ , noted  $u^-$ , and positive fluctuation of  $w$ , noted  $w^+$ ), transporting a negative momentum flux. This event is associated with positive fluctuations of heat ( $\theta^+$ ) and dust ( $d^+$ ). Hence, this  $uw$ -ejection motion transports simultaneously low momentum, warm air, and high dust concentration. Event B is an  $uw$ -sweep event ( $u^+$  and  $w^-$ ) transporting simultaneously high momentum, cool air ( $\theta^-$ ), and

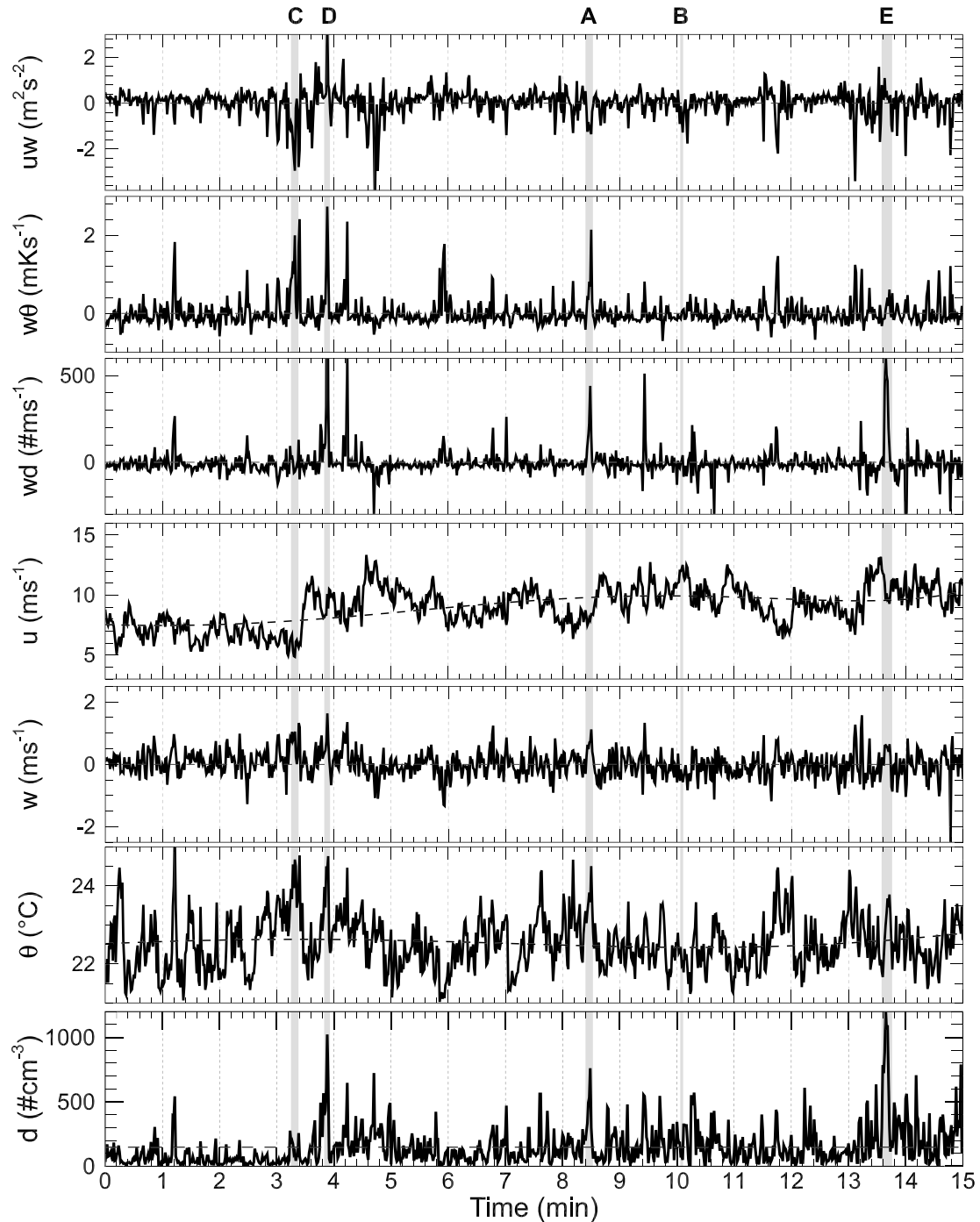


**Figure 4.** Time series of instantaneous momentum flux ( $uw$ ), heat flux ( $w\theta$ ), total dust flux ( $wd$ ), longitudinal wind velocity ( $u$ ), vertical wind velocity ( $w$ ), air temperature ( $\theta$ ), and total dust number concentration ( $d$ ), measured at 3-m height during the first wind event, 2 hr after the beginning of the 9 March wind event (vertical orange line in Figure 2). The horizontal dashed lines represent the average 15-min trend. The letters and gray areas highlight specific events (see the text).

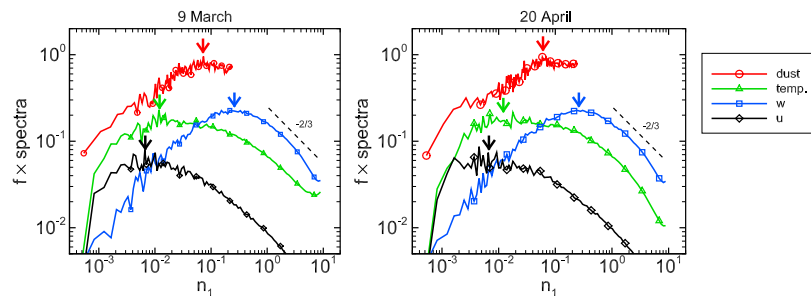


**Figure 5.** Ensemble-averaged 15-min energy spectra of the longitudinal velocity, vertical velocity, air temperature, and total dust number concentration for the 9 March and 20 April events. The frequency  $f$  is normalized by the measurement height  $z$  and the mean wind speed at the same height ( $u$ ) such as  $n_1 = fz/\langle u \rangle$ . Dust and longitudinal velocity spectra are shifted upward and downward, respectively, to permit comparison. The arrows indicate the position of the spectrum peaks. Equivalent figures for the 7 and 8 March and 14 and 16 April events are available in Figure S1.

low dust concentration ( $d^-$ ). Both events A and B appear in line with a similarity of turbulent transport between momentum, heat, and dust. On the other hand, other events show some dissimilarities. Event C is an  $uw$ -ejection event transporting low momentum ( $u^-$ ) and warm air ( $\theta^+$ ) but no significant dust fluctuations ( $wd$  is near zero). For this event, the turbulent transport of dust appears dissimilar with the momentum and heat ones. Events D and E are upward motions ( $w^+$ ) that transport high momentum ( $u^+$ ), warm air ( $\theta^+$ , especially for event D), and high dust concentration ( $d^+$ ). Here the turbulent transport of momentum appears dissimilar with the heat and dust ones. Although heat and dust fluxes have the same sign during both events, their amplitude compared to the momentum is different between both events.

In conclusion, the similarity between turbulent transport of momentum, heat, and dust is not systematic. One should, therefore, better characterize and understand the dissimilarity between these quantities.

#### 4.2. Energy Spectra

The ensemble-averaged 15-min energy spectra of  $u$  and  $w$  during both 9 March and 20 April events display the familiar shape of atmospheric surface-layer spectra with a well-defined  $-2/3$  power law in the inertial subrange and  $+1$  power law in the energy-containing range for the  $w$  spectra (Figure 5). The peak positions of the  $u$  and  $w$  spectra are distant from each other,  $n_1 = 0.008$  and  $0.32$ , respectively, where  $n_1 = fz/\langle u \rangle$  is the normalized frequency using the measurement height  $z$  and the mean wind speed at the same height ( $u$ ). This distance between peak positions is explained by the low roughness of our bare surface, as discussed in Dupont et al. (2018). This reflects the strong anisotropy of the flow near the surface, with large-scale elongated structures corresponding to the low- and high-speed streaks discussed in section 1. The flow becomes isotropic only for frequencies higher than about  $n_1 = 1$ , when the  $w$  spectra reach a  $-2/3$  power law.

The air temperature spectra display a much flatter peak, located between the  $u$ - and  $w$ -spectrum peaks. This flatter peak is consistent with previous observation in near-neutral conditions (e.g., Kaimal et al., 1972), with a peak located here around  $n_1 = 0.015$  against  $0.030$  in Kaimal et al. (1972). For frequencies larger than the  $w$ -spectrum peak position, the  $\theta$  spectra exhibit a slope lower than  $-2/3$ , meaning that large-scale fluctuations may still contribute to temperature fluctuations at high frequencies (e.g., Warhaft, 2000).

As other variables, the dust spectra exhibit a well-defined energy-containing range with a near  $+1$  power law. The dust-spectrum peak at an intermediate position between  $\theta$  and  $w$  spectra, near  $n_1 = 0.07$  and  $0.06$  for the 9 March and 20 April events, respectively. Compared to heat and momentum, the higher frequency position of the dust-spectrum peak could reflect the more local emission of dust with lower mesoscale dust concentration fluctuations. Importantly, after reaching their peak, the dust spectra decrease with the same slope as the temperature spectra up to the cutoff frequency of the dust sensor (1 Hz). This demonstrates the suitability of our dust sensor in measuring dust fluctuations up to 1 Hz.

This behavior of meteorological and dust spectra was observed for all events (Figure S1), except for the 14 April event. For this last event, the dust spectrum appears noisier at high frequency due to the low dust number concentration of this event.

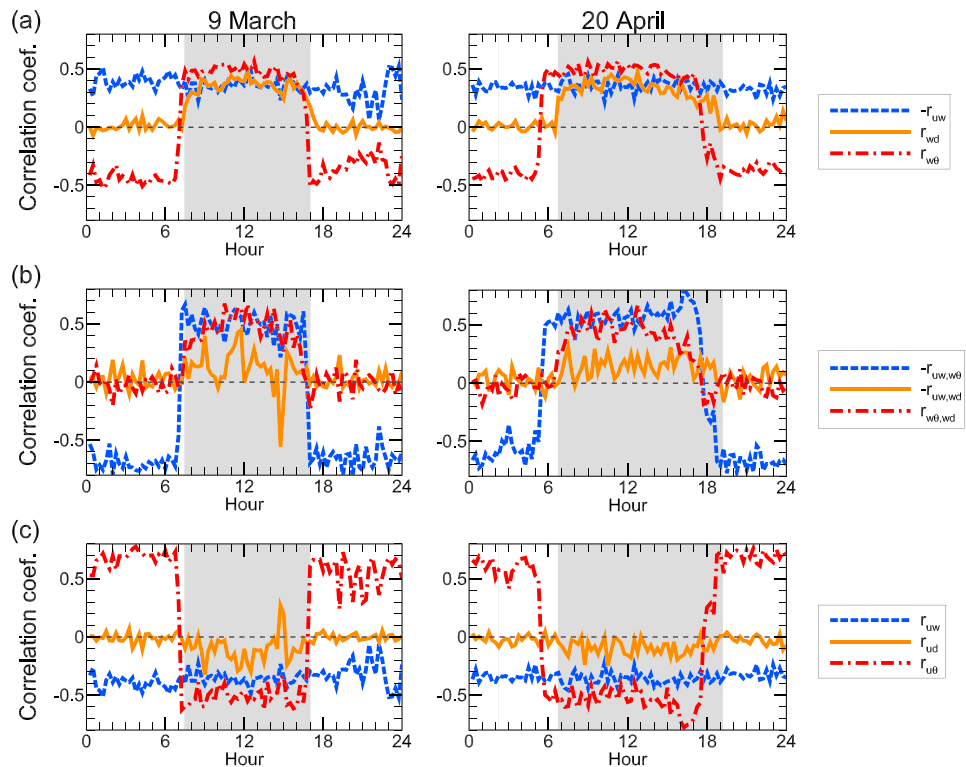


**Figure 6.** Time variation of the correlation coefficients (a) between the vertical wind velocity and the longitudinal wind velocity, the air temperature, and the concentration of 2.5- $\mu\text{m}$  diameter dust particles ( $-r_{uw}$ ,  $r_{w\theta}$ , and  $r_{wd}$ ), (b) between momentum, heat, and 2.5- $\mu\text{m}$  dust fluxes ( $-r_{uw,w\theta}$ ,  $r_{w\theta,wd}$ , and  $-r_{uw,wd}$ ), and (c) between the longitudinal wind velocity and the vertical wind velocity, the air temperature, and the concentration of 2.5- $\mu\text{m}$  diameter dust particles ( $r_{uw}$ ,  $r_{u\theta}$ , and  $r_{ud}$ ), for the 9 March and 20 April events. Dashed areas indicate periods of wind erosion. Equivalent figures for the 7 and 8 March and 14 and 16 April events are available in Figure S2.

### 4.3. Correlation Coefficients

During both 9 March and 20 April events, the correlation coefficients for the momentum and heat fluxes,  $r_{uw}$  and  $r_{w\theta}$ , respectively, reach on average usual values observed in the surface boundary layer (e.g., Kaimal & Finnigan, 1994), about  $-0.35$  for  $r_{uw}$  and  $+0.50$  and  $-0.40$  for  $r_{w\theta}$  during daytime and nighttime, respectively (Figure 6a). The difference between  $r_{uw}$  and  $r_{w\theta}$  shows that heat is more efficiently transported by the  $w$  fluctuations than the momentum. Note that  $r_{w\theta}$  changes sign as a consequence of the diurnal cycle. Interestingly, both correlation coefficients appear unaffected by the presence of soil erosion (dashed areas in Figure 6a). The correlation coefficient  $r_{wd}$  for 2.5- $\mu\text{m}$  particles (bin 4) is close to  $-r_{uw}$  during both erosion events. As expected, without erosion,  $r_{wd}$  is close to zero.

The momentum and heat fluxes appear well correlated,  $r_{uw,w\theta} \approx -0.50$  during daytime, with a slightly higher correlation on the 20 April event, probably related to a small difference in atmospheric stability (Figure 6b). The heat and 2.5- $\mu\text{m}$  dust fluxes are also relatively well correlated during the erosion events;  $r_{w\theta,wd}$  is close to  $-r_{uw,w\theta}$ . However,  $r_{uw,wd}$  is low, around  $-0.2$  with large fluctuations, while separately, heat and dust fluxes, and heat and momentum fluxes, are correlated. This may suggest that the correlation between heat and dust does not have the same distribution in frequency as the correlation between heat and momentum. Figure 6c shows that the low value of  $r_{uw,wd}$  is due to the poor correlation between  $d$  and  $u$  fluctuations compared to that between  $\theta$  and  $u$  and between  $w$  and  $u$  fluctuations ( $r_{ud} \approx -0.1$ ,  $r_{uw} \approx -0.4$ ,  $r_{u\theta} \approx -0.6$ ). In conclusion, when integrating over all eddy sizes, a larger dissimilarity exists in the turbulent transport between momentum and dust than between heat and dust.

In other erosion events (supporting information S1), the correlation coefficients exhibit similar behaviors. The coefficient  $r_{uw}$  is slightly lower at midday on 7 March and 14 April due to the more convective conditions (see Figure S2). Interestingly, the dust concentration and streamwise velocity fluctuations correlate

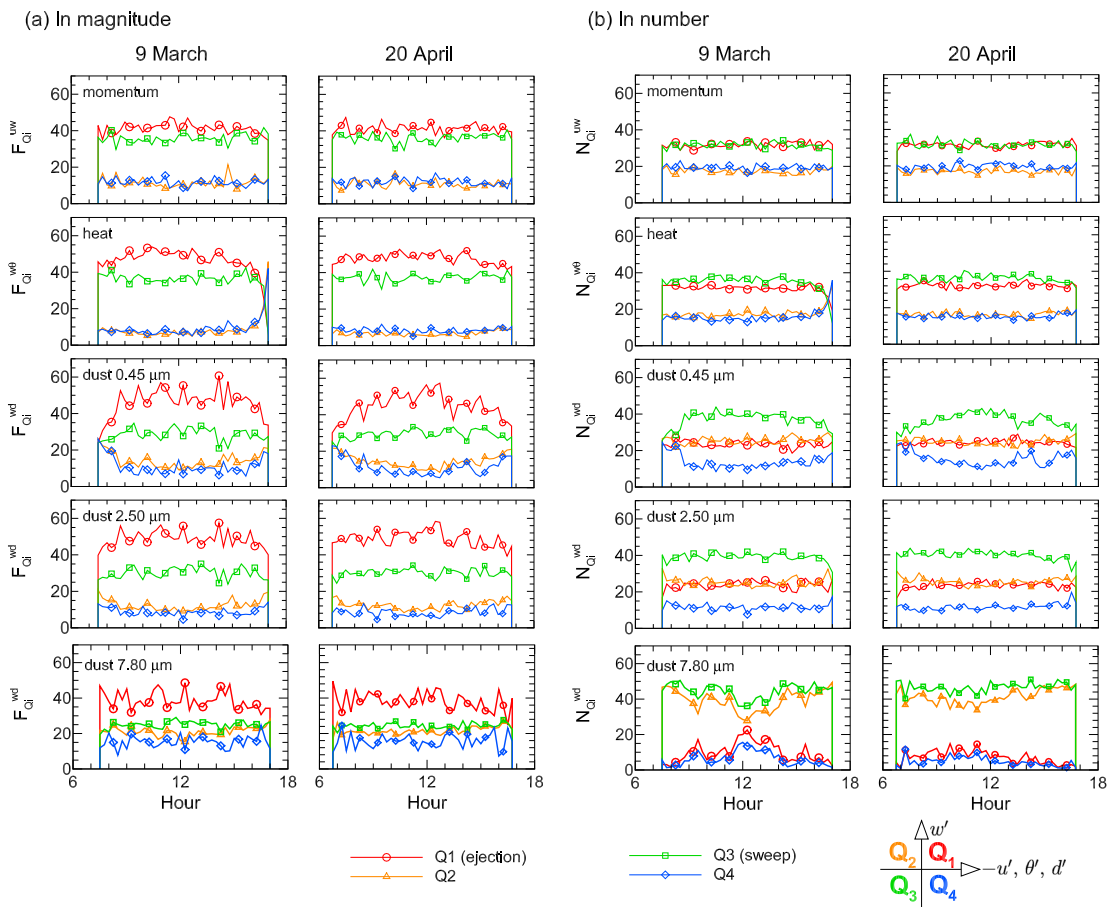


**Figure 7.** Time variation of the fractions in magnitude (a) and in event number (b), of the momentum ( $\langle u'w' \rangle$ ), heat ( $\langle w'\theta' \rangle$ ), and size-resolved dust ( $\langle w'd' \rangle$ ) fluxes in each quadrant as defined in equations (2) and (3), respectively, for the 9 March and 20 April events. For clarity purpose, values outside wind erosion periods are not presented. Equivalent figures for the 7 and 8 March and 14 and 16 April events are available in Figure S3.

better around 1 pm and from 10 am to 2 pm during the 8 March and 16 April events, respectively ( $r_{ud} \approx 0.4$ , Figure S2), leading to higher values of  $r_{uw,wd} (\approx -0.4)$ . These two periods were characterized by high wind speed, suggesting that the wind intensity may impact  $r_{ud}$  and  $r_{uw,wd}$ . Regarding the sensitivity of the correlation coefficients to the particle size (result not shown), similar correlation coefficients were observed for all particle diameters lower than  $7.80 \mu\text{m}$  (bins 1 to 5). For larger particles (bins 6 and 7), the correlation coefficients decrease as particles become less numerous. The volume of the sampling air collected by the particle spectrometer is probably too low to reach a meaningful dust concentration for such large and rare particles. This was visible from the step-function aspect of the concentration signal for large particles, that is, a signal with visible incremental variations of low dust particle number.

#### 4.4. Quadrant Analysis

The percentages of the vertical momentum  $\langle u'w' \rangle$ , heat  $\langle w'\theta' \rangle$ , and dust  $\langle w'd' \rangle$  fluxes, in each quadrant, are presented in number of events and in magnitude of the flux, as defined in equations (2) and (3), in Figures 7a and 7b, respectively, during the 9 March and 20 April events. For clarity, values outside the erosion events are not presented. The mean values obtained for each event are summarized in Table 1. This quadrant partition of the dust flux is presented in Figure 7 for three particle sizes,  $0.45$ ,  $2.50$ , and  $7.80 \mu\text{m}$ , corresponding to bins 1, 4, and 6 in Figure 3a and for all particle bins in Table 1.

In agreement with current understanding (e.g., Robinson, 1991), the turbulent transport of momentum and heat in near-neutral surface boundary layer occurs mainly via sweeps (Q3) and ejections (Q1), with a slight domination of ejections in magnitude and domination of sweeps in number, especially for heat. Ejections and sweeps transport on average about 41% and 36% (32% and 32%) of the momentum flux in magnitude (in



number), respectively, and 47% and 36% (31% and 35%) of the heat flux. This partition in quadrants exhibits low variability during and between erosion events (Figures 7a and 7b), except for the inversion of the heat flux partition due to the diurnal cycle. This partition in quadrants of the momentum and heat fluxes confirms a relative close similarity in turbulent transport between momentum and heat in near-neutral conditions.

The partition of the dust flux between the four quadrants is slightly different. As momentum and heat, dust appears mainly transported by ejections (Q1) and sweeps (Q3) for particles smaller than  $7.80\ \mu\text{m}$  (first five bins), with small partition differences according to the particle size (Table 1). In magnitude, the Q1 contribution dominates with a similar proportion as for the heat flux (near 49%). The Q3 contribution appears lower than for momentum and heat fluxes, near 30% against 36%, respectively, although it is still higher than the contributions from Q2 and Q4. In number, this is the opposite; Q3 dominates with a larger proportion than for momentum and heat fluxes, 39% against 32% and 35%, respectively, and Q1 has a lower contribution than for momentum and heat, near 24% against 32% and 32%, respectively. The most striking feature is the higher contribution of Q2 in number in the dust flux than in the momentum and heat fluxes, about 25% against 17%, respectively. Hence, the Q2 contribution in number is slightly higher than the Q1 contribution in transporting dust particles. In magnitude, Q1 remains larger than Q2 as for heat and momentum fluxes. This dust partition is observed for all events (see Figure S3).

Interestingly, in magnitude, the Q1 contribution seems to increase with wind intensity for  $0.45\text{-}\mu\text{m}$  particles (less for particles  $>0.45$  and  $\leq 7.80\ \mu\text{m}$ ), while Q2 and Q4 contributions decrease, and Q3 contribution remains stable (Figure 7a). This dependence to the wind intensity is especially visible on the 7 and 8 March and 16 April events whose mean wind speeds vary significantly during the event (Figure S3). This is less visible in number.

For larger particles ( $>7.80\ \mu\text{m}$ , the last two bins), the contribution in number of quadrants with negative dust fluctuations (Q2 and Q3) increases, to represent almost 50% of the events for particles larger than  $10\ \mu\text{m}$  (Table 1). This results from the scarcity of large particles in the air.

#### 4.5. Octant Analysis

To identify whether momentum quadrant events transport positive or negative heat ( $\theta$ ) and dust ( $d$ ) fluctuations, Figures 8a and 8b present the octant analysis of the momentum flux following the sign of the temperature and dust fluctuations for both main erosion events. As for the quadrant analysis, dust fluctuations are presented for three particle bins,  $0.45$ ,  $2.50$ , and  $7.80\ \mu\text{m}$ .

As expected,  $uw$ -ejection (Q1) and  $uw$ -sweep (Q3) motions correlate well with  $\theta^+$  and  $\theta^-$ , respectively. This result is verified for all wind events (see also Figure S4) and for the quadrant partition of the momentum flux in both magnitude and number of events. Although the atmospheric stability is near-neutral, the correlation of the momentum flux with the temperature fluctuations is not zero because the erosion events occurred mostly in the unstable side of the near-neutral conditions. Hence, heat is closely transported as momentum.

Conversely to temperature fluctuations,  $uw$  ejections (Q1) appear weakly correlated in magnitude with positive dust fluctuations of small particles ( $< 7.80\ \mu\text{m}$ ), Q1 ( $d^+$ ) being slightly larger than Q1 ( $d^-$ ) in Figure 8. In number,  $uw$  ejections are mostly uncorrelated with fluctuations of small dust particles, meaning that the dust emission does not occur preferentially during  $uw$  ejections. However,  $uw$  ejections and  $uw$  sweeps correlate better with  $d^+$  and  $d^-$ , respectively, with increasing wind speed. This is especially visible in magnitude partition for  $2.50\text{-}\mu\text{m}$  particles during the 7 and 8 March and 16 April events (Figure S4). It is worth noting that  $uw$ -Q4 motions ( $u^-$  and  $w^-$ ) appear better correlated with  $d^-$  than with  $d^+$ , which was not observed for temperature fluctuations.

Overall,  $uw$  ejections clearly do not transport heat and small dust particles similarly when including all ejection frequency range. These results are confirmed by other events (see Figure S4). For particles larger than  $7.80\ \mu\text{m}$ ,  $uw$  ejection and  $uw$  sweep become more correlated with  $d^-$  due to the scarcity of large particles.

#### 4.6. Fourier Cospectra

To identify the time frequency of the main turbulent structures contributing to the vertical momentum, heat, and dust fluxes, Figure 9a compares the ensemble-averaged 15-min  $-uw$ ,  $w\theta$ , and  $wd$  cospectra ( $-S_{uw}$ ,  $S_{w\theta}$ , and  $S_{wd}$ ) obtained at 3-m height, for both erosion events. The cospectra have been normalized by their maximum values in order to compare their distribution. We only present dust flux cospectra for  $2.50\text{-}\mu\text{m}$ -diameter particles as other particle sizes give similar behavior. Although large particles ( $\geq 7.80\ \mu\text{m}$ ) were rare and



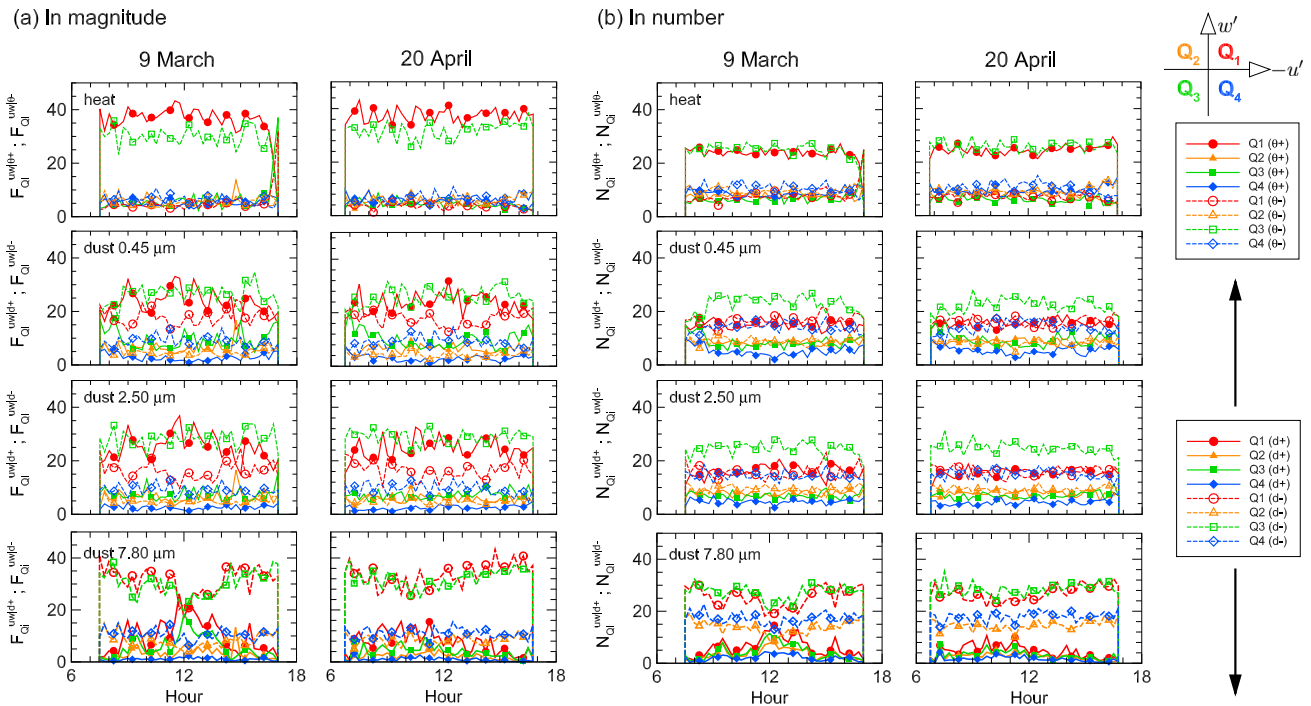


**Figure 8.** Time variation of the fractions in magnitude (a) and in event number (b), of the momentum flux ( $\langle u'w' \rangle$ ) in each quadrant and associated with positive or negative temperature ( $\theta^+$ ,  $\theta^-$ ) and size-resolved dust concentration ( $d^+$ ,  $d^-$ ) fluctuations, as defined in equations (6)–(9), for the 9 March and 20 April events. For clarity purpose, values outside wind erosion periods are not presented. Equivalent figures for the 7 and 8 March and 14 and 16 April events are available in Figure S4.

probably undersampled by the particle spectrometer, the cospectra of their flux have a similar distribution with frequency as smaller particles, with more perturbations (result not shown).

The  $-uw$  and  $w\theta$  cospectra display an expected shape with a well-defined  $-4/3$  power law in the inertial subrange and  $+1$  power law in the energy-containing range (power laws not shown in Figure 9 as the figure is in semilog coordinates). Both cospectra superpose in the energy-containing range, that is, low-frequency side of the peak. As observed by Kaimal et al. (1972), the peak of the  $w\theta$  cospectra is flatter than the  $uw$ -cospectrum peak, shifting the inertial subrange of the  $w\theta$  cospectra to higher frequencies. This shift means that smaller eddies transport more efficiently heat than momentum. The peak locations of the  $uw$  and  $w\theta$  cospectra are close to the values reported in Kaimal et al. (1972), around  $n_1 = 0.03$  and  $0.05$ – $0.10$  here, against  $n_1 = 0.07$  and  $0.10$  in Kaimal et al., 1972, respectively.

Despite the low frequency of our particle spectrometer (1 Hz), most of the dust flux was captured (more than 80%), only the high-frequency part was missing (Figure 9a). The  $wd$  cospectra exhibit a peak close to the  $uw$ -cospectrum ones, around  $n_1 = 0.03$ , for both events. In the energy-containing range, the  $wd$  cospectra have less energy with a steeper slope than the  $uw$  and  $w\theta$  cospectra. This means that dust is not vertically transported or emitted by large-scale motions as well as momentum and heat. Passing the cospectrum peak, the  $wd$  cospectra decrease on the high-frequency side similarly as the  $uw$  cospectra, with a slightly steeper slope in the inertial subrange. Since the decrease of the  $d$  spectrum at this frequency range ( $0.07 \leq n_1 \leq 0.20$ ) was consistent with the  $\theta$ -spectrum one (Figure 5), this steeper slope of the  $wd$  cospectra is expected to be true and not related to a loss of correlation of the dust sensor with the flow. The time lag between  $w$  and  $d$  was also too small to lead to a loss of correlation (see section 2.3). This behavior of  $wd$  cospectra is supported by other events (see Figure S5a).

At low frequencies, heat and dust appear horizontally transported differently (Figure 9b). While the  $u\theta$  cospectra exhibit a similar shape as the one observed in Kaimal et al. (1972), with one main peak near  $n_1 = 0.01$ , the  $ud$  cospectra exhibit surprisingly two peaks, a positive one at low frequency, near  $n_1 = 0.002$ , and a negative one at midfrequency range, near  $n_1 = 0.03$ , close to the  $uw$ -cospectrum peak. This behavior is confirmed by other erosion events (see Figure S5b), although the positive peak at low frequency appears

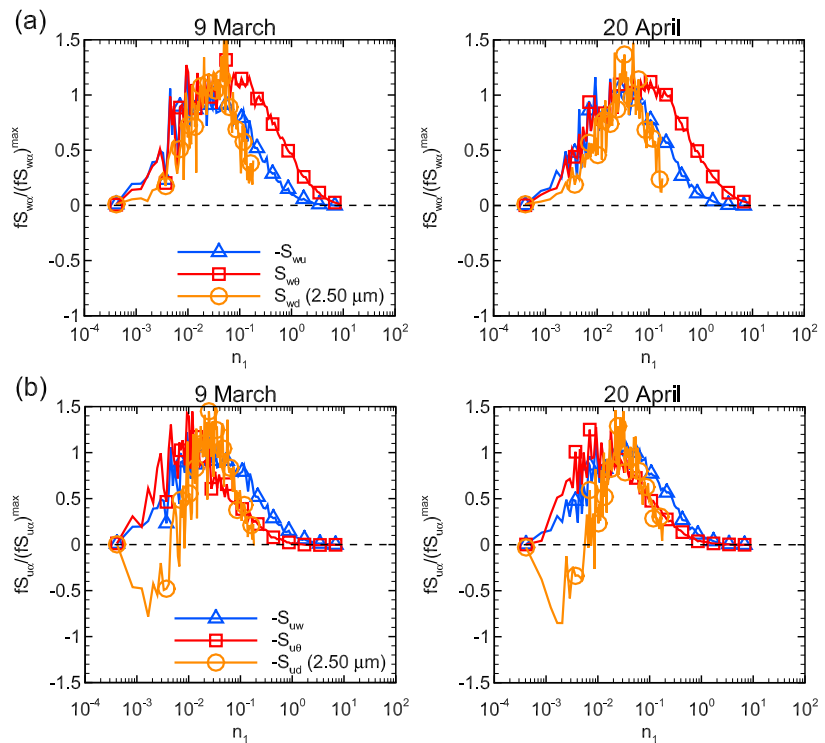


**Figure 9.** Comparison of the ensemble-averaged 15-min normalized Fourier cospectra of the vertical (a) and horizontal (b) momentum, heat, and 2.5- $\mu\text{m}$  dust fluxes, at 3-m height, for the 9 March (left figures) and 20 April (right figures) events. Cospectra are normalized by their maximum. The frequency  $f$  is normalized by the measurement height  $z$  and the mean wind speed at the same height  $\langle u \rangle$  such as  $n_1 = fz/\langle u \rangle$ . Equivalent figures for the 7 and 8 March and 14 and 16 April events are available in Figure S5.

weaker for the 8 March and 16 April events. The negative peaks of the  $u\theta$  and  $ud$  cospectra, around  $n_1 = 0.01$  and  $0.03$ , respectively, result from both the maximum of the vertical heat and dust fluxes (emission) and the large negative correlation between  $w$  and  $u$ , at these frequencies (Figure 9a). Hence, heat and dust emissions are mainly explained by  $uw$ -ejection and  $uw$ -sweep motions at these frequencies. The difference between  $u\theta$  and  $ud$  cospectra at low frequencies suggests a different emission or horizontal transport between heat and dust at these frequencies. This is discussed in section 5.

#### 4.7. MRD Cospectra

The MRD cospectra of the vertical and horizontal momentum, heat, and dust fluxes exhibit the same shape as the Fourier cospectra for all events (Figures 10 and S6). The main difference lays on the peak locations, which are slightly shifted toward higher time scales in the MRD cospectra. This shift is explained by the difference of definition of turbulent structures between MRD and Fourier methods. Turbulent structures are defined in time scale in MRD and in frequency of passage in Fourier method. Hence, the MRD-cospectrum peaks correspond to the time scales of the main eddies contributing to the flux, while the Fourier-cospectrum peaks correspond to the frequencies of these main eddies. The similarity in cospectrum shape between both methods gives us confidence in the significance of the differences observed in the previous section between Fourier cospectra of heat, momentum, and dust fluxes.

The MRD method allows to look at the partition of the MRD cospectra between the positive and negative component of the fluxes, referred hereafter by the exponents  $^+$  and  $^-$ , respectively. The distribution in magnitude between scales of the positive and negative (negative and positive) components of the vertical heat (momentum) and dust fluxes appears similar in both erosion events (Figure 11a). Here the MRD cospectra have been normalized by the maximum of their positive component (negative component for the momentum flux) to facilitate their comparison. Only a lower contribution of the large scales to  $wd^+$  is visible compared to  $w\theta^+$  and  $uw^-$ . This explains the lower contribution of low frequency motions to the dust flux observed from the  $wd$  cospectra compared to the  $uw$  and  $w\theta$  cospectra (Fourier cospectra in Figure 9a and

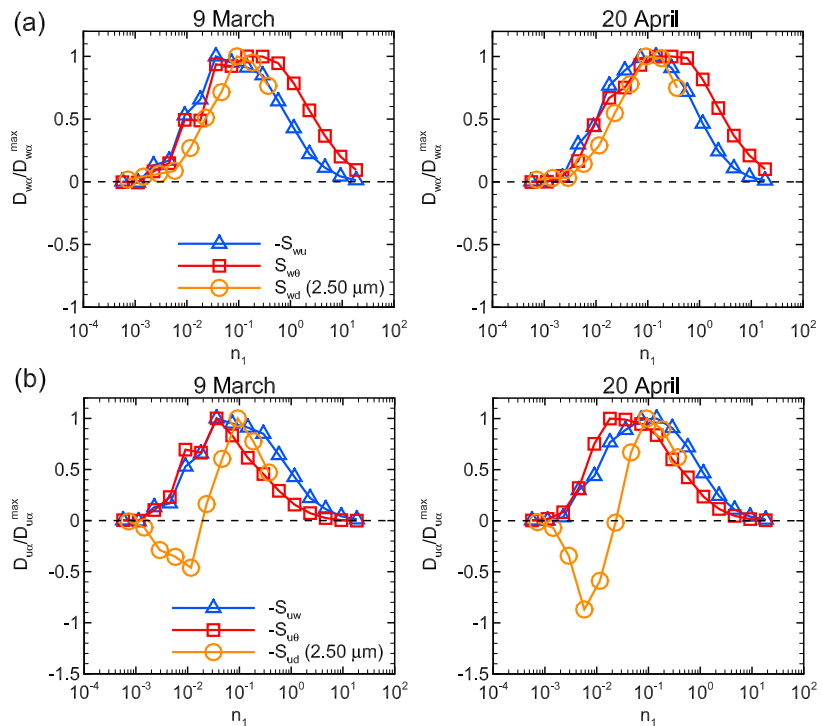


**Figure 10.** Same as Figure 9 but for the multiresolution decomposition cospectra. On the abscissa, the inverse time scale is normalized by the measurement height  $z$  and the mean wind speed at the same height  $\langle u \rangle$  such as  $n_1 = z / (\text{timescale} \times \langle u \rangle)$ . Equivalent figures for the 7 and 8 March and 14 and 16 April events are available in Figure S6.

MRD cospectra in Figure 10a). The  $uw^+$  and  $w\theta^-$  cospectra have similar shape, while the  $wd^-$  cospectrum slightly increases at inverse time scales higher than  $n_1 = 0.1$ . This explains the subtle faster decrease in the inertial subrange of the  $wd$  cospectrum compared to  $uw$  and  $w\theta$  cospectra (Fourier cospectra in Figure 9a and MRD cospectra in Figure 10a).

The partition of the MRD cospectra of horizontal fluxes between their positive and negative components shows differences between heat and dust fluxes (partition in magnitude in Figure 11b and in number in Figure 12b) for both erosion events. Here the cospectra have been normalized by the maximum of the negative component of the cospectra (positive component for the momentum flux). On one side, the  $u\theta^+$  and  $ud^+$  cospectra exhibit the same distribution with inverse time scale, with the same peak location around  $n_1 = 0.01$ , while  $uw^+$  peaks at higher inverse time scales, around  $n_1 = 0.4$ . On the other side, the  $ud^-$  cospectra appear much lower in amplitude than the  $u\theta^-$  cospectra, with a peak shifted toward higher inverse time scales (Figure 11b). This lower amplitude of  $ud^-$  cospectra is related to the largest number of eddies carrying negative correlations between  $u$  and  $d$  fluctuations, especially at small inverse time scales (Figure 12b). This difference explains the positive horizontal dust flux at low frequency observed in Fourier and MRD cospectra (Figures 9b and 10b) and the shifted maximum toward high frequencies of the Fourier and MRD  $ud$  cospectra compared to the  $u\theta$  cospectra.

As for Fourier cospectra, other erosion events confirm this partition of MRD cospectra between positive and negative components of the fluxes (see Figures S7 and S8). This partition is also not significantly affected by the size of the particles (result not shown).

## 5. Discussion

The main goal of the present study was to verify the hypothesis of similarity between dust, heat, and momentum transport during aeolian soil erosion, a hypothesis usually considered when assessing the particle flux from an indirect approach such as the flux-gradient, flux-variance, or relaxed eddy accumulation methods.

As expected, the dissimilarity between momentum and heat transport remained limited during erosion events as the atmospheric stability was near-neutral. The heat flux was too low to produce significant buoy-

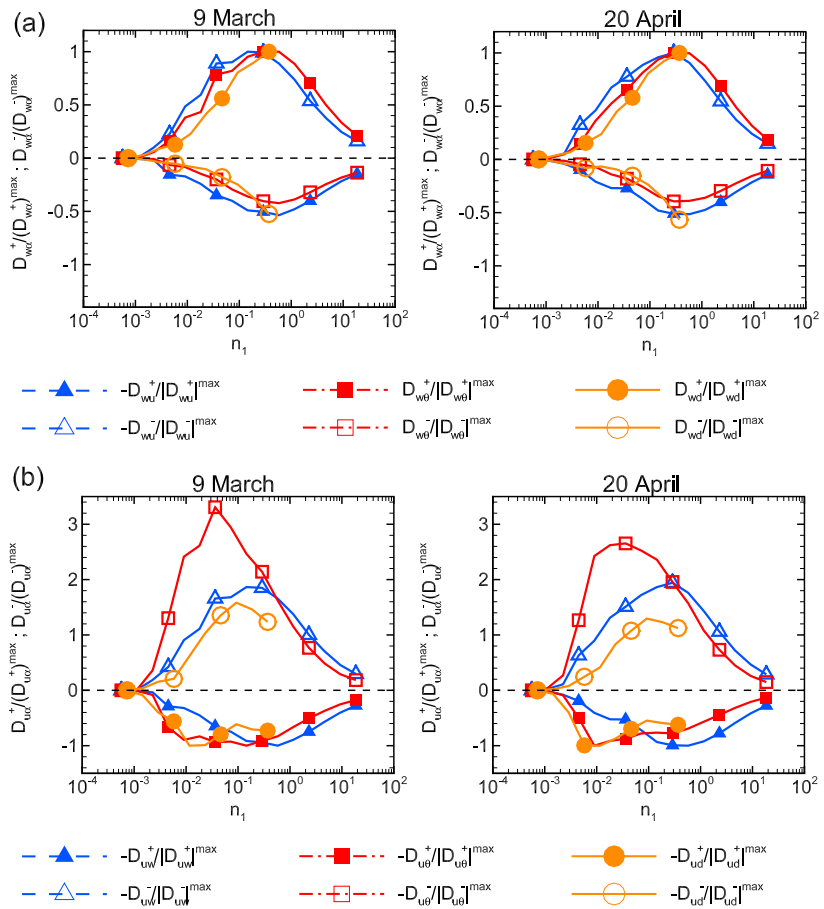


**Figure 11.** Same as Figure 10 but the multiresolution decomposition cospectra have been partitioned in magnitude between the positive and negative components of the fluxes (equations (15) and (16)). The cospectra of vertical (horizontal) fluxes have been normalized by the maximum of the positive (negative) component of the cospectra. Equivalent figures for the 7 and 8 March and 14 and 16 April events are available in Figure S7.

antly driven turbulence. As previously observed in surface boundary layer (e.g., Kaimal et al., 1972), the main difference between turbulent transport of heat and momentum was the higher efficiency of turbulence, especially small eddies, at transporting heat than momentum. This was visible from (1) the larger correlation coefficient  $r_{w\theta}$  than  $r_{uw}$  (Figure 6), (2) the higher proportion of  $w\theta$  ejections at transporting heat than  $uw$  ejections at transporting momentum (Table 1), and (3) the larger contribution of the  $w\theta$  cospectra at high frequency (Figure 9a). This weak dissimilarity between heat and momentum results from the occurrence of soil erosion during daytime, leading to stability conditions preferentially located on the unstable side of the near-neutral conditions.

Our measurements revealed a different partition of the dust and momentum-heat fluxes following the type and time scale of turbulent structures. In particular, the partition of the vertical fluxes in quadrants showed a much lower number of events contributing to the vertical transport of positive dust fluctuations ( $w^+d^+$ ) than to the vertical transport of positive heat ( $w^+\theta^+$ ) and negative momentum ( $w^+u^-$ ) fluctuations, while the vertical transport of negative dust fluctuations ( $w^+d^-$ ) was higher (Table 1). The distribution of the fluxes according to the eddy frequencies (Fourier cospectra) and the eddy time scales (MRD cospectra) further showed a difference in transport between dust and momentum-heat. Dust was not transported vertically by the low-frequency motions as well as heat and momentum, the dust flux cospectra increasing slower with increasing frequency in the energy-containing range (Figure 9a). Unlike heat and momentum, dust fluctuations correlated also differently with  $u$  fluctuations between low- and high-frequency motions. At low frequency ( $n_1 < 0.006$ ),  $u$  correlated positively with  $d$ , while it correlated negatively with  $\theta$  and  $w$  fluctuations (Figures 9b and S5b). This opposite correlation of  $d$  and  $u$  between low and high frequencies

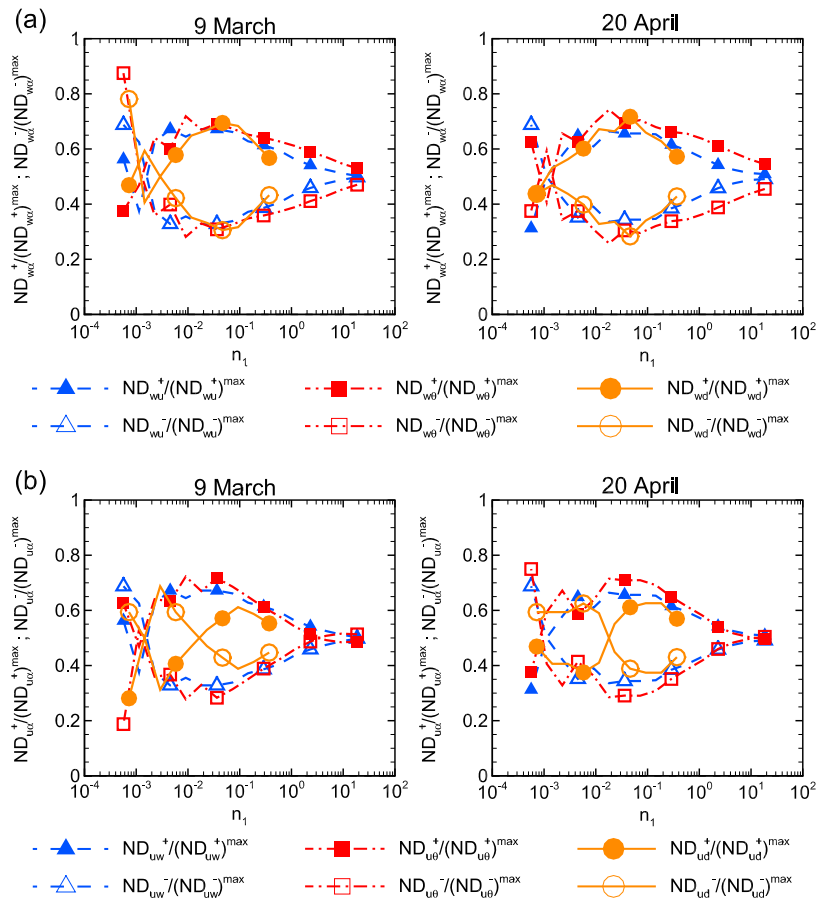


**Figure 12.** Same as Figure 11 but the partition has been done in number instead of in magnitude (equations (17) and (18)). Equivalent figures for the 7 and 8 March and 14 and 16 April events are available in Figure S8.

led to a poor correlation between the vertical dust and momentum fluxes when integrating over all eddy sizes (Figure 6). At small scales, dust appeared closely transported as momentum, although for some events, the  $wd$  cospectra decrease slightly faster with frequency than the  $uw$  cospectra. This last feature is more pronounced on the Fourier cospectra than on the MRD ones (see Figures 9a and 10a). As momentum, dust is, thus, less efficiently vertically transported than heat by small eddies. However, measurements with an higher frequency dust sensor would be necessary to confirm this result at small scales.

The dissimilarity between dust and momentum-heat fluxes was observed for all particle sizes between 0.3 and 5.6  $\mu\text{m}$  (first five bins) as well as for all erosion events, with roughly the same level of dissimilarity. Above 7.8  $\mu\text{m}$  (last two bins), the number of detected dust particles was too low to reach meaningful correlations with wind velocity fluctuations although  $wd$  cospectra exhibit the same pattern as for smaller particles. This last behavior suggests that the same mechanism of turbulent transport still occurs for larger particles, at least up to 20  $\mu\text{m}$ . Above this size, particle inertia and gravity are known to become significant.

This dissimilarity is most likely related to differences in the surface sources/sinks between dust and momentum-heat. Indeed, at 3-m height, the turbulence transporting momentum, heat, and mass are dominated by anisotropic attached eddies, that is, eddies in contact with the surface (Townsend, 1976). Eddies become isotropic only for  $n_1 > 1$  following the location of the inertial range of the  $w$ -Fourier spectrum (Figure 5). Conversely to heat emission and momentum absorption, dust emission is conditioned by a threshold surface wind shear above which occur successively saltation and dust emission through sandblasting. This mechanism may lead to a more intermittent dust emission compared to the more continuous heat emission and momentum absorption, especially at large scales ( $n_1 < 0.006$ ). Hence, all eddies in contact with the surface do not lead simultaneously to emission of heat and dust and to absorption of momentum,

and thus do not transport similarly dust and momentum-heat. The impact of the dust emission intermittency on the dust turbulent transport at 3 m high is probably accentuated here by the dominant local origin of dust particles from our isolated plot.

The intermittency of soil erosion is well known and visible from the blowing sand structures near the surface, known as aeolian streamers (e.g., Baas & Sherman, 2005; Dupont et al., 2013), surrounded by regions of lower or no saltation (no dust emission) according to the wind intensity. The presence of aeolian streamers surrounded by regions without saltation was clearly observed on the field during erosion events. This intermittency was visible in our measurements from (1) the instantaneous time series of dust concentration compared to temperature and horizontal wind velocity time series (Figure 4), (2) the larger number of ejections transporting low momentum ( $w^+u^-$ ), warm air ( $w^+\theta^+$ ), and “clean air” ( $w^+d^-$ ) instead of “dusty air” ( $w^+d^+$ ), as shown by the quadrant analysis (Table 1), and (3) the positive correlation of  $u^+$  and  $d^+$  at large scales (Figures 9b and 10b). Interestingly, Porch and Gillette (1977) also observed a larger intermittency for dust concentration than for horizontal wind speed time series but to a lesser extent than here. Our MRD partition analysis further showed that the lower efficiency of large-scale motions at transporting dust vertically is related to a lower contribution of the positive component of the flux (Figure 11a), itself probably due to the scarcer emission of dust.

The spatial heterogeneity of the saltation process and, thus, of the dust emission is more likely related to the flow turbulence rather than to the heterogeneity of the surface (Dupont et al., 2013). As reviewed in section 1, the main turbulent structures present at large scales in the near-surface atmospheric layer are juxtaposed meandering regions of low- and high-speed streaks, often referred to as Very Large Scale Motions. These large-scale structures with time scales of about few minutes are responsible for most of the saltation flux variability (see, e.g., the Figure 7 of Liu et al., 2018). We suspect that for our wind conditions, the saltation occurred essentially during high-speed streaks, as the threshold velocity for particles to enter into saltation should have been more often exceeded during such structures. This would explain the positive correlation between  $u^+$  and  $d^+$  observed at large scales (a few minutes time scale as well). Positive fluctuations of temperature ( $\theta^+$ ) do not correlate with  $u^+$  at large scales because of the more continuous emission of heat over the eddy size range of the flow and the absence of a threshold mechanism linked to the wind intensity for releasing heat. This active role of strong large-scale motions to release dust, and not only transporting dust as for momentum and heat, was first mentioned by Gillette and Porch (1978) who also observed from a field experiment that a large portion of the dust flux was correlated to the strongest horizontal wind speeds. More recently, Wang et al. (2017) also observed a positive correlation between  $u$  and mineral dust concentration ( $PM_{10}$ ) for time scales of several minutes. They also attributed this correlation to the link between dust emission and the passage of high-speed Very Large Scale Motions. At high frequency ( $n_1 > 0.006$ ), ejection motions ( $w^+$  and  $u^-$ ) are the most energetic gusts transporting-releasing dust ( $d^+$ ) and heat ( $\theta^+$ ; Figure 9a). Hence, positive fluctuations of dust and temperature become correlated with  $u^-$ . These ejection motions are expected to be embedded within the larger-scale streaks. The passage of large-scale elongated structures with intense wind, during several minutes, producing saltation, with local gusts releasing dust in the atmosphere, was inferred on the field from the observation of elongated high dust concentration plumes.

With increasing friction velocity, the dissimilarity between dust and momentum-heat turbulent transports diminishes for small particles ( $\leq 2.5 \mu\text{m}$ ). This is inferred from (1) the enhancement of the percentage of  $w^+d^+$  in magnitude of the dust flux and, to a lesser extent, in event number, with the friction velocity, reaching values close to those for the heat flux (Figures 13a and 7 for the dust and heat flux quadrants, respectively), (2) the increase of the proportion of  $uw$  ejection carrying  $d^+$  with the friction velocity (Figure 13b), and (3) the increase of the correlation coefficient between momentum and dust fluxes with the friction velocity (Figure 14). We suspect that with increasing wind speed, aeolian streamers become more spatially continuous and thus dust emission. According to the saltation transport patterns identified by Baas and Sherman (2005) following the wind conditions, aeolian streamers become embedded in larger saltation structures in higher wind conditions. Hence, under high wind conditions, saltation and dust emission are no longer restrained to the passage of large-scale high-speed streaks but become more homogeneous in space and in frequency as are heat and momentum. This explains the lower positive correlation between  $d$  and  $u$  observed at large scales for the 8 March and 16 April events (Figure S5b), whose wind intensities were slightly larger than for the other events. Our measurements indicate that dust transport becomes closer to the momentum and heat ones for friction velocities above 2.5 to 3.0 times the threshold friction velocity (i.e.,  $u_{*0}$  around 0.55 and 0.66  $\text{ms}^{-1}$ ), based on the extrapolation of the  $-r_{uw,wd}$  trend with  $u_{*0}$  to the value





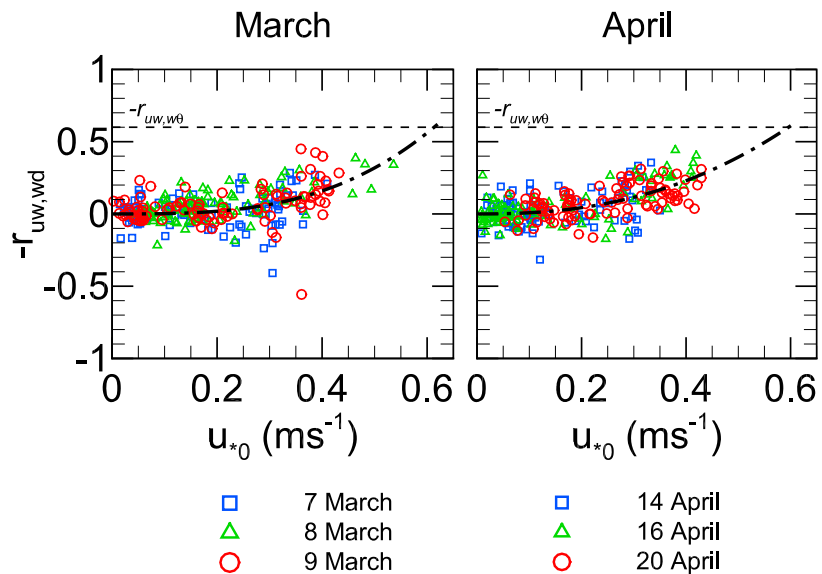


**Figure 14.** Correlation coefficient between momentum and 2.5- $\mu\text{m}$  dust fluxes ( $-r_{uw,wd}$ ) as a function of the surface friction velocity, for all erosion events. The dashed horizontal lines indicate the mean value of  $-r_{uw,w\theta}$  during daytime, and the dash-dotted lines represent a power fit up to the value of  $-r_{uw,w\theta}$ .

Overall, our results show strong evidence of dissimilarity between the transport of dust, heat, and momentum for wind conditions leading to sparse saltation patterns. For stronger winds, when saltation becomes fully spatially developed, the dust turbulent transport gets closer to the momentum one, although the dust concentration still appears more intermittent than the temperature and wind velocities. The link between the sparseness of dust emission and the dissimilarity between dust and momentum transports suggests that this dissimilarity could be accentuated with decreasing surface erodibility such as in presence of crusting surface. Indeed, the presence of nonerrodible roughness elements on the surface may attenuate the spatial development of saltation patterns while impacting less the heat emission and momentum absorption.

This dissimilarity between dust and momentum-heat for wind conditions where saltation is not fully spatially developed, may impact the evaluation of the dust flux from the traditional flux-gradient approach or other approaches assessing dust flux based on the similarity with other scalar quantities, such as the flux variance (e.g., Katul et al., 1995) or relaxed eddy accumulation (e.g., Businger & Oncley, 1990) methods. It is, however, difficult to quantify the error on the dust flux resulting from the assumption of similarity between dust and momentum (or heat) transports. The eddy diffusivity considered in the flux-gradient approach could be corrected by applying a Schmidt number similarly as a Prandtl number for the heat flux, but this Schmidt number should depend on the friction velocity. A proper comparison of the dust fluxes obtained from the eddy covariance and flux-gradient techniques will be the subject of a future study.

## 6. Conclusion

The partition of the near-surface dust flux in number according to the type and time scale of turbulent structures has been analyzed for the first time during the aeolian erosion of an isolated bare plot and compared with the partition of the heat and momentum fluxes. This was made possible by measuring size-resolved dust flux in number near the surface using the eddy covariance method. With this technique, we were able to capture the main eddies responsible for the net emission dust flux, confirming the potential of the eddy covariance technique for estimating dust flux close to the surface.

Contrary to the usual assumption, for moderate wind conditions and an isolated erodible plot typical of semiarid regions, dust did not appear transported similarly as momentum or heat near the surface. Although dust was mainly transported by ejection and sweep motions as heat and momentum, the partition of the dust flux between ejection and sweep motions as well as between eddy time scales was significantly different from that of momentum and heat fluxes. This was observed for all particle sizes lower than 6  $\mu\text{m}$  as well as for all erosion events. Importantly, this was observed for local erosion events with net emission fluxes, that



is, emission larger than deposition. This dissimilarity would probably be lower (1) for emission events where most of the near-surface dust particles were not locally emitted such as over a very wide erodible surface and (2) for deposition events of large-scale advected dust.

This dissimilarity results from the intermittency of dust emission compared to the more continuous surface heat emission and momentum absorption. The threshold condition of dust release according to the wind intensity reduces the number of upward motions in contact with the surface transporting all together high dust concentration, warm air, and low momentum. Many upward motions transported low dust concentration with warm air and low momentum. This dissimilarity was more pronounced at large scales (several minutes time scale) due to the dominant saltation occurrence, and thus dust emission, during the passage of high-speed streaky flow structures. This dissimilarity diminishes with increasing wind speed. A rapid extrapolation of our results suggests that a similarity in turbulent transport between dust and heat-momentum could only be reached for strong erosion events with friction velocities above 2.5 to 3.0 times the threshold friction velocity.

Our findings suggest that assuming similarity between dust and momentum fluxes when estimating the dust flux, such as with the flux-gradient approach, could lead to an error, especially when saltation is not fully spatially developed. A proper comparison between dust fluxes estimated from both approaches, eddy covariance and flux gradient, is necessary to quantify this possible error.

Finally, this dissimilarity in turbulent transport of particles, heat, and momentum may hold true for other passive abiotic and biotic particles for which emission is mechanically and biologically conditioned by environmental forcing with a threshold effect as for mineral dust.

#### Acknowledgments

We acknowledge the support of the French National Research Agency (ANR) under the grant ANR-15-CE02-0013 (project WIND-O-V). We would like to thank (i) Houcine Khatteli, Director of the Institut des Régions Arides (IRA) of Médenine, for the constant support of IRA in all research related to wind erosion, and in particular for giving us access to the Dar Dhaoui's experimental range and for the IRA's logistic help during the all experiment to ensure the success of the campaign, (ii) the guards of the experimental stations (Noureddine Boukhli, Mokhtar Elghoul, and Mousbah Elghoul) for their constant help and surveillance of the experimental system, and (iii) Christophe Chipeaux for his help with the data-acquisition setup from Raspberry PI. Finally, we thank the three anonymous reviewers for their helpful comments. The processed data used in this study are available at the WIND-O-V Web site (<https://www6.inra.fr/anr-windov/>).

#### References

- Adrian, R. J. (2007). Hairpin vortex organization in wall turbulence. *Physics of Fluids*, *19*(4), 041301. <https://doi.org/10.1063/1.2717527>
- Alfaro, S. C., Gaudichet, A., Gomes, L., & Maillé, M. (1997). Modeling the size distribution of a soil aerosol produced by sandblasting. *Journal of Geophysical Research*, *102*(D10), 11,239–11,249.
- Baas, A. C. W., & Sherman, D. J. (2005). Formation and behavior of aeolian streamers. *Journal of Geophysical Research*, *110*, F03011. <https://doi.org/10.1029/2004JF000270>
- Bonasoni, P., Cristofanelli, P., Calzolari, F., Bonafé, U., Evangelisti, F., Stohl, A., et al. (2004). Aerosol-ozone correlations during dust transport episodes. *Atmosphere Chemical Physics*, *4*, 1201–1215.
- Businger, J. A., & Oncley, S. P. (1990). Flux measurement with conditional sampling. *Journal of Atmospheric and Oceanic Technology*, *7*, 349–352.
- Businger, J. A., Wyngaard, J. C., Izumi, Y., & Bradley, E. F. (1971). Flux-profile relationships in atmospheric surface layer. *Journal of the Atmospheric Sciences*, *28*(2), 181–189.
- Cava, D., Katul, G. G., Semperviva, A. M., Giostra, U., & Scrimieri, A. (2008). On the anomalous behaviour of scalar flux-variance similarity functions within the canopy sub-layer of a dense alpine forest. *Boundary-Layer Meteorology*, *128*(1), 33–57.
- Damay, P. E., Maro, D., Coppalle, A., Lamaud, E., Connan, O., Hébert, D., et al. (2009). Size-resolved eddy covariance measurements of fine particle vertical fluxes. *Journal of Aerosol Science*, *40*(12), 1050–1058.
- Derbyshire, E. (2007). Natural minerogenic dust and human health. *Ambio*, *36*(1), 73–77.
- Deventer, M. J., El-Madany, T., Griessbaum, F., & Klemm, O. (2015). One-year measurement of size-resolved particle fluxes in an urban area. *Tellus B*, *67*(1).
- Deventer, M. J., Held, A., El-Madany, T. S., & Klemm, O. (2015). Size-resolved eddy covariance fluxes of nucleation to accumulation mode aerosol particles over a coniferous forest. *Agricultural and Forest Meteorology*, *214*–*215*, 328–340.
- Dorsey, J. R., Nemitz, E., Gallagher, M. W., Fowler, D., Williams, P. I., Bower, K. N., & Beswick, K. M. (2002). Direct measurements and parameterisation of aerosol flux, concentration and emission velocity above a city. *Atmospheric Environment*, *36*(5), 791–800.
- Dupont, S., Bergametti, G., Marticorena, B., & Simoëns, S. (2013). Modeling saltation intermittency. *Journal of Geophysical Research: Atmospheres*, *118*, 1–20.
- Dupont, S., & Patton, E. G. (2012). Momentum and scalar transport within a vegetation canopy following atmospheric stability and seasonal canopy changes: The CHATS experiment. *Atmosphere Chemical Physics*, *12*, 5913–5935.
- Dupont, S., Rajot, J.-L., Labiadh, M., Bergametti, G., Alfaro, S., Bouet, C., et al. (2018). Aerodynamic parameters over an eroding bare surface: Reconciliation of the law-of-the-wall and eddy-covariance determinations. *Journal of Geophysical Research: Atmospheres*, *123*, 4490–4508. <https://doi.org/10.1029/2017JD027984>
- Foken, T., Göckede, M., Mauder, M., Mahrt, L., Amiro, B. D., & Munger, J. W. (2004). Post-field data quality control. In X. Lee (Ed.), *Handbook of micrometeorology: A guide for surface flux measurements*. Netherlands: 2004 Kluwer Academic Publishers.
- Fratini, G., Ciccioli, P., Febo, A., Forgiione, A., & Valentini, R. (2007). Size-segregated fluxes of mineral dust from a desert area of northern China by eddy covariance. *Atmospheric Chemistry and Physics*, *7*(11), 2839–2854.
- Fryrear, D. W. (1986). A field dust sampler. *Journal of Soil and Water Conservation*, *41*(2), 117–120.
- Gillette, D. A., Blifford, Jr. I. H., & Fenster, C. R. (1972). Measurements of aerosol size distributions and vertical fluxes of aerosols on land subject to wind erosion. *Journal of Applied Meteorology*, *11*, 977–987.
- Gillette, D. A., & Porch, W. M. (1978). The role of fluctuations of vertical and horizontal wind and particle concentration in the deposition of dust suspended by wind. *Journal of Geophysical Research*, *83*(C1), 409–414.
- Gomes, L., Bergametti, G., Coudé-Gaussen, G., & Rognon, P. (1990). Submicron desert dusts: A sandblasting process. *Journal of Geophysical Research*, *95*(D9), 13,927–13,935.

- Howell, J. F., & Mahrt, L. (1997). Multiresolution flux decomposition. *Boundary-Layer Meteorology*, *83*, 117–137.
- Hutchins, N., Chauhan, K., Marusic, I., Monty, J., & Klewicki, J. (2012). Towards reconciling the large-scale structure of turbulent boundary layers in the atmosphere and laboratory. *Boundary-Layer Meteorology*, *145*(2), 273–306.
- IPCC (2013). Climate change: The physical science basis. In T. F. Stocker et al. (Eds.), *Contribution of Working Group I to the Fifth Assessment Report of the Intergovernmental Panel on Climate Change* (pp. 2013). Cambridge: Cambridge University Press.
- Ishizuka, M., Mikami, M., Leys, J. F., Shao, Y., Yamada, Y., & Heidenreich, S. (2014). Power law relation between size-resolved vertical dust flux and friction velocity measured in a fallow wheat field. *Aeolian Research*, *12*, 87–99.
- Kaimal, J. C., & Finnigan, J. J. (1994). *Atmospheric boundary layer flows. Their structure and measurements*, pp. 289. New York: Oxford University Press.
- Kaimal, J. C., Wyngaard, J. C., Izumi, Y., & Coté, O. R. (1972). Spectral characteristics of surface-layer turbulence. *Quarterly Journal of the Royal Meteorological Society*, *98*, 563–589.
- Katul, G., Goltz, S. M., Hsieh, C. I., Cheng, Y., Mowry, F., & Sigmon, J. (1995). Estimation of surface heat and momentum fluxes using the flux-variance method above uniform and non-uniform terrain. *Boundary-Layer Meteorology*, *74*(3), 237–260.
- Katul, G., Kuhn, G., Schiedge, J., & Hsieh, C. I. (1997). The ejection-sweep character of scalar fluxes in the unstable surface layer. *Boundary-Layer Meteorology*, *83*, 1–26.
- Katul, G. G., Sempreviva, A. M., & Cava, D. (2008). The temperature-humidity covariance in the marine surface layer: A one-dimensional analytical model. *Boundary-Layer Meteorology*, *126*(2), 263–278.
- Kays, W. M. (1994). Turbulent Prandtl number—Where are we? *Journal of Heat Transfer*, *116*(2), 284–295.
- Lamaud, E., & Irvine, M. (2006). Temperature-humidity dissimilarity and heat-to-water-vapour transport efficiency above and within a pine forest canopy: The role of the Bowen ratio. *Boundary-Layer Meteorology*, *120*(1), 87–109.
- Lettau, K., & Lettau, H. (1978). *Experimental and Micro-meteorological field studies of dune migration*, vol. Exploring the World's Driest Climate (pp. 110–147). Madison: Inst. for Environ. Stud., Univ. of Wisc.
- Li, D., & Bou-Zeid, E. (2011). Coherent structures and the dissimilarity of turbulent transport of momentum and scalars in the unstable atmospheric surface layer. *Boundary-Layer Meteorology*, *140*(2), 243–262.
- Liu, D., Ishizuka, M., Mikami, M., & Shao, Y. (2018). Turbulent characteristics of saltation and uncertainty of saltation model parameters. *Atmospheric Chemistry and Physics*, *18*, 7595–7606.
- Mahowald, N. (2011). Aerosol indirect effect on biogeochemical cycles and climate. *Science*, *334*(6057), 794–796.
- Mårtensson, E. M., Nilsson, E. D., Buzorius, G., & Johansson, C. (2006). Eddy covariance measurements and parameterisation of traffic related particle emissions in an urban environment. *Atmospheric Chemistry & Physics*, *6*, 769–785.
- Moene, A. F., Michels, B. I., & Holtslag, A. A. M. (2006). Scaling variances of scalars in a convective boundary layer under different entrainment regimes. *Boundary-Layer Meteorology*, *120*, 257–274.
- Neakrase, L. D. V., Balme, M. R., Esposito, F., Kelling, T., Klose, M., Kok, J. F., et al. (2016). Particle lifting processes in dust devils. *Space Science Reviews*, *203*, 347–376.
- Nickling, W. G., & Gillies, J. A. (1993). Dust emission and transport in Mali, West Africa. *Sedimentology*, *40*, 859–868.
- Nilsson, E. O., Sahlée, E., & Rutgersson, A. (2014). Turbulent momentum flux characterization using extended multiresolution analysis. *Quarterly Journal of the Royal Meteorological Society*, *140*, 1715–1728.
- Onclay, S. P., Friehe, C. A., Larue, J. C., Businger, J. A., Itsweire, E. C., & Chang, S. S. (1996). Surface-layer fluxes, profiles, and turbulence measurements over uniform terrain under near-neutral conditions. *Journal Atmospheric Sciences*, *53*(7), 1029–1044.
- Pierre, C., Kergoat, L., Hiernaux, P., Baron, C., Bergametti, G., Rajot, J. L., et al. (2018). Impact of agropastoral management on wind erosion in Sahelian croplands. *Land Degradation and Development*, *29*, 800–811.
- Porch, W. M., & Gillette, D. A. (1977). A comparison of aerosol and momentum mixing in dust storms using fast-response instruments. *Journal of Applied Meteorology*, *16*, 1273–1281.
- Robinson, S. K. (1991). Coherent motions in the turbulent boundary-layer. *Annual Review of Fluid Mechanics*, *23*, 601–639.
- Salesky, S. T., Chamecki, M., & Bou-Zeid, E. (2017). On the nature of the transition between roll and cellular organization in the convective boundary layer. *Boundary-Layer Meteorology*, *163*, 41–68.
- Shao, Y. (2008). *Physics and modelling of wind erosion*, 2nd revised and expanded edition (pp. 467). Berlin, Germany: Springer.
- Shao, Y., Ishizuka, M., Mikami, M., & Leys, J. F. (2011). Parameterization of size-resolved dust emission and validation with measurements. *Journal of Geophysical Research*, *116*, D08203. <https://doi.org/10.1029/2010JD014527>
- Shao, Y., Wyrwoll, K.-H., Chappell, A., Huang, J., Lin, Z., McTainsh, G. H., et al. (2011). Dust cycle: An emerging core theme in Earth system science. *Aeolian Research*, *2*(4), 181–204.
- Sow, M., Alfaro, S. C., Rajot, J. L., & Marticorena, B. (2009). Size resolved dust emission fluxes measured in Niger during 3 dust storms of the AMMA experiment. *Atmosphere Chemical Physics*, *9*(12), 3881–3891.
- Stull, R. B. (1988). *An introduction to boundary layer meteorology* (pp. 666). Dordrecht, The Netherlands: Kluwer Academic Pub.
- Townsend, A. A. (1976). *The structure of turbulent shear flow*, Cambridge.
- Vickers, D., & Mahrt, L. (2003). The cospectral gap and turbulent flux calculations. *Journal of Atmospheric and Oceanic Technology*, *20*, 660–672.
- Vinkovic, I., Doppler, D., Lelouvetel, J., & Buffat, M. (2011). Direct numerical simulation of particle interaction with ejections in turbulent channel flows. *International Journal of Multiphase Flow*, *37*(2), 187–197.
- Wang, G., Zheng, X., & Tao, J. (2017). Very large scale motion and PM10 concentration in a high-Re boundary layer. *Physical Fluids*, *29*, 61701.
- Warhaft, Z. (2000). Passive scalars in turbulent flows. *Annual Review of Fluid Mechanics*, *32*, 203–240.
- Williams, C. A., Scanlon, T. M., & Albertson, J. D. (2007). Influence of surface heterogeneity on scalar dissimilarity in the roughness sublayer. *Boundary-Layer Meteorology*, *122*, 149–165.
- Yin, Y., Wurzler, S., Levin, Z., & Reisin, T. G. (2002). Interactions of mineral dust particles and clouds: Effects on precipitation and cloud optical properties. *Journal of Geophysical Research*, *107*, D234724. <https://doi.org/10.1029/2001JD001544>
- Yu, H., Chin, M., Yuan, T., Bian, H., Remer, L. A., Prospero, J. M., et al. (2015). The fertilizing role of African dust in the Amazon rainforest: A first multiyear assessment based on data from cloud-aerosol lidar and infrared pathfinder satellite observations. *Geophysical Research Letters*, *42*, 1984–1991.



# References

- Ackerman, S. A. and H. Chung (1992). "Radiative Effects of Airborne Dust on Regional Energy Budgets at the Top of the Atmosphere". In: *J. Appl. Meteorol.* 31.2, pp. 223–233. DOI: [10.1175/1520-0450\(1992\)031<0223:RE0AD0>2.0.CO;2](https://doi.org/10.1175/1520-0450(1992)031<0223:RE0AD0>2.0.CO;2).
- Alfaro, S. C. *et al.* (1997). "Modeling the size distribution of a soil aerosol produced by sand-blasting". In: *J. Geophys. Res.* 102.D10, pp. 11239–11249. DOI: [10.1029/97JD00403](https://doi.org/10.1029/97JD00403).
- Alfaro, S. C. and L. Gomes (2001). "Modeling mineral aerosol production by wind erosion: Emission intensities and aerosol size distributions in source areas". In: *J. Geophys. Res.* 106.D16, pp. 18075–18084. DOI: [10.1029/2000JD900339](https://doi.org/10.1029/2000JD900339).
- Ammi, M. *et al.* (2009). "Three-dimensional analysis of the collision process of a bead on a granular packing". In: *Phys. Rev. E.* 79, p. 021305. DOI: [10.1103/PhysRevE.79.021305](https://doi.org/10.1103/PhysRevE.79.021305).
- Anderson, R. S. and B. Hallet (1986). "Sediment transport by wind: Toward a general model". In: *GSA Bulletin* 97.5, p. 523. DOI: [10.1130/0016-7606\(1986\)97<523:STBWTA>2.0.CO;2](https://doi.org/10.1130/0016-7606(1986)97<523:STBWTA>2.0.CO;2).
- Anderson, R. S. and P. K. Haff (1991). "Wind modification and bed response during saltation of sand in air". In: *Acta. Mech. Supp.* 1, pp. 21–51. DOI: [10.1007/978-3-7091-6706-9\\_2](https://doi.org/10.1007/978-3-7091-6706-9_2).
- Arnalds, O. and S. Archer (2013). *Rangeland Desertification*. Advances in Vegetation Science. Springer Netherlands. ISBN: 9789401596022.
- Ash, J. E. and R. J. Wasson (1983). "Vegetation and sand mobility in the Australian desert dunefield." In: *Z. Geomorphol.* 45, pp. 7–25.
- Aylor, D. E. (1982). "Modeling spore dispersal in a barley crop". In: *Agricultural Meteorology* 26.3, pp. 215–219. DOI: [10.1016/0002-1571\(82\)90032-2](https://doi.org/10.1016/0002-1571(82)90032-2).
- Baas, A. C. W. and D. J. Sherman (2005). "Formation and behavior of aeolian streamers". In: *J. Geophys. Res. Earth Surf.* 110.F3. DOI: [10.1029/2004JF000270](https://doi.org/10.1029/2004JF000270).
- Baas, A. C. W. and J. M. Nield (2007). "Modelling vegetated dune landscapes". In: *Geophys. Res. Lett.* 34.L06. DOI: [10.1029/2006GL029152](https://doi.org/10.1029/2006GL029152).
- Bagnold, R. A. (1937). "The size-garding of sand by wind." In: *Proc. Royal Soc. Lond.* 163.913, pp. 250–264. DOI: [10.1098/rspa.1937.0225](https://doi.org/10.1098/rspa.1937.0225).
- Bagnold, R. (1941). *The Physics of Blown Sand and Desert Dunes*. Dover Earth Science. Dover Publications. ISBN: 9780486141190.
- Bailey, R. M. (2011). "Spatial and temporal signatures of fragility and threshold proximity in modelled semi-arid vegetation". In: *Proc. Royal Soc. B.* 278.1708, pp. 1064–1071. DOI: [10.1098/rspb.2010.1750](https://doi.org/10.1098/rspb.2010.1750).

- Bechet, J. *et al.* (2015). "Erosion processes in black marl soils at the millimetre scale: Preliminary insights from an analogous model". In: *Hydrol. Earth Syst. Sci.* 19, pp. 1849–1855. DOI: [10.5194/hess-19-1849-2015](https://doi.org/10.5194/hess-19-1849-2015).
- Brazel, A. J. and W. G. Nickling (1987). "Dust storms and their relation to moisture in the Sonoran-Mojave Desert Region of southwestern United States." In: *J. Environ. Manage.* 24.3, pp. 279–291.
- Burri, K. *et al.* (2011). "Aeolian sediment transport over vegetation canopies: A wind tunnel study with live plants." In: *Aeolian Res.* 3, pp. 205–213. DOI: [10.1016/j.aeolia.2011.01.003](https://doi.org/10.1016/j.aeolia.2011.01.003).
- Carnerio, M. V., K. Rasmussen, and H. J. Herrmann (2015). "Bursts in discontinuous Aeolian saltation". In: *Scientific Res.* 5. DOI: [10.1038/srep11109](https://doi.org/10.1038/srep11109).
- Cerdà, A. (1997). "Soil erosion after land abandonment in a semiarid environment of southeastern Spain". In: *Arid Soil Res. Rehabil.* 11.2, pp. 163–176. DOI: [10.1080/15324989709381469](https://doi.org/10.1080/15324989709381469).
- Chepil, W. S. (1951). "Properties of Soil which Influence Wind Erosion". In: *Soil Sci.* 72, pp. 387–402. DOI: [10.1097/00010694-195111000-00007](https://doi.org/10.1097/00010694-195111000-00007).
- Chun, Y. *et al.* (2008). "Historical records of Asian dust events (Hwangsa) in Korea". In: *Bull. Amer. Meteor. Soc.* 89, pp. 823–827. DOI: [10.1175/2008BAMS2159.1](https://doi.org/10.1175/2008BAMS2159.1).
- Claquin, T. *et al.* (2003). "Radiative forcing of climate by ice-age atmospheric dust". In: *Clim. Dyn.* 20.2, pp. 193–202. DOI: [10.1007/s00382-002-0269-1](https://doi.org/10.1007/s00382-002-0269-1).
- Cleugh, H. A. (1998). "Effects of windbreaks on airflow, microclimates and crop yields". In: *Agrofor. Syst.* 41, pp. 55–84. DOI: [10.1023/A:1006019805109](https://doi.org/10.1023/A:1006019805109).
- Clift, R. *et al.* (1978). *Bubbles, Drops, and Particles*. Academic Press. ISBN: 9780121769505.
- Cody, B. F. *et al.* (2014). "Spatial and temporal patterns of dust emissions (2004–2012) in semi-arid landscapes, southeastern Utah, USA". In: *Aeolian Res.* 15, pp. 31–43. DOI: [10.1016/j.aeolia.2013.10.002](https://doi.org/10.1016/j.aeolia.2013.10.002).
- Crank, J. and P. Nicolson (1996). "A practical method for numerical evaluation of solutions of partial differential equations of the heat conduction type." In: *P. Adv. Comput. Math.* 6, pp. 207–226. DOI: [10.1007/BF02127704](https://doi.org/10.1007/BF02127704).
- Darwin, C. (1909). *The Voyage of the Beagle*. 29. P.F. Collier. ISBN: 9780140432688.
- Davidson, I. C., M. J. Miller, and A. M. Pleskow (1982). "The Influence of Surface Structure on Predicted Particle Dry Deposition to Natural Grass Canopies". In: *Water Air Soil Pollut.* 18, pp. 25–43. DOI: [10.1007/BF02419401](https://doi.org/10.1007/BF02419401).
- Davies, C. N. (1960). *Aerosol Science*. Academic, New York.
- Derbyshire, E. (2007). "Natural Minerogenic Dust and Human Health". In: *AMBIO* 36.1, pp. 73–77. DOI: [10.1579/0044-7447\(2007\)36\[73:NMDAHH\]2.0.CO;2](https://doi.org/10.1579/0044-7447(2007)36[73:NMDAHH]2.0.CO;2).
- Dupont, S. and Y. Brunet (2008a). "Edge Flow and Canopy Structure: A Large-Eddy Simulation Study". In: *Boundary Layer Meteorol.* 126, pp. 51–71. DOI: [10.1007/s10546-007-9216-3](https://doi.org/10.1007/s10546-007-9216-3).
- Dupont, S., Y. Brunet, and J. J. Finnigan (2008b). "Large-eddy simulation of turbulent flow over a forested hill: Validation and coherent structure identification". In: *Q. J. Royal Meteorol. Soc.* 134.636, pp. 1911–1929. DOI: [10.1002/qj.328](https://doi.org/10.1002/qj.328).

- Dupont, S. *et al.* (2010). “Modelling waving crops using large-eddy simulation: comparison with experiments and a linear stability analysis”. In: *J. Fluid Mech.* 652, pp. 5–44. DOI: [10.1017/S0022112010000686](https://doi.org/10.1017/S0022112010000686).
- Dupont, S. *et al.* (2013). “Modeling saltation intermittency”. In: *J. Geophys. Res. Atmos.* 118.13, pp. 7109–7128. DOI: [10.1002/jgrd.50528](https://doi.org/10.1002/jgrd.50528).
- Dupont, S., G. Bergametti, and S. Simoëns (2014). “Modelling Aeolian Erosion in Presence of Vegetation”. In: *Procedia IUTAM* 17, pp. 91–100. DOI: [10.1016/j.piutam.2015.06.013](https://doi.org/10.1016/j.piutam.2015.06.013).
- Dupont, S. *et al.* (2015). “Near-surface dust flux enrichment in small particles during erosion events”. In: *Geophys. Res. Lett.* 42.6, pp. 1992–2000. DOI: [10.1002/2015GL063116](https://doi.org/10.1002/2015GL063116).
- Dupont, S. *et al.* (2018). “Aerodynamic Parameters Over an Eroding Bare Surface: Reconciliation of the Law of the Wall and Eddy Covariance Determinations”. In: *J. Geophys. Res. Atmos.* 123.9, pp. 4490–4508. DOI: [10.1029/2017JD027984](https://doi.org/10.1029/2017JD027984).
- Dupont, S. *et al.* (2019a). “Comparison between Flux-Gradient and Eddy-Covariance dust flux measurements during wind erosion events”. In: *Atmos. Environ.* In preparation.
- Dupont, S. *et al.* (2019b). “Dissimilarity Between Dust, Heat, and Momentum Turbulent Transports During Aeolian Soil Erosion”. In: *J. Geophys. Res. Atmos.* DOI: [10.1029/2018JD029048](https://doi.org/10.1029/2018JD029048).
- Durán, O., P. Claudin, and B. Andreotti (2014). “Direct numerical simulations of aeolian sand ripples”. In: *Proc. Nat. Acad. Sci.* 111.44, pp. 15665–15668. DOI: [10.1073/pnas.1413058111](https://doi.org/10.1073/pnas.1413058111).
- EEA (2014). *Air quality in Europe*. Tech. rep. European Environment Agency.
- Edward, A. (1997). *World Atlas of Desertification*. Ed. by N. J. Middleton and D. S. G. Thomas.
- Ellis, J. *et al.* (2012). “Temporal and spatial variability of aeolian sand transport: Implications for field measurements”. In: *Aeolian Res.* 3, pp. 379–387. DOI: [10.1016/j.aeolia.2011.06.001](https://doi.org/10.1016/j.aeolia.2011.06.001).
- Evan, A. T., A. K. Heidinger, and P. Knippertz (2006). “Analysis of winter dust activity off the coast of West Africa using a new 24-year over-water advanced very high resolution radiometer satellite dust climatology”. In: *J. Geophys. Res. Atmos.* 111.D12. DOI: [10.1029/2005JD006336](https://doi.org/10.1029/2005JD006336).
- Fernandes, R., S. Dupont, and Lamaud E. (2019). “Investigating the role of deposition on the size distribution of near-surface dust flux during erosion events”. In: *Aeolian Res.* 37, pp. 32–43. DOI: [10.1016/j.aeolia.2019.02.002](https://doi.org/10.1016/j.aeolia.2019.02.002).
- Feuerstein, S. and K. Schepanski (2019). “Identification of Dust Sources in a Saharan Dust Hot-Spot and Their Implementation in a Dust-Emission Model”. In: *Remote Sens.* 11.1. DOI: [10.3390/rs11010004](https://doi.org/10.3390/rs11010004).
- Fratini, G. *et al.* (2007). “Size-segregated fluxes of mineral dust from a desert area of northern China by eddy covariance”. In: *Atmos. Chem. Phys.* 7.11, pp. 2839–2854. DOI: [10.5194/acp-7-2839-2007](https://doi.org/10.5194/acp-7-2839-2007).
- Fryrear, D. F. *et al.* (2000). “RWEQ: Improved wind erosion technology”. In: *Soil Water Conserv.* 55.2, pp. 183–189.
- Fryrear, W. D. (1986). “A field dust sampler”. In: *J. Soil Water Conserv.* 41, pp. 183–189.
- Fuchs, N. A. (1964). *The mechanics of aerosols*. Pergamon Press, New York.



- Gares, P. *et al.* (1996). "Alongshore variations in aeolian sediment transport: Carrick Finn Strand, Ireland". In: *J. Coast. Res.* 12.3, pp. 673–682.
- Gibbens, R. P. *et al.* (1983). "Soil movement in mesquite dunelands and former grasslands of southern New Mexico from 1933 to 1980 *Prosopis glandulosa*, erosion rates." In: *J. Range Manage. Arch.* 36.2.
- Gillette, D. A., I. H. Blifford, and C. R. Fenster (1972). "Measurements of aerosol size distributions and vertical fluxes of aerosols on land subject to wind erosion". In: *J. Appl. Meteorol.* 11, pp. 977–987. DOI: [10.1175/1520-0450\(1972\)011<0977:MOASDA>2.0.CO;2](https://doi.org/10.1175/1520-0450(1972)011<0977:MOASDA>2.0.CO;2).
- Gillette, D. A., I. H. Blifford, and D. W. Fryrear (1974). "The influence of wind velocity on the size distributions of aerosols generated by the wind erosion of soils". In: *J. Geophys. Res.* 79.27, pp. 4068–4075. DOI: [10.1029/JC079i027p04068](https://doi.org/10.1029/JC079i027p04068).
- Gillette, D. A. and R. Passi (1988). "Modeling dust emission caused by wind erosion". In: *J. Geophys. Res. Atmos.* 93.D11, pp. 14233–14242. DOI: [10.1029/JD093iD11p14233](https://doi.org/10.1029/JD093iD11p14233).
- Gillette, D. A. and P. H. Stockton (1989). "The effect of nonerodible particles on wind erosion of erodible surfaces." In: *J. Geophys. Res. Atmos.* 94.D10, pp. 12885–12893. DOI: [10.1029/JD094iD10p12885](https://doi.org/10.1029/JD094iD10p12885).
- Gillette, D., D. Ono, and K. Richmond (2004). "A combined modeling and measurement technique for estimating windblown dust emissions at Owens (dry) Lake, California". In: *J. Geophys. Res. Earth Surf.* 109. DOI: [10.1029/2003jf000025](https://doi.org/10.1029/2003jf000025).
- Gillette, D.A. (1977). "Fine particulate emissions due to wind erosion." In: *Trans. ASAE* 20, pp. 890–897.
- Gillies, J. A. *et al.* (2000). "Field determination of drag forces and shear stress partitioning effects for a desert shrub (*Sarcobatus vermiculatus*, greasewood)." In: *J. Geophys. Res. Atmos.* 105.D20, pp. 24871–24880. DOI: [10.1029/2000JD900431](https://doi.org/10.1029/2000JD900431).
- Gillies, J. A., Joanna M., and W. G. Nickling (2014). "Wind speed and sediment transport recovery in the lee of a vegetated and denuded nebkha within a nebkha dune field." In: *Aeolian Res.* 12.7. DOI: [10.1016/j.aeolia.2013.12.005](https://doi.org/10.1016/j.aeolia.2013.12.005).
- Gillies, J.A. and L. Berkofsky (2004). "Aeolian Suspension Above the Saltation Layer, the Concentration Profile". In: *J. Sed. Res.* 74, pp. 176–183. DOI: [10.1306/091303740176](https://doi.org/10.1306/091303740176).
- Gomes, L. *et al.* (1990). "Submicron desert dusts: A sandblasting process". In: *J. Geophys. Res. Atmos.* 95.D9, pp. 13927–13935. DOI: [10.1029/JD095iD09p13927](https://doi.org/10.1029/JD095iD09p13927).
- Gomes, L. *et al.* (2003). "Validation of a dust production model from measurements performed in semi-arid agricultural areas of Spain and Niger". In: *CATENA* 52.3, pp. 257–271. DOI: [10.1016/S0341-8162\(03\)00017-1](https://doi.org/10.1016/S0341-8162(03)00017-1).
- Greeley, R. and J. D. Iversen (1987). *Wind as a Geological Process: On Earth, Mars, Venus and Titan*. Cambridge Planetary Science Old. Cambridge University Press. ISBN: 9780521359627.
- Griffin, D. W., C. A. Kellogg, and E. A. Shinn (2001). "Dust in the Wind: Long Range Transport of Dust in the Atmosphere and Its Implications for Global Public and Ecosystem Health". In: *Glob. Chang. Hum. Health* 2.1, pp. 20–33. DOI: [10.1023/A:1011910224374](https://doi.org/10.1023/A:1011910224374).

- Grini, A., C. S. Zender, and P. R. Colarco (2002). "Saltation Sandblasting behavior during mineral dust aerosol production". In: *Geophys. Res. Lett.* 29.18, pp. 15–1–15–4. DOI: [10.1029/2002GL015248](https://doi.org/10.1029/2002GL015248).
- Hagen, L. J. (1994). "Plant canopy effects on wind erosion saltation." In: *Trans ASAE* 37.2, pp. 461–465.
- Hagen, L.J. and N.P. Woodruff (1973). "Air pollution from duststorms in the great plains". In: *Atmos. Environ.* 7.3, pp. 323–332. DOI: [10.1016/0004-6981\(73\)90081-4](https://doi.org/10.1016/0004-6981(73)90081-4).
- Harikishan, G. *et al.* (2015). "Radiative effect of dust aerosols on cloud microphysics and meso-scale dynamics during monsoon breaks over Arabian sea". In: *Atmos. Environ.* 105, pp. 22–31. DOI: [10.1016/j.atmosenv.2015.01.037](https://doi.org/10.1016/j.atmosenv.2015.01.037).
- Högström, U. (1988). "Non-dimensional wind and temperature profiles in the atmospheric surface layer: A re-evaluation". In: *Boundary Layer Meteorol.* 42.1, pp. 55–78. DOI: [10.1007/BF00119875](https://doi.org/10.1007/BF00119875).
- Horst, T. W. (1997). "A simple formula for attenuation of eddy fluxes measured with first-order-response scalar sensors". In: *Boundary Layer Meteorol.* 82, pp. 219–233. DOI: [10.1023/A:1000229130034](https://doi.org/10.1023/A:1000229130034).
- Husar, R. B. *et al.* (2001). "Asian dust events of April 1998". In: *J. Geophys. Res. Atmos.* 106.D16, pp. 18317–18330. DOI: [10.1029/2000JD900788](https://doi.org/10.1029/2000JD900788).
- Husar, R. (June 2004). "Intercontinental Transport of Dust: Historical and Recent Observational Evidence". In: vol. 4, pp. 277–294. DOI: [10.1007/b94531](https://doi.org/10.1007/b94531).
- IPBES (2018). *Assessment Report on Land Degradation and Restoration*. Tech. rep. Intergovernmental Science-Policy Platform on Biodiversity and Ecosystem Services.
- IPCC (2014). *Fifth Assessment Report: Climate Change 2007: The AR5 Synthesis Report*. Tech. rep. Intergovernmental Panel on Climate Change.
- Ishizuka, M. *et al.* (2008). "Effects of soil moisture and dried raindroplet crust on saltation and dust emission". In: *J. Geophys. Res. Atmos.* 113. DOI: [10.1029/2008JD009955](https://doi.org/10.1029/2008JD009955).
- Iverson, J. D. and B. R. White (1982). "Saltation threshold on Earth, Mars and Venus". In: *Sedimentology* 29.1, pp. 111–119. DOI: [10.1111/j.1365-3091.1982.tb01713.x](https://doi.org/10.1111/j.1365-3091.1982.tb01713.x).
- Jackson, N.L. *et al.* (Dec. 2006). "Small-scale spatial variations in aeolian sediment transport on a fine-sand beach". In: *J. Coast. Res.* 39, pp. 379–383.
- Joffre, S.M. and T. Laurila (1987). "Standard Deviations of Wind Speed and Direction from Observations over a Smooth Surface". In: *J. Appl. Meteorol.* 27, pp. 550–561. DOI: [10.1175/1520-0450\(1988\)027<0550:SDOWSA>2.0.CO;2](https://doi.org/10.1175/1520-0450(1988)027<0550:SDOWSA>2.0.CO;2).
- Joussaume, S. (1990). "Three-dimensional simulations of the atmospheric cycle of desert dust particles using a general circulation model". In: *J. Geophys. Res. Atmos.* 95.D2, pp. 1909–1941. DOI: [10.1029/JD095iD02p01909](https://doi.org/10.1029/JD095iD02p01909).
- Judd, M. J., M.R. Raupach, and J. Finnigan (1996). "A wind tunnel study of turbulent flow around single and multiple windbreaks, part I: Velocity fields". In: *Boundary Layer Meteorol.* 80, pp. 127–165. DOI: [10.1007/BF00119015](https://doi.org/10.1007/BF00119015).



- Kaimal, J.C. and J.J. Finnigan (1994). *Atmospheric Boundary Layer Flows: Their Structure and Measurement*. Oxford University Press. ISBN: 9780195062397.
- Kamawura, R. (1951). *Study of sand movement by wind*. Tech. rep. Hydraul Eng Lab, Univ of Calif.
- Katsuyuki, M. (2009). "Soil and humanity: Culture, civilization, livelihood and health". In: *J. Soil Sci. Plant Nutr.* 55.5, pp. 603–615. DOI: [10.1111/j.1747-0765.2009.00401.x](https://doi.org/10.1111/j.1747-0765.2009.00401.x).
- Katul, G. G. *et al.* (2010). "Predicting the dry deposition of aerosol-sized particles using layer-resolved canopy and pipe flow analogy models: Role of turbophoresis". In: *J. Geophys. Res. Atmos.* 115. DOI: [10.1029/2009JD012853](https://doi.org/10.1029/2009JD012853).
- Kawamura, R (1964). "Study of Sand Movement by Wind". In: *Univ. Tokyo, Rep. Inst. Sci. Technol.* 5.
- Kim, D. S., G. H. Cho, and B. R. White (2000). "A Wind-tunnel Study of Atmospheric Boundary-Layer Flow over Vegetated Surfaces to Suppress PM10 Emission on Owens (dry) Lake". In: *Boundary Layer Meteorol.* 97.2, pp. 309–329. DOI: [10.1023/A:1002786323224](https://doi.org/10.1023/A:1002786323224).
- Klose, M. and Y. Shao (2013). "Large-eddy simulation of turbulent dust emission". In: *Aeolian Res.* 8, pp. 49–58. DOI: [10.1016/j.aeolia.2012.10.010](https://doi.org/10.1016/j.aeolia.2012.10.010).
- Knippertz, P. and J.B.W. Stuut (2014). *Mineral Dust: A Key Player in the Earth System*. Springer Netherlands. ISBN: 9789401789776.
- Kok, J. F. (2011a). "Does the size distribution of mineral dust aerosols depend on the wind speed at emission?" In: *Atmos. Chem. Phys.* 11.19, pp. 10149–10156. DOI: [10.5194/acp-11-10149-2011](https://doi.org/10.5194/acp-11-10149-2011).
- Kok, J. F. *et al.* (2014). "An improved dust emission model – Part 1: Model description and comparison against measurements". In: *Atmos. Chem. Phys.* 14.23, pp. 13023–13041. DOI: [10.5194/acp-14-13023-2014](https://doi.org/10.5194/acp-14-13023-2014).
- Kok, Jasper F. (2011b). "A scaling theory for the size distribution of emitted dust aerosols suggests climate models underestimate the size of the global dust cycle". In: *Proc. Natl. Acad. Sci.* 108.3, pp. 1016–1021. DOI: [10.1073/pnas.1014798108](https://doi.org/10.1073/pnas.1014798108).
- Kok, Jasper F. and Nilton O. Renno (2009). "A comprehensive numerical model of steady state saltation (COMSALT)". In: *J. Geophys. Res. Atmos.* 114.D17. DOI: [10.1029/2009JD011702](https://doi.org/10.1029/2009JD011702).
- Kok, Jasper F. *et al.* (2012). "The physics of wind-blown sand and dust". In: *Rep. Prog. Phys.* 75.10, p. 106901. DOI: [10.1088/0034-4885/75/10/106901](https://doi.org/10.1088/0034-4885/75/10/106901).
- Kolmogorov, A N (1941). "Local structure of turbulence in an incompressible viscous fluid at very high reynolds numbers". In: *Soviet Phys. Uspekhi* 10.6, pp. 734–746.
- Lancaster, N. and A. Baas (1998). "Influence of vegetation cover on sand transport by wind: field studies at Owens Lake, California". In: *Earth Surf. Proc. Land.* 23.1, pp. 69–82. DOI: [10.1002/\(SICI\)1096-9837\(199801\)23:1<69::AID-ESP823>3.0.CO;2-G](https://doi.org/10.1002/(SICI)1096-9837(199801)23:1<69::AID-ESP823>3.0.CO;2-G).
- Lebel, T. *et al.* (2010). "The AMMA field campaigns: multiscale and multidisciplinary observations in the West African region". In: *Q. J. Royal Meteorol. Soc.* 136.S1, pp. 8–33. DOI: [10.1002/qj.486](https://doi.org/10.1002/qj.486).

- Leenders, J. K., J. H. van Boxel, and G. Sterk (2007). "The effect of single vegetation elements on wind speed and sediment transport in the Sahelian zone of Burkina Faso". In: *Earth Surf. Proc. Land*. 32.10, pp. 1454–1474. DOI: [10.1002/esp.1452](https://doi.org/10.1002/esp.1452).
- Legg, B. J. and F. A. Powell (1979). "Spore dispersal in a barley crop: A mathematical model". In: *Agri. Meteorol.* 20, pp. 47–67. DOI: [10.1016/0002-1571\(79\)90050-5](https://doi.org/10.1016/0002-1571(79)90050-5).
- Lettau, K. and H. H. Lettau (1978). "Experimental and micro-meteorological field studies of dune migration, exploring the world's driest climate". In: *IES Report 101, Univ of Wisconsin-Madison, Institute for Env. Studies, Madison, USA*, pp. 110–147.
- Li, D. and E. Bou-Zeid (2011). "Coherent Structures and the Dissimilarity of Turbulent Transport of Momentum and Scalars in the Unstable Atmospheric Surface Layer". In: *Boundary Layer Meteorol.* 140.2, pp. 243–262. DOI: [10.1007/s10546-011-9613-5](https://doi.org/10.1007/s10546-011-9613-5).
- Logie, M. (1982). "Influence of roughness elements and soil moisture and the resistance of sand to wind erosion." In: *Catena* 1, pp. 161–173.
- Lowdermilk, W. C. (1975). *Conquest of the Land Through Seven Thousand Years*. Agriculture information bulletin. U.S. Department of Agriculture, Soil Conservation Service.
- Maria, K., M. Stelios, and T. Kostas (2018). "Aerosols in atmospheric chemistry and biogeochemical cycles of nutrients". In: *Environ. Res. Lett.* 13.6. DOI: [10.1088/1748-9326/aabcdb](https://doi.org/10.1088/1748-9326/aabcdb).
- Marshall, J. H. *et al.* (2013). "Meteorology and dust in the central Sahara: Observations from Fennec supersite-1 during the June 2011 Intensive Observation Period". In: *J. Geophys. Res. Atmos* 118.10, pp. 4069–4089. DOI: [10.1002/jgrd.50211](https://doi.org/10.1002/jgrd.50211).
- Marticorena, B. and G. Bergametti (1995). "Modeling the atmospheric dust cycle: 1. Design of a soil-derived dust emission scheme". In: *J. Geophys. Res., Atmos.* 100.D8, pp. 16415–16430. DOI: [10.1029/95JD00690](https://doi.org/10.1029/95JD00690).
- Martin, J. H., M. Gordon, and S. E. Fitzwater (1991). "The case for iron". In: *Limnol Oceanogr.* 36.8, pp. 1793–1802. DOI: [10.4319/lo.1991.36.8.1793](https://doi.org/10.4319/lo.1991.36.8.1793).
- Mayaud, J. R., G. F. S. Wiggs, and R. M. Bailey (2016a). "Characterizing turbulent wind flow around dryland vegetation". In: *Earth Surf. Proc. Land*. 41.10, pp. 1421–1436. DOI: [10.1002/esp.3934](https://doi.org/10.1002/esp.3934).
- Mayaud, J.R., G. F. S. Wiggs, and R. M. Bailey (2016b). "Dynamics of skimming flow in the wake of a vegetation patch". In: *Aeolian Res.* 22, pp. 141–151. DOI: [10.1016/j.aeolia.2016.08.001](https://doi.org/10.1016/j.aeolia.2016.08.001).
- McLeman, R. A. *et al.* (2014). "What we learned from the Dust Bowl: lessons in science, policy, and adaptation". In: *Popul. Environ.* 35.4, pp. 417–440.
- Mekonnen, M. M. and A. Y. Hoekstra (2011). "The green, blue and grey water footprint of crops and derived crop products". In: *Hydrol. Earth Syst. Sci.* 15.5, pp. 1577–1600. DOI: [10.5194/hess-15-1577-2011](https://doi.org/10.5194/hess-15-1577-2011).
- Menut, L., I. Chiapello, and C. Moulin (2009). "Previsibility of mineral dust concentrations: The CHIMERE-DUST forecast during the first AMMA experiment dry season". In: *J. Geophys. Res.* 114.

- Meron, Ehud *et al.* (2004). "Vegetation patterns along a rainfall gradient". In: *Chaos Solitons Fract.* 19.2, pp. 367–376. DOI: [10.1016/S0960-0779\(03\)00049-3](https://doi.org/10.1016/S0960-0779(03)00049-3).
- Middleton, N., D. S. G. Thomas, and UNEP (1997). *World Atlas of Desertification*. Arnold. ISBN: 9780470244197.
- Monin and Obukhov (1954). "Basic laws of turbulent mixing in the surface layer of the atmosphere". In: *Akad. Nauk SSSR Geophys. Inst.* 24, pp. 163–187.
- Montgomery, D. R. (2007). "Soil erosion and agricultural sustainability". In: *Proc. Nat. Acad. Sci.* 104.33, pp. 13268–13272. DOI: [10.1073/pnas.0611508104](https://doi.org/10.1073/pnas.0611508104).
- Munson, S. M., J. Belnap, and G. S. Okin (2011). "Responses of wind erosion to climate-induced vegetation changes on the Colorado Plateau". In: *Proc. Natl. Acad. Sci.* 108.10, pp. 3854–3859. DOI: [10.1073/pnas.1014947108](https://doi.org/10.1073/pnas.1014947108).
- Musick, H. B. and D. A. Gillette (1990). "Field evaluation of relationships between a vegetation structural parameter and sheltering against wind erosion". In: *Land Degrad. Dev.* 2.2, pp. 87–94. DOI: [10.1002/ldr.3400020203](https://doi.org/10.1002/ldr.3400020203).
- Neuman, C. M. (2004). "Effects of temperature and humidity upon the transport of sedimentary particles by wind". In: *Sedimentology* 51.1, pp. 1–17. DOI: [10.1046/j.1365-3091.2003.00604.x](https://doi.org/10.1046/j.1365-3091.2003.00604.x).
- Nickling, W. G. and J. A. Gillies (1993). "Dust emission and transport in Mali, West Africa". In: *Sedimentology* 40.5, pp. 859–868. DOI: [10.1111/j.1365-3091.1993.tb01365.x](https://doi.org/10.1111/j.1365-3091.1993.tb01365.x).
- Núñez, M. *et al.* (2013). "Assessing potential desertification environmental impact in life cycle assessment. Part 2: Agricultural case study in Spain and Argentina". In: *Int. J. Life Cycle Ass.* 18.7, pp. 1302–1315. DOI: [10.1007/s11367-013-0582-4](https://doi.org/10.1007/s11367-013-0582-4).
- Otto, S. *et al.* (2007). "Atmospheric radiative effects of an in situ measured Saharan dust plume and the role of large particles". In: *Atmos. Chem. Phys.* 7.18, pp. 4887–4903. DOI: [10.5194/acp-7-4887-2007](https://doi.org/10.5194/acp-7-4887-2007).
- Ouchene, R. *et al.* (2018). "Acceleration statistics of prolate spheroidal particles in turbulent channel flow". In: *J. Turbulence* 19.10, pp. 827–848. DOI: [10.1080/14685248.2018.1516043](https://doi.org/10.1080/14685248.2018.1516043).
- Owen, P. R. (1964). "Saltation of uniform grains in air". In: *J. Fluid Mech.* 20.2, 225–242. DOI: [10.1017/S0022112064001173](https://doi.org/10.1017/S0022112064001173).
- Peters, K. and R. Eiden (1992). "Modelling the dry deposition velocity of aerosol particles to a spruce forest". In: *Atmos. Environ.* 26.14, pp. 2555–2564. DOI: [10.1016/0960-1686\(92\)90108-W](https://doi.org/10.1016/0960-1686(92)90108-W).
- Petroff, A. *et al.* (2008). "Aerosol dry deposition on vegetative canopies. Part II: A new modelling approach and applications." In: *Atmos. Environ.*
- Petroff, A. and L. Zhang (2010). "Development and validation of a size-resolved particle dry deposition scheme for application in aerosol transport models". In: *Geosci. Model Dev.* 3.2, pp. 753–769. DOI: [10.5194/gmd-3-753-2010](https://doi.org/10.5194/gmd-3-753-2010).
- Pierre, C. *et al.* (2012). "Impact of vegetation and soil moisture seasonal dynamics on dust emissions over the Sahel". In: *J. Geophys. Res. Atmos.* 117.D6. DOI: [10.1029/2011JD016950](https://doi.org/10.1029/2011JD016950).

- Pimentel, D.C. *et al.* (1995). "Environmental and Economic Cost of Soil Erosion and Conservation Benefits". In: *Science* 267. DOI: [10.1126/science.267.5201.1117](https://doi.org/10.1126/science.267.5201.1117).
- Pryor, S. C. *et al.* (2008). "Upward fluxes of particles over forests: when, where, why?" In: *Tellus B* 60, pp. 372–380. DOI: [10.1111/j.1600-0889.2008.00341.x](https://doi.org/10.1111/j.1600-0889.2008.00341.x).
- Pye, K. and H. Tsoar (1990). *Aeolian sand and sand dunes*. Springer Netherlands. ISBN: 9789401159883.
- Rasmussen, K. R., M. Sorensen, and B.B. Willetts (1985). "Measurement of saltation and wind strength on beaches". In: *Proceedings of International Workshop on the Physics of Blown Sand*. Ed. by O. E. Barndorff-Nielsen *et al.* Vol. 8. 2. Dep. of Theor. Stat., Aarhus Univ. Aarhus, Denmark.
- Raupach, M R (1991). "Saltation layers, vegetation canopies and roughness lengths". In: *Acta Mech. Supp.* DOI: [10.1007/978-3-7091-6706-9\\_5](https://doi.org/10.1007/978-3-7091-6706-9_5).
- Raupach, M.R. (1992). "Drag and drag partition on rough surfaces". In: *Boundary Layer Meteorol.* 60, pp. 375–395. DOI: [10.1007/BF00155203](https://doi.org/10.1007/BF00155203).
- Ravi, S. *et al.* (Apr. 2010). "Land degradation in drylands: Interactions among hydrologic-aeolian erosion and vegetation dynamics". In: *Geomorphol.* 116.3-4, pp. 236–245. DOI: [10.1016/j.geomorph.2009.11.023](https://doi.org/10.1016/j.geomorph.2009.11.023).
- Reid, J. S. *et al.* (2008). "Dynamics of southwest Asian dust particle size characteristics with implications for global dust research". In: *J. Geophys. Res. Atmos.* 113.D14. DOI: [10.1029/2007JD009752](https://doi.org/10.1029/2007JD009752).
- Reynolds, O. (1895). "IV. On the dynamical theory of incompressible viscous fluids and the determination of the criterion". In: *Philos. Trans. Royal Soc.* 186, pp. 123–164. DOI: [10.1098/rsta.1895.0004](https://doi.org/10.1098/rsta.1895.0004).
- Rice, M. A., B. B. Willetts, and I. K. McEwan (1995). "An experimental study of multiple grain-size ejecta produced by collisions of saltating grains with a flat bed". In: *Sedimentology* 42.4, pp. 695–706. DOI: [10.1111/j.1365-3091.1995.tb00401.x](https://doi.org/10.1111/j.1365-3091.1995.tb00401.x).
- Sabbah, I. *et al.* (2012). "Remote sensing of desert dust over Kuwait: long-term variation". In: *Atmos. Pollut. Res.* 3.1, pp. 95–104. DOI: [10.5094/APR.2012.009](https://doi.org/10.5094/APR.2012.009).
- Scherr, S. J. (1999). *Soil Degradation: A Threat to Developing-country Food Security by 2020?* Food, agriculture, and the environment discussion paper. International Food Policy Research Institute. ISBN: 9780896296312.
- Seinfeld, J. H. and S. N. Pandis (1998). *Atmospheric chemistry and physics: from air pollution to climate change*. A Wiley interscience publication. Wiley. ISBN: 9780471178156.
- Sequeira, R. (1993). "On the large-scale impact of arid dust on precipitation chemistry of the continental northern hemisphere". In: *Atmos. Environ.* 27.10, pp. 1553–1565. DOI: [10.1016/0960-1686\(93\)90155-R](https://doi.org/10.1016/0960-1686(93)90155-R).
- Shao (2008). *Physics and Modelling of Wind Erosion*. Springer Netherlands. DOI: [10.1007/978-1-4020-8895-7](https://doi.org/10.1007/978-1-4020-8895-7).
- Shao, Y. (2001). "A model for mineral dust emission". In: *J. Geophys. Res. Atmos.* 106.D17, pp. 20239–20254. DOI: [10.1029/2001JD900171](https://doi.org/10.1029/2001JD900171).

- Shao, Y., M. R. Raupach, and P. A. Findlater (1993). "Effect of saltation bombardment on the entrainment of dust by wind". In: *J. Geophys. Res. Atmos.* 98.D7, pp. 12719–12726. DOI: [10.1029/93JD00396](https://doi.org/10.1029/93JD00396).
- Shao, Y., M. R. Raupach, and Leys J. F. (1996). "A model for predicting aeolian sand drift and dust entrainment on scales from paddock to region". In: *Soil Res.* 34, pp. 309–342. DOI: [10.1071/SR9960309](https://doi.org/10.1071/SR9960309).
- Shao, Y. and A. Li (1999). "Numerical Modelling of Saltation in the Atmospheric Surface Layer". In: *Boundary Layer Meteorol.* 91, pp. 199–225. DOI: [10.1023/A:1001816013475](https://doi.org/10.1023/A:1001816013475).
- Shao, Y. and H. Lu (2000). "A simple expression for wind erosion threshold friction velocity". In: *J. Geophys. Res. Atmos.* 105.D17, pp. 22437–22443. DOI: [10.1029/2000JD900304](https://doi.org/10.1029/2000JD900304).
- Shao, Y. *et al.* (2011). "Parameterization of size-resolved dust emission and validation with measurements". In: *J. Geophys. Res. Atmos.* 116.D8. DOI: [10.1029/2010JD014527](https://doi.org/10.1029/2010JD014527).
- Sharratt, B. S. *et al.* (2015). "Implications of climate change on wind erosion of agricultural lands in the Columbia plateau". In: *Weather Clim. Extrem.* 10, pp. 20–31. DOI: [10.1016/j.wace.2015.06.001](https://doi.org/10.1016/j.wace.2015.06.001).
- She, L. *et al.* (2018). "Dust Detection and Intensity Estimation Using Himawari-8/AHI Observation". In: *Remote Sens.* 10.4. DOI: [10.3390/rs10040490](https://doi.org/10.3390/rs10040490).
- Simonneaux, V. *et al.* (2015). "Land use and climate change effects on soil erosion in a semi-arid mountainous watershed (High Atlas, Morocco)". In: *J. Arid Environ.* 122, pp. 64–75. DOI: [10.1016/j.jaridenv.2015.06.002](https://doi.org/10.1016/j.jaridenv.2015.06.002).
- Slinn, S. A. and W. G. N. Slinn (1980). "Predictions for particle deposition on natural waters". In: *Atmos. Environ.* 14.9, pp. 1013–1016. DOI: [10.1016/0004-6981\(80\)90032-3](https://doi.org/10.1016/0004-6981(80)90032-3).
- Slinn, W. G. N. (1982). "Predictions for particle deposition to vegetative canopies". In: *Atmos. Environ.* 16.7, pp. 1785–1794. DOI: [10.1016/0004-6981\(82\)90271-2](https://doi.org/10.1016/0004-6981(82)90271-2).
- Smedman, A-S. *et al.* (2007). "Heat/mass transfer in the slightly unstable atmospheric surface layer". In: *Q. J. Roy. Meteor. Soc.* 133.622, pp. 37–51. DOI: [10.1002/qj.7](https://doi.org/10.1002/qj.7).
- Sofue, Y. *et al.* (2017). "The Interactions Between Precipitation, Vegetation and Dust Emission Over Semi-Arid Mongolia". In: *Atmos. Chem. Phys.* 2017. DOI: [10.5194/acp-2017-83](https://doi.org/10.5194/acp-2017-83).
- Sow, M. *et al.* (2009). "Size resolved dust emission fluxes measured in Niger during 3 dust storms of the AMMA experiment". In: *Atmos. Chem. Phys.* 9.12, pp. 3881–3891. DOI: [10.5194/acp-9-3881-2009](https://doi.org/10.5194/acp-9-3881-2009).
- Sow, M., S. C. Alfaro, and J. L. Rajot (2011). "Comparison of the size-resolved dust emission fluxes measured over a Sahelian source with the Dust Production Model (DPM) predictions". In: *Atmos. Chem. Phys.* 11, pp. 11077–11107. DOI: [10.5194/acpd-11-11077-2011](https://doi.org/10.5194/acpd-11-11077-2011).
- Sowden, M., U. Mueller, and D. Blake (2018). "Review of surface particulate monitoring of dust events using geostationary satellite remote sensing". In: *Atmos. Environ.* 183, pp. 154–164. DOI: [10.1016/j.atmosenv.2018.04.020](https://doi.org/10.1016/j.atmosenv.2018.04.020).
- Sterk, G. (2003). "Causes, consequences and control of wind erosion in Sahelian Africa: a review". In: *Land Degrad. Dev.* 14.1, pp. 95–108. DOI: [10.1002/ldr.526](https://doi.org/10.1002/ldr.526).



- Stewart, J. *et al.* (2014). "Modeling emergent patterns of dynamic desert ecosystems". In: *Ecol. Monographs* 84.3, pp. 373–410. DOI: [10.1890/12-1253.1](https://doi.org/10.1890/12-1253.1).
- Stout, J. E. and T. M. Zobeck (1997). "Intermittent saltation". In: *Sedimentology* 44.5, pp. 959–970. DOI: [10.1046/j.1365-3091.1997.d01-55.x](https://doi.org/10.1046/j.1365-3091.1997.d01-55.x).
- Stull, R. B. (1988). *An Introduction to Boundary Layer Meteorology*. Atmospheric and Oceanographic Sciences Library. Springer Netherlands. ISBN: 9789027727695.
- Sutton, S. L. F. and C. McKenna-Neuman (2008). "Variation in bed level shear stress on surfaces sheltered by nonerrodible roughness elements". In: *J. Geophys. Res. Earth Surf.* 113.F3. DOI: [10.1029/2007JF000967](https://doi.org/10.1029/2007JF000967).
- Swap, R. *et al.* (1992). "Saharan dust in the Amazon Basin". In: *Tellus B* 44.2, pp. 133–149. DOI: [10.1034/j.1600-0889.1992.t01-1-00005.x](https://doi.org/10.1034/j.1600-0889.1992.t01-1-00005.x).
- Tatarko, J. and L. Wagner (2007). "An introduction to the Wind Erosion Prediction System (WEPS)". In: vol. 5. DOI: [10.13031/2013.23376](https://doi.org/10.13031/2013.23376).
- Tatarko, J. and D. Presley (2009). "Principles of Wind Erosion and its Control". In: *K-State Research and Extension Publication MF-2860*.
- Tegen, I. and I. Fung (1995). "Contribution to the atmospheric mineral aerosol load from land surface modification". In: *J. Geophys. Res. Atmos.* 100.D9, pp. 18707–18726. DOI: [10.1029/95JD02051](https://doi.org/10.1029/95JD02051).
- Telles, T. S., M. F. Guimarães, and S. C. F. Dechen (Apr. 2011). "The costs of soil erosion". In: *Rev. Bras. Cienc. Solo.* 35, pp. 287–298. DOI: [10.1590/S0100-06832011000200001](https://doi.org/10.1590/S0100-06832011000200001).
- Urban, F. E., R. L. Reynolds, and R. Fulton (2009). "The dynamic interaction of climate, vegetation, and dust emission, Mojave Desert, USA". In: *Arid Environ. Wind Erosion*, pp. 243–267.
- Ven, T. A. M. van de, D. W. Fryrear, and W. P. Spaan (1989). "Vegetation characteristics and soil loss by wind." In: *J. Soil Water Conserv.* 44, pp. 347–49.
- Vinkovic, I., C. Aguirre, and S. Simoëns (2005). "Large Eddy Simulation of the Dispersion of Solid Particles and Droplets in a Turbulent Boundary Layer Flow". In: *Engineering Turbulence Modelling and Experiments*, pp. 969–978.
- Wallace, J. M. (2016). "Quadrant Analysis in Turbulence Research: History and Evolution". In: *Annu. Rev. Fluid Mech.* 48.1, pp. 131–158. DOI: [10.1146/annurev-fluid-122414-034550](https://doi.org/10.1146/annurev-fluid-122414-034550).
- Washington, R. *et al.* (2006a). "African Climate Change: Taking the Shorter Route". In: *Bull. Amer. Meteor. Soc.* 87.10, pp. 1355–1366. DOI: [10.1175/BAMS-87-10-1355](https://doi.org/10.1175/BAMS-87-10-1355).
- Washington, R. *et al.* (2006b). "Dust and the low-level circulation over the Bodélé Depression, Chad: Observations from BoDEx 2005". In: *J. Geophys. Res. Atmos.* 111.D3. DOI: [10.1029/2005JD006502](https://doi.org/10.1029/2005JD006502).
- Wasson, R. J. and P. M. Nanninga (1986). "Estimating wind transport of sand on vegetated surfaces". In: *Earth Surf. Proc. Land.* 11.5, pp. 505–514. DOI: [10.1002/esp.3290110505](https://doi.org/10.1002/esp.3290110505).
- Wesely, M.L. (1989). "Parameterization of surface resistances to gaseous dry deposition in regional-scale numerical models". In: *Atmos. Environ.* 23, pp. 1293–1304. DOI: [10.1016/0004-6981\(89\)90153-4](https://doi.org/10.1016/0004-6981(89)90153-4).

- Weuve, Jennifer *et al.* (2012). "Exposure to Particulate Air Pollution and Cognitive Decline in Older Women". In: *Arch. Intern. Med.* 172, pp. 219–227. DOI: [10.1001/archinternmed.2011.683](https://doi.org/10.1001/archinternmed.2011.683).
- White, B. R. (1979). "Soil transport by winds on Mars". In: *J. Geophys. Res. Solid Earth* 84.B9, pp. 4643–4651. DOI: [10.1029/JB084iB09p04643](https://doi.org/10.1029/JB084iB09p04643).
- Wiggs, G. F. S. *et al.* (1994). "Effect of vegetation removal on airflow patterns and dune dynamics in the southwest Kalahari desert". In: *Land Degrad. Dev.* 5.1, pp. 13–24. DOI: [10.1002/ldr.3400050103](https://doi.org/10.1002/ldr.3400050103).
- Wiman, L. B. and G.I. Ågren (Dec. 1985). "Aerosol depletion and deposition in forests—A model analysis". In: *Atmos. Environ.* 19, pp. 335–347. DOI: [10.1016/0004-6981\(85\)90101-5](https://doi.org/10.1016/0004-6981(85)90101-5).
- Wolfe, S. A. and W. G. Nickling (1993). "The protective role of sparse vegetation in wind erosion". In: *Prog. Phys. Geogr. Earth Environ.* 17.1, pp. 50–68. DOI: [10.1177/030913339301700104](https://doi.org/10.1177/030913339301700104).
- Woodruff, N. P. and F.H.A. Siddoway (1965). "Wind Erosion Equation 1". In: *Soil Sci. Soc. Am. J.* 29, 602–608. DOI: [10.1007/978-1-4020-3995-9\\_640](https://doi.org/10.1007/978-1-4020-3995-9_640).
- Xue, M. *et al.* (1995). "ARPS Version 4.0 User's Guide". In: *Cent. Anal. Predict. Storms, Univ. of Okla., Norman*.
- Zender, C. S. and E. Y. Kwon (2005). "Regional contrasts in dust emission responses to climate". In: *J. Geophys. Res. Atmos.* 110.D13. DOI: [10.1029/2004JD005501](https://doi.org/10.1029/2004JD005501).
- Zhang, J., Y. Shao, and N. Huang (2014). "Measurements of dust deposition velocity in a wind-tunnel experiment". In: *Atmos. Chem. Phys.* 14.17, pp. 8869–8882. DOI: [10.5194/acp-14-8869-2014](https://doi.org/10.5194/acp-14-8869-2014).
- Zhao, T. L. *et al.* (2003). "Modeled size-segregated wet and dry deposition budgets of soil dust aerosol during ACE-Asia 2001: Implications for trans-Pacific transport". In: *J. Geophys. Res. Atmos.* 108.D23. DOI: [10.1029/2002JD003363](https://doi.org/10.1029/2002JD003363).
- Zobeck, T. M. and R. Scott Van Pelt (2006). "Wind-induced dust generation and transport mechanics on a bare agricultural field". In: *J. Hazard. Mater.* 132.1, pp. 26–38. DOI: [10.1016/j.jhazmat.2005.11.090](https://doi.org/10.1016/j.jhazmat.2005.11.090).